Doctoral theses at NTNU, 2023:197

Miran Cemalovic

Earthquake response of bridges supported by vertical and batter piles accounting for nonlinear soil-structure interaction

Doctoral thesis

NTNU
Norwegian University of Science and Technology
Thesis for the Degree of
Philosophiae Doctor
Faculty of Engineering
Department of Structural Engineering

NTNU
Norwegian University of
Science and Technology

Miran Cemalovic

Earthquake response of bridges supported by vertical and batter piles accounting for nonlinear soil-structure interaction

Thesis for the Degree of Philosophiae Doctor

Trondheim, June 2023

Norwegian University of Science and Technology
Faculty of Engineering
Department of Structural Engineering

NTNU
Norwegian University of
Science and Technology

NTNU
Norwegian University of Science and Technology

Thesis for the Degree of Philosophiae Doctor

Faculty of Engineering
Department of Structural Engineering

ISBN 978-82-326-7096-3 (printed ver.)
ISBN 978-82-326-7095-6 (electronic ver.)
ISSN 1503-8181 (printed ver.)
ISSN 2703-8084 (online ver.)

Doctoral theses at NTNU, 2023:197

Printed by NTNU Grafisk senter

Preface

This thesis is submitted in partial fulfilment of the requirements for the degree Philosophiae Doctor at the Norwegian University of Science and Technology. The work has been carried out at the Department of Structural Engineering, Faculty of Engineering. Professor Amir M. Kaynia and Associate Professor Jan B. Husebø (Department of Civil Engineering, Western Norway University of Applied Sciences and Sweco Norway AS) have supervised the work. Sweco Norway AS and The Research Council of Norway have funded the work.

Publications

This thesis is based on three journal papers [1, 2, 3] that have been published in the international peer-reviewed journal *Earthquake Engineering & Structural Dynamics* (EESD). In addition, a fourth paper is presently being prepared for submission to a journal. The content in this thesis is however more extensive than the journal papers. The papers are listed below.

Paper 1: *Cemalovic M, Husebø JB, Kaynia AM. Simplified computational methods for estimating dynamic impedance of batter pile groups in homogeneous soil. Earthquake Engng Struct Dyn.2021;50:3894–3915.*

Paper 2: *Cemalovic M, Husebø JB, Kaynia AM. Kinematic response of vertical and batter pile groups in non-linear soft soil. Earthquake Engng Struct Dyn. 2022;51:2248-2266.*

Paper 3: *Cemalovic M, Castro JM, Kaynia AM. Practical macro-element for vertical and batter pile groups. Earthquake Engng Struct Dyn. 2023;52:1091–1111.*

Paper 4: *Cemalovic M, Husebø JB, Kaynia AM. Earthquake response of IABs supported by vertical and batter piles accounting for nonlinear soil-structure interaction: A macro-element approach. In preparation for journal submission.*

In Paper 1, Miran Cemalovic and Amir M. Kaynia planned direction of the study. Cemalovic developed the theoretical framework, the numerical tools and wrote the manuscript in discussions with Professor Amir M. Kaynia and Jan B. Husebø. Both co-authors contributed with proof-reading of the manuscript. In Paper 2, Miran Cemalovic and Amir M. Kaynia planned direction of the study. Cemalovic implemented the numerical tools, performed the analyses and wrote the manuscript in discussions with Professor Amir M. Kaynia and Jan B. Husebø. Both co-authors contributed with proof-reading of the manuscript. In Paper 3, Miran Cemalovic and Amir M. Kaynia planned direction of the study. Cemalovic developed the theoretical framework and the numerical schemes, performed the analyses and wrote the manuscript in discussions with Professor Amir M. Kaynia and Professor José Miguel Castro. Both co-authors contributed with proof-reading of the manuscript. In Paper 4, Miran Cemalovic and Amir M. Kaynia planned direction of the study. Cemalovic developed the numerical tools, performed the analyses and wrote the manuscript in discussions with Professor Amir M. Kaynia and Jan B. Husebø. Both co-authors contributed with proof-reading of the manuscript.

Abstract

Around the world, large structures such as bridges, harbours and skyscrapers, are built in areas where the seismic risk is relatively high. In many cases, these structures are supported by deep foundations due to overlaying soft soil. During an earthquake, the response of the structure and the response of the soil depend on each other. The ground motion influences the displacements of the structure and the motion of the structure influences the displacements of the soil. This is referred to as *soil-structure interaction* (SSI) and the phenomena may be particularly important for structures supported by deep foundations. Easy access to commercial FE-software allows for accurate assessment of most structural and geotechnical problems. However, obtaining rigorous numerical solutions for dynamic soil-structure interaction response is a challenging and time-consuming process that often requires a cross-disciplinary skill set. As a result, simplified methods that are robust, user-friendly, and verifiable are often preferred in practical engineering.

The main objective of this doctoral work is to aid the industry with practical computational methods for analyzing structures, particularly bridges, that are supported by deep foundations using both vertical and batter piles. These methods aim to capture the essence of SSI while also being straight-forward to understand, implement and apply.

The thesis is divided into four parts. The first part investigates the kinematic response of vertical and batter pile groups by evaluating how non-linearity, batter angle, pile spacing and excitation frequency affect pile-cap displacements, rotations, maximum pile moments, shear forces and axial forces. The second part introduces a diagonal impedance matrix for vertical and batter pile groups in linear, homogeneous soil that takes into account pile-soil-pile interaction. The solution is suited for low-exaction seismic problems, vibration problems or estimates in the early-stage design process. The third part presents a nonlinear macro-element for vertical and batter pile groups. The solution is intended for realistic nonlinear time-history analyses and efficient estimation of equivalent linear properties. The fourth part introduces a finite element framework for seismic analysis of structures that incorporates the previously developed solutions.

Acknowledgements

I would like to extend my sincere gratitude to all those who have contributed to this thesis.

I am especially grateful to Sweco Norway AS for affording me the opportunity to pursue my PhD. I would also like to extend a special acknowledgment to Kristian Rommetveit Dahl for his support of this research project, and for facilitating my dual roles as a consultant and a PhD student in the most effective way possible.

To my main supervisor, Professor Amir M. Kaynia, from The Norwegian University of Science and Technology, for generously sharing his extensive knowledge and experience in the field of earthquake engineering. It is truly a privilege to learn from you.

To my co-supervisor, Associate Professor Jan Bernt Husebø, from The Western Norway University of Applied Sciences and Sweco Norway AS, not only for your contributions to this thesis, but also for the guidance and countless discussions throughout my career as a bridge engineer at Sweco.

To Associate Professor Jose Miguel Castro and The University of Porto for providing me with the opportunity to be a guest researcher at their institution.

To Professor Anders Rønnquist and the administrative staff at the Department of Structural Engineering for all of the resources and support they provided.

Last but certainly not least, to Marie, to my mother and to the rest of my family for their support and patience throughout this entire process.

Contents

Chapter 1

Introduction

1.1 Research background

1.1.1 Industrial ph.d.-program

The funding for this research was provided through an industrial Ph.D.-program as a collaboration between *Sweco Norway AS*, *Norwegian University of Science and Technology* (NTNU) and *The Research Council of Norway* (RCN). The industrial Ph.D. program in Norway allows companies to apply for research funding through a doctoral program for their employees. This program is a governmental initiative aimed at promoting collaboration between educational institutions and the industry, as well as encouraging research and development that can benefit companies and the industry as a whole.

This doctoral work was a three-plus-one year-program, where one year was dedicated to project work within company. During this period, the author was engaged in multiple projects and tasks for the company:

- Design of a pedestrian concrete bridge in Bergen, Norway supported by steel core piles. The bridge is a part of the Light Railway system in the inner city of Bergen.
- Design of a post-tensioned road bridge in Askøy, Norway. The bridge is a part of the new E-road (E39) along Norway's coastline.
- Design of two concrete culverts. The culverts are a part of the Light Railway system in the inner city of Bergen.

- Design of a small pedestrian timber bridge.
- Retrofitting of a small road bridge outside Bergen, Norway using FRP-plates.
- Development of a fully-automatized code that utilizes a commercial FE-software for the calculation and design of simple culverts. The input and output generated by the code comply with both Eurocode and the demands from the Norwegian Public Roads Administration. This allows for the design of such structures in a fraction of the expected timeframe. The code was developed as part of an E-road project that contained multiple similar culverts.
- Development of templates for design reports that comply with Eurocode and the demands from the Norwegian Public Road Administration.
- Supervision of a master's thesis titled *Analysis and design of concrete culverts - Comparison between shell and frame models*

The purpose of this industrial Ph.D.-program is to (1) enhance the in-house earthquake engineering expertise and (2) bridge the gap (no pun intended) between the geotechnical and structural engineering departments. The research project is shaped by the authors' background in the consultancy industry, as well as the overall framework established by the funding parties. The overarching philosophy emphasizes the practicality and applicability of engineering principles in real-world scenarios.

1.1.2 Problem and motivation

Around the world, large structures such as bridges, harbours and skyscrapers, are built in areas where the seismic risk is relatively high. In many cases, these structures are supported by deep foundations due to overlaying soft soil. During an earthquake, the response of the structure and the response of the soil depend on each other. The ground motion influences the displacements of the structure and the motion of the structure influences the displacements of the soil. This is referred to as *soil-structure interaction* (SSI) and the phenomena may be particularly important for structures supported by deep foundations. First recognized in the late 19th century, SSI began to receive more attention in the late 20th century, mainly driven by the safety demands of nuclear power plants and offshore structures [4, 5]. Today, SSI is recognized as an inherent part of seismic design.

In recent decades, *performance-based earthquake engineering* (PBEE) has become the standard practice in earthquake engineering. Traditionally, design codes and guidelines prescribe a fixed set of requirements that must be met in seismic design of structures. Such requirements ensure that the structure has adequate strength and ductility to safely resist the seismic forces. This is known as *force-based design* (FBD). In contrast, PBEE focuses on design methods that predict actual structural behavior during and after an earthquake. This approach enables solutions that consider how the structure responds to site-specific earthquake excitation based on factors such as structural configuration, materials, seismic data, and more. As PBEE involves an accurate evaluation of structural response, SSI plays a crucial role in such design approaches.

Easy access to commercial FE-software allows for accurate assessment of most structural and geotechnical problems. However, obtaining rigorous numerical solutions for dynamic soil-structure interaction response is a challenging and time-consuming process that often requires a cross-disciplinary skill set. As a result, simplified methods that are robust, user-friendly, and verifiable are often preferred in practical engineering. Numerous simplified methods have been developed and incorporated in the current design codes with the purpose of providing practitioners with safe, simple and time-efficient guidelines. However, such solutions are not always able to capture the intrinsic features of SSI, which may lead to unrealistic assessment of the overall structural response.

1.1.3 Objectives, organization and novelty

The overall objective of this doctoral work is to aid the industry with practical computational methods for analyzing structures, particularly bridges, that are supported by deep foundations using both vertical and batter piles. These methods aim to capture the essence of soil-structure interaction while also being straightforward to understand, implement and apply. Given in the following is an outline of the thesis' organization, along with specific objectives assigned to each chapter.

Chapter 1 presents the introduction. The main objective of Chapter 1 is to (1) briefly summarize the theoretical framework and (2) provide a broad reference list on the relevant topics.

Chapter 2 evaluates the kinematic interaction of vertical and batter pile groups. The content is based on the published work of Cemalovic et al. [2]. The main objective of Chapter 2 is to provide further insight into how non-linearity, batter angle, pile spacing and excitation frequency affect pile-cap displacements, rotations, maximum pile moments, shear forces and axial forces in the kinematic response of vertical and batter pile groups. The novelty of Chapter 2 is summarized below:

- Comprehensive numerical study on kinematic response of vertical and batter pile groups in nonlinear soil.
- Exploration of how the frequency-dependent results relate to the system response when subjected to real earthquake time histories.
- Assessment of nonlinear kinematic interaction factors and estimation of pile-cap response.

Chapter 3 presents a linear, diagonal impedance matrix for vertical and batter pile groups in homogeneous soil. The content is based on the published work of Cemalovic et al. [1]. The main objective of Chapter 3 is to formulate a diagonal impedance matrix for vertical and batter pile groups in linear, homogeneous soil that takes into account pile-soil-pile interaction. The solution is intended for low-exaction seismic problems, vibration problems or estimates in the early-stage design process. The novelty of Chapter 3 is summarized below:

- Closed-form solution of a *beam-on-Winkler foundation* problem for estimating the impedance matrix of vertical and batter pile groups and accounting for pile-soil-pile interaction.
- Hybrid-model with pile-soil-pile interaction elements.

Chapter 4 presents a nonlinear, fully-coupled macro-element (stiffness matrix) with three degrees of freedom for vertical and batter pile groups. The content is based on the published work of Cemalovic et al. [3]. The main objective of Chapter 4 is to formulate a practical and robust macro-element for vertical and batter pile groups. The solution is intended for realistic nonlinear time-history analyses and efficient estimation of equivalent linear properties. The novelty of Chapter 4 is summarized below:

- Nonlinear macro-element for vertical and batter pile groups with no restrictions regarding pile group configuration, soil type or soil profile, and with straight-forward calibration procedure.
- Description of transverse unloading/reloading behavior within the bounding plasticity and macro-element framework, which may also be implemented in other formulations.
- Description of axial load-displacement behavior that considers compression and tension differences within the bounding plasticity and macro-element framework.

- Description of implicit horizontal-rotational coupling within the bounding plasticity and macro-element framework.

Chapter 5 presents a new finite element framework for seismic analysis of structures accounting for SSI. The main objective of Chapter 5 is to (1) architecture a finite element software for seismic analysis of bridges and other relevant structures that utilizes the macro-element and the linear impedance matrix, (2) demonstrate how the macro-element and the linear impedance matrix may be implemented in a general finite element solution and (3) perform a set of *incremental dynamic analyses* (IDA) of an *integral abutment bridge* (IAB) founded on vertical and batter piles in order to evaluate the effect of SSI, batter angle and pile spacing.

The novelty of Chapter 5 is summarized below:

- Practical finite element framework for seismic analysis of structures accounting for linear and nonlinear SSI.
- Guidelines on how to implement the macro-element and the linear impedance matrix in a general finite element solution.
- IDA-analyses of an IAB founded on vertical and batter piles in order to evaluate the effect of SSI, batter angle and pile spacing.

1.2 Post-earthquake observations

Earthquakes are one of the deadliest and costliest natural hazards. Between the years 2000 and 2019, earthquakes represented only 8% of global disaster occurrences, while causing 58% of total deaths during the same period according to *United Nations Office of Disaster Risk Reduction* (UNDRR) [6]. Figure 1.1 shows the death tolls of the ten deadliest natural disasters from 2000 to 2019. The list is clearly dominated by earthquakes and earthquake-related disasters. In addition to the loss of life, earthquakes may cause tremendous economic damages. The most detrimental earthquake in terms of economic loss occurred in Japan in 2011 (earthquake and tsunami) and caused damages worth 239 billion USD.

There are several observations of post-earthquake damage to structures with deep foundations. In September 1985, Mexico City was struck by an earthquake with earthquake magnitude (M_w) equal to 8. Even though the epicenter was located 350-400 km away from the city, the earthquake killed over 5000 people and caused severe damage to the city's infrastructure. The main reason for this was the fact that low-frequency content was amplified by the soft, deep clay deposits in certain

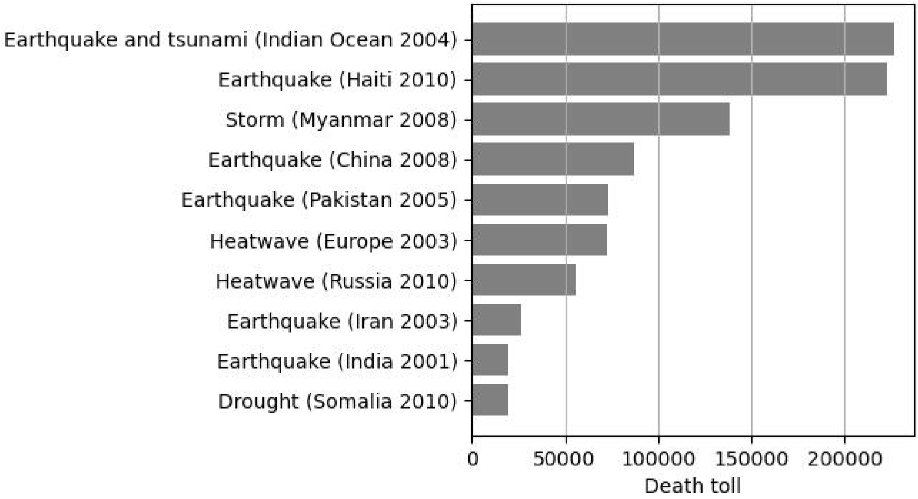

Figure 1.1: Ten deadliest natural disasters from 2000 to 2019 [6]

parts of the city, resulting in ground shaking motions dominated by periods of approximately two seconds. The most severe cases of damage were observed for intermediate tall structures supported by frictional piles.

Another earthquake that caused serious damage to piled structures occurred in Loma Prieta, October 1989 ($M_w = 7.0$). The collapse of a bridge on Highway 1 (Figure 1.2) was partly caused by inadequate lateral soil resistance around the piles. This was concluded based on the fact that (1) liquefaction was discarded (upper part of the soil deposit consisted of soft clay and no settlements were observed) and (2) large gaps of about 300-450 mm formed around the piles. SSI also played an important role in the collapse of the Cypress Freeway and San Francisco-Oakland Bay Bridge.

The infamous Kobe earthquake ($M_w = 7.2$) in Japan, January 1995, caused the failure of the pile-supported Hanshin Expressway. Gazateas and Mylonakis [7] suggested that period lengthening due to foundation flexibility (SSI-effect) may have increased the inertial forces during the earthquake.

Issues with batter piles

Particular poor performance has been observed for deep foundation with batter piles. Until the early 1990s, batter piles were commonly used in seismic design of bridges and other large structures to improve the lateral capacity. In the fol-

(a) Overview **(b)** Overview **(c)** Deck

(d) Pile gap **(e)** Pile gap **(f)** Column/deck joint

Figure 1.2: Highway 1 bridge, Struve Slough, 1989 Loma Prieta earthquake [8, 9]

(a) Port of San Francisco **(b)** Port of Oakland **(c)** Rio Banano Bridge

Figure 1.3: Damage to batter piles [10]

lowing years however, batter piles became generally discouraged due to several earthquakes where batter piles experienced serious damage. Figure 1.3 shows examples of damaged batter piles.

In the above-mentioned Loma Prieta-earthquake, harbour ports supported by batter piles suffered severe damage. Several of the squared, pre-stressed concrete piles supporting the Public Container Wharf in the Port of Oakland failed in tension near the connection to the deck. Due to liquefaction, the batter piles settled and attracted large moments. Similar failure was observed at The Matson Terminal Wharf and the Oakland Outer Harbor Pier 7. The pre-stressed concrete batter piles supporting the Ferry Plaza Pier in San Francisco failed in tension, and some of the piles also punched through the deck.

In April 1991, Costa Rica was struck by an earthquake with $M_w = 7.2$. The Rio Banano bridge was severely damaged due to liquefaction. At one of the abutments, it was observed that the battered piles in front suffered substantial bending and shear damage, whereas the vertical piles at the rear were less damaged.

As of today, numerous governing codes, including Eurocode 8 [11], recommend that batter piles are avoided in seismic design of deep foundations. However, the advancement in computational methods during the last two decades has facilitated numerous numerical studies that spurred on a more positive outlook on the use of batter piles in seismic design. Sadek and Isam [12] showed that batter micro-piles lead to a decrease in both shear force and bending moment induced by seismic loading. Gerolymos and Giannakou [13] concluded that batter piles with hinged pile-to-cap connections performed better than vertical piles when supporting tall, slender structures. Giannakou et al. [14] concluded along the same lines, emphasizing that vertical piles attracted larger axial forces when supporting tall structures. Medina et al. [15] explored how batter pile groups influence the overall response of slender and non-slender structures using a substructure approach. It was shown that batter piles reduce pile-cap displacements and base shear forces for non-slender structures. Carbonari et al. [16] investigated the seismic response of bridge piers on batter pile groups using a direct approach in the frequency domain. It was demonstrated that batter piles reduce pile-cap displacements but increase rotations. A few experimental studies revealed similar advantages. Escoffier [17] performed an experimental study elucidating frequency-dependent behaviour of a two-by-one pile group. It was shown that batter piles reduce pile-cap displacements. Subramanian et al. [18] found that the lateral displacement and bending strain in the resonance region decrease with increasing batter angle for a two-by-one pile group subjected to lateral loads. Bharathi et al. [19] found that peak displacements of batter pile groups were significantly reduced compared to vertical pile groups. It has also been suggested that the inadequate performance of inclined piles has been due to poor design rather than the fundamental behaviour of the pile itself [20].

1.3 Computational models for deep foundations

1.3.1 Beam on Winkler foundation

Winkler [21] stated that the *subgrade reaction* on a beam at a given point is proportional to the deflection of the beam at that point and is independent of the reaction at any other points. The *beam-on-Winkler foundation* (BWF) method refers to an externally loaded pile on discrete springs, where the reaction in each spring is characterized by the *subgrade modulus* and is independent of the reactions in the other springs. The Winkler method is governed by the fourth order differential equation

$$E_p I_p \frac{\partial^4 y}{\partial y^4} = -E_s y \tag{1.1}$$

first presented by Hetényi [22]. Here, E_p is the Young's modulus of the pile, I_p is the second moment of inertia of the pile cross section, y is the horizontal pile deflection and E_s is the subgrade modulus of the soil. Contrary to closed-form solutions, which are restricted by linearity and non-arbitrary distribution of subgrade reactions, the general Winkler method allows for non-linearity and arbitrary soil profiles.

The subgrade reaction modulus of a laterally loaded pile in soil depends on the deflection of the pile. Figure 1.4 shows the stress distribution in a laterally loaded, cylindrical pile. When the pile head is unloaded, the stresses from the soil acting on the pile are radial and evenly distributed. When the pile head is loaded, the pile deflects along the depth, which causes a redistribution of stresses. The stresses on back-side decrease, the stresses on the front-side increase, and some parts of the pile perimeter also experience shear stresses. In addition, the stress-strain relationship in soils is generally highly nonlinear.

1.3.2 P-y curves

The assessment of the nonlinear relationship between the subgrade reaction and pile deflection along the pile depth is what constitutes *p-y curves* . These curves are essentially nonlinear numerical models most commonly obtained from experimental field tests. P-y curves may be directly employed in a nonlinear analysis, or they may be used to obtain equivalent-linear subgrade reaction modulus for linear analysis.

The concept of the p-y method was first introduced by McClelland and Focht [23], who presented a procedure for estimating the subgrade reaction modulus in layered soil profiles. Later, Brooms [24, 25] suggested a method that evaluates the lateral deflection at pile head level together with the ultimate pile resistance. The method

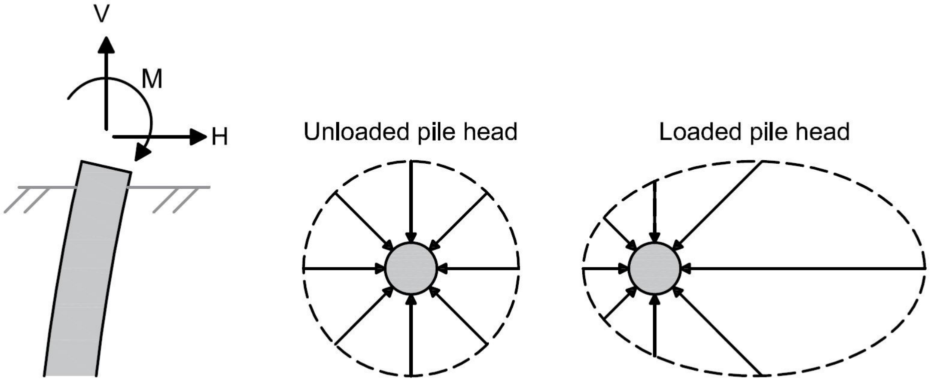

Figure 1.4: Stress distribution in the soil around a laterally loaded pile

provides solutions for both short and long piles in cohesive and cohesionless soil. Also, free and fixed head conditions were considered. The method is a rather straight-forward procedure that uses graphical (and tabular) relations between dimensionless variables. However, the method is restricted to homogeneous soil. Matlock and Reese [26, 27] purposed a solution for static and cyclic response of long piles through a set of generalized equations and dimensionless factors. The solution involves an iterative procedure, where the subgrade reaction modulus is adjusted for each iteration until convergence is achieved. Using this approach, Matlock [28] prospered p-y curves for soft clay and Reese [29] proposed a similar model for stiff clay. Both models apply for free water conditions, i.e. cases where water is allowed to fill the gap between pile and soil during cyclic loading. Welch and Reese [30] presented p-y curves for stiff clay without free water. The main concern with free water is related to the corrosive effect of water filling and leaving the gap during cyclic loading, which leads to softer subgrade reactions. Reese et al. [31] presented p-y curves for sand above and below water and Reese and Nyman [32] for presented p-y curves for weak and strong rock. In the following years, numerous models for static and cyclic loading were developed [33, 34, 35, 36, 37, 38, 39].

A simplified approach of estimating p-y curves commonly referred to as the *characteristic load method* was presented by Duncan et al. [40]. It is based on numerous nonlinear p-y analysis for piles and drilled shafts. The results are given as relationships between dimensionless key variables. The main drawback with the characteristic load method is that it only applicable for long piles. A more advanced method was purposed by Brown et al. [41]. The method utilizes inclinometer data together with a least-square regression technique to obtain solutions that minimizes the error between predicted and measured p-y curves. This method was further developed by Lin and Liao [42] and Pinto et al. [43].

Ashour [44] introduced a theoretically rigorous model referred to as the *strain wedge* (SW) model. The solution is based on the formation of a three-dimensional passive wedge during lateral displacement of piles rather than empirical expressions based on field tests. The reader is referred to the literature for more details on SW models [44, 45, 46, 47, 48, 49, 50, 51, 52, 53, 54].

The models mentioned thus far are developed based on quasi-static loading. In cases of rate dependent response, researchers have developed numerous solutions for lateral response of piles [55, 56, 57, 58, 59, 60, 61, 62, 63, 64, 65, 66, 67, 68, 69, 70, 71, 72, 73]. The axial response of piles has also been thoroughly studied [62, 64, 74, 75, 76, 77, 78].

1.3.3 Continuum models

Rather than considering the deep foundation as discretized beams on springs, continuum models consider the pile-soil system as a whole. Elastic continuum models are based on Mindlin's solution for a homogeneous, isotropic solid subjected to a concentrated load [79]. Such models are limited to non-arbitrary soil profiles and linear or equivalent-linear response.

Poulos [80, 81] presented a solution for the horizontal displacement and rotation of vertical single piles and pile groups subjected to static lateral loading and moment in elastic medium. Novak [82, 83] presented a closed-form solution of an elastic, dynamic BWF-problem (lateral and vertical) assuming plane-strain conditions, which became the basis for many proposed solutions in the following years. Nogami and Novak [84, 85] and Novak and Nogami [86] presented solutions for horizontal and vertical loading which included end-bearing piles. Novak and Aboul-Ella [87] presented a closed-form solution for the complex stiffness of an infinitely long cylindrical pile in layered soil. Randolph [88] presented solutions for single piles and pile groups in terms of charts and closed-form solutions. Gazetas and Dobry [89] presented a method for estimating impedance functions based on static pile-head stiffness values. Gazetas [90] presented comprehensive guidelines for determining the pile-head static stiffness and dynamic impedance of single single piles for non-arbitrary soil profiles.

The dynamic impedance matrix for vertical and batter pile groups presented in Chapter 3 is based on closed-form solutions (continuum models) of a BWF-problem assuming plane-strain conditions. Also, a *macro-element* (Section 1.4.4 and Chapter 4) may be regarded as an in-elastic, nonlinear continuum model.

1.3.4 Advanced constitutive models

Complex scenarios may require computational accuracy that is beyond the reach of the aforementioned, simplified computational models. In those cases, three-dimensional finite element analyses are required. The constitutive models of soil are usually rate-independent, plasticity models restricted to small deformations and isothermal conditions[1]. The main concept of plasticity is that the material response may be irreversible, i.e. that a part of the strains are not recovered upon unloading. The strains are divided into elastic strains (recovered) and plastic strains (not recovered). There is no unique relationship between stress and strain, and the constitutive equations must therefore be formulated in rate form. The conventional theory of plasticity is generally based on three main constituents, i.e. (1) the *yield criterion*, (2) the *flow rule* and (3) the *work-hardening rule*.

In conventional, rate-independent plasticity, there exists an elastic domain where all strains are elastic. As the stress magnitude increases, the material reaches a stress state where plastic deformations start to occur. This stress state is called the yield limit and is described by the yield criterion

$$f(\boldsymbol{\sigma}) = 0 \tag{1.2}$$

which defines the yield surface. The elastic domain is defined by $f(\boldsymbol{\sigma}) < 0$ and $f(\boldsymbol{\sigma}) > 0$ is inadmissible. The yield function may be regarded as a surface in stress space as shown in Figure 1.5. The flow rule defines the plastic strain increment such that negative dissipation may not occur. The flow rule may be *associated* or *non-associated*. The former implies that the plastic potential functions is associated with the yield function. The work hardening rule defines the expansion and relocation of the yield surface as a function of loading conditions. The reader is referred to the literature for further details on conventional plasticity theory [91, 92].

The first yield criteria was proposed by Tresca [93]. The formulation is isotropic and pressure independent, and yielding is governed by a critical shear stress. In the three-dimensional stress space, the yield surface consists of a regular hexagonal prism with the center line aligned with the hydrostatic axis. Von Mises [94] proposed a criteria similar to Tresca, where the yield surface in the three-dimensional stress space is a cylinder enclosing the Tresca-surface. The Hershey criteria [95] consists of an yield surface in-between Von-Mises and Tresca. The Drucker-Prager criteria [96] is an extension of the Von-Mises criteria, and is valid for pressure-dependent materials such as sandy soils and rocks. The Lade-Duncan criteria [97]

---

[1] Small deformation theory implies that the distinction between reference and spatial configurations is unnecessary. Relatively large strains may however still occur.

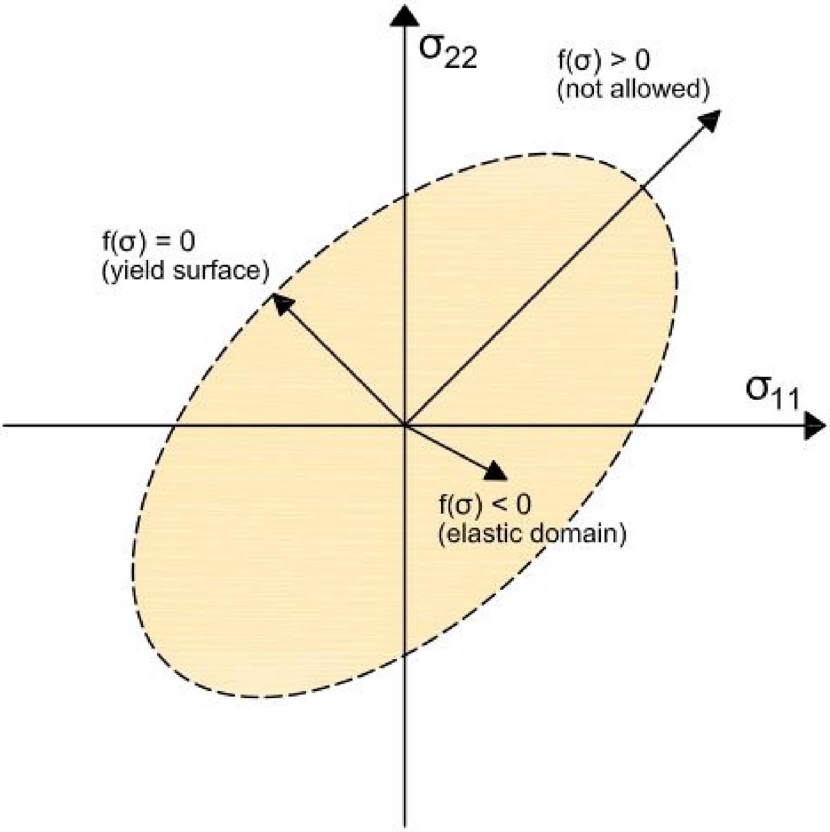

Figure 1.5: Two-dimensional yield surface

and the Matsuoka-Nakai criteria [98] are modified versions of the Drucker-Prager criteria. The aforementioned yield criteria applies for isotropic materials only. The Hill criteria [99] was developed for orthotropic materials, and Barlat et al. [100] developed a method that allows isotropic formulations to be applied for anistropic materials.

A important constitutive model for soil was presented by Drucker et al. [101], who introduced the first *cap model* with the purpose of including dilatancy. In the following years, several cap models were developed [102, 103, 104, 105, 106, 107, 108, 109, 110, 111].

Another important family of constitutive models are the *multi-surface plasticity* *models* [112, 113, 114, 115, 116, 117, 118, 119, 120, 121, 122]. The main difference between multi-surface plasticity and conventional rate-independent plasticity is that the former consists of multiple yield surfaces, which allows for plastic deformations to occur before the stress reaches the outer yield surface.

Bounding plasticity models [123, 124, 125, 126] also have the ability to produce plastic deformations before the outer yield surface is reached. Contrary to multi-surface plasticity, there are no distinct yield surfaces except for the bounding surface. The current stress surface itself is a yield surface, and the bounding surface represents the maximum allowed stress state. The plastic modulus is usually defined as a function of the distance between the current stress state and image points on the bounding surface and other defined surfaces. As mentioned earlier, macro-elements may be regarded as in-elastic, nonlinear continuum models. However, the formulation of such elements is often closely related to advanced constitutive models. In fact, the formulation of the macro-element presented in Chapter 4 is based on the principles of bounding plasticity.

In numerical modelling of deep foundations, it is often desirable to model piles as beams rather than solids. Traditionally, nonlinear behaviour of beams (piles) was accounted for using *lumped plasticity elements*. Such elements are often referred to as *plastic-hinge elements*. The main disadvantage using such elements is that the plastic hinge length, which depends on loading conditions and characteristics of the beam, must be determined a priori. *Distributed plasticity elements* on the other hand, allow for the plastic behaviour to be spread throughout the element without the need for calibration. Such elements are formulated based on two different approaches; (1) displacement-based formulation (DB), which is the textbook finite element formulation, and the force-based formulation (FB). In the former, the element is imposed with a displacement field. In the latter, force and moment fields are imposed. The validation model used to validate the results presented in Chapters 4 and 5 uses distributed plasticity elements. The reader is referred to literature for further details on distributed plasticity elements [127, 128].

1.4 Soil-structure interaction

1.4.1 Soil-structure-interaction phenomena

The SSI-phenomena may be divided into two parts. Considering the presence of a massless, deep foundation on a relatively soft deposit subjected to seismic excitation, the rigid structure will resist the propagating waves due to the difference in flexibility between the soil and the structure. Consequently, the foundation motion will deviate from the free-field motion. In addition, the soil in the vicinity

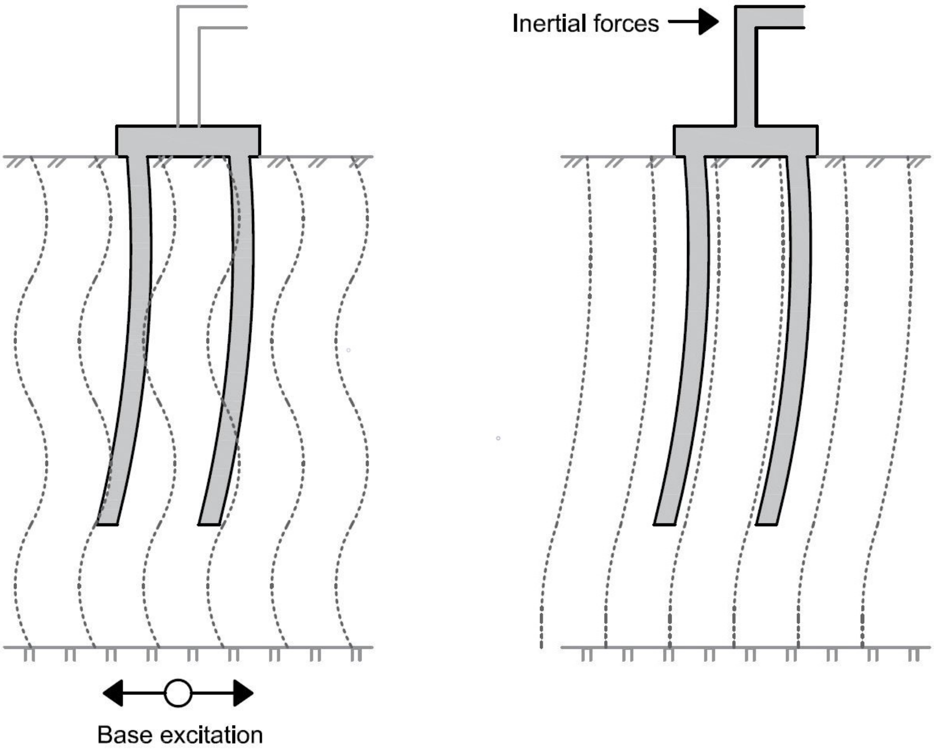

(a) Kinematic interaction **(b)** Inertial interaction

Figure 1.6: Schematic sketch of the soil-structure interaction problem

of the structure will deform. This is referred to as *kinematic interaction* (Figure 1.6(a)). In turn, the foundation motion will excite the superstructure and produce inertial forces that are transmitted back to the foundation, which in turn will cause additional soil deformations. This is referred to as *inertial interaction* (Figure 1.6(b)). In addition to SSI, certain conditions require the assessment of *structure-soil-structure interaction* (SSSI) which considers the dynamic interaction of adjacent structures [5, 129]. This is however outside the scope of this thesis.

There are three main effects from arising from SSI; (1) the relative displacements between the soil and structure produce hysteretic and radiation damping, (2) the flexibility of the structural foundation is considered (as opposed to fixed conditions) and (3) permanent displacements of the structure may occur. The first effect increases the overall damping. Hysteretic damping, or material damping, is usually predominant for large displacements and low-frequency exitation. Radiation damping, or geometric damping, becomes more important for small displacements and high-frequency excitation. In both cases, the damping has favourable effects on the seismic response of a structure. This is one of the reasons that for most cases, including SSI is deemed beneficial in the analysis of structures. However, as several authors have demonstrated [130, 131, 132], this is not always the case. Note that the second effect inherently causes period lengthening of the soil-structure system. For a structure founded on soft soil, where the fixed-base natural period is lower than the fundamental period of the soil deposit, the response of the system may result in resonance due to period lengthening. The third effect becomes particularly important when considering tall, closely spaced structures. The importance of SSI, and whether it contributes beneficially of detrimentally, depends highly on the characteristics of the soil, structure and seismic data. Generally, the effects are small for flexible structures on stiff soil, but significant for stiff structures on soft soil.

1.4.2 Substructure approach

The principal idea behind substructure approach is to divide the complex soil-structure interaction into kinematic and inertial response. Considering a soil-structure system, the kinematic response of the system subjected to a displacement history at the boundaries is obtained by solving the equation of motion of the system without the structural mass present, i.e.,

$$\boldsymbol{M}_{soil}\ddot{\boldsymbol{d}}_F + \boldsymbol{C}(\dot{\boldsymbol{d}}_F - \dot{\boldsymbol{d}}_g) + \boldsymbol{K}(\boldsymbol{d}_F - \boldsymbol{d}_g) = \boldsymbol{0} \tag{1.3}$$

where $\boldsymbol{d}_g$ is the displacement history input vector, $\boldsymbol{M}_{soil}$ is the mass matrix corresponding to the soil, $\boldsymbol{C}$ is total damping matrix, $\boldsymbol{K}$ is total stiffness matrix and $\boldsymbol{d}_F$ is the total displacement from the kinematic response. Equation 1.3 may be written as

$$\boldsymbol{M}_{soil}(\ddot{\boldsymbol{d}}_{rk} + \ddot{\boldsymbol{d}}_g) + \boldsymbol{C}\dot{\boldsymbol{d}}_{rk} + \boldsymbol{K}\boldsymbol{d}_{rk} = \boldsymbol{0} \tag{1.4}$$

where

$$\boldsymbol{d}_{rk} = \boldsymbol{d}_F - \boldsymbol{d}_g \tag{1.5}$$

is the relative displacement due to kinematic interaction. The inertial response is obtained by subjecting the structure, and only the structure, to inertial forces arising from the total displacement from the kinematic response. The equation of motion may then be written as

$$\boldsymbol{M}\ddot{\boldsymbol{d}}_{ri} + \boldsymbol{M}_{str}(\ddot{\boldsymbol{d}}_{rk} + \ddot{\boldsymbol{d}}_g) + \boldsymbol{C}\dot{\boldsymbol{d}}_{ri} + \boldsymbol{K}\boldsymbol{d}_{ri} = \boldsymbol{0} \tag{1.6}$$

where $\boldsymbol{M}$ is the total mass matrix, $\boldsymbol{M}_{str}$ is the mass matrix corresponding to the structure and $\boldsymbol{d}_{ri}$ is the relative displacement due to inertial interaction. The

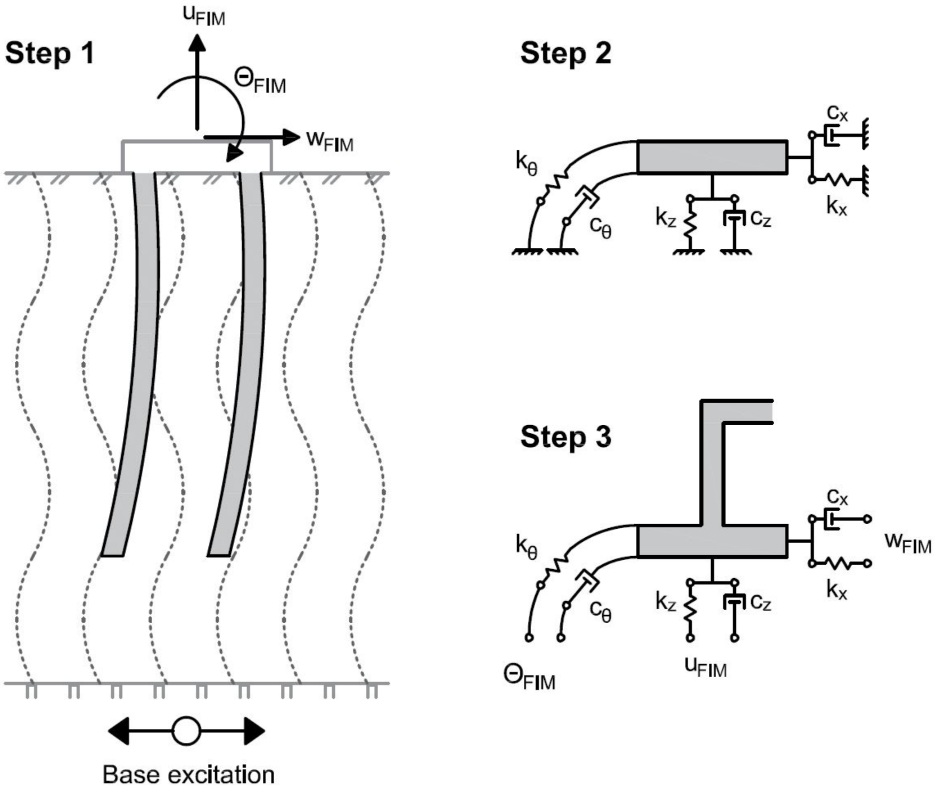

Figure 1.7: Substructure approach according to Kausel [133]

equation of motion of the total system is obtained by adding Equations 1.4 and 1.6, i.e.,

$$\boldsymbol{M}\ddot{\boldsymbol{d}}_r + \boldsymbol{C}\dot{\boldsymbol{d}}_r + \boldsymbol{K}\boldsymbol{d}_r = -\boldsymbol{M}\ddot{\boldsymbol{d}}_g \tag{1.7}$$

where

$$\boldsymbol{d}_r = \boldsymbol{d}_{rk} + \boldsymbol{d}_{ri} \tag{1.8}$$

is total relative displacement. In practice, the substructure method is particularly useful when simplified models are utilized, both for kinematic and inertial response.

Perhaps the most well-known substructure approach was proposed by Kausel [133]. This method divides the calculation procedure into three steps which are schematically shown in Figure 1.7. In the first step, the total displacement from the kinematic response is calculated. This displacement field is often referred to as *foundation input motion* (FIM) since it is the motion that the foundation of the structure is subjected to in a subsequent step. Most conveniently, FIM is set equal to the free-field time-history provided, which inherently neglects the kinematic interaction. Kinematic interaction effects may be considered by modelling both soil and foundation as described above. The calculation may be performed in the time domain given adequate level of detailing for the task at hand, or in the frequency domain. The latter is particularly convenient if simplified, frequency-dependent models are used. Kinematic interaction effects may also be considered through the use of *kinematic interaction factors*. In this approach, the free-field response is first calculated, i.e. the displacement field at the top of the soil profile without the presence of the piles. In the next step, the free-field displacements are multiplied by the corresponding kinematic interaction factors and FIM is obtained. Since the kinematic interaction factors available in the literature [134, 135, 136, 137, 138, 139, 140, 141, 142, 143, 144, 145, 146] are usually frequency-dependent, the free-field displacements must be computed in (or transferred to) the frequency domain. In addition to adjusting the input motion, kinematic effects may also impose additional stresses on the foundation, especially in the case of deep foundations. In that case, the use of kinematic interaction factors is insufficient, since no information on pile stresses may be retrieved. Further details on kinematic interaction of deep foundations is provided in Chapter 2.

In the second step, the dynamic impedance matrix representing the soil-foundation response is assembled. The impedance matrix is normally frequency-dependent with damping coefficients representing material and radiation damping, and may account for pile-soil-pile interaction in the case of deep foundations. Further details on dynamic impedance matrices of deep foundations is provided in Chapter 3.

In the third and final step, the system is subjected to FIM, the structural response is calculated and the kinematic and inertial effects are superimposed. The advantage of this method lies within its simplicity, especially when utilizing the analytical solutions provided in the literature for kinematic interaction factors and dynamic impedances.

1.4.3 Direct method

The direct method refers to solving the equation of motion for the total system. In terms of total displacements, the equation of motion may be expressed as

$$\boldsymbol{M}\ddot{\boldsymbol{d}} + \boldsymbol{C}\dot{\boldsymbol{d}} + \boldsymbol{K}\boldsymbol{d} = \boldsymbol{F} \tag{1.9}$$

where $\boldsymbol{d}$ is the total displacement vector and $\boldsymbol{F}$ is the force vector. For seismic loading, the input motion may be enforced using suitable prescribed displacement techniques. The developed FE-code presented in Chapter 5 uses the penalty method to enforce the input motion. In that case, $\boldsymbol{K}$ and $\boldsymbol{F}$ are manipulated such that the input motion is ensured at the respective degrees of freedom. The reader is refereed to the literature [147, 148] for further details on the theory and implementation of penalty constraints.

In terms of relative displacements, the direct method implies directly solving Equation 1.7. The main advantage of Equation 1.9 over Equation 1.7 is that the former does not require an explicit definition of the seismic force vector, which may be a cumbersome task for larger or more complicated systems.

Since there are no simplifications other than those inherent to a finite element solution (such as domain size, spatial discretization of the problem and the limitation of the constitutive models), the direct method is regarded as the most accurate approach in seismic analyses of structures. However, such models are generally complex, time-consuming, and demanding of cross-disciplinary set of skills. Among the challenges are nonlinear constitutive models that often require a lot of parameters (pressure dependence/independence, degradation of strength, liquefaction etc.), modelling of pile-soil interfaces, choice of boundary elements and domain size, meshing strategies, appropriate integration schemes and solutions algorithms, correct application of seismic loading and the need for multi-stage analyses. Further details on the direct method is given in Section 2.2, which describes the finite element modelling strategies used throughout this thesis.

1.4.4 Macro-element approach

As previously mentioned, a macro-element may be regarded as nonlinear continuum model described by advanced constitutive laws. The main advantage of the macro-element approach is that the complex soil-foundation response is condensed into a single element as shown in Figure 1.8. However, such elements require pre-defined parameters that must be calibrated, and are often restricted to a specific foundation configuration, soil profile or soil type. Inherently, analysing soil-structure problems using macro-elements introduces an approximation since the analysis is fundamentally nonlinear, while kinematic and inertial effects are not assessed simultaneously. Therefore, the macro-element approach may be regarded as a method in-between the inertial analysis of the substructure approach and the direct approach.

The term *macro-element* was first introduced by Nova and Montrasio [149], who

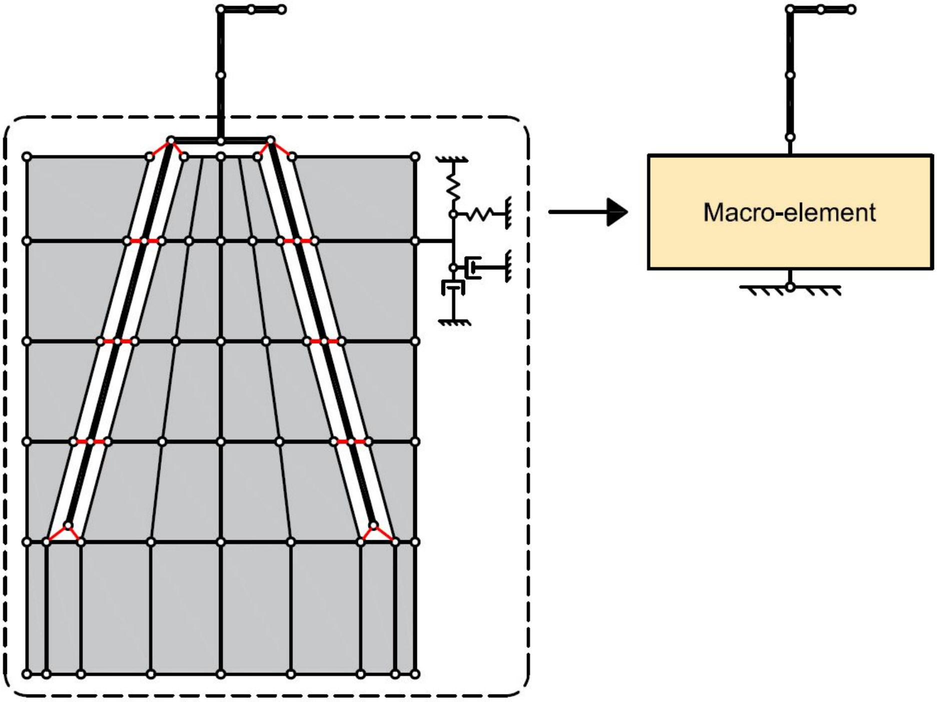

Figure 1.8: Macro-element concept

formulated an elastoplastic model with isotropic hardening for shallow foundations on sand. The concept of condensing the complex soil-foundation into a single element enabled engineers to consider soil-structure interaction using a simple, yet realistic approach. Following this, several macro-elements for shallow foundations were devolved. Paolucci [150] and Pedretti [151] extended the work of Nova and Montrasio [149] and adapted the model to seismic loading. Gottardi et al. [152] performed experimental tests to describe the yield surface for circular footings on dense sand. Le Pape et al. [153] formulated a macro-element for seismic response based on thermodynamics. Cremer et al. [154] developed a macro-element for shallow foundations on cohesive soil that accounted for cyclic loading, soil plasticity and uplift. The element was later applied on the seismic analysis of a bridge pier foundation [155]. Martin and Houlsby [156, 157] presented a monotonic model for spudcan footings on clay based on experimental tests. A similar model was developed by Houlsby and Cassidy [158] for sand. Cassidy et al. [159] presented a monotonic macro-element for spudcan footings with six degrees-of-freedom. Houlsby et al. [160] presented a model based on Winkler springs for quasi-static loading. Einav and Cassidy [161] developed a model similar to Houlsby et al. [160]. Salciarini and Tamagnini [162] formulated a model for shallow footings on sand which shared some similarities with the work of Nova and Montrasio [149]. Chatzigogos et al. [163] presented a bounding plasticity model considering soil inelasticity and nonlinear uplift mechanism. Chatzigogos et al. [164] extended this model to include sliding. Figini et al.[165] expanded on the work of Chatzigogos et al. [163, 164] and validated the results using cyclic and dynamic large-scale laboratory tests. Ibsen et al. [166] and Foglia et al. [167] investigated the response of bucket foundations on dry sand. Skau et al. [168] presented a macro-element for bucket foundations based on multi-surface plasticity. Tistel and Grimstad [169] presented a monotonic model for an anchor block foundation on sand. Millen et al. [170] presented a macro-element for shallow foundations based on the work of Chatzigogos et al. [163] and Figini et al. [165].

In recent years, attempts have been made to develop macro-elements for deep foundations. Correia [171] and Correia and Pecker [172] presented a pile-head macro-element for monoshaft foundations. The formulation accounted for nonlinear behaviour of pile, soil and separation effects. In addition, a rigorous calibration procedure was presented. Inspired by the work of Salciarini and Tamagnini [162], Liu et al. [173, 174] first developed a macro-element for single piles embedded in homogeneous sand, which they later extended to single batter piles. Page et al. [175] presented a macro-element model for mono-pile foundations based on multi-surface plasticity and verified it against large-scale model tests [176]. Perez [177] presented a macro-element for vertical pile groups based on the work of Liu [178].

To the authors knowledge, there are no macro-elements developed for pile groups with vertical and batter piles that take into account the inelastic behaviour of both pile and soil.

Chapter 2

Kinematic response

2.1 Introduction

Extensive studies have been performed on kinematic interaction of vertical piles using linear models [134, 135, 136, 137, 138, 139, 140, 141, 142, 143, 144, 145, 146], but substantially less attention has been paid to batter piles. Medina et al. [179] presented a comprehensive linear method based on a BEM-FEM coupled formulation for estimating kinematic interaction of batter pile groups. Dezi et al. [180] presented a numerical model for dynamic analysis of batter pile groups in layered soil. Carbonari et al. [181] presented an analytical, closed-form solution for dynamic stiffness and kinematic response of single batter piles. Indeed, a few authors have carried out nonlinear studies using vertical and batter piles [67, 182, 183, 184, 185], but kinematic interaction of batter pile groups in nonlinear soil has yet to be investigated.

Kinematic interaction is most prominent in soft soils, and several researchers [14, 136, 146] have elucidated the importance of soil profile on kinematic interaction of pile groups. This chapter focuses therefore on the kinematic response of vertical and batter pile groups in soft clay using a simplified, yet realistic clay profile. The investigated system is the two-by-one pile group depicted in Figure 2.1, which is representative of a bridge abutment or pier foundation. The total profile height H is $24m$, the pile length l_p is $18m$ and the pile diameter d_p is $1m$. This study considers three different pile-to-pile spacings S_0 equal to $2d_p$, $6d_p$ and $10d_p$ together with three different batter angles β equal to 0°, 7.5° and 15°, all of which are considered to be within realistic range of values. Vertically propagating seismic S-waves cause horizontal displacement of the free-field soil. Rigid structures such

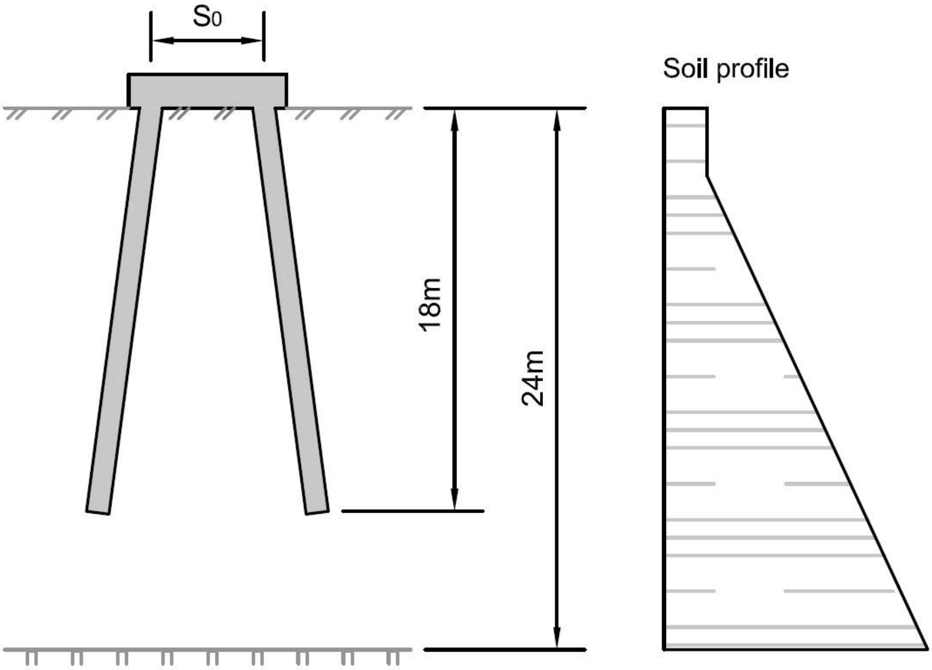

Figure 2.1: Schematic sketch of the investigated pile-soil system

as deep foundations tend to resist the free-field motion, generating modified displacements and rotations of the pile-cap. The relationship between the free-field and pile-cap motion is often expressed through horizontal and rotational kinematic interaction factors,

$$I_x(\omega) = \frac{U_p(\omega)}{U_f(\omega)}, \quad I_r(\omega) = \frac{\phi_p(\omega)\, d_p}{U_f(\omega)} \tag{2.1}$$

where U_p is the horizontal pile-cap displacement amplitude, U_f is the horizontal free-field displacement amplitude, ϕ_p is the pile-cap rotation and ω is the angular frequency. Note that the literature occasionally presents I_r as a function of S_0 instead of d_p. The nomenclature in this thesis is motivated by the desire to clearly express how rotation varies with pile spacing. In the rather convenient realm of linearity, the kinematic interaction factors may readily be applied in the substructure method by multiplying the free-field motion in the frequency domain with the corresponding interaction factor. Since this procedure implies superposition, interaction factors lack the practical applicability in nonlinear analysis in the most rigorous sense. Nevertheless, nonlinear interaction factors provide useful information about kinematic response of pile groups. First, frequency-dependent modification of the free-field motion is readily depicted. Second, linear and nonlinear interaction factors are directly comparable, providing insight into differences in kinematic pile-soil interaction between linear and nonlinear models. Perhaps somewhat obvious, it is worth mentioning that interaction factors presented in the frequency domain equivalently provide information about differences in pile-cap accelerations.

The main objective of this chapter is to provide further insight into how nonlinearity, batter angle, pile spacing and excitation frequency affect pile-cap displacements, rotations, maximum pile moments, shear forces and axial forces.

Section 2.2 presents the finite element model used in the analysis. The description applies for the other chapters as well, where the model has been used to validate the developed solutions. Section 2.3 presents a verification of the model. Section 2.4 presents and discusses the results from harmonic base motion analyses. Section 2.5 further extends the analyses to time domain, discusses the findings in relation to previously discussed frequency-dependent behaviour and demonstrates how nonlinear interaction factors may be applied to estimate pile-cap response based on a single free-field analysis. Section 2.6 presents the summary.

2.2 Finite element model in OpenSees MP

2.2.1 General

This section describes the numerical models used throughout the thesis. The numerical models are constructed in OpenSees MP [186] together with the pre- and post-processing tool STKO [187]. Parallel computing is utilized for better (faster) performance. The ground is modelled as a half-space when suitable. In most cases, the soil profile is either homogeneous or linearly varying. In the latter case, the soil profile is divided into eight layers, where each layer has a height $h_{lay} = 3m$. In this chapter, the numerical model is used to evaluate the kinematic response of batter pile groups. Otherwise, the numerical models are used to validate the developed solutions. The finite element model is illustrated in Figure 2.2.

2.2.2 Material models

Soil

The soil is modelled using two types of material models. The adopted material model for linear analysis is a simple isotropic model where the input parameters are the elastic modulus E_s, Poisson's ratio μ and mass density ρ_s. For nonlinear

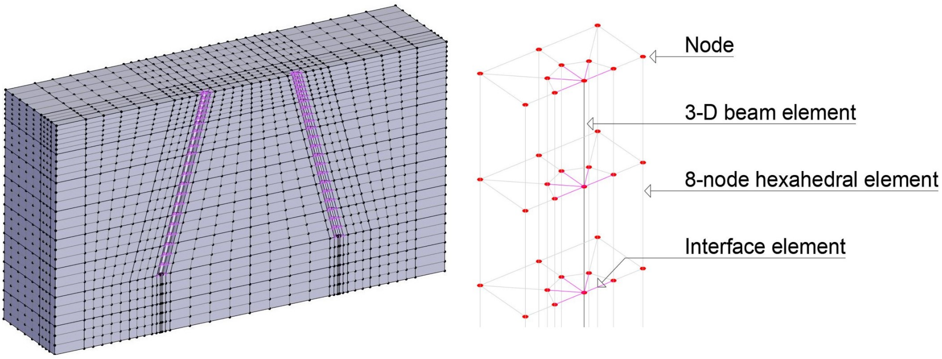

Figure 2.2: Three-dimensional finite element model

analysis, the soil behaviour is simulated using an elastic-plastic, soil model suited for clay [188]. The model is denoted as *PIMY* in OpenSees. Plasticity is only considered for the deviatoric stress-strain response using an associative flow rule. The input parameters are the small-strain shear modulus G_{max}, small-strain bulk modulus B_{max}, cohesion c, maximum shear strain γ_{max}, friction angle ϕ, reference confining pressure p'_r and a material parameter d controlling pressure dependence.

According to Mesri [189], the undrained shear strength of clay may be expressed as

$$\tau_f = s_u = 0.22\,\sigma'_c = 0.22\,(\gamma_s - \gamma_w)\,h \tag{2.2}$$

where σ'_c is the vertical pre-consolidation pressure, h is the soil depth and γ_s and γ_w are the specific weights of soil and water, respectively. According to Andersen [190], small-strain shear modulus may be estimated as

$$G_{max} = 1000\,s_u \tag{2.3}$$

for a clay with plasticity index about 25%. The small-strain bulk modulus follows from linear elastic laws for homogeneous materials, i.e.,

$$B_{max} = \frac{2\,G_{max}(1+\mu)}{3(1-2\mu)} \tag{2.4}$$

Here, μ is the Poisson's ratio set equal to 0.49. The backbone curve is determined as

$$\tau = \frac{G_{max}\,\gamma}{1+\dfrac{\gamma}{\gamma_r}} \tag{2.5}$$

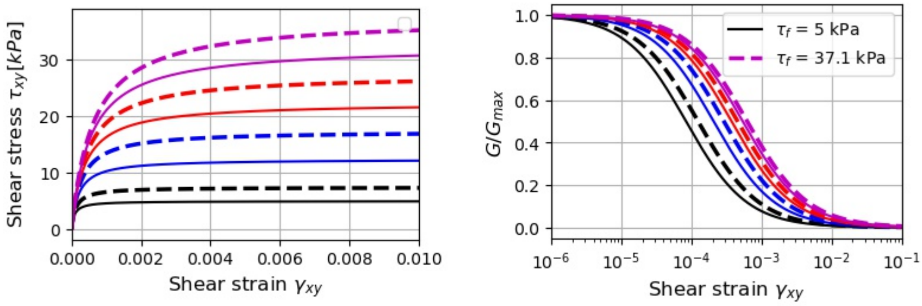

(a) Shear stress τ_{xy}. **(b)** G/G_{max}.

Figure 2.3: Pressure Independent Multi-Yield (PIMY) material model.

where

$$\gamma_r = \frac{\tau_f \, \gamma_{max}}{G_{max} \, \gamma_{max} - \tau_f} \tag{2.6}$$

Here, γ_{max} is the peak shear strain set equal to 0.1. The average shear wave velocity of the profile is approximated as

$$V_{s,H} = \frac{H}{\sum_{i=1}^{n_{lay}} \frac{h_{lay}}{V_{s,lay}}} = 91.8 \frac{m}{s} \tag{2.7}$$

where n_{lay} is the total number of soil layers, h_{lay} is the layer height and $V_{s,lay}$ is the shear wave velocity of the layer.

The soil properties for each layer are shown in Table 2.1, the maximum shear strength is shown in Figure 2.3(a) and the shear modulus reduction curves are shown in Figure 2.3(b).

Structure

The adopted material model for linear analysis is a simple uni-axial model where the only input parameter is the elastic modulus E_p. The nonlinear behaviour of reinforced concrete piles is represented using fibre sections. The confined and unconfined concrete is simulated using the uni-axial material models *ConfinedConcrete01* [191] and *Concrete01* [192], respectively. The reinforcement is simulated using the uni-axial material model *Steel02* [193].

2.2.3 Elements

The soil is modelled using eight-noded hexahedral elements with a single integration point to prevent locking behaviour. The piles are modelled using elastic

Table 2.1: Soil profile parameters for $f = 10Hz$. Density $\rho_s = 1750kg/m^3$, Poisson's ratio $\nu = 0.49$ and angle of friction $\phi = 0°$

Soil parameters	**0-3m**	**3-6m**	**6-9m**	**9-12m**	**12-15m**	**15-18m**	**18-21m**	**21-24m**
Undrained shear strength s_u $[kPa]$	5.0	7.4	12.4	17.3	22.3	27.2	32.2	37.1
Cohesion c $[kPa]$	5.3	7.9	13.1	18.4	23.6	28.9	34.1	39.4
Young's modulus E_{max} $[kPa]$	14900	22127	36878	51629	66380	81131	95882	110633
Shear modulus G_{max} $[kPa]$	5000	7425	12375	17325	22275	27225	32175	37125
Bulk modulus B_{max} $[MPa]$	248	369	615	860	1106	1352	1598	1844
Shear wave velocity V_s $[m/s]$	53	65	84	100	113	125	136	146
Pressure wave velocity V_p $[m/s]$	382	465	601	711	806	891	968	1040
Viscous damper c_h $[Ns/mm]$	94	114	147	174	197	218	237	255
Viscous damper c_v $[Ns/mm]$	668	814	1051	1243	1410	1559	1695	1820
Minimum wavelength λ $[m]$	5.4	6.5	8.4	10.0	11.3	12.5	13.6	14.6
Max. element size l_e $[m]$	0.594	0.724	0.934	1.106	1.254	1.386	1.507	1.618
Natural period T $[s]$	0.22	0.18	0.14	0.12	0.11	0.10	0.09	0.08
Ratio E_{max}/E_p	2349	1582	949	678	527	431	365	316
Shear wave travel time h/V_s $[s]$	0.056	0.046	0.036	0.030	0.027	0.024	0.022	0.021

Euler-Bernoulli beam-column elements (linear analysis) and displacement-based beam-column elements (nonlinear analysis).

The pile-soil interface has been considered to be an important aspect for both static and dynamic impedance of pile groups. However, recent studies [194, 195, 196] have shown that separation effects are of less significance when plasticity is considered. When suitable, the interface between beams and solids is modelled using rigid-link-constraints (full bonding), connecting each beam node to the corresponding soil nodes such that the pile section in the given beam node acts like a rigid disk. The constraints are enforced using penalty functions [147, 148]. The penalty values are obtained by approximating the order of largest entry of the stiffness matrix, i.e.,

$$O = \log^{10}(k_{max}) \tag{2.8}$$

The penalty value is the obtained as

$$p = 10^{(O+8)} \tag{2.9}$$

Otherwise, the pile-soil interface is modelled using frictional contact elements based on the Mohr-Coulomb criterion, penalty constraints and an implicit-explicit solution scheme [187, 197].

2.2.4 Damping

Rayleigh damping

Rayleigh damping is used for linear analysis. For nonlinear analysis, adding damping is not a straight-forward task since (1) material damping is an inherent part of the material model and (2) the stiffness matrix is continuously changing throughout the system response. Most conveniently, a constant damping matrix may be added using the initial stiffness matrix such that

$$\boldsymbol{C} = \alpha_{0,i}\boldsymbol{M} + \alpha_{1,i}\boldsymbol{K}_i \tag{2.10}$$

where $\alpha_{0,i}$ and $\alpha_{1,i}$ are the inital Rayleigh-coefficients and $\boldsymbol{K}_i$ is the initial stiffness matrix. The main drawback with this approach is that artificial damping may be generated as the systems yields. Another approach is to keep the initial Rayleigh-coefficients, but use the tangent stiffness matrix, i.e,

$$\boldsymbol{C} = \alpha_{0,i}\boldsymbol{M} + \alpha_{1,i}\boldsymbol{K}_t \tag{2.11}$$

where $\boldsymbol{K}_t$ is the tangent stiffness matrix. It should be noted that the tangent stiffness matrix can either be the tangent stiffness matrix for each iteration, or the tangent stiffness corresponding to the last converged solution. Finally, the damping matrix may be obtained by updating both the Rayleigh-coefficients and the tangent stiffness matrix, i.e.,

$$\boldsymbol{C} = \alpha_{0,t}\boldsymbol{M} + \alpha_{1,t}\boldsymbol{K}_t \tag{2.12}$$

To the authors knowledge, OpenSees does not provide the option of updating the Rayleigh-coefficients during the analysis in a straight-forward manner, only the stiffness matrix. Even if this option was available, it would be computationally demanding for large models and long time-histories. However, the software allows the user to choose between the tangent stiffness matrix in each iteration and the last converged stiffness matrix. Using the former, convergence may be difficult to achieve in some cases. Damping is therefore added using Equation 2.11 where suitable. The reader is refereed to the literature for further details regarding damping in nonlinear systems [198, 199, 200].

Spurious damping

Issues related to spurious damping due to discretization in space are avoided by choosing a sufficiently refined element mesh. The maximum element size in each layer is determined based on the shortest occurring wavelength, i.e.,

$$\omega_{max} = \frac{V_s\, a_{0,max}}{d_p} \rightarrow \lambda_{wave,min} = \frac{2\pi V_s}{\omega_{max}} \tag{2.13}$$

where ω_{max} is the highest angular load frequency and $a_{0,max}$ is the highest normalized angular load frequency. In order to correctly represent a wave, it is necessary to use at least eight nodes per wavelength in the direction of wave propagation [201]. Thus, the element length is kept below approximately

$$l_e = \frac{\lambda_{wave,min}}{7} \tag{2.14}$$

The final element mesh is established by verifying that refinement does not alter the results significantly. Shear wave velocity is determined using initial strain properties for nonlinear analysis. Table 2.1 shows shear (and pressure) wave velocities and maximum element length for each layer. The values correspond to a frequency $f = 10Hz$.

2.2.5 Boundaries

For dynamic analysis, the boundaries need to simulate wave propagation correctly. When loads are applied within the boundary, the outer boundaries are represented using viscous zero-length elements developed by Lysmerand and Kuhlemeyer [202]. The damping coefficients are determined as the product of soil density, wave velocity and boundary area. Pressure wave velocity is used for damping coefficients normal to the boundary, and shear wave velocity is used for damping coefficients tangential to the boundary, i.e.,

$$c_H = V_s \rho_s A_n, \; c_v = V_p \rho_s A_n \tag{2.15}$$

Here, A_n is the boundary area represented by the given node. The zero-length elements are connected to fixed nodes. Table 2.1 shows the damping coefficients per unit area for each layer.

When the loads are applied at the boundary, the outer, vertical boundaries perpendicular to the loading direction are represented using tied-node conditions as first suggested by Zienkiewicz et al. [203]. The side boundaries are restrained from movement perpendicular to boundary plane. The base motion is applied using prescribed displacements. In both cases, the bottom nodes representing bedrock are restrained in the vertical direction. Shear- and pressure wave velocities are determined using initial strain properties for nonlinear analysis.

2.2.6 Analysis

Integrator and solver

The dynamic system is integrated using the Hilber-Hughes-Taylor method [204, 205]. The method is very similar to the Newmark's method [206]. Although both methods are able to introduce algorithmic damping to higher modes, the Hilber-Hughes-Taylor method introduces less algorithmic damping in lower modes. The TRBDF2 integrator [207] is used in some cases.

The nonlinear system is solved using the Krylov-Newton implicit scheme [208]. In order to increase the probability of convergence and also to speed up the analysis, adaptive time steps are applied. If convergence is not achieved for a given time step, the time step is reduced by a factor of 2. If convergence is achieved before a desired number of iterations, the time step is increased by a factor of 1.5. The chosen convergence criteria generally depends on the task at hand. If we are using penalty values as constraints, convergence is achieved when the l_2-norm of the displacement increment vector is less than a prescribed tolerance value.

Multi-stage analysis

In some cases, multi-stage analyses are performed to capture the correct stress state prior to dynamic or quasi-static loading. The first stage is a gravity analysis of the soil domain. In the second stage, a new gravity analysis is performed where the soil corresponding to the pile geometry is removed. In the third stage, a new gravity analysis is performed which includes the piles and contact elements. In the fourth and final stage, the quasi-static pile-head load analysis is performed. Prior to each analysis, the displacement field is set equal to zero.

2.3 Model verification

Static

The finite element model described in Section 2.2 is used to evaluate the kinematic response of the pile-soil-system shown in Figure 2.1. First, the model is compared against the solution for static stiffness of a single pile as proposed by Gazetas [90]. The closed-form expression is strictly valid for a perfect Gibson soil, but is used

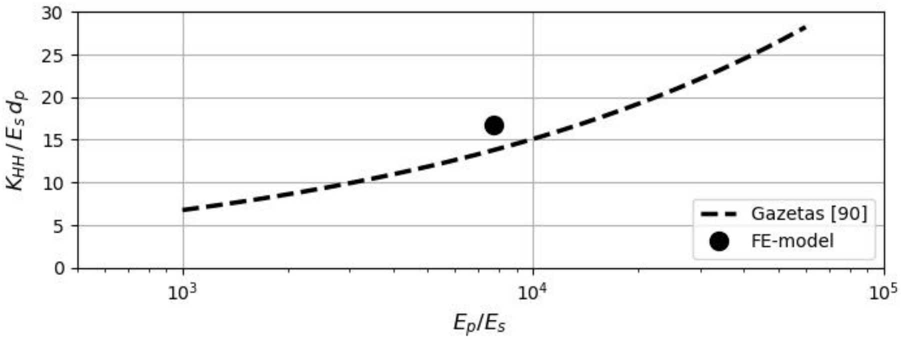

(a) Static stiffness.

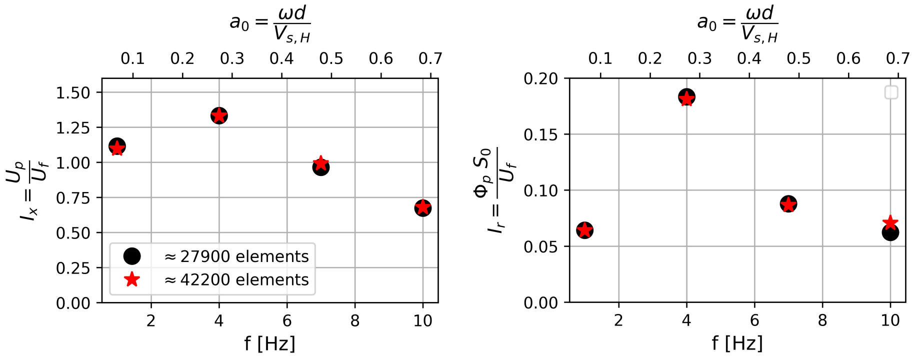

(b) Horizontal interaction I_x

(c) Rotational interaction I_r

Figure 2.4: Validation of FE-model in terms of (a) static stiffness for a single pile, (b) horizontal kinematic interaction I_x and (c) rotational kinematic interaction I_r. Kinematic interaction factors in a) and b) are computed for a two-by one pile group ($S_0 = 6d$ and $\beta = 0°$) and plotted against frequency f and dimensionless angular frequency a_0.

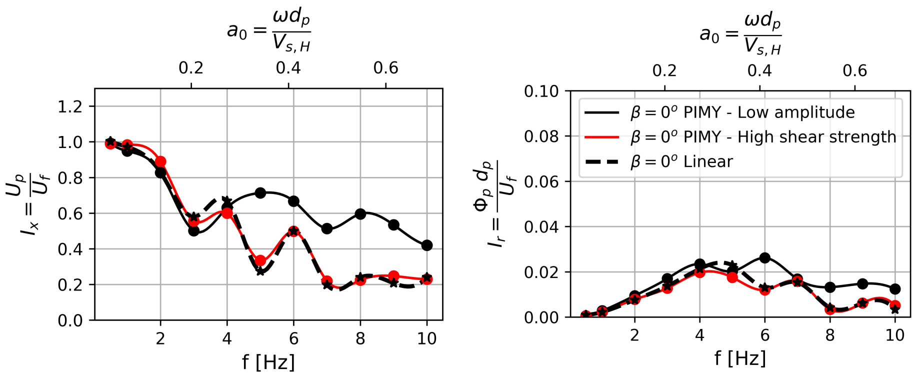

(a) Horizontal interaction I_x.

(b) Rotational interaction I_r.

Figure 2.5: Convergence of linear and nonlinear models. Kinematic interaction factors are computed for a two-by one pile group ($S_0 = 6d$ and $\beta = 0°$) and plotted against frequency f and dimensionless angular frequency a_0.

here only as an approximation in order to verify the FE-model. The comparison is shown in Figure 2.4(a) and the results are in reasonable agreement.

Dynamic

The final element mesh ($\approx$ 27900 elements) and boundary conditions are verified by comparing the applied FE-model against a model with larger width and finer mesh ($\approx$ 42200 elements). Interaction factors I_x and I_r are computed using the two models and the results are shown in Figures 2.4(b) and 2.4(c). The results match fairly well.

Two additional nonlinear analysis are performed, where (1) the base motion amplitude is low ($U_b = 0.001 d_p$) and (2) the shear strength is set to an excessively high value to simulate linear response using the nonlinear model. The results are shown in Figure 2.5. Note that we are imposing displacements at the base, which means that increasing frequency implies quadratically increasing base motion acceleration. For low base motion amplitude, it observed that the results converge in the low-frequency range. However, high shear strength yields linear response for the entire frequency range. Hence, it is concluded that the FE-model is adequate for the task at hand.

2.4 Harmonic response

2.4.1 Kinematic interaction factors

The results are presented in terms of horizontal and rotational interaction factors (Figures 2.6 and 2.7), normalized horizontal pile-cap displacements (Figure 2.8), normalized pile-cap rotations (Figure 2.9), normalized maximum moments (Figure 2.10), normalized maximum shear forces (Figure 2.11) and normalized maximum axial forces (Figure 2.12). The results are plotted against both frequency and dimensionless angular frequency

$$a_0 = \frac{\omega d_p}{V_{s,H}} \tag{2.16}$$

Normalization is achieved by dividing the results with the peak value in each figure. Maximum moments and forces are given independent of depth. Each plot shows three batter angle configurations ($\beta = 0°, 7.5°$ and $15°$) for a specific combination of pile-to-pile spacing ($S_0 = 2d_p, 6d_p$ and $10d_p$) and base motion amplitude ($U_B = 0.01d_p, 0.03d_p$ and $0.05d_p$). Each combination is analysed for 11 different harmonic base motion histories with frequencies between $0.5Hz$ and $10Hz$. The figures are organized such that base motion amplitude is constant column-wise and pile spacing is constant row-wise. The plots are a result of 297 nonlinear (denoted P in the plot legend) and 99 linear (denoted L in the plot legend) time-history analysis in three-dimensional space. The linear analyses are performed using small-strain properties of the soil model and 5% damping. Note that we are using the approximated small-strain shear wave velocity of the soil profile to normalize the angular frequency. Otherwise, a_0 would generally not be constant in space and time, nor would it be linear with respect to angular frequency, and therefore meaningless as a plotting variable. The single-valued conversion from time to frequency domain is achieved by averaging the horizontal and rotational amplitudes during steady state response. The time domain analysis is therefore performed over a sufficiently long period in order to achieve satisfactory results.

Figure 2.6 shows that soil non-linearity has a substantial impact on the horizontal kinematic interaction. While linear models de-amplify the horizontal ground motion for almost all configurations and frequencies, nonlinear models show fairly large amplification for a wide range of frequencies. Generally, both I_x and I_r increase slightly with base motion amplitude and the difference between 0.1d and 0.3d is more prominent compared to the difference between 0.03d and 0.05d. In fact, the difference between 0.03d and 0.05d is rather negligible in most cases.

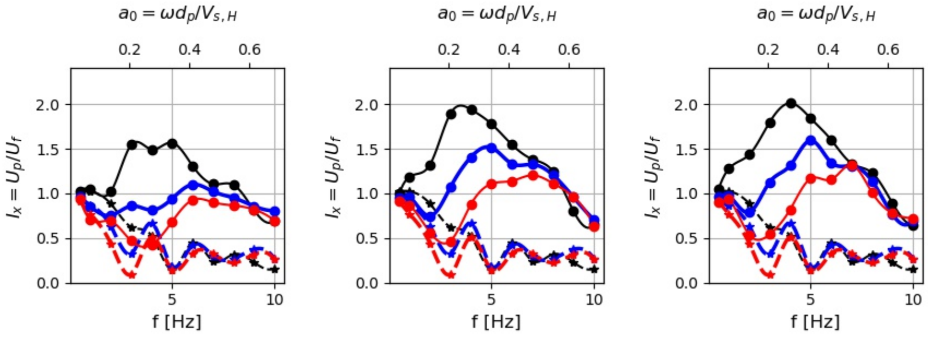

(a) $S_0 = 2d_p, U_b = 0.01d_p$ **(b)** $S_0 = 2d_p, U_b = 0.03d_p$ **(c)** $S_0 = 2d_p, U_b = 0.05d_p$

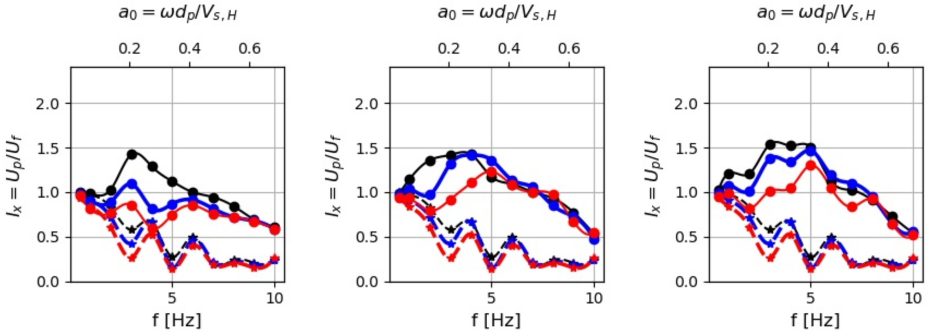

(d) $S_0 = 6d_p, U_b = 0.01d_p$ **(e)** $S_0 = 6d_p, U_b = 0.03d_p$ **(f)** $S_0 = 6d_p, U_b = 0.05d_p$

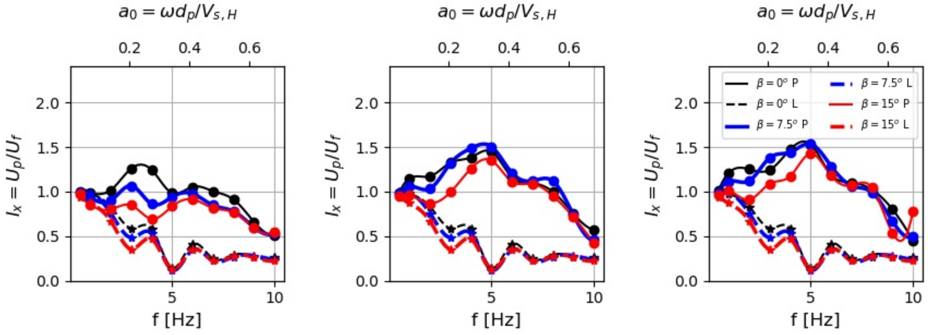

(g) $S_0 = 10d_p, U_b = 0.01d_p$ **(h)** $S_0 = 10d_p, U_b = 0.03d_p$ **(i)** $S_0 = 10d_p, U_b = 0.05d_p$

Figure 2.6: Absolute horizontal kinematic interaction factor I_x plotted against frequency f and dimensionless angular frequency a_0 for different pile-to-pile spacing S_0, batter angles β and base motion amplitudes U_b

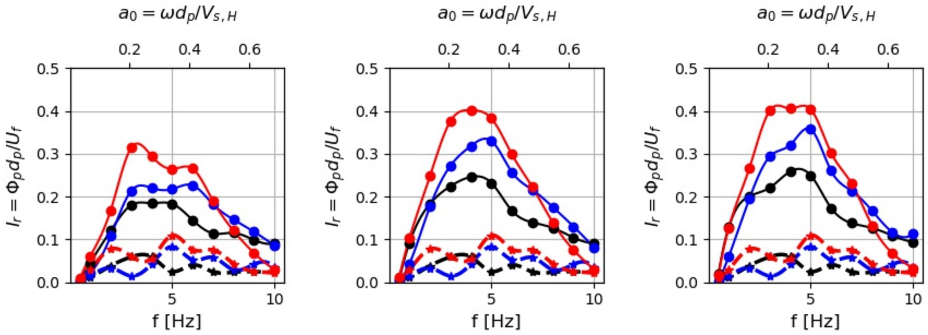

(a) $S_0 = 2d_p, U_b = 0.01d_p$ **(b)** $S_0 = 2d_p, U_b = 0.03d_p$ **(c)** $S_0 = 2d_p, U_b = 0.05d_p$

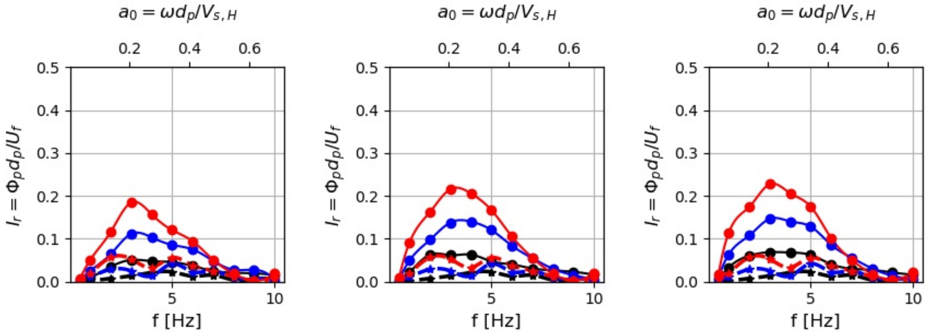

(d) $S_0 = 6d_p, U_b = 0.01d_p$ **(e)** $S_0 = 6d_p, U_b = 0.03d_p$ **(f)** $S_0 = 6d_p, U_b = 0.05d_p$

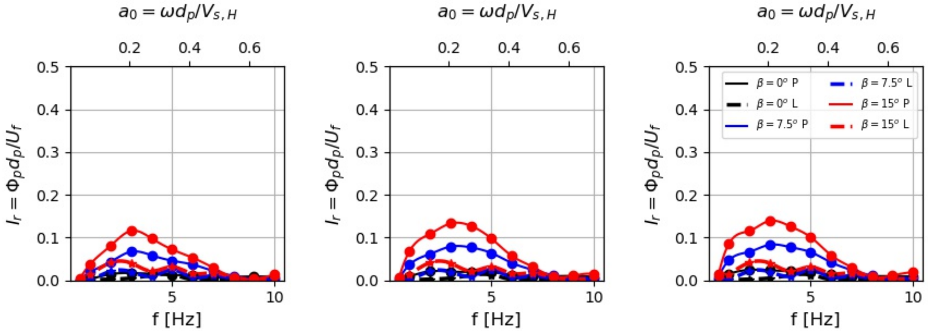

(g) $S_0 = 10d_p, U_b = 0.01d_p$ **(h)** $S_0 = 10d_p, U_b = 0.03d_p$ **(i)** $S_0 = 10d_p, U_b = 0.05d_p$

Figure 2.7: Absolute rotational kinematic interaction factor I_r plotted against frequency f and dimensionless angular frequency a_0 for different pile-to-pile spacing S_0, batter angles β and base motion amplitudes U_b

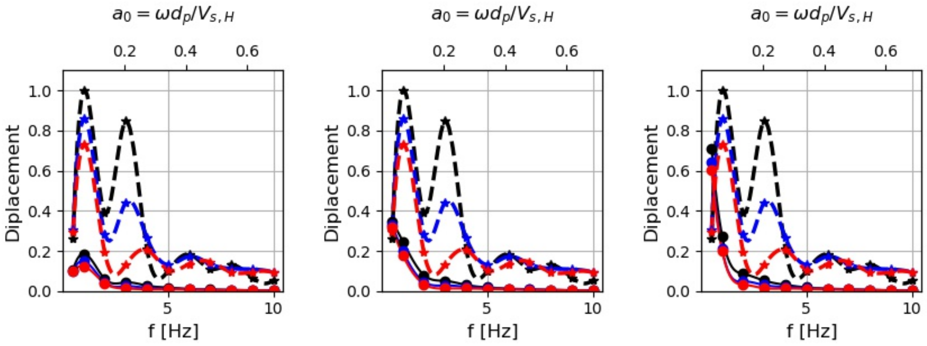

(a) $S_0 = 2d_p, U_b = 0.01d_p$ **(b)** $S_0 = 2d_p, U_b = 0.03d_p$ **(c)** $S_0 = 2d_p, U_b = 0.05d_p$

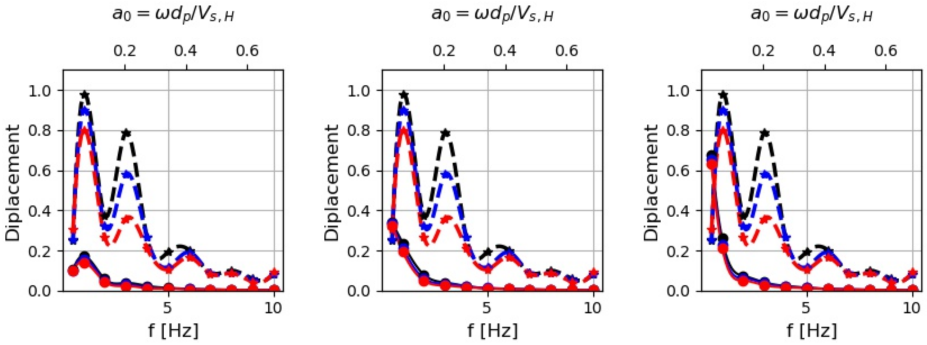

(d) $S_0 = 6d_p, U_b = 0.01d_p$ **(e)** $S_0 = 6d_p, U_b = 0.03d_p$ **(f)** $S_0 = 6d_p, U_b = 0.05d_p$

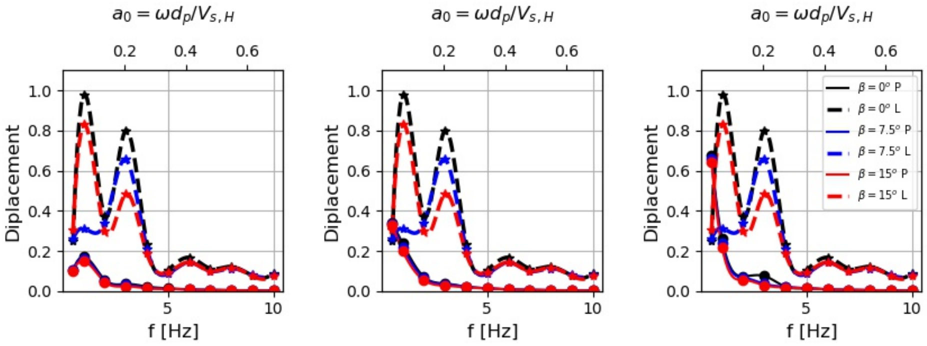

(g) $S_0 = 10d_p, U_b = 0.01d_p$ **(h)** $S_0 = 10d_p, U_b = 0.03d_p$ **(i)** $S_0 = 10d_p, U_b = 0.05d_p$

Figure 2.8: Horizontal displacement amplitude normalized by the peak value and plotted against frequency f and dimensionless angular frequency a_0 for different pile-to-pile spacing S_0, batter angles β and base motion amplitudes U_b

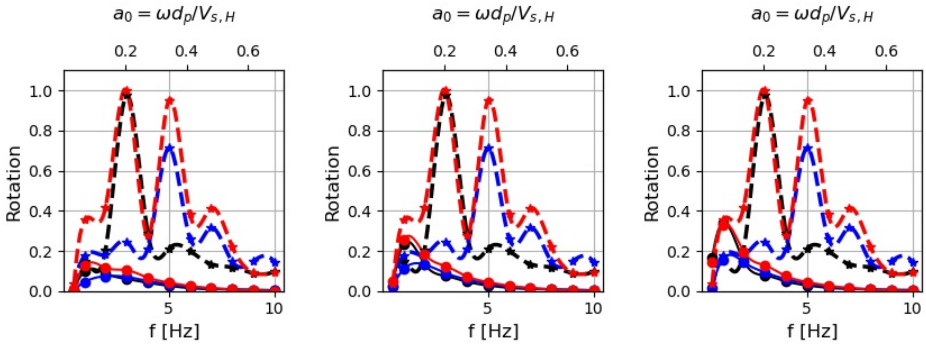

(a) $S_0 = 2d_p, U_b = 0.01d_p$ **(b)** $S_0 = 2d_p, U_b = 0.03d_p$ **(c)** $S_0 = 2d_p, U_b = 0.05d_p$

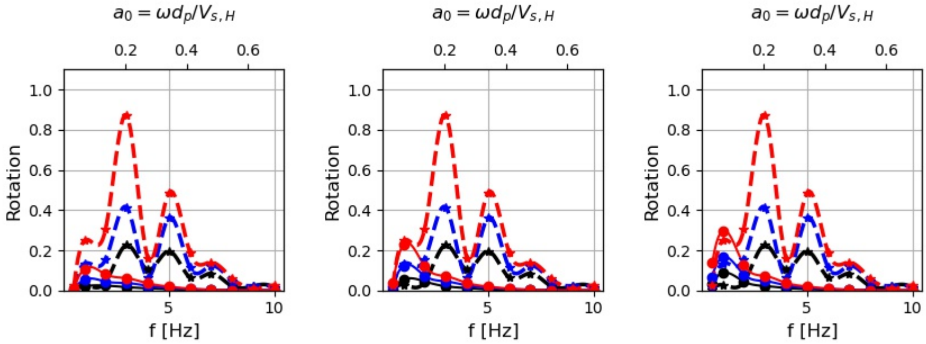

(d) $S_0 = 6d_p, U_b = 0.01d_p$ **(e)** $S_0 = 6d_p, U_b = 0.03d_p$ **(f)** $S_0 = 6d_p, U_b = 0.05d_p$

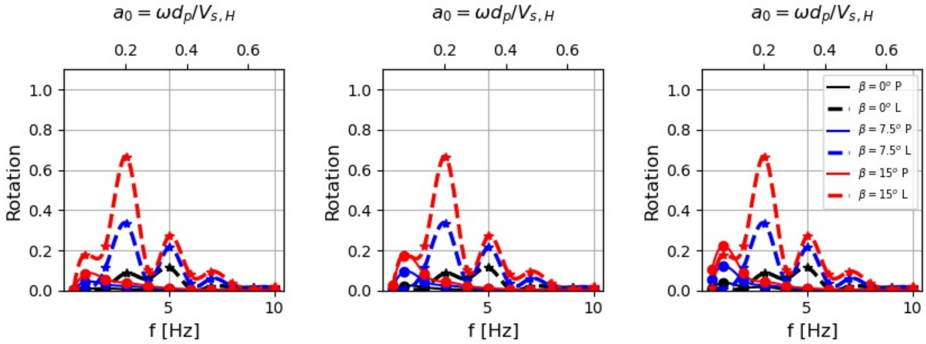

(g) $S_0 = 10d_p, U_b = 0.01d_p$ **(h)** $S_0 = 10d_p, U_b = 0.03d_p$ **(i)** $S_0 = 10d_p, U_b = 0.05d_p$

Figure 2.9: Rotation amplitude normalized by the peak value and plotted against frequency f and dimensionless angular frequency a_0 for different pile-to-pile spacing S_0, batter angles β and base motion amplitudes U_b

This is an inherent part of the nonlinear material behaviour shown in Figure 2.3. It is also observed that base motion amplitude is most significant for small pile spacing. The largest differences between the different batter angles are observed in the low-to-mid frequency range for most configurations. As frequency increases, the difference decreases and I_x generally decreases. In the high-frequency range, I_x is practically unaffected by batter angle.

Eigenfrequencies of the linear soil profile may be estimated using Equation 2.7, i.e,

$$f_{H,1} = \frac{V_{s,H}}{4H} = 0.96Hz,\ f_{H,2} = \frac{3V_{s,H}}{4H} = 2.87Hz,\ f_{H,3} = \frac{5V_{s,H}}{4H} = 4.78Hz... \tag{2.17}$$

Figure 2.6 clearly shows that horizontal interaction using linear models is most prominent near these frequencies, starting from the second eigenfrequency. For the first soil mode in the linear case, the soil response has small variations close to the surface, and the pile conforms relatively well to the soil displacements. At higher frequencies with smaller wavelengths, the pile is unable to follow the soil displacements which leads to small I_x-values. In nonlinear soil, the dramatic reduction of the soil stiffness close to the surface results in the pile's stiffness dominating the soil response, which leads to pile displacements larger than in the free-field.

Figure 2.7 shows that non-linearity significantly increases I_r for all configurations. nonlinear models show a clear tendency with respect to frequency, where rotation peaks at the mid-range frequencies and decays to diminishing small values as frequency increases. Linear models however, do not show a clear trend, but rather a steady fluctuation at relativity small values compared to the nonlinear model. Linear and nonlinear models seemingly tend towards convergence at higher frequencies. I_r increases with batter angle for all configurations, especially for nonlinear models. Similar results were obtained in previous studies [14, 179, 209, 210] using linear models. There may evidently exist cut-off frequencies where increasing batter angle in fact decreases rotation, but this behaviour occurs in the high-frequency range where rotation is generally small. I_r decreases significantly as pile spacing increases for all batter angles and base motion amplitudes. Similar results were obtained by Medina et al. [179]. The results also show that as pile spacing increases, batter angle becomes a more governing factor.

2.4.2 Displacement and rotation amplitudes

It is important to note that the differences between linear and nonlinear models shown in Figures 2.6 and 2.7 only reflect differences regarding pile-soil interaction, not differences between displacements and rotation values. In other words, these results should not be interpreted as if nonlinear models produce larger pile-cap displacements and rotations. On the contrary, Figures 2.8 and 2.9 show that soil non-linearity in most cases substantially reduces displacements and rotations. As expected, Figure 2.8 shows that displacements peak at the first eigenfrequencies in case of linear soil. The nonlinear models however, do not exhibit this behaviour. Except for a small peak at the fundamental frequency in combination with small base motion amplitudes, displacements generally decrease as frequency increases. The peak is explained by the fact that small base motion amplitude in combination with low excitation frequency results in a more linear behaviour of the soil. Consistent with the findings regarding horizontal interaction in Figure 2.6, non-linearity not only reduces displacements, but also yields less frequency dependent behaviour. Moving past the mid-to-high frequency range, nonlinear models produce diminishingly small pile-cap displacements. Figure 2.9 reveals similar results for rotations. As was shown for rotational interaction in Figure 2.7, rotations decrease with increasing pile spacing for both the linear and nonlinear models.

2.4.3 Section moments and forces

Figure 2.10 shows the maximum moment in a pile independent of depth normalized by the maximum moment occurring for all the cases considered (therefore, there is only one case in the figures that reaches 1.0). Results presented in Figures 2.8 - 2.9 clearly show that non-linearity reduces displacement and rotations, and it may readily be shown that same applies to moment and forces. Therefore, moments and forces will only be presented for the nonlinear case. By doing so, one may observe trends with respect to base motion amplitude, batter angle and pile spacing rather clearly within the nonlinear domain. Generally, Figure 2.10 shows that moments peak at the fundamental frequency and decay as frequency increases. Moments increase with batter angle, but only at or near the fundamental frequency. The difference is most prominent for small pile spacing and large shaking. Except for small differences at the fundamental frequency, moments are practically independent of batter angle for large pile spacing. It is also observed that moments tend towards small values in the mid-to-high frequency range for all configurations. Moments also generally increase with increasing pile spacing and shaking.

Figure 2.11 shows the maximum shear force in the same manner as moments. As in the case for moments, shear forces peak at the fundamental frequency, increase with pile spacing and base motion amplitude and decay as frequency increases. Shear forces also slightly increase with batter angle, but the differences are smaller compared to moments. For practical purposes, shear forces can be considered independent of batter angle.

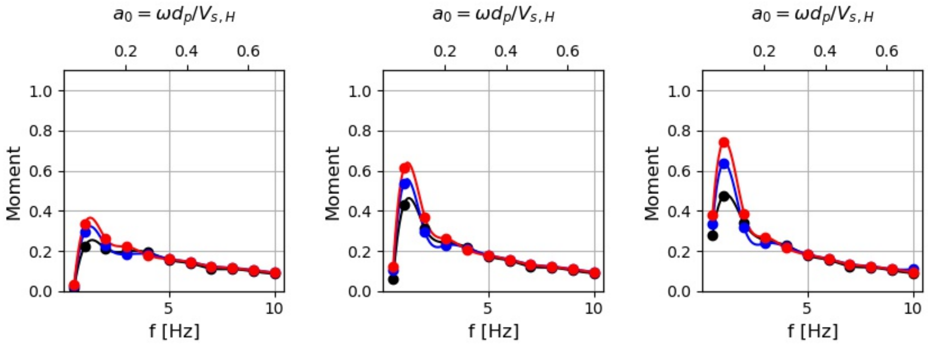

(a) $S_0 = 2d_p, U_b = 0.01d_p$ **(b)** $S_0 = 2d_p, U_b = 0.03d_p$ **(c)** $S_0 = 2d_p, U_b = 0.05d_p$

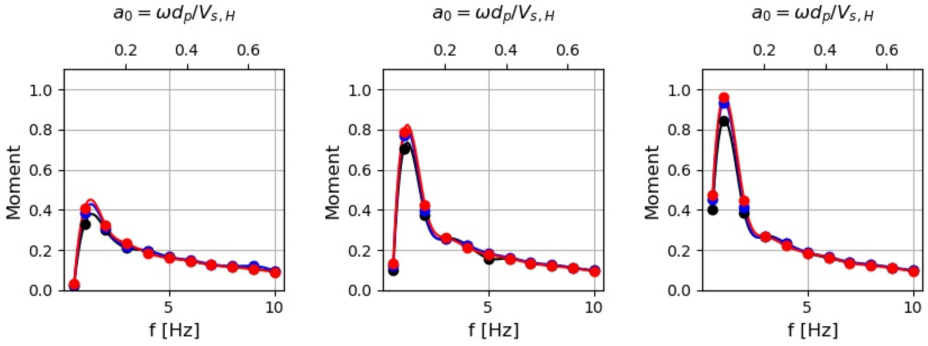

(d) $S_0 = 6d_p, U_b = 0.01d_p$ **(e)** $S_0 = 6d_p, U_b = 0.03d_p$ **(f)** $S_0 = 6d_p, U_b = 0.05d_p$

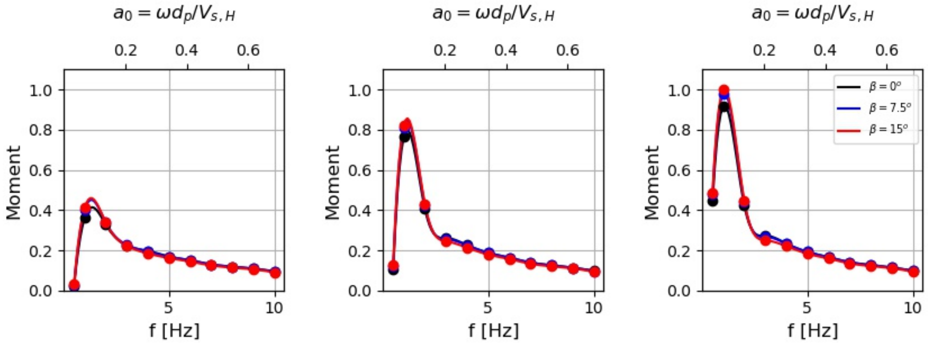

(g) $S_0 = 10d_p, U_b = 0.01d_p$ **(h)** $S_0 = 10d_p, U_b = 0.03d_p$ **(i)** $S_0 = 10d_p, U_b = 0.05d_p$

Figure 2.10: Maximum moment independent of depth normalized by the peak value and plotted against frequency f and dimensionless angular frequency a_0 for different pile-to-pile spacing S_0, batter angles β and base motion amplitudes U_b

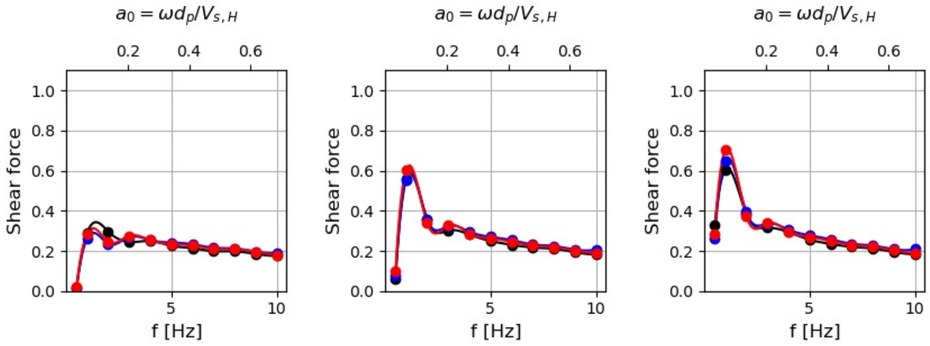

(a) $S_0 = 2d_p, U_b = 0.01d_p$ **(b)** $S_0 = 2d_p, U_b = 0.03d_p$ **(c)** $S_0 = 2d_p, U_b = 0.05d_p$

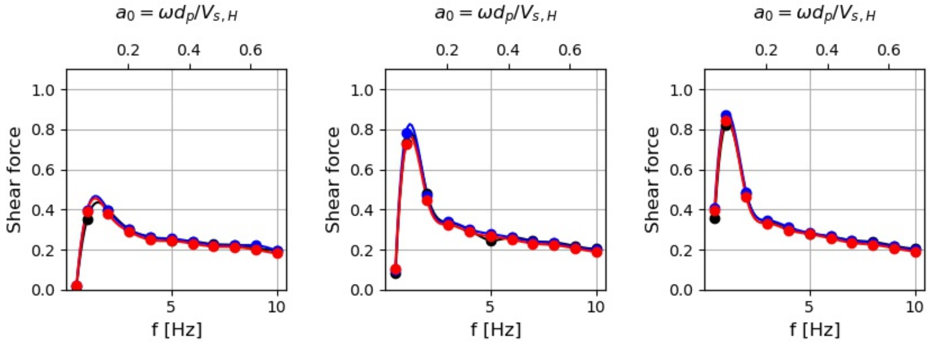

(d) $S_0 = 6d_p, U_b = 0.01d_p$ **(e)** $S_0 = 6d_p, U_b = 0.03d_p$ **(f)** $S_0 = 6d_p, U_b = 0.05d_p$

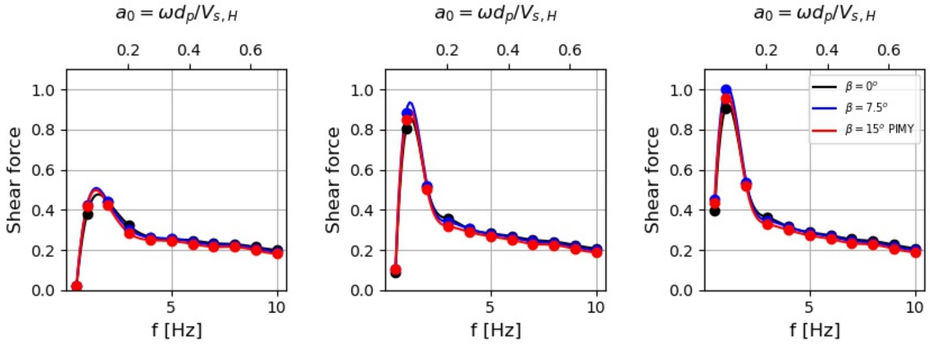

(g) $S_0 = 10d_p, U_b = 0.01d_p$ **(h)** $S_0 = 10d_p, U_b = 0.03d_p$ **(i)** $S_0 = 10d_p, U_b = 0.05d_p$

Figure 2.11: Maximum shear force independent of depth normalized by the peak value and plotted against frequency f and dimensionless angular frequency a_0 for different pile-to-pile spacing S_0, batter angles β and base motion amplitudes U_b

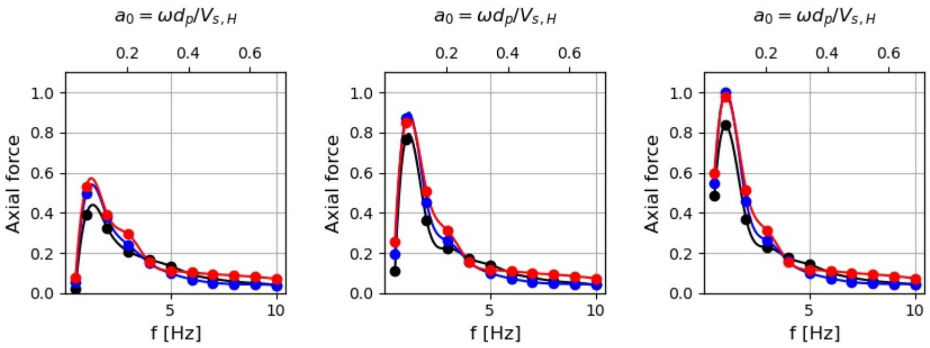

(a) $S_0 = 2d_p, U_b = 0.01d_p$ **(b)** $S_0 = 2d_p, U_b = 0.03d_p$ **(c)** $S_0 = 2d_p, U_b = 0.05d_p$

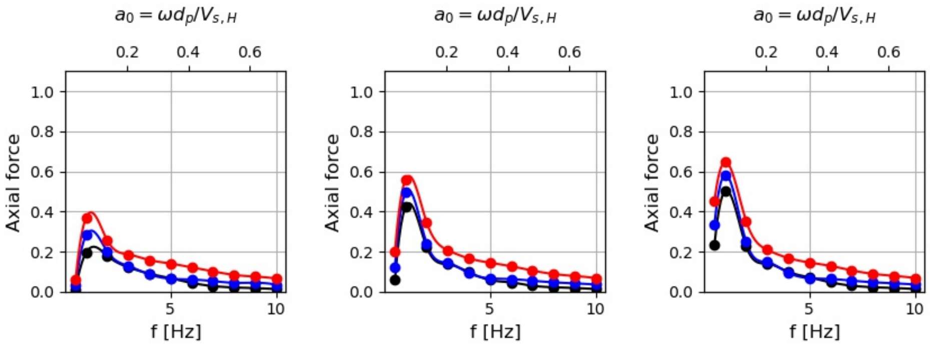

(d) $S_0 = 6d_p, U_b = 0.01d_p$ **(e)** $S_0 = 6d_p, U_b = 0.03d_p$ **(f)** $S_0 = 6d_p, U_b = 0.05d_p$

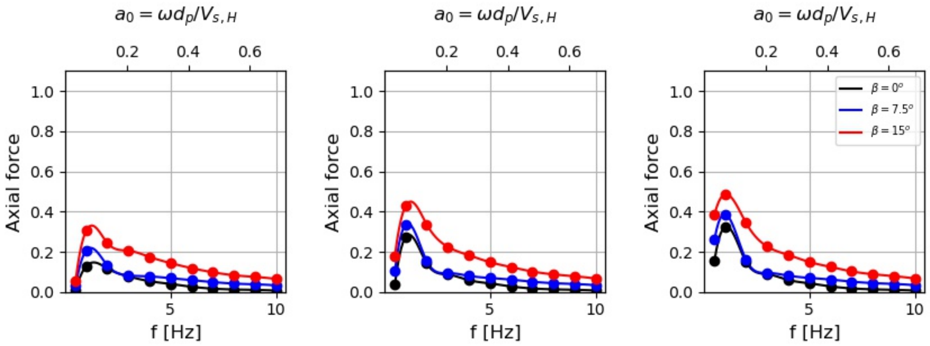

(g) $S_0 = 10d_p, U_b = 0.01d_p$ **(h)** $S_0 = 10d_p, U_b = 0.03d_p$ **(i)** $S_0 = 10d_p, U_b = 0.05d_p$

Figure 2.12: Maximum axial force independent of depth normalized by the peak value and plotted against frequency f and dimensionless angular frequency a_0 for different pile-to-pile spacing S_0, batter angles β and base motion amplitudes U_b

Figures 2.12 shows the maximum occurring axial force in the same manner as moments and shear forces. Axial forces peak at the fundamental frequency, increase with base motion amplitude and decay as frequency increases. Contrary to moments and shear forces, axial forces decrease with increasing pile spacing. It is interesting that as pile spacing increases, the two configurations with $\beta = 0°$ and $\beta = 7.5°$ converge, while the difference compared to the configuration with $\beta = 15°$ increases. This might suggest a cut-off combination of batter angle and pile spacing, where axial forces begin to increase.

2.4.4 Other practical observations

A common characteristic in the kinematic response of the two-by-one pile groups depicted in Figures 2.6 - 2.12, is that batter angle becomes less important as frequency increases beyond a certain value. This behaviour is attributed to the short-wavelength excitation causing reversing soil displacements over the pile length. Figure 2.13 shows deformation patterns at maximum pile-cap displacement for pile groups with $S_0 = 2d_p$ subjected to harmonic excitations at $3Hz$ and $8Hz$, respectively. These frequencies are chosen to represent the mid-to-low frequency range where large differences in kinematic interaction between batter and vertical piles begin to occur, and a high frequency range, where batter and vertical piles begin to converge. In the mid-to-low frequency range, the soil displacements are relativity uniform over the pile length, causing a large portion of piles to move somewhat uniformly in one direction. The vertical pile groups then displays a rather cantilever-like deformation pattern as is shown in Figure 2.13(a). When the pile-cap moves to the right, it rotates clock-wise. The maximum displacement and rotation are in phase and the axial pair of forces is working in the opposite direction of rotation. The batter pile group on the other hand, shows a completely different deformation pattern for the same base excitation as clearly illustrated in Figure 2.13(c). When the pile-cap moves to the right, it rotates counter clock-wise. It can be shown that the maximum displacement and rotation are in fact out of phase, and that the axial pair of forces is working in the direction of rotation. This observation is consistent with the findings of Giannakou et al. [14], who also reported out-of-phase displacement and rotations for batter pile groups. This indicates that increased pile-cap rotation of batter piles groups is not solely caused by increased axial force magnitude, but also by the direction in which they act. This observation is supported by the results presented in Figures 2.7(b) and 2.12(b), which show large differences in rotation between the different batter angles at the mid-to low frequency range, but relatively small differences in axial force.

Contrary to low-frequency excitation, high frequencies cause soil displacements

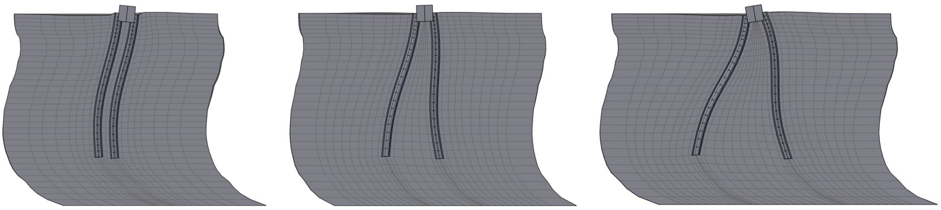

(a) $\beta = 0^\circ$ and $f = 3Hz$ **(b)** $\beta = 7.5^\circ$ and $f = 3Hz$ **(c)** $\beta = 15^\circ$ and $f = 3Hz$

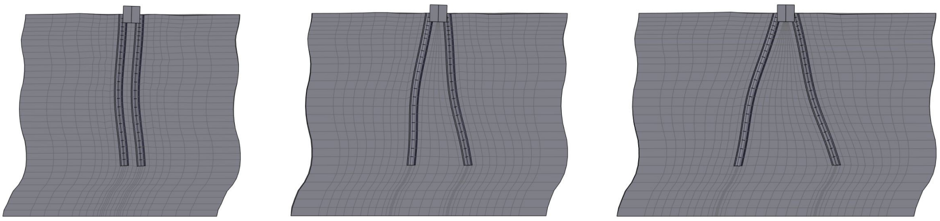

(d) $\beta = 0^\circ$ and $f = 8Hz$ **(e)** $\beta = 7.5^\circ$ and $f = 8Hz$ **(f)** $\beta = 15^\circ$ and $f = 8Hz$

Figure 2.13: Comparison of deformed shape for various batter angles and excitation frequencies. $S_0 = 2d$ and $U_b = 0.03d$

that reverse multiple times over the pile length, which in turn produce smaller net displacement and rotation, and thus also more similar behaviour for vertical and batter pile groups. This deformation pattern is depicted in Figures 2.13(d) - 2.13(f), which further illustrates why (1) I_x and I_r tend to insignificant values as frequency increases, and (2) that shear forces are relatively larger in the high frequency range compared to moments and axial forces as can be seen in Figures 2.10 - 2.12.

Another common characteristic is that moments and forces imposed by kinematic interaction of pile groups are not grossly increased by batter angle, while pile-cap displacements are significantly reduced with increasing batter angle, especially for smaller pile spacing. Since inertial forces from the superstructure are governed by the magnitude of pile-cap displacements and rotations, there is reason to suspect that batter piles may be beneficial to the overall response.

2.5 Transient response

2.5.1 General behaviour

The results presented in the previous sections are frequency-dependent values obtained from nonlinear analyses with imposed harmonic base motions. In this section, we explore how the frequency-dependent findings may relate to the system response when subjected to real earthquake time histories. In order to investigate this, four different pile groups using the largest and smallest values of pile spacing S_0 and batter angle β are subjected to the horizontal component of the 1979 Imperial Valley-06 earthquake ($M = 6.4$, $PGA = 0.15g$, dominant period $T_p \approx 0.1 - 1.0s$). The results are presented as normalized horizontal and angular acceleration of the pile-cap in both time and frequency domain, in addition to normalized moments, shear forces and axial forces in the piles.

Figure 2.14 shows the horizontal and angular acceleration of the pile-cap for a group with $S_0 = 2d_p$. The results reveal that increasing batter angle decreases horizontal acceleration but increases angular acceleration. Further, the largest differences of displacements are observed in the low-to-mid frequency range, while the largest differences in angular accelerations are observed in the mid-range frequencies. These observations are in line with the frequency-dependent interaction factors presented in Figures 2.6 and 2.7.

Figure 2.15 shows the same results, but for a pile group with $S_0 = 10d_p$. As for close pile spacing, increasing batter angle decreases horizontal displacements and increases rotations. However, two distinctions are observed; (1) there is less difference in horizontal acceleration between the two batter angles and (2) the difference in angular rotation is substantially increased. These observations are also in line with the frequency-dependent interaction factors presented in Figures 2.6 and 2.7.

Figure 2.16 compares the linear model against the nonlinear model. The linear model yields large peaks near the estimated eigenfrequencies of the soil profile and generally produces larger displacements and rotations, as was also demonstrated in Figures 2.8 and 2.9.

Figures 2.17-2.20 show the horizontal and angular acceleration of the pile-cap subjected to scaled values of the 1979 Imperial Valley-06 earthquake. It is observed that the relative behaviour of vertical and batter pile groups is not heavily influenced by the input motion PGA once the system is in the nonlinear domain.

Figures 2.21 and 2.22 show the response spectrum of the scaled input motions and the resulting horizontal pile-cap motions for vertical and batter pile group with $S_0 = 2d_p$. Figure 2.21 shows the normalized response spectra for each case and Figure 2.22 shows the response spectrum of the horizontal pile-cap motion divided by the spectrum of the input motion, which is here referred to as response spectrum ratio. For low PGA, the system behaves practically linearly and the spectral accelerations are greatly amplified for both pile groups. The peak is observed near the estimated fundamental period of the soil profile. As PGA increases, the pile-

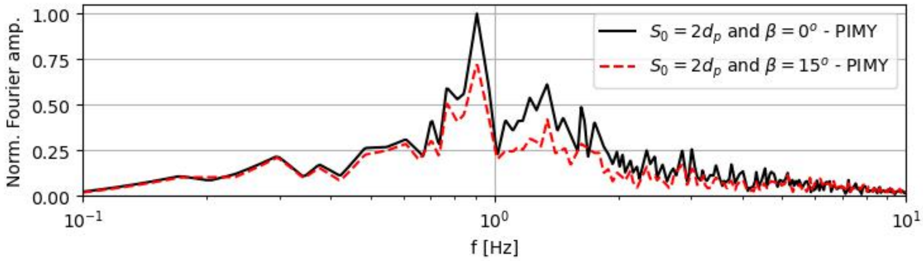

(a) Horizontal acceleration in frequency domain

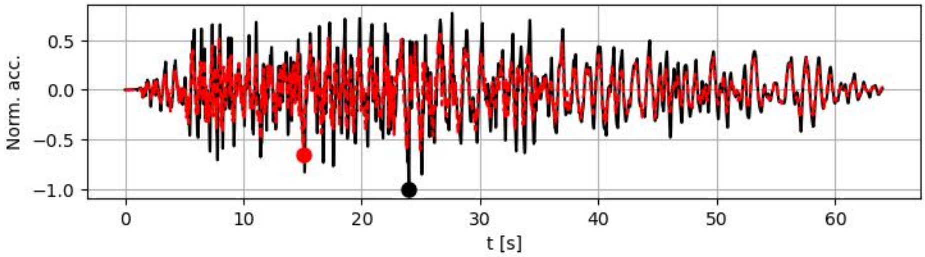

(b) Horizontal acceleration in time domain

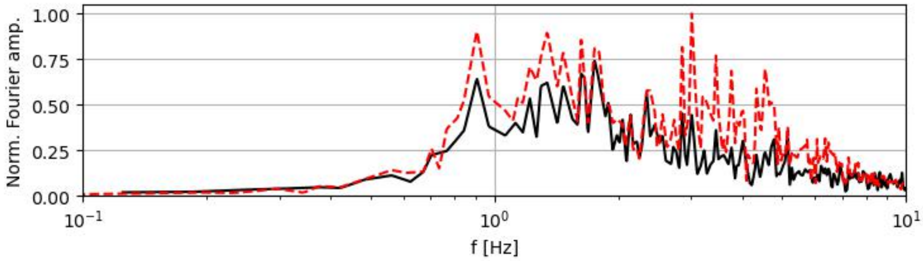

(c) Angular acceleration in frequency domain

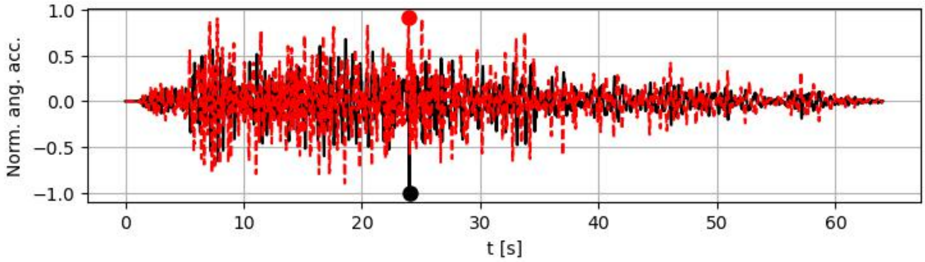

(d) Angular acceleration in time domain

Figure 2.14: Comparison of batter angle. $S_0 = 2d_p$

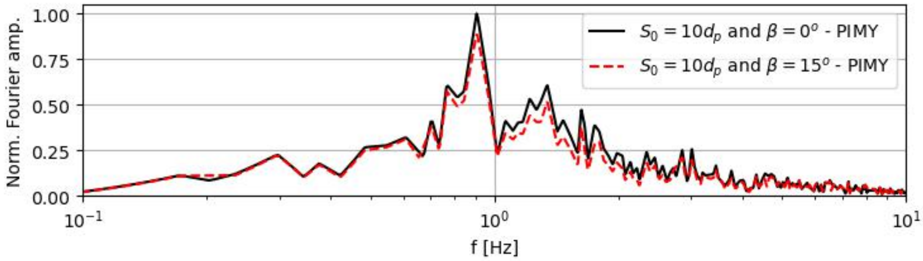

(a) Horizontal acceleration in frequency domain

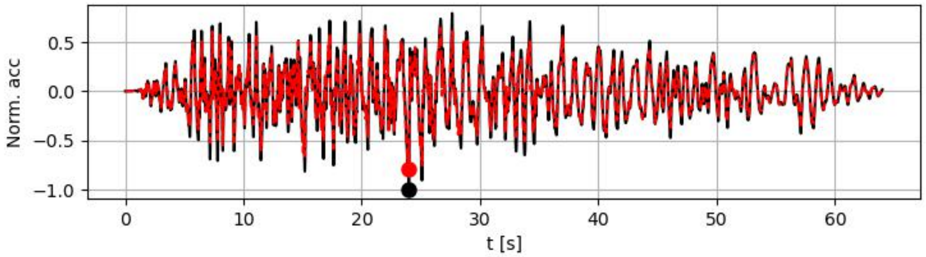

(b) Horizontal acceleration in time domain

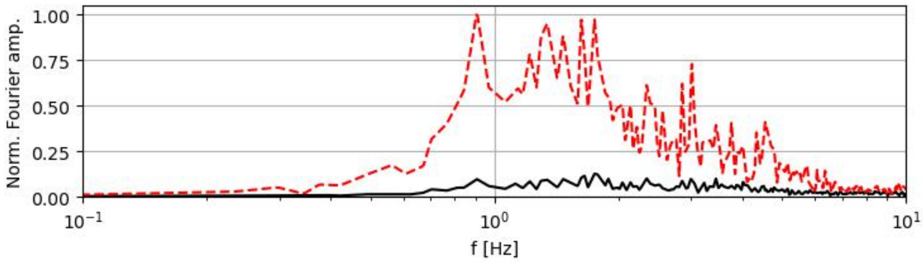

(c) Angular acceleration in frequency domain.

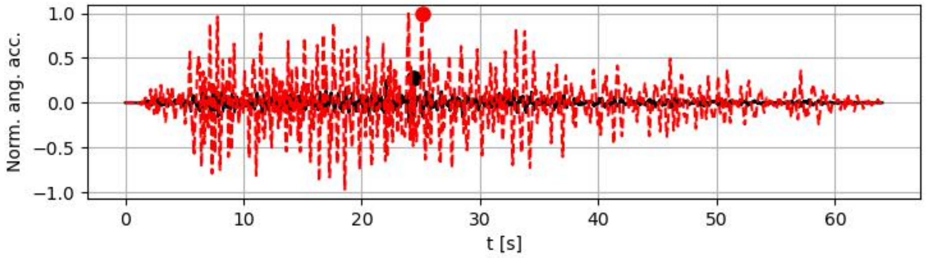

(d) Angular acceleration in time domain

Figure 2.15: Comparison of batter angle. $S_0 = 10d_p$

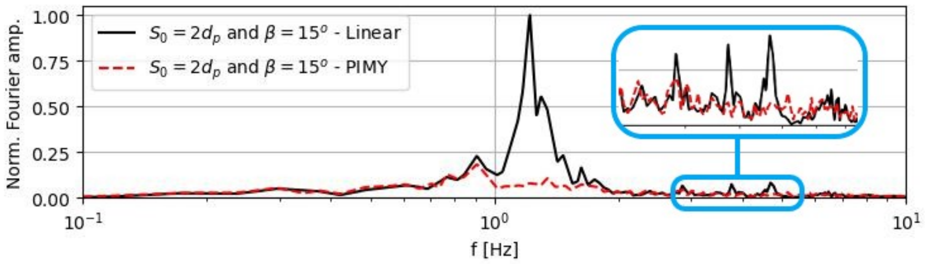

(a) Horizontal acceleration in frequency domain

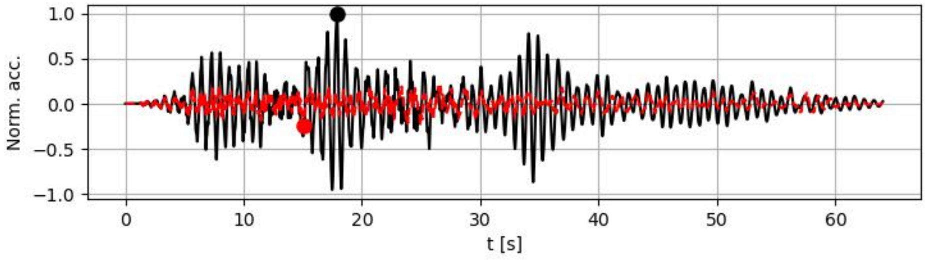

(b) Horizontal acceleration in time domain.

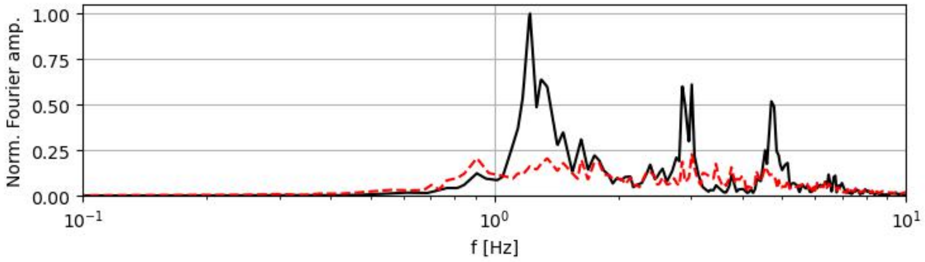

(c) Angular acceleration in frequency domain

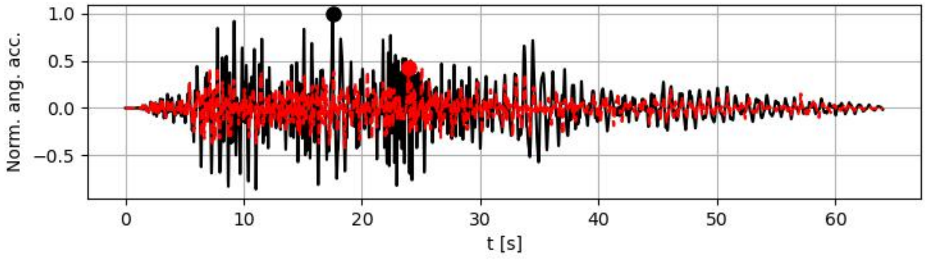

(d) Angular acceleration in time domain

Figure 2.16: Comparison of linear and nonlinear models. $S_0 = 2d_p$

cap amplification diminishes. For low periods, the spectral accelerations are in fact reduced, particularly for batter pile groups. As was also observed in Figures 2.17 and 2.18, the relative behaviour of vertical and batter pile groups is not dependent on input motion PGA when the pile-soil system is responding well in the nonlinear range. Batter pile groups generally yield lower spectral accelerations, and the difference between vertical and batter pile groups seems to be almost independent of period.

Figure 2.23 shows the maximum moment, shear force and axial force in a pile independent of depth normalized by the peak value computed in all four configurations. First, we observe that both moment and shear force increase with both pile spacing and batter angle. Second, the axial force increases with batter angle, but substantially decreases with pile spacing. Both observation are in line with the frequency-dependent results shown in Figures 2.10 - 2.12.

The above results indicate that the frequency-dependent results presented in Section 2.4 may indeed provide insight into how deep foundations respond to seismic loading and could be used to guide arrangements of the piles.

2.5.2 Estimation of FIM

If soil-structure interaction effects are to be considered, an important part of the analysis is the assessment of foundation input motion (FIM), usually given as kinematic pile-cap response in one node. In practice, there is often a need to experiment with different batter angles and pile spacings in order to achieve satisfactory results for both foundation and superstructure. Utilizing kinematic interaction factors is quite efficient. This method implies a single computation of the free-field where the pile-cap response may readily be obtained for various pile spacings and batter angles. The superposition principle strictly restricts the method to linear soil. However, the results obtained in Section 2.5.1 together with the fact that kinematic interaction factors tend to be less dependent of base motion amplitude (PGA) well in the nonlinear range, seems at least to provide some optimism with respect to applying the kinematic interaction factors in a traditional sense as a means for estimating the pile-cap response. An attempt is made in the following to examine how nonlinear kinematic interactions can provide an estimate of the pile-cap response using both vertical and batter piles.

Figures 2.24 and 2.25 show the estimated horizontal and angular acceleration of the pile-cap using nonlinear interaction factors compared against the FE-solution. The results are normalized by the peak value in each plot. Figures 2.24(a) and 2.24(b) show that the horizontal acceleration is generally somewhat overestimated

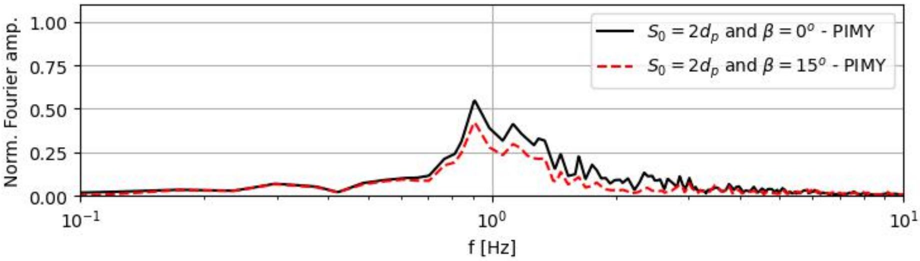

(a) $PGA = 0.05g$.

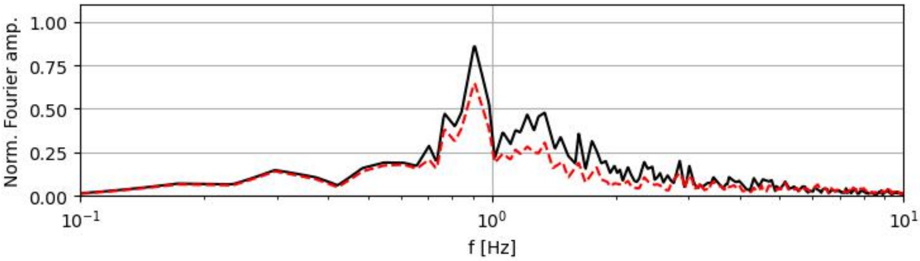

(b) $PGA = 0.10g$.

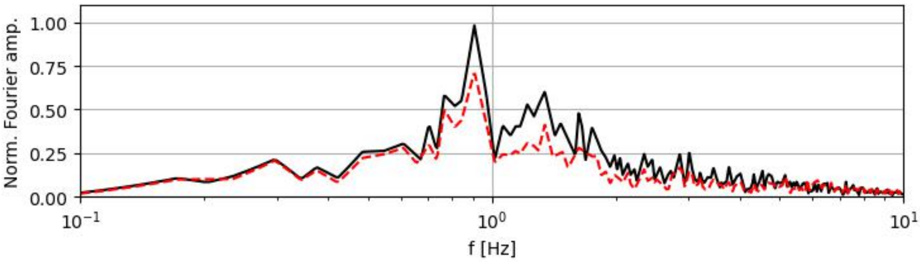

(c) $PGA = 0.15g$.

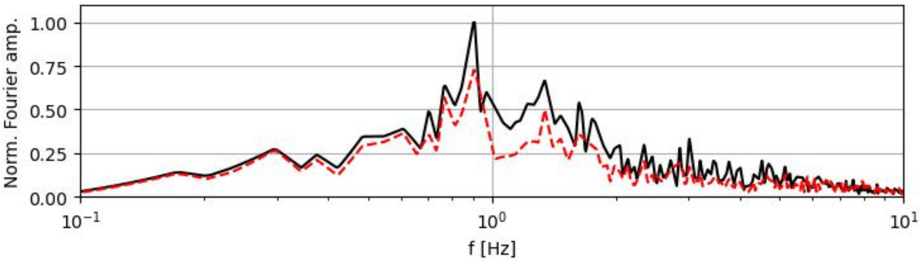

(d) $PGA = 0.20g$.

Figure 2.17: Hor. acceleration, frequency domain. Comparison of PGA. $S_0 = 2d_p$

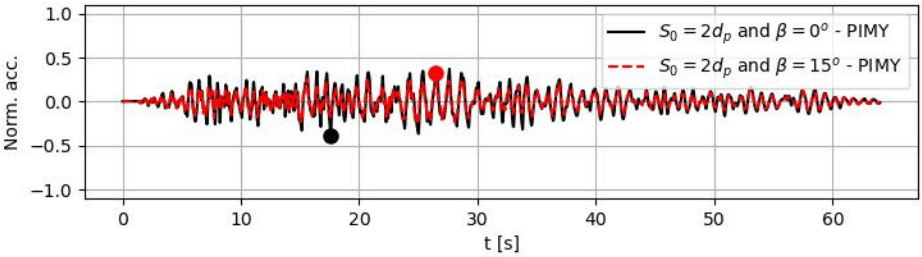

(a) $PGA = 0.05g$.

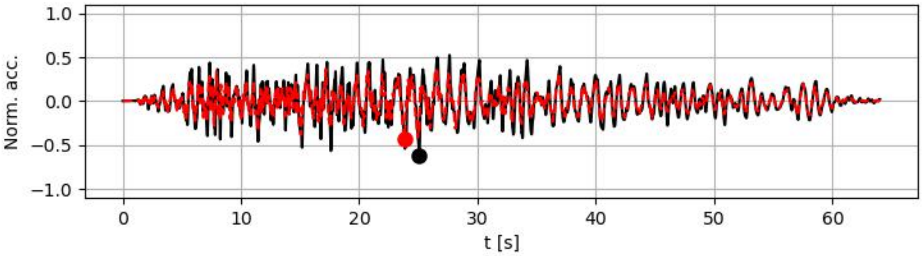

(b) $PGA = 0.10g$.

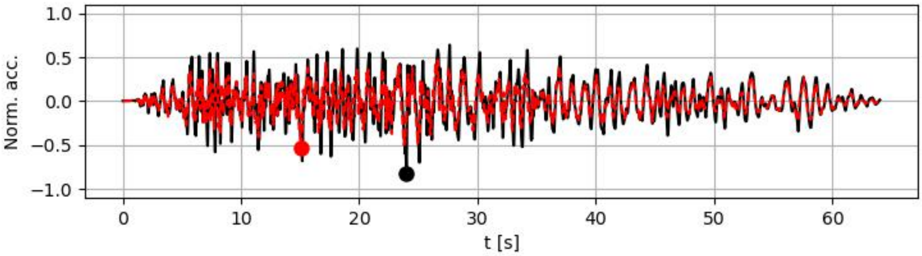

(c) $PGA = 0.15g$.

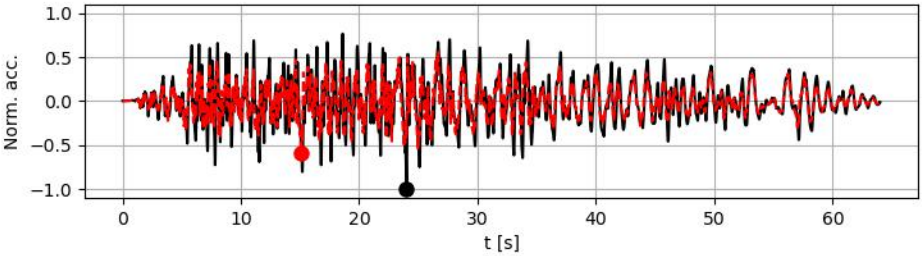

(d) $PGA = 0.20g$.

Figure 2.18: Hor. acceleration, time domain. Comparison of PGA. $S_0 = 2d_p$

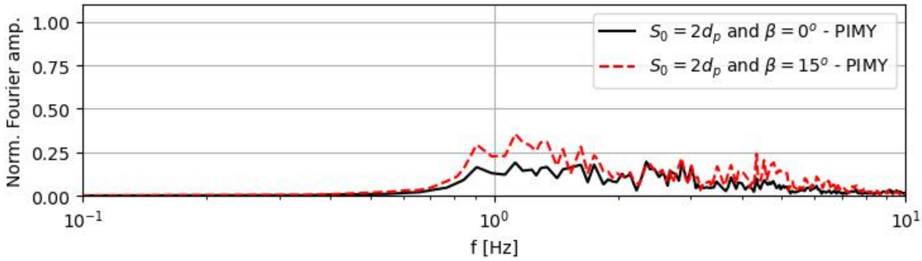

(a) $PGA = 0.05g$

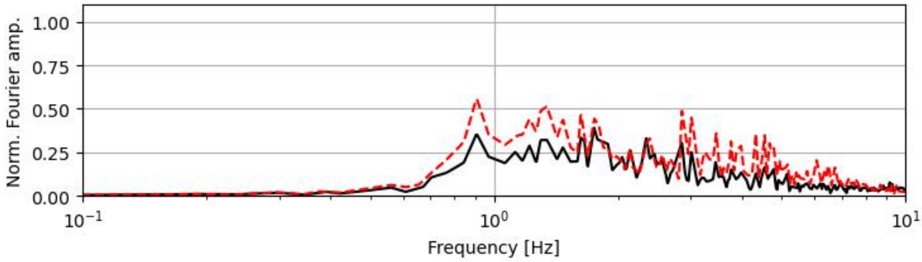

(b) $PGA = 0.10g$

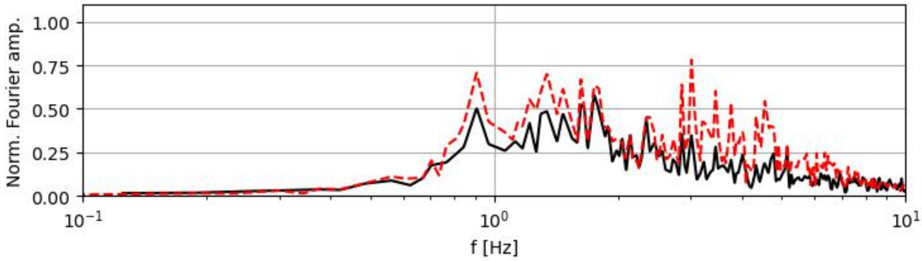

(c) $PGA = 0.15g$

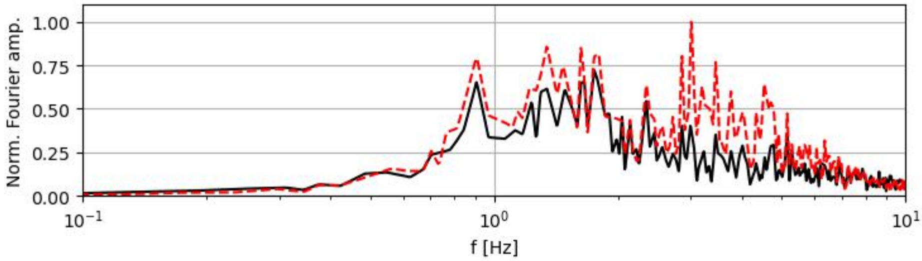

(d) $PGA = 0.20g$

Figure 2.19: Ang. acceleration, frequency domain. Comparison of PGA. $S_0 = 2d_p$

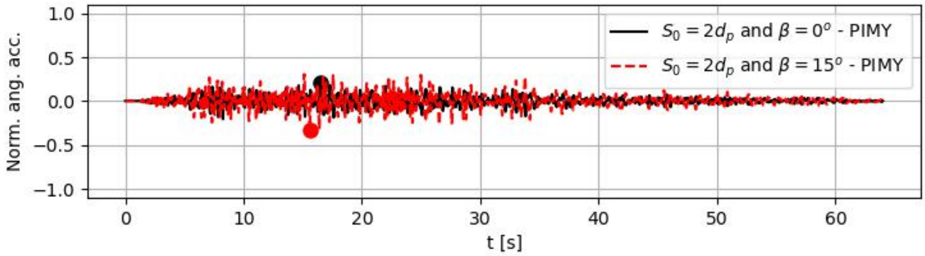

(a) $PGA = 0.05g$.

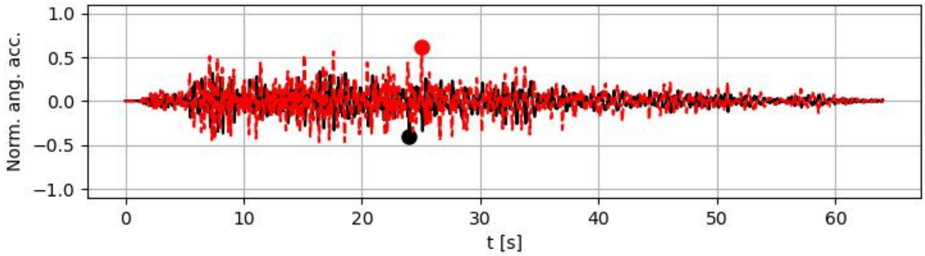

(b) $PGA = 0.10g$.

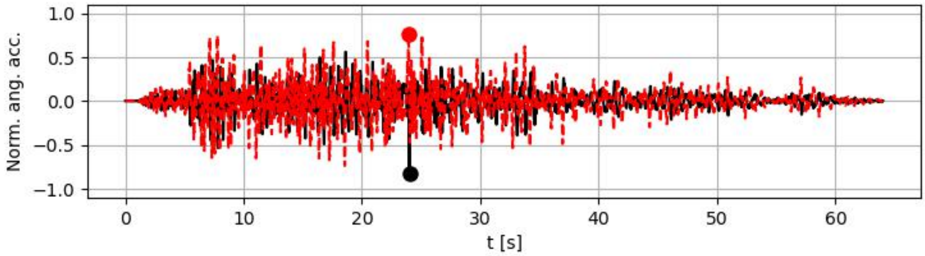

(c) $PGA = 0.15g$.

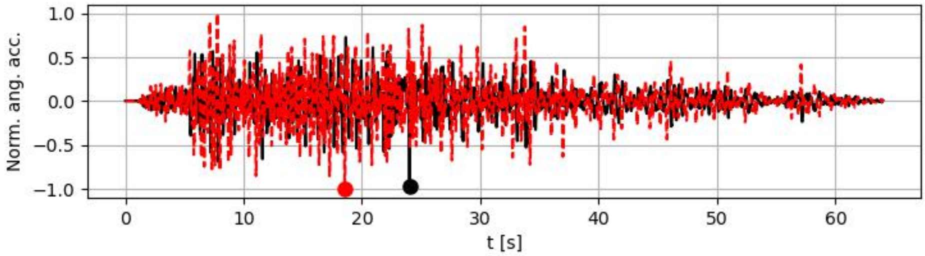

(d) $PGA = 0.20g$.

Figure 2.20: Ang. acceleration, time domain. Comparison of PGA. $S_0 = 2d_p$

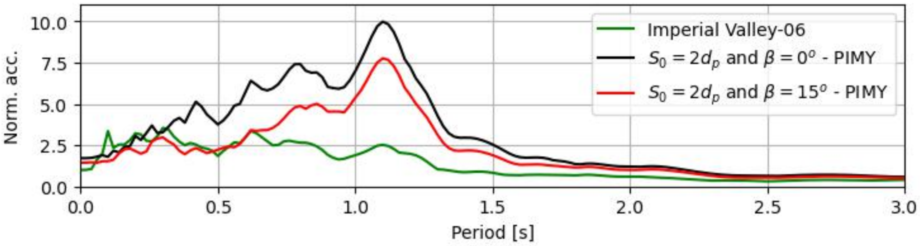

(a) $PGA = 0.05g$

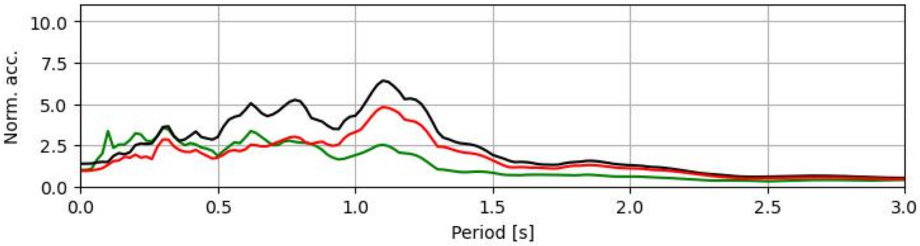

(b) $PGA = 0.10g$

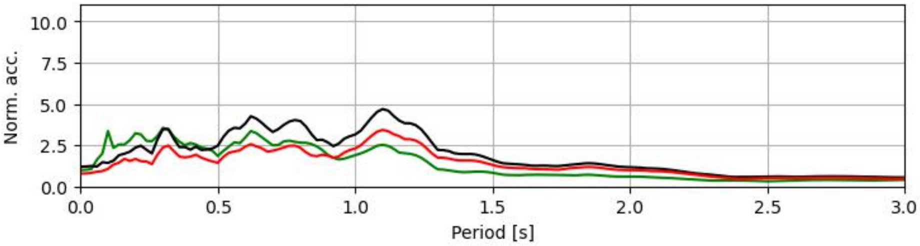

(c) $PGA = 0.15g$

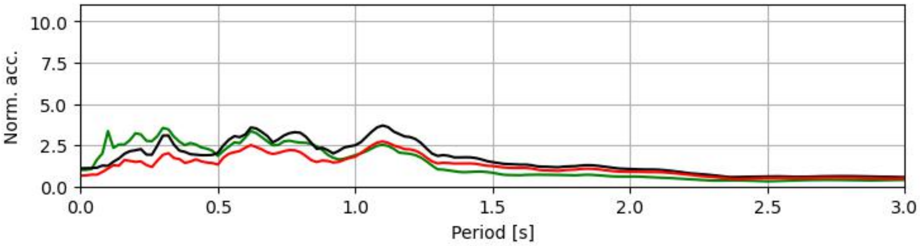

(d) $PGA = 0.20g$

Figure 2.21: Response spectrum with 5% damping. Comparison input motion and pile-cap response

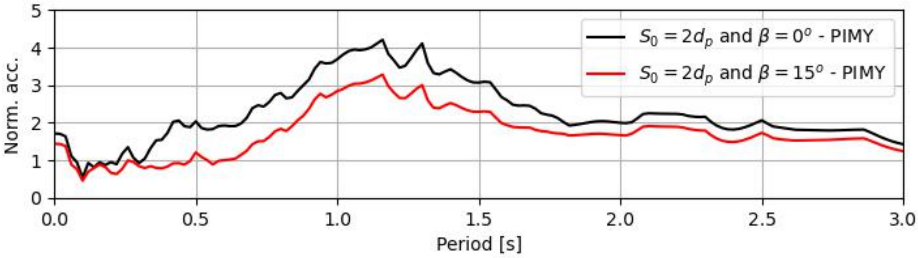

(a) Response spectrum ratio. $PGA = 0.05g$.

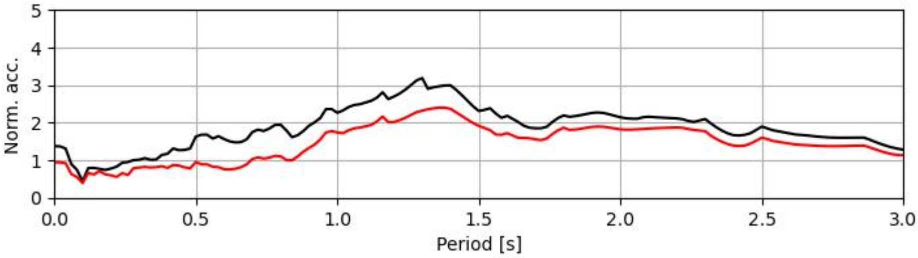

(b) Response spectrum ratio. $PGA = 0.10g$.

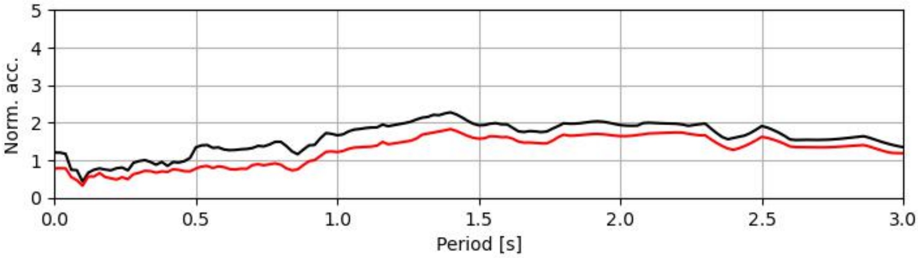

(c) Response spectrum ratio. $PGA = 0.15g$.

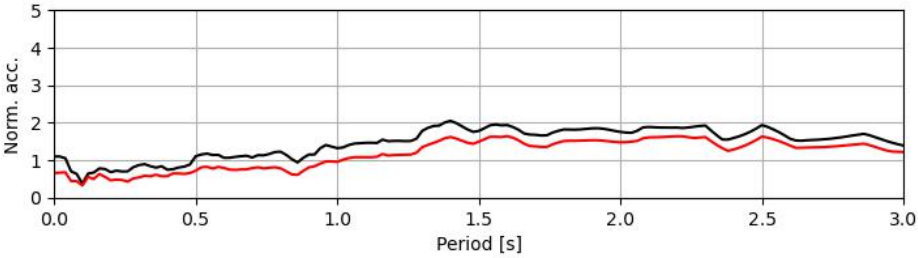

(d) Response spectrum ratio. $PGA = 0.20g$.

Figure 2.22: Response spectrum ratio with 5% damping

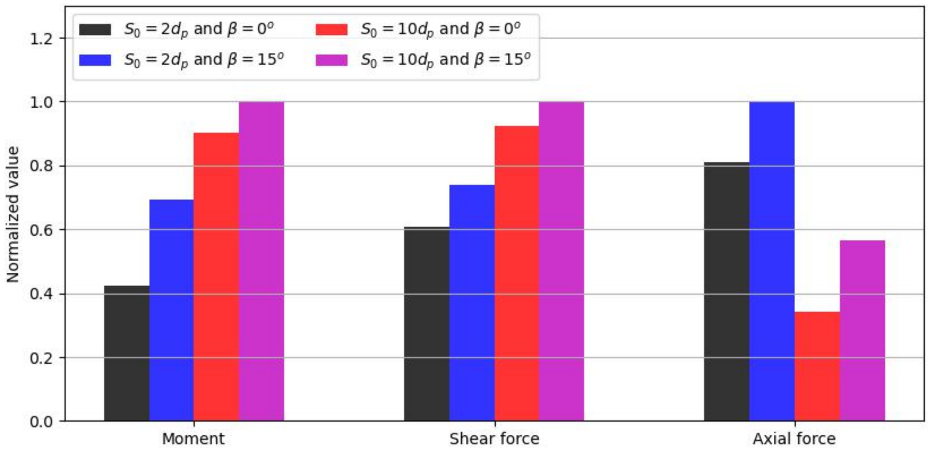

Figure 2.23: Normalized maximum forces.

for vertical piles, but that the trends with respect to frequency are captured fairly well. Figures 2.24(c) and 2.24(d) indicate similar results for batter piles. Figures 2.25(a) and 2.25(b) show that angular acceleration of the pile-cap for vertical piles is overestimated to a greater degree compared to horizontal acceleration. Figures 2.25(c) and 2.25(d) show similar results for batter piles.

Figure 2.26 compares the estimated horizontal and angular acceleration for vertical and batter pile groups. The result show that batter piles yield lower horizontal accelerations and higher angular accelerations.

These results demonstrate that although the method overestimates the response, it is evidently able to roughly capture the effects with respect to batter angle and frequency. Perhaps most importantly, the method is able to produce a rotational time-history which is not explicitly available from free-field site response analyses. Since base motion amplitude (PGA) does not affect the kinematic interaction factors, the utilized interaction factors were taken from Figures 2.6(b) and 2.7(b) for these analyses. Note that the kinematic interaction factors presented in Figures 2.6 and 2.7 are given in absolute form, and are therefore lacking information about phase differences between free-field and pile-cap response. However, the interaction factors applied in the estimation are in fact complex numbers containing information about the phase. The results also show that phase shifts are roughly captured for the most important frequencies.

These results strengthen the earlier observation that the nonlinear kinematic in-

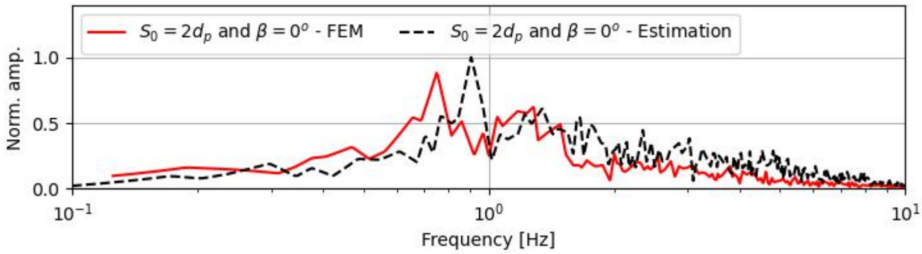

(a) Frequency domain, $\beta = 0°$.

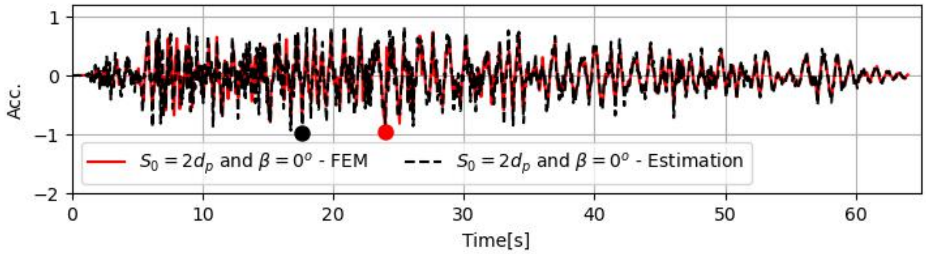

(b) Time domain, $\beta = 0°$.

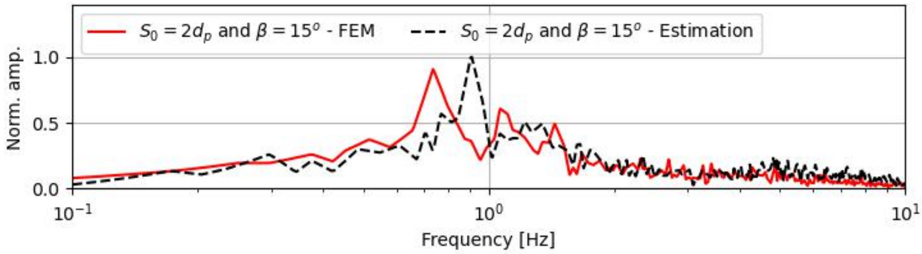

(c) Frequency domain, $\beta = 15°$.

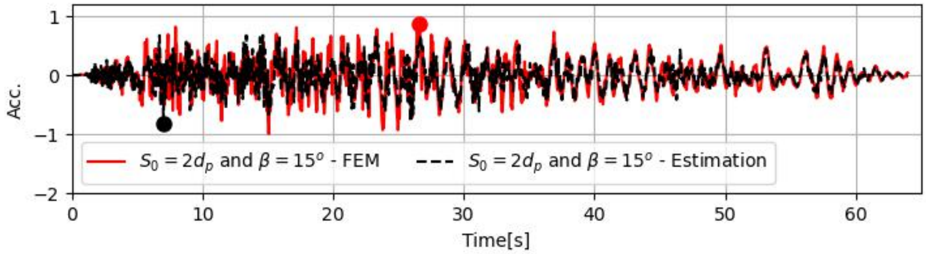

(d) Time domain, $\beta = 15°$.

Figure 2.24: Hor. acceleration, time domain. Estimation. $S_0 = 2d_p$

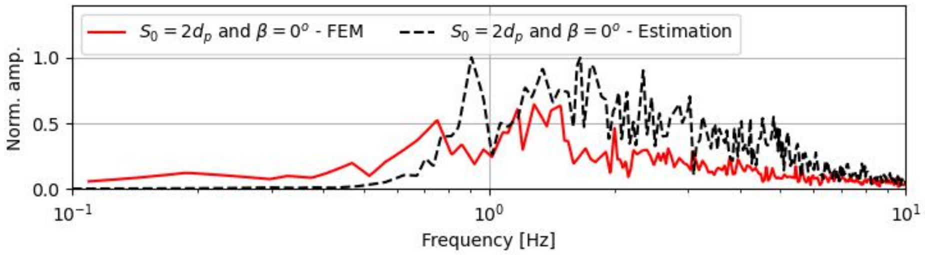

(a) Frequency domain, $\beta = 0°$.

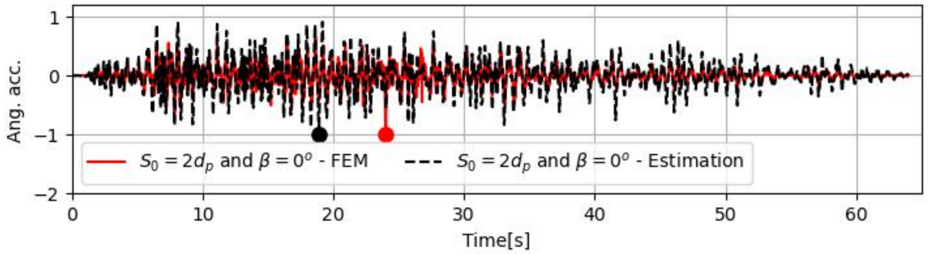

(b) Time domain, $\beta = 0°$.

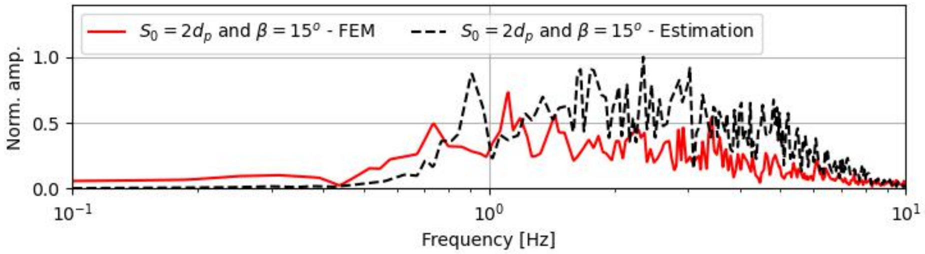

(c) Frequency domain, $\beta = 15°$.

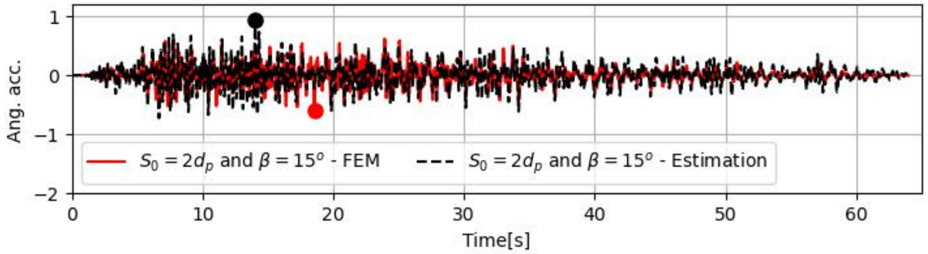

(d) Time domain, $\beta = 15°$.

Figure 2.25: Ang. acceleration, time domain. Estimation. $S_0 = 2d_p$

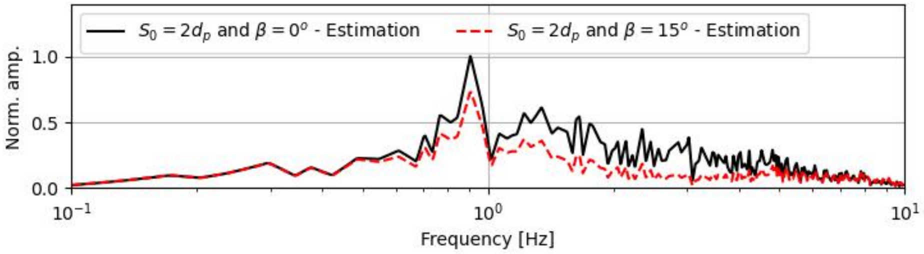

(a) Hor. acceleration, frequency domain.

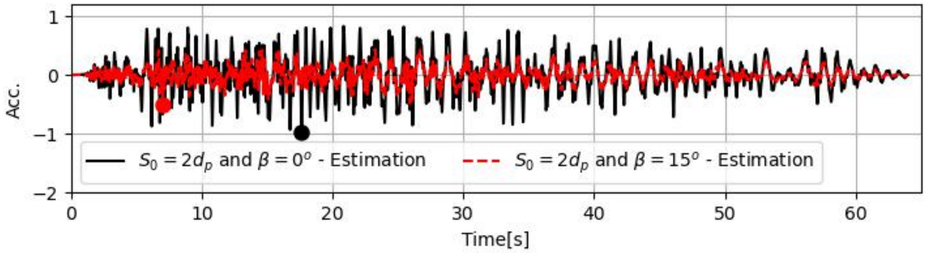

(b) Hor. acceleration, time domain.

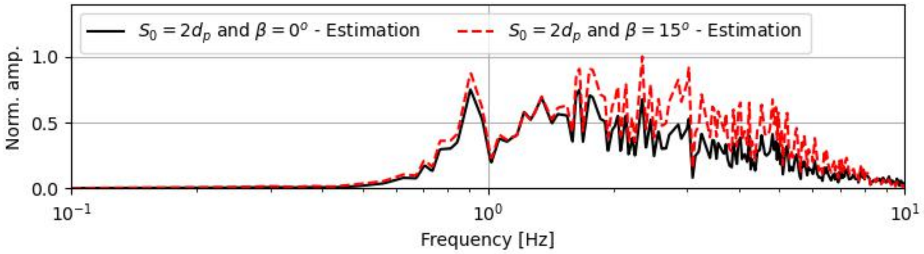

(c) Ang. acceleration, frequency domain.

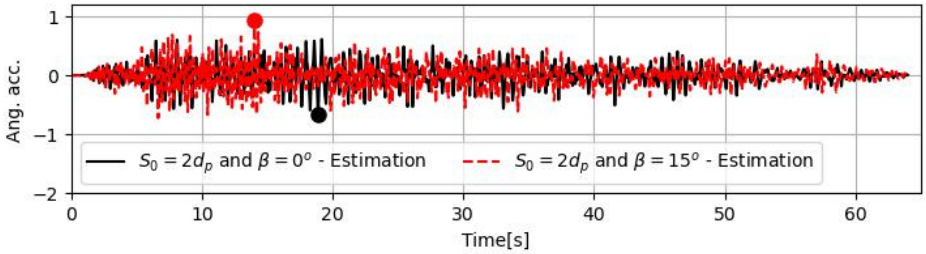

(d) Ang. acceleration, time domain.

Figure 2.26: Comparison of batter angle using estimated solution. $S_0 = 2d_p$

teraction factors can be suitable in a preliminary design stage or as a means of investigating the effects of batter angle and pile spacing rather than producing accurate results. However, the assessment of the kinematic interaction factors relied on the outcomes of detailed finite element analyses. Incorporating this step into a simplified method that prioritizes practicality could potentially make the solution strategy more complex, to the point where it may no longer serve its intended purpose.

2.6 Summary

1. Soil non-linearity has a profound impact on the horizontal kinematic interaction, where nonlinear models may amplify the ground motion for a wide range of configurations and frequencies. Soil non-linearity significantly increases rotational kinematic interaction for all considered configurations. However, non-linearity in most cases substantially reduces displacements and rotations amplitudes.

2. Soil non-linearity produces less frequency-dependent results.

3. Increasing batter angle decreases horizontal displacements and increases pile-cap rotations. The largest differences in kinematic interaction between the different batter angles is observed in the low-to-mid frequency range for most configurations. Moments, shear forces and normal forces generally increase with batter angle.

4. Increasing pile spacing decreases pile-cap rotation, while batter angle simultaneously becomes a more governing factor. Moments and shear forces increase with increasing pile spacing, while axial forces simultaneously decrease.

5. Increasing base motion amplitude does not significantly affect the kinematic interaction factors, but generally increases displacements, rotations, moments, shear forces and axial forces.

6. Pile-cap displacements, rotations, pile moments, shear forces and axial forces generally decrease with increasing frequency, primarily driven by the short-wavelength excitation causing reversing soil displacements over the pile length. Batter angle becomes less important as frequency increases.

7. Different deformation patterns occur for vertical and batter pile groups. Pile-cap displacements and rotations are in phase for vertical pile groups and out of phase for batter pile groups, which indicates that the increased pile-cap

rotation of batter pile groups is not solely caused by increased axial force magnitude, but also by the direction in which they act.

8. For input motions with high PGA, the spectral accelerations of the pile-cap may be lower compared to the spectral acceleration of the input motion.
9. Batter pile groups generally yield lower spectral accelerations, and the difference between vertical and batter pile groups seems to be almost independent of period.
10. Estimation using nonlinear kinematic interaction factors conservatively estimates the pile-cap displacements and rotations, while roughly captures the effects with respect to batter angle and frequency content.

Chapter 3

Linear impedance matrix

3.1 Introduction

Due to the discouragement of inclined piles in seismic areas, researchers have in the last decades mainly focused on vertical pile groups in the development of computational methods. Kaynia [134] proposed a solution elucidating dynamic pile-soil-pile interaction and validating the superposition principle for dynamic response. Dobry and Gazetas [211] proposed a simple method for estimating the dynamic impedance of a pile group by directly applying simple wave attenuation functions as interaction factors. Gazetas and Makris [138, 212] further studied the interaction factors in a two-part article series, where the inertial and flexural resistance of the receiver pile was recognized for lateral interaction. Makris and Gazetas [213] also investigated the effect of phase differences in the interaction factor approach. Mylonakis and Gazetas [214] extended the interaction method by taking into account finite pile length and soil layering. Takewaki and Kishida [215] applied the principles of the interaction factor method in order to estimate the interstory drifts in buildings. Wang et al. [216] extended the interaction factor method by including shear deformations and rotational inertia of the piles and shear deformations of soil.

In the recent years however, attempts have been made to develop simplified methods also for batter pile groups. Ghasemzadeh and Alibeikloo [217] presented a simple, closed-form solution for infinitely long piles in homogeneous soil. A similar approach was presented by Ghazavi et al. [218]. Wang et al. [219] extended his shear and multi-layer model to inclined piles. Goit and Saitoh [220] performed an experimental study to asses the impact of non-linearity on interaction factors for batter pile groups and proposed additional multiplication factors.

The main objective of this chapter is to formulate a diagonal impedance matrix for vertical and batter pile groups in linear, homogeneous soil that takes into account pile-soil-pile interaction. The solution is intended for low-exaction seismic problems, vibration problems or estimates in the early-stage design process. Although it is understood that simplified, linear methods are bound to limited accuracy, certain criteria must be met for the solution to be applicable in practice. First, the solution must be sufficiently accurate for the intended field of application. Second, the solution must capture the trends intrinsic to pile group configuration, pile spacing and batter angle. Third, the solution must be easy to understand and implement.

The presented impedance matrix is a closed-form solution of a BWF-problem that closely follows the methods for dynamic pile-soil-pile interaction available in the literature [138, 211, 212, 213, 217, 218]. The limitations of the method include linear response, plain-strain conditions, inertial loading, long (floating) piles, homogeneous deposits, cylindrical pile shapes and fixed-head conditions. Note that other boundary conditions may of course be enforced, but every specific combination of conditions requires an unique solution.

This chapter is divided in five sections. Section 3.2 presents the single-pile formulation. Section 3.3 discusses the assumptions for wave propagation and derives the interaction factors. Section 3.4 presents the pile group matrix assembly and validates the solution against a rigorous numerical model in OpenSees MP. The effects of load frequency, batter angle and pile spacing are evaluated. Section 3.5 presents a hybrid model where the piles are modelled as finite element beams, while the soil and the pile-soil-pile interaction is represented using elements based on the analytical approach. The summary is given in Section 3.6.

3.2 Single piles

3.2.1 Winkler's springs and dashpots

The piles are modelled as bars (axial loads) and Euler-Bernoulli beams (lateral loads). The soil is modelled using well-known Winkler springs and dashpots [89, 213, 221]. Expressions used for the springs are

$$k_z = 0.6E_s\left(1 + \frac{1}{2}\sqrt{a_0}\right) \tag{3.1a}$$

$$k_x = 1.2E_s \tag{3.1b}$$

where subscripts z and x denote axial and lateral deformation, respectively. E_s is the Young's modulus of soil and a_0 is the dimensionless frequency

$$a_0 = \frac{\omega d_p}{V_s} \tag{3.2}$$

where d_p is pile diameter, ω is the angular excitation frequency and V_s is the shear wave velocity. The expressions used for dashpots consist of radiation damping and hysteretic damping, i.e.,

$$c_z = 1.2a_0^{-\frac{1}{4}}\pi d_p \rho_s V_s + 2\beta\frac{k_z}{\omega} \tag{3.3a}$$

$$c_x = 2a_0^{-\frac{1}{4}} d_p \rho_s V_s \left(1 + \left(\frac{V_{La}}{V_s}\right)^{\frac{5}{4}}\right) + 2\beta\frac{k_x}{\omega} \tag{3.3b}$$

Here, ρ_s is the soil density, β is hysteretic damping factor of the soil and

$$V_{La} = \frac{3.4V_s}{\pi(1-\nu)} \tag{3.4}$$

is the Lysmer's analogue velocity where ν is the Poisson's ratio of the soil.

3.2.2 Axial impedance

Governing bar equation

With reference to Figure 3.1, the force equilibrium in a bar may expressed as

$$-N(z,t) + N(z,t) + dN(z,t) - \rho_p A_p(z)\frac{\partial^2 u(z,t)}{\partial t^2}dz - f(z,t)dz = 0 \tag{3.5}$$

where ρ_p is density of the pile and $A_p(z)$ is the cross subsectional area of the pile. The incremental increase of the normal force may be expressed as

$$dN(z,t) = \frac{\partial N(z,t)}{\partial z}dz \tag{3.6}$$

Inserting Equation 3.6 into Equation 3.5,

$$\frac{\partial N(z,t)}{\partial z}dz - \rho_p A\frac{\partial^2 u(z,t)}{\partial t^2}dz - f(z,t)dz = 0 \tag{3.7}$$

The normal force may be expressed as a function of stress, i.e.,

$$N(z,t) = \sigma(z,t)A_p(z) = E_p A_p(z)\frac{\partial u(z,t)}{\partial z} \tag{3.8}$$

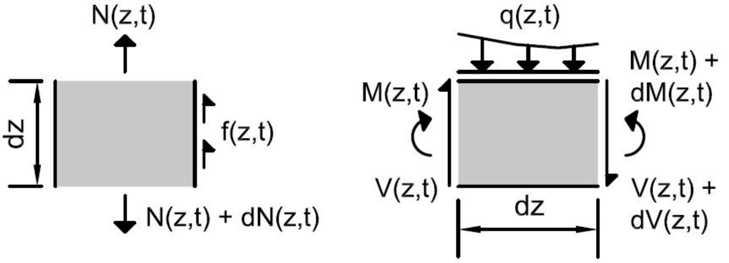

Figure 3.1: Equilibrium of an infinitesimal element of the bar and the beam

where E_p is the Young's modulus of the pile. Combining Equations 3.7 and 3.8,

$$E_pA_p(z)\frac{\partial^2 u(z,t)}{\partial z^2} - \rho_p A_p(z)\frac{\partial^2 u(z,t)}{\partial t^2} - f(z,t) = 0 \tag{3.9}$$

Assuming a constant cross section, the pile mass per unit length is

$$m_p = \rho_p A_p \tag{3.10}$$

Expressing $f(z,t)$ with uniformly distributed springs and dashpots,

$$f(z,t) = k_z u(z,t) + c_z \frac{\partial u(z,t)}{\partial t} \tag{3.11}$$

The equation of motion for the bar element is then given as

$$E_pA_p\frac{\partial^2 u(z,t)}{\partial z^2} - \left(m_p\frac{\partial^2 u(z,t)}{\partial t^2} + c_z\frac{\partial u(z,t)}{\partial t} + k_z u(z,t)\right) = 0 \tag{3.12}$$

The vertical displacement and the inherent derivatives in time and space of a harmonically oscillating bar may be expressed as

$$u(z,t) = u(z)e^{i\omega t} \tag{3.13a}$$

$$\frac{\partial u(z,t)}{\partial t} = i\omega u(z)e^{i\omega t} \tag{3.13b}$$

$$\frac{\partial^2 u(z,t)}{\partial t^2} = -\omega^2 u(z)e^{i\omega t} \tag{3.13c}$$

$$\frac{\partial^n u(z,t)}{\partial z^n} = \frac{\partial^n u(z)}{\partial z^n}e^{i\omega t} \tag{3.13d}$$

Inserting Equation 3.13 into Equation 3.12, the final equation of motion for harmonic excitation is expressed as

$$E_pA_p\frac{\partial^2 u(z)}{\partial z^2} - \left((k_z - m_p\omega^2) + i\omega c_z\right)u(z) = 0 \tag{3.14}$$

Solution for harmonic excitation at the pile head

Solutions are sought separately for $\omega < \omega_z$ and $\omega > \omega_z$, where

$$\omega_z = \sqrt{\frac{k_z}{m_p}} \tag{3.15}$$

For simplicity, derivations are only presented for $\omega < \omega_z$. The solution for $\omega > \omega_z$ is obtained through a nearly identical procedure. The general solution for the free vibration response for $\omega < \omega_z$ is

$$u(z) = A_1 e^{r_1 z} + A_2 e^{r_2 z} \tag{3.16}$$

The roots are

$$r_{1,2} = \pm\Lambda \tag{3.17}$$

where

$$\Lambda = \left(\frac{(k_z - m_p\omega^2) + i\omega c_z}{E_p A_p}\right)^{\frac{1}{2}} \tag{3.18}$$

Alternatively, the roots may be expressed as

$$r_{1,2} = \pm R\left[\cos\frac{\theta_z}{2} + isin\frac{\theta_z}{2}\right] \tag{3.19}$$

where

$$R = \left[\frac{(k_z - m_p\omega^2)^2 + (\omega c_z)^2}{(E_p A_p)^2}\right]^{\frac{1}{4}} \tag{3.20}$$

and

$$\theta_z = \arctan\left[\frac{\omega c_z}{k_z - m_p\omega^2}\right], \quad 0 < \theta_z < \frac{\pi}{2} \tag{3.21}$$

Applying the condition

$$u(0,t) = U_0 \tag{3.22}$$

and insuring a finite displacement as z tends to infinity, A_1 must be equal to zero. The displacement is then expressed as

$$u(z,t) = U_0 e^{-\Lambda z} \tag{3.23}$$

Combining Equations 3.8 and 3.14,

$$N(z) = \big((k_z - m_p\omega^2) + i\omega c_z\big)\int u(z,t)dz \tag{3.24}$$

Inserting Equation 3.23 into Equation 3.24 and solving the integral,

$$N(z) = -\frac{\left((k_z - m_p\omega^2) + i\omega c_z\right) U_0 e^{-\Lambda z}}{\Lambda} + C \tag{3.25}$$

Applying the condition

$$N(z, U_0 = 0) = 0 \tag{3.26}$$

it is observed that $C = 0$. The harmonic load applied at the pile head is expressed as

$$P^s(z = 0, t) = P_0^s e^{i\omega t} \tag{3.27}$$

where P_0^s is the load amplitude. The pile-head force amplitude is then

$$N(z = 0) = -P_0^s \tag{3.28}$$

Combining Equations 3.25 and 3.28, the pile head displacement ($z = 0$) may be expressed as

$$U_0 = \frac{P_0^s \Lambda}{((k_z - m_p\omega^2) + i\omega c_z)} \tag{3.29}$$

The static case ($\omega = 0$) is reduced to

$$U_{0,static} = \frac{P_0^s}{\sqrt{E_p A_p k_z}} \tag{3.30}$$

The complex impedance of a single pile is expressed as

$$\hat{K}_z^S(\omega) = K_z^S(\omega) + i\omega C_z^S(\omega) \tag{3.31}$$

where $K_z^S(\omega)$ is the dynamic stiffness and $C_z^S(\omega)$ is the damping coefficient. Rearranging Equation 3.29, the dynamic stiffness and damping coefficient for a single pile may be expressed as

$$K_z^S(\omega) = Re\left(\frac{\left((k_z - m_p\omega^2) + i\omega c_z\right)}{\Lambda}\right) \tag{3.32a}$$

$$C_z^S(\omega) = \frac{1}{\omega} Im\left(\frac{\left((k_z - m_p\omega^2) + i\omega c_z\right)}{\Lambda}\right) \tag{3.32b}$$

3.2.3 Lateral impedance

Governing beam equation

With reference to Figure 3.1, the force and moment equilibrium in a beam may be expressed as

$$-\rho_p A_p(z)\frac{\partial^2 w(z,t)}{\partial t^2}dz + V(z,t) - V(z,t) - dV(z,t) - q(z,t)dz = 0 \quad (3.33)$$

$$-M(z,t) + M(z,t) + dM(z,t) - (V(z,t) + dV(z,t))dz - q(z,t)\frac{(dz)^2}{2} = 0 \quad (3.34)$$

The incremental increase of shear force and moment is expressed as

$$dV(z,t) = \frac{\partial V(z,t)}{\partial z}dz \quad (3.35)$$

$$dM(z,t) = \frac{\partial M(z,t)}{\partial z}dz \quad (3.36)$$

Inserting Equation 3.35 into Equation 3.33 and Equations 3.35 and 3.36 into Equation 3.34,

$$\rho_p A_p(z)\frac{\partial^2 w(z,t)}{\partial t^2} + \frac{V(z,t)}{\partial z} + q(z,t) = 0 \quad (3.37)$$

$$V(z,t) = \frac{\partial M(z,t)}{\partial z} \quad (3.38)$$

where $dz^2 \approx 0$. Inserting Equation 3.38 into 3.37,

$$\rho_p A_p(z)\frac{\partial^2 w(z,t)}{\partial t^2} + \frac{\partial^2 M(z,t)}{\partial z^2} + q(z,t) = 0 \quad (3.39)$$

The moment in a beam may be expressed as

$$M(z,t) = E_p I_p(z)\frac{\partial^2 w(z,t)}{\partial z^2} \quad (3.40)$$

Expressing $q(z,t)$ with uniformly distributed springs and dashpots,

$$q(z,t) = k_x w(z,t) + c_x\frac{\partial w(z,t)}{\partial t} \quad (3.41)$$

Combining Equations 3.10, 3.39, 3.40 and 3.41, the equation of motion is given as

$$E_p I_p\frac{\partial^4 w(z,t)}{\partial z^4} + m_p\frac{\partial^2 w(z,t)}{\partial t^2} + c_x\frac{\partial w(z,t)}{\partial t} + k_x w(z,t) = 0 \quad (3.42)$$

Inserting Equation 3.13 (and replacing $u(z)$ with $w(z)$) into Equation 3.42, the final equation of motion for harmonic excitation is expressed as

$$E_p I_p\frac{\partial^4 w(z)}{\partial z^4} + \left((k_x - m_p\omega^2) + i\omega c_x\right) w(z) = 0 \quad (3.43)$$

Solution for harmonic excitation at the pile head

The solution of Equation 3.43 is obtained by applying the Laplace transformation while directly incorporating the boundary condition for no rotation at the pile head, i.e.,

$$\frac{\partial u(0)}{\partial z} = 0 \tag{3.44}$$

As for axial response, derivations are only presented for $\omega < \omega_x$.

A complex number in polar form may be expressed as

$$(a + ib)^N = R^N(\cos N\theta_x + i \sin N\theta_x) \tag{3.45}$$

We may then define

$$\begin{aligned} \lambda &:= \left(\frac{((k_x - m_p\omega^2) + i\omega c_x]}{4E_pI_p} \right)^{\frac{1}{4}} \\ &= \left(\frac{((k_x - m_p\omega^2)^2 + (\omega c_x)^2}{(4E_pI_p)^2} \right)^{\frac{1}{8}} \left(\cos\frac{\theta_x}{4} + i \sin\frac{\theta_x}{4} \right) \end{aligned} \tag{3.46}$$

where

$$Z := \left(\frac{((k_x - m_p\omega^2)^2 + (\omega c_x)^2}{(4E_pI_p)^2} \right)^{\frac{1}{8}} \tag{3.47}$$

$$p := \left(\cos\frac{\theta_x}{4} + i \sin\frac{\theta_x}{4} \right) \tag{3.48}$$

$$\theta_x = \arctan\left(\frac{\omega c_x}{k_x - m_p\omega^2} \right), \quad 0 < \theta_x < \frac{\pi}{2} \tag{3.49}$$

The equilibrium equation in the transformed space is then

$$w(s) = \frac{\partial^3 w(0)}{\partial z^3}\frac{1}{s^4 + \lambda^4} + \frac{\partial^2 w(0)}{\partial z^2}\frac{s}{s^4 + \lambda^4} + u(0)\frac{s^3}{s^4 + \lambda^4} \tag{3.50}$$

Applying inverse Laplace transformation,

$$\begin{aligned} w(z) = {} & \frac{w'''(0)}{4\lambda^3}(\cosh \lambda z \sin \lambda z - \cos \lambda z \sinh \lambda z) \\ & + \frac{w''(0)}{2\lambda^2} \sinh \lambda z \sin \lambda z + u(0) \cosh \lambda z \cos \lambda z \end{aligned} \tag{3.51}$$

Utilizing trigonometric relations and writing out the expressions,

$$\begin{aligned}
w(z) = {} & \frac{e^{i\lambda z} - e^{-i\lambda z}}{2i} \left(\frac{w'''(0)}{4\lambda^3} \frac{e^{\lambda z} + e^{-\lambda z}}{2} + \frac{w''(0)}{2\lambda^2} \frac{e^{\lambda z} + e^{-\lambda z}}{2} \right) \\
& + \frac{e^{i\lambda z} + e^{-i\lambda z}}{2} \left(- \frac{w'''(0)}{4\lambda^3} \frac{e^{\lambda z} - e^{-\lambda z}}{2} + w(0) \frac{e^{\lambda z} + e^{-\lambda z}}{2} \right) \\
& - i(e^{i\lambda z} - e^{-i\lambda z}) \left(\frac{w'''(0)e^{\lambda z}}{16\lambda^3} + \frac{w'''(0)e^{-\lambda z}}{16\lambda^3} + \frac{w''(0)e^{\lambda z}}{8\lambda^2} - \frac{w''(0)e^{-\lambda z}}{8\lambda^2} \right) \\
& + i(e^{i\lambda z} + e^{-i\lambda z}) \left(- \frac{w'''(0)e^{\lambda z}}{16\lambda^3} + \frac{w'''(0)e^{-\lambda z}}{16\lambda^3} + \frac{w(0)e^{\lambda z}}{4} + \frac{w''(0)e^{-\lambda z}}{4} \right)
\end{aligned} \tag{3.52}$$

In order to express the somewhat tedious equations derived so far more conveniently, the products containing Euler's number are considered first. As an example,

$$e^{\lambda z} e^{-i\lambda z} = e^{(1-i)\lambda z} = e^{(1-i)Zpz} \tag{3.53}$$

where

$$\begin{aligned}
(1-i)p = (1-i) \left(\cos\frac{\theta_x}{4} + i \sin\frac{\theta_x}{4} \right) = \cos\frac{\theta_x}{4} + i \sin\frac{\theta_x}{4} - i \cos\frac{\theta_x}{4} + \sin\frac{\theta_x}{4} \\
= -i \left(\cos\frac{\theta_x}{4} - \sin\frac{\theta_x}{4} \right) + \cos\frac{\theta_x}{4} + \sin\frac{\theta_x}{4}
\end{aligned} \tag{3.54}$$

Equation 3.53 may then be expressed as

$$e^{-\lambda z} e^{i\lambda z} = e^{(1-i)Zpz} = e^{-iRbz} e^{Raz} \tag{3.55}$$

where

$$a = \cos\frac{\theta_x}{4} + \sin\frac{\theta_x}{4} > 0 \tag{3.56a}$$

$$b = \cos\frac{\theta_x}{4} - \sin\frac{\theta_x}{4} > 0 \tag{3.56b}$$

Identical procedures are performed for the remaining products, i.e.,

$$\begin{aligned}
e^{\lambda z} e^{-i\lambda z} = e^{-iRbz} e^{Raz}, \quad e^{-\lambda z} e^{-i\lambda z} = e^{-iRaz} e^{-Rbz}, \\
e^{\lambda z} e^{i\lambda z} = e^{iRaz} e^{Rbz}, \quad e^{-\lambda z} e^{i\lambda z} = e^{-iRbz} e^{Raz}
\end{aligned} \tag{3.57}$$

Using the relations in Equation 3.57 and rearranging Equation 3.52,

$$\begin{aligned} w(z) = &-i\left(\frac{w'''(0)}{16\lambda^3}+\frac{w''(0)}{8\lambda^2}\right)\left(e^{iRaz}e^{Rbz}-e^{-iRbz}e^{Raz}\right) \\ &-i\left(\frac{w'''(0)}{16\lambda^3}-\frac{w''(0)}{8\lambda^2}\right)\left(e^{iRbz}e^{-Raz}-e^{-iRaz}e^{-Rbz}\right) \\ &+\left(-\frac{w'''(0)}{16\lambda^3}-\frac{w(0)}{4}\right)\left(e^{iRaz}e^{Rbz}-e^{-iRbz}e^{Raz}\right) \\ &+\left(\frac{w'''(0)}{16\lambda^3}+\frac{w'(0)}{4}\right)\left(e^{iRbz}e^{-Raz}-e^{-iRaz}e^{-Rbz}\right) \end{aligned} \tag{3.58}$$

Ensuring a finite displacement amplitude as z tends towards infinity, we enforce the conditions

$$\left(\frac{w'''(0)}{16\lambda^3}+\frac{w''(0)}{8\lambda^2}\right)=0 \tag{3.59a}$$

$$\left(-\frac{w'''(0)}{16\lambda^3}-\frac{w(0)}{4}\right)=0 \tag{3.59b}$$

Combining Equations 3.58 and 3.59, the steady-state response is obtained as

$$w(z,t)=\frac{W_0}{2}\left((1+i)e^{-Z(b+ia)z}+(1-i)e^{Z(ib-a)z}\right) \tag{3.60}$$

Combining Equations 3.38, 3.40 and 3.43, the shear force is expressed as

$$V(z)=-\left[(k_x-m_p\omega^2)^2+(\omega c_x)^2\right]\int w(z)dz \tag{3.61}$$

Inserting Equation 3.60 into Equation 3.61 and solving the integral,

$$\begin{aligned} V(z) = &\left((k_x-m_p\omega^2)+i\omega c_x\right)\frac{W_0}{2}\ \times\cdots \\ &\left(\frac{(1+i)}{(b+ia)Z}e^{-Z(b+ia)z}+\frac{(1-i)}{(a-ib)Z}e^{-Z(a-ib)z}\right)+C \end{aligned} \tag{3.62}$$

Applying the condition

$$V(z,W_0=0)=0 \tag{3.63}$$

it is observed that $C = 0$. The harmonic load applied at the pile head is expressed as

$$H^s(z=0,t) = H_0^s e^{i\omega t} \tag{3.64}$$

where H_0^s is the load amplitude. The shear force amplitude acting at the pile-head is thus

$$V(z=0) = H_0^s \tag{3.65}$$

Combining Equations 3.62 and 3.65 and multiplying each term in the right parentheses in Equation 3.62 with the respective complex conjugate, the lateral displacement at the pile head is obtained as

$$W_0 = \frac{H_0^s Z(a^2+b^2)}{4E_pI_p\lambda^4((a+b)+i(b-a))} \tag{3.66}$$

The static case ($\omega = 0$) is reduced to

$$W_{0,s} = \frac{H_0^s}{4E_pI_p\lambda_s^3} \tag{3.67}$$

where

$$\lambda_s = \left(\frac{k_x}{4E_pI_p}\right)^{\frac{1}{4}} \tag{3.68}$$

The complex impedance of one single pile is expressed as

$$\hat{K}_x^S(\omega) = K_x^S(\omega) + i\omega C_x^S(\omega) \tag{3.69}$$

where $K_x^S(\omega)$ is the dynamic stiffness and $C_x^S(\omega)$ is the damping coefficient. Rearranging Equation 3.66, the lateral stiffness and damping coefficient for a single pile may be expressed as

$$K_x^S(\omega) = Re\left(\frac{4EI\lambda^4((a+b)+i(b-a))}{Z(a^2+b^2)}\right) \tag{3.70a}$$

$$C_z^S(\omega) = \frac{1}{\omega}Im\left(\frac{4EI\lambda^4((a+b)+i(b-a))}{Z(a^2+b^2)}\right) \tag{3.70b}$$

3.3 Pile-soil-pile interaction

3.3.1 Attenuation functions

The displacement field generated by a vibrating pile will affect the displacement of neighbouring piles. This is referred to as *pile-soil-pile interaction*. The vibrating pile will emit P- and S-waves is all directions, and the waves are reflected from the soil surface and other boundaries. See Figure 3.2. Although rigorous computational methods may capture such behaviour, substantial simplifications are required for closed-form solutions. The solution presented in this chapter utilizes simplified plane-strain attenuation functions which are well-established and discussed throughout the literature [138, 211, 212, 213, 217, 218, 219].

Axial vibration

When the pile is vibrating in the axial direction, cylindrical SV-waves emanate from the pile surface. The attenuation function is then given as

$$\psi_u = \left(\frac{r_p}{S(z)}\right)^{\frac{1}{2}} \exp\left(\frac{-\beta\omega S(z)}{V_s}\right) \exp\left(\frac{-i\omega S(z)}{V_s}\right) \tag{3.71}$$

where r_p is the pile radius and β is the damping ratio (not to be confused with the batter angle).

Lateral vibration

It is assumed that the laterally vibrating pile emanates P-waves in the direction of vibration and SH-waves perpendicular to the direction of vibration [138, 211, 212, 213]. The attenuation functions are thus expressed as

$$\psi_w(\theta = 0^\circ) = \left(\frac{r_p}{S(z)}\right)^{\frac{1}{2}} \exp\left(\frac{-\beta\omega S(z)}{V_{La}}\right) \exp\left(\frac{-i\omega S(z)}{V_{La}}\right) \tag{3.72}$$

$$\psi_w(\theta = 90^\circ) = \left(\frac{r_p}{S(z)}\right)^{\frac{1}{2}} \exp\left(\frac{-\beta\omega S(z)}{V_s}\right) \exp\left(\frac{-i\omega S(z)}{V_s}\right) \tag{3.73}$$

Here, we have introduced θ as the angle between the direction of vibration and the center-to-center line between the two piles. The wave field for any value of θ between 0° and 90° may be expressed as

$$\psi_w \simeq \psi_w(\theta = 0^\circ)\cos^2(\theta) + \psi_w(\theta = 90^\circ)\sin^2(\theta) \tag{3.74}$$

with sufficient accuracy [138, 211].

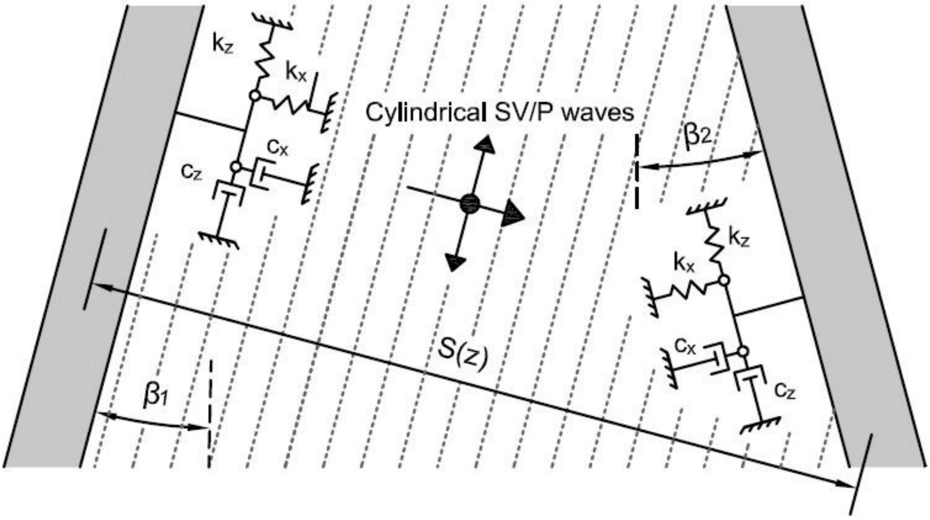

Figure 3.2: Schematic sketch of pile-soil-pile interaction

3.3.2 Assuming simultaneous wave emission

It is assumed that the waves generated from a vibrating pile are simultaneously emanated from all points along the pile perimeter. This assumption is intuitively sound for short and stiff piles. For long and slender piles, however, this assumptions requires more attention.

Axial vibration

Replacing Λ with Equation 3.19, Equation 3.23 gives the phase velocity of the wave propagating down the pile as

$$\Upsilon_u = \frac{\omega}{R \sin \frac{\theta_z}{2}} \tag{3.75}$$

Figure 3.3(a) shows the ratio Υ_u/V_s plotted against the dimensionless frequency a_0 for the frequency range of practical interest. The velocity of waves propagating down the pile is much larger than the velocity of waves travelling through the soil from one pile to another. In other words, the cylindrical wave front emerging from the vibrating pile is barely altered by the phase lag arising from waves propagating down the pile. Figure 3.3(b) shows that the phase angle along the pile relative to the pile head is less than 12 degrees for the given pile length, stiffness ratios and dimensionless frequency. It is therefore reasonable to assume that the assumptions of a simultaneously emitted wave front is valid within the described framework.

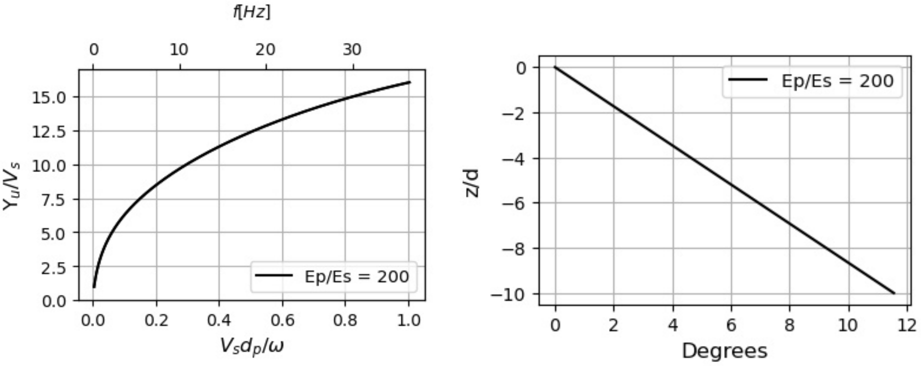

(a) Relative phase velocity **(b)** Phase angle

Figure 3.3: Relative phase velocity and phase angle. Axial response. Normalized angular frequency a_0 = 0.5, E_p/E_s = 200, damping ratio β = 0.05 and ρ_s=0.75ρ_p

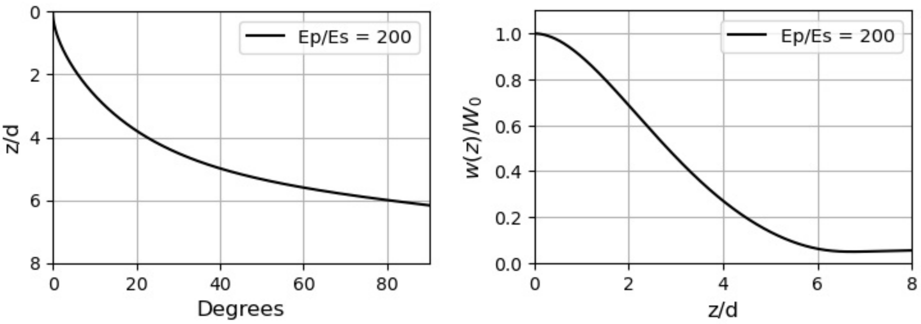

(a) Phase angle **(b)** Normalized displacement

Figure 3.4: Phase angle and normalized displacement along the pile relative to the pile head. Lateral response. Normalized angular frequency $a_0 = 0.5$, E_p/E_s = 200, damping ratio β = 0.05 and ρ_s=0.75ρ_p

Lateral vibration

Figure 3.4 shows the phase angle and normalized displacement along the pile relative to the pile head for the given stiffness ratios and dimensionless frequency. It is clear that phase angle is indeed significant as z increases. However, the actual displacement decreases with z and tends to smaller values as the phase lag becomes relevant. It is therefore reasonable to assume that the phase lag only occurs for displacement values that have negligible effect on the neighboring piles.

3.3.3 Interaction factor matrix

Pile-soil-pile interaction may be accounted for using interaction factors. The interaction matrix $\boldsymbol{\alpha_{ij}}$ defines the additional displacement of receiver pile i due to the displacement of the adjacent, source pile j, divided by the displacement of source pile j due to its own load. The displacement vector for a pile i in local coordinates may then be expressed as

$$\boldsymbol{d_i^l} = \begin{bmatrix} u_i^l \\ w_i^l \\ \theta_i^l \end{bmatrix} = \sum_{j=1}^{N} \boldsymbol{\alpha_{ij}^l d_j^l} \tag{3.76}$$

where

$$\boldsymbol{\alpha_{ij}^l} = \begin{cases} \begin{bmatrix} \alpha_{aa} & \alpha_{al} & 0 \\ \alpha_{la} & \alpha_{ll} & 0 \\ 0 & 0 & 0 \end{bmatrix}, & \text{if } i \neq j \text{ ,} \\ \boldsymbol{I}, & \text{if } i = j \end{cases} \tag{3.77}$$

The first and second subscript in the matrix entries of $\boldsymbol{\alpha_{ij}^l}$ denote the displacement direction of the receiver pile and the source pile, respectively. E.g., the interaction factor α_{la} represents the lateral displacement of the receiver pile i due to axial displacement of the source pile j , divided by the axial displacement of the source pile j due to its own load. Note that if $i = j$, the interaction matrix $\boldsymbol{\alpha_{ij}}$ must equal the unity matrix $\boldsymbol{I}$.

Past studies have shown that rotational interaction is negligible for vertical piles [134, 222]. The same arguments apply to batter piles.

The derivation of the closed-form expressions for $\boldsymbol{\alpha_{ij}^l}$ is presented in the following sections.

3.3.4 Axial-axial interaction

If damping is neglected when deriving the axial response of a single pile, Equation 3.23 is simplified to

$$u(z) = U_0 e^{-\Lambda_s z} \tag{3.78}$$

where

$$\Lambda_s = \left(\frac{k_z - m_p \omega^2}{E_p A_p} \right)^{\frac{1}{2}} \tag{3.79}$$

Figure 3.5(a) shows the normalized axial displacement plotted against the ratio between depth and pile diameter at $t = 0$ using Equations 3.23 and 3.78. For the frequency range of interest, the results show that even though the actual wave

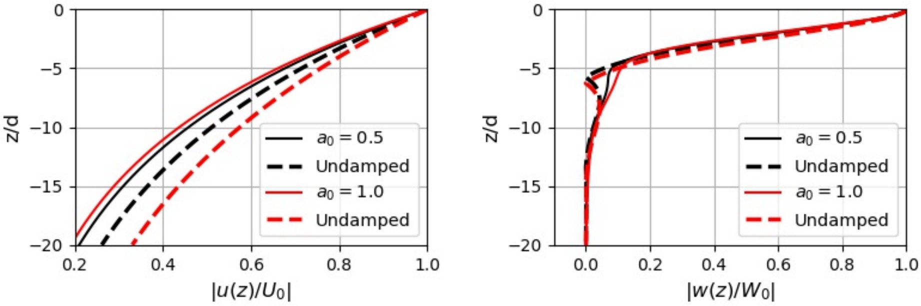

(a) Axial displacement **(b)** Lateral displacement

Figure 3.5: Normalized displacement of source pile with and without damping plotted against the ratio between depth and pile diameter at time $t = 0$. E_p/E_s = 200, damping ratio β = 0.05 and ρ_s=0.75ρ_p

propagating down the pile is completely different for the damped and undamped system, the soil displacement distribution is very similar. For higher frequency values however, the displacement distribution is somewhat different. In order to simplify the algebraic expressions, Equation 3.78 will be used in the following derivations and examples. A similar simplification was proposed by Makris and Gazetas [138] for lateral response.

The flexibility of the receiver pile will resist the soil deflection, resulting in a modified displacement profile. The mathematical formulation for the axial displacement of receiver pile i due to the axial displacement of source pile j is then the non-homogeneous differential equation for the dynamic bar. The bar is loaded with a distributed load equal to the induced soil displacement multiplied by the soil impedance, i.e.,

$$\begin{aligned} E_pA_p\frac{\partial^2 u(z)}{\partial z^2} - \left((k_z - m_p\omega^2) + i\omega c_z\right) u(z) = \\ -(k_z + i\omega c_z)\psi_u U_0 \cos(\beta_1 - \beta_2) e^{-\Lambda_s z} \end{aligned} \tag{3.80}$$

For vertical piles, the center-to-center distance $S(z)$ between two piles is constant along the pile length. For batter piles however, the distance $S(z)$ varies linearly. With reference to Figure 3.2, the distance between two piles at an arbitrary depth measured radially from the vibrating pile is expressed as

$$S(z) = S_0\left(\cos\beta_1 + \sin\beta_1 \tan\left(\beta_1 - \beta_2\right)\right) + \frac{\tan\left(\beta_1 - \beta_2\right)}{\cos\beta_1} z \tag{3.81}$$

Note that the batter angle β is, by definition, positive clock-wise. By introducing the variable z in the attenuation function, the solution of Equation 3.80 becomes inconveniently complex. In order to investigate the effect of a varying distance $S(z)$, Equation 3.71 and 3.72 are further explored. The first and second factor express the decay in displacement amplitude due to radiation and hysteretic damping, respectively. The third factor expresses the phase lag at a distance $S(z)$. Figure 3.6 shows the total amplitude and phase lag as functions of $S(z)$ for different values of a_0. First, it is observed that the attenuation function amplitude decays rapidly in the vicinity of the source, but that the function smooths out as the distance increases. The observation is independent of frequency. Second, the phase lag becomes quite prominent for both shear and pressure waves as the frequency increases. When the piles are vertical, $S(z)$ is constant and the phase lag is solely governed by the finite wave velocity of waves propagating down the source pile (Section 3.3.2). For batter piles however, the phase lag contains an additional factor introduced by the varying attenuation function along the pile length. In addition, the interaction in the vicinity of the pile cap is further complicated and the plane-strain attenuation functions together with the mathematical and geometrical treatment of the loaded receiver pile are likely to be less valid. As stated before, applying a varying distance $S(z)$ yields an exceedingly complex solution. Since we are seeking to develop simple and practical models, such solutions would arguably contribute to the opposite, especially if applying a constant attenuation function results in errors of acceptable magnitude. We will therefore proceed the derivations by assuming a constant attention function, and assess the possible shortcomings in a finite-element and hybrid model comparison.

Assuming a constant distance $S(z) = S(0)$, the general solution of Equation 3.80 is obtained as

$$u(z) = Ae^{\Lambda z} + Be^{-\Lambda z} + \frac{\Gamma_{aa}}{\Lambda_s^2 - \Lambda^2} e^{-\Lambda_s z} \tag{3.82}$$

where

$$\Gamma_{aa} = \frac{(k_z + i\omega c_z)\psi_u U_0 \cos(\beta_1 - \beta_2)}{E_p A_p} \tag{3.83}$$

In order to determine the constants in Equation 3.82, boundary conditions are enforced. First, it is observed that A must vanish if $u(z)$ is to remain finite as z approaches infinity. Second, the normal force at the top of the receiver pile must be zero. The two boundary conditions give the total solution

$$u(z) = \frac{\Gamma_{aa}(\Lambda_s e^{-\Lambda z} - \Lambda e^{-\Lambda_s z})}{\Lambda_s^2 \Lambda - \Lambda^3} \tag{3.84}$$

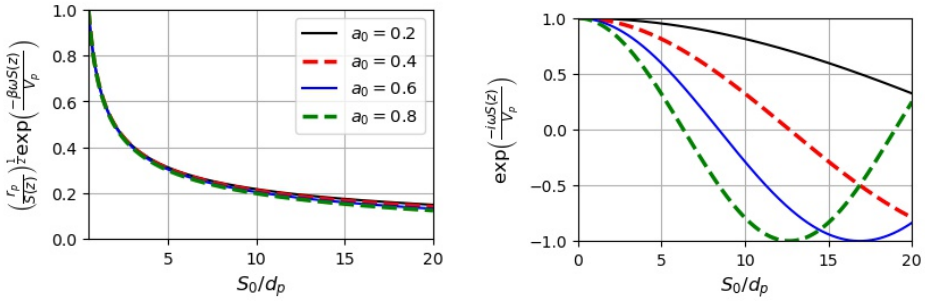

(a) Pressure wave amplitude

(b) Pressure wave phase lag

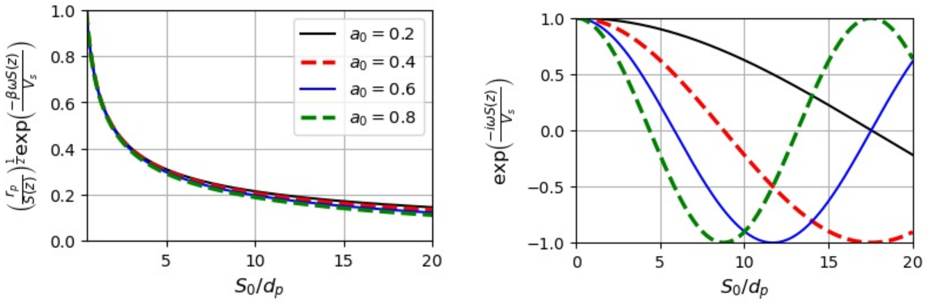

(c) Shear wave amplitude

(d) Shear wave phase lag

Figure 3.6: Attenuation function amplitude and phase lag. E_p/E_s = 200, damping ratio β = 0.05 and ρ_s=0.75ρ_p

The interaction factor is established by dividing Equation 3.84 by Equation 3.78. At the pile head ($z = 0$), the interaction factor for inertial loading is

$$\alpha_{aa} = \frac{(k_z + i\omega c_z)\psi_u \cos(\beta_1 - \beta_2)}{E_p A_p \Lambda(\Lambda + \Lambda_s)} \tag{3.85}$$

Figure 3.7 shows the interaction factor α_{aa} plotted against frequency f and dimensionless frequency a_0 (Equation 3.2). It is observed that the additional axial displacement of receiver pile i due to the axial displacement of source pile j slightly decreases as the batter angles increases. The use of a constant attenuation function for axial-axial interaction may thus be argued on the basis of (1) the decreasing displacements along the pile length and (2) the fact that axial-axial interaction decreases with increasing batter angle, although both arguments are expected to have a limited impact.

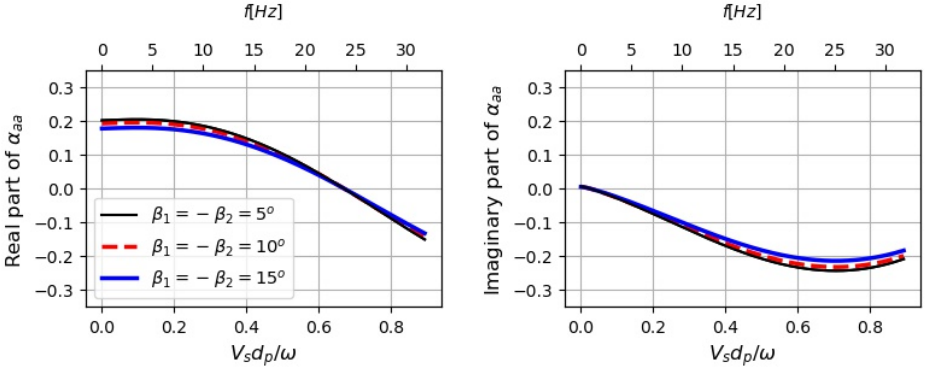

(a) Real part, S/d= 3.

(b) Imaginary part, S/d= 3.

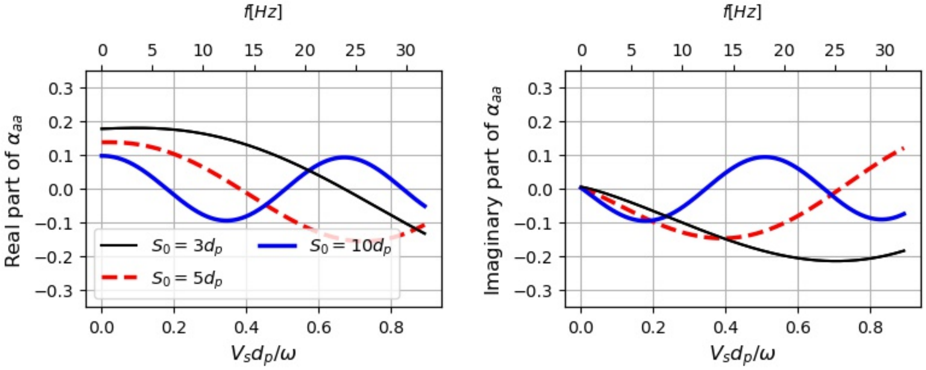

(c) Real part, $\beta_1 = -\beta_2 = 15^0$.

(d) Imaginary part, $\beta_1 = -\beta_2 = 15^0$.

Figure 3.7: Dynamic axial-axial interaction factor for batter piles. E_p/E_s = 200, damping ratio β = 0.05 and ρ_s=0.75ρ_p

3.3.5 Lateral-axial interaction

The mathematical formulation for the lateral displacement of receiver pile i due to the axial displacement of source pile j is the non-homogeneous differential equation for the dynamic beam, i.e.,

$$E_p I_p \frac{\partial^4 w(z)}{\partial z^4} + \left((k_x - m_p\omega^2) + i\omega c_x\right) w(z) = \\ (k_x + i\omega c_x)\, \psi_u U_0 \sin(\beta_1 - \beta_2) e^{-\Lambda_s z} \tag{3.86}$$

If we assume a constant attenuation function, the general solution is obtained as

$$\begin{aligned} w(z) &= e^{\lambda z}\left(A\cos\lambda z + B\sin\lambda z\right) + \\ & e^{-\lambda z}\left(C\cos\lambda z + D\sin\lambda z\right) + \frac{\Gamma_{la}}{\Lambda_s^4 + 4\lambda^4} e^{-\Lambda_s z} \end{aligned} \tag{3.87}$$

where

$$\lambda = \left(\frac{\left((k_x - m_p\omega^2) + i\omega c_x\right)}{4E_pI_p}\right)^{\frac{1}{4}} \tag{3.88}$$

and

$$\Gamma_{la} = \frac{(k_x + i\omega c_x)\psi_u U_0 \sin(\beta_1 - \beta_2)}{E_pI_p} \tag{3.89}$$

In order to determine the constants in Equation 3.87, boundary conditions are enforced. First, it is observed that A and B must vanish if $w(z)$ is to approach zero as z approaches infinity. Second, the slope of deflection and the shear force are both zero at the pile head. The two boundary conditions yield

$$\begin{bmatrix} -1 & 1 \\ 2 & 2 \end{bmatrix} \begin{bmatrix} C \\ D \end{bmatrix} = \begin{bmatrix} \dfrac{\Gamma_{la}\Lambda_s}{\lambda(\Lambda_s^4 + 4\lambda^4)} \\ \dfrac{\Gamma_{la}\Lambda_s^3}{\lambda^3(\Lambda_s^4 + 4\lambda^4)} \end{bmatrix} \tag{3.90}$$

Figure 3.8(a) compares the total, particular and homogeneous solution presented in Equation 3.87 with constants determined from Equation 3.90 . It is clear that the homogeneous part is negligible except for a small contribution at the top. Therefore, the homogeneous part may for all practical purposes be neglected. The lateral pile deflection may thus be reduced to

$$w(z) = \frac{(k_x + i\omega c_x)\psi_u \sin(\beta_1 - \beta_2)U_0}{E_pI_p(\Lambda_s^4 + 4\lambda^4)} e^{-\Lambda_s z} \tag{3.91}$$

The interaction factor is obtained by dividing Equation 3.91 by Equation 3.78. At the pile head ($z = 0$), the interaction factor is

$$\alpha_{la} = \frac{(k_x + i\omega c_x)\psi_u \sin(\beta_1 - \beta_2)}{E_pI_p(\Lambda_s^4 + 4\lambda^4)} \tag{3.92}$$

Figure 3.9 shows the interaction factor α_{la} plotted against frequency f and dimensionless frequency a_0 (Equation 3.2). It is observed that the additional lateral displacement of receiver pile i due to the axial displacement of source pile j increases as the batter angles increase, which argues against the use of a constant attenuation function.

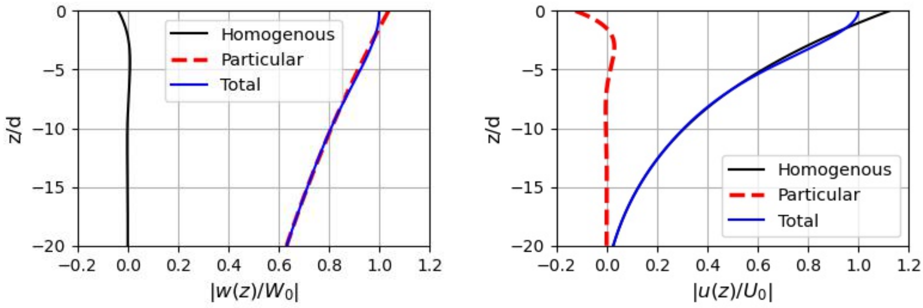

(a) Lateral displacement of receiver pile due to axial displacement of source pile

(b) Axial displacement of receiver pile due to lateral displacement of source pile

Figure 3.8: Normalized displacement of receiver pile divided in homogeneous and particular part and plotted at time $t = 0$. E_p/E_s = 200, damping ratio β = 0.05 and ρ_s=0.75ρ_p.

3.3.6 Lateral-lateral interaction

If the damping is neglected, Equation 3.60 is simplified to

$$w(z) = W_0 e^{-\lambda z} \left(\sin \lambda z + \cos \lambda z\right) \tag{3.93}$$

Figure 3.5(b) shows the normalized displacement plotted against the ratio between depth and pile diameter at $t = 0$ using Equations 3.60 and 3.93. It is clear that the soil displacement distribution is very similar within the frequency range of interest. In order to simply the algebraic expressions, Equation 3.93 will be used in the following derivations and examples.

The mathematical formulation for the lateral displacement of receiver pile i due to the lateral displacement of source pile j is the non-homogeneous differential equation for the dynamic beam, i.e.,

$$\begin{gathered} E_p I_p \frac{\partial^4 w(z)}{\partial z^4} + \left(\left(k_x - m_p \omega^2\right) + i\omega c_x\right) w(z) = \\ \left(k_x + i\omega c_x\right) \psi_w W_0 \left(\sin \lambda z + \cos \lambda z\right) \cos(\beta_1 - \beta_2) e^{-\lambda z} \end{gathered} \tag{3.94}$$

Regarding the varying attenuation function depicted in Figure 3.6, the same observation are made for lateral vibrations as for axial vibrations. We will proceed with a constant attenuation function due to the substantial simplification of the algebraic expressions obtained by solving the governing differential equation. The solution of Equation 3.94 is obtained by applying the Laplace transformation while directly

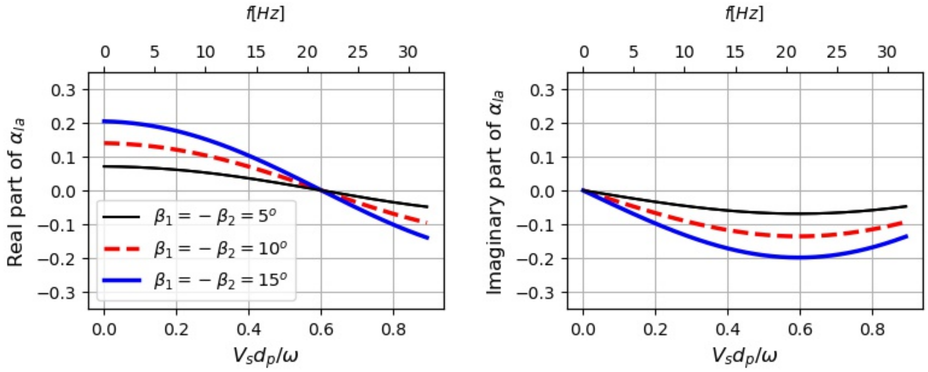

(a) Real part, S/d= 3. **(b)** Imaginary part, S/d= 3.

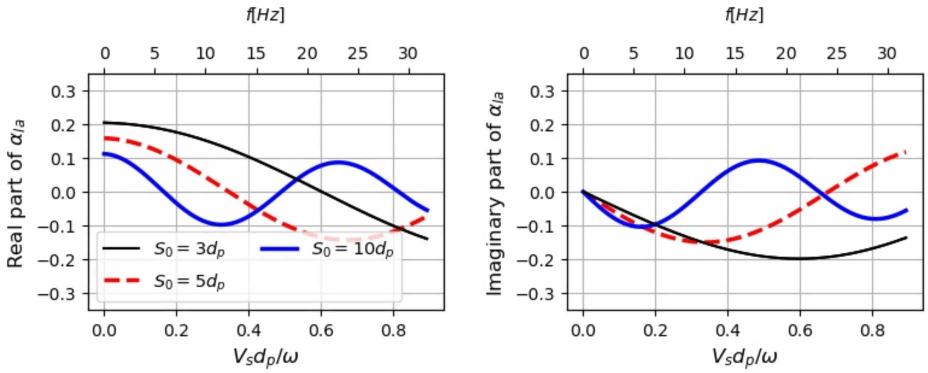

(c) Real part, $\beta_1 = -\beta_2 = 15^0$. **(d)** Imaginary part, $\beta_1 = -\beta_2 = 15^0$..

Figure 3.9: Dynamic lateral-axial interaction factor for batter piles. E_p/E_s = 200, damping ratio β = 0.05 and ρ_s=0.75ρ_p

incorporating the boundary condition for no rotation at the pile head,

$$\frac{\partial u(0)}{\partial z} = 0 \tag{3.95}$$

The displacement in the transformed space is

$$w(s) = \frac{\partial^2 w(0)}{\partial z^2}\frac{s}{s^4+\lambda^4} + w(0)\frac{s^3}{s^4+\lambda^4} + \Gamma_{ll}\left[\frac{s+2\lambda}{(s^4+\lambda^4)\left[(s+\lambda)^2+\lambda^2)\right]}\right] \tag{3.96}$$

where

$$\Gamma_{ll} = \frac{[k_x + i\omega c_x]\,\psi_w W_0}{E_p I_p}\cos(\beta_1+\beta_2) \tag{3.97}$$

Utilizing trigonometric relations and writing out the expressions,

$$\begin{aligned}
w(z) = \frac{e^{\lambda z} - e^{-\lambda z}}{2} & \left[-\frac{w'''(0)}{4\lambda^3}\cos(\lambda z) - \frac{3\Gamma_{ll}}{16\lambda^4}\cos(\lambda z) \right] + \\
& \frac{e^{\lambda z} - e^{-\lambda z}}{2}\left[\frac{w''(0)}{2\lambda^2}\sin(\lambda z) - \frac{\Gamma_{ll} z}{8\lambda^3}\sin(\lambda z) - \frac{\Gamma_{ll}}{8\lambda^4}\sin(\lambda z) \right] + \\
& \frac{e^{\lambda z} + e^{-\lambda z}}{2}\left[w(0)\cos(\lambda z) + \frac{\Gamma_{ll} z}{8\lambda^3}\sin(\lambda z) + \frac{w'''(0)}{4\lambda^3}\sin(\lambda z) + \frac{3\Gamma_{ll}}{16\lambda^4}\sin(\lambda z) \right]
\end{aligned} \tag{3.98}$$

Rearranging Equation 3.98,

$$\begin{aligned}
w(z) = e^{\lambda z}\cos(\lambda z) & \left[-\frac{w'''(0)}{8\lambda^3} - \frac{3\Gamma_{ll}}{32\lambda^4} + \frac{1}{2}w(0) \right] + \\
& e^{\lambda z}\sin(\lambda z)\left[\frac{w'''(0)}{8\lambda^3} + \frac{w''(0)}{4\lambda^2} + \frac{\Gamma_{ll}}{32\lambda^4} \right] + \\
& e^{-\lambda z}\cos(\lambda z)\left[\frac{w'''(0)}{8\lambda^3} + \frac{3\Gamma_{ll}}{32\lambda^4} + \frac{1}{2}w(0) \right] + \\
& e^{-\lambda z}\sin(\lambda z)\left[\frac{w'''(0)}{8\lambda^3} - \frac{w''(0)}{4\lambda^2} + \frac{5\Gamma_{ll}}{32\lambda^4} + \frac{\Gamma_{ll} z}{8\lambda^3} \right]
\end{aligned} \tag{3.99}$$

Ensuring a finite displacement amplitude as z tends towards infinity and enforcing the boundary condition for zero shear force at the pile head,

$$w'''(0) = 0 \tag{3.100}$$

the total solution may be expressed as

$$\begin{aligned}
w(z) = \frac{3}{4}\psi_w \frac{(k_x + i\omega c_x)}{((k_x - m_p\omega^2) + i\omega c_x)} W_0 \cos(\beta_1 + \beta_2) \times \cdots \\
\left(\cos\lambda z + \sin\lambda z + \frac{2}{3}\lambda z \sin\lambda z \right) e^{-\lambda z}
\end{aligned} \tag{3.101}$$

At the pile head ($z = 0$), the interaction factor is

$$\alpha_{ll} = \frac{3\psi_w\,(k_x + i\omega c_x)\cos(\beta_1 - \beta_2)}{4\,((k_x - m_p\omega^2) + i\omega c_x)} \tag{3.102}$$

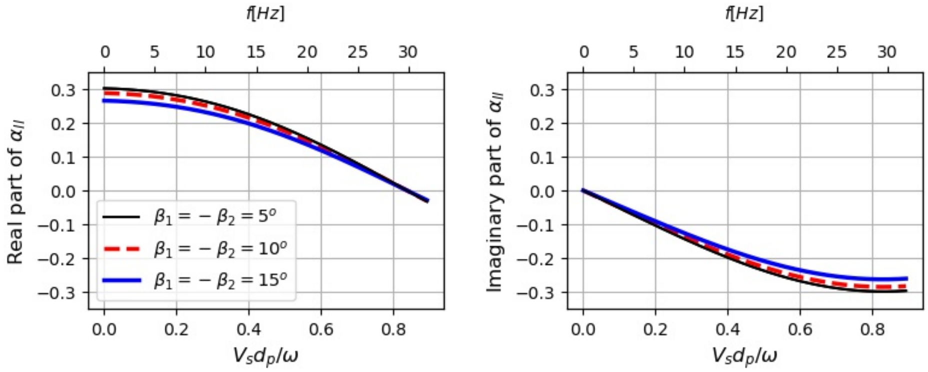

(a) Real part, S/d= 3.

(b) Imaginary part, S/d= 3.

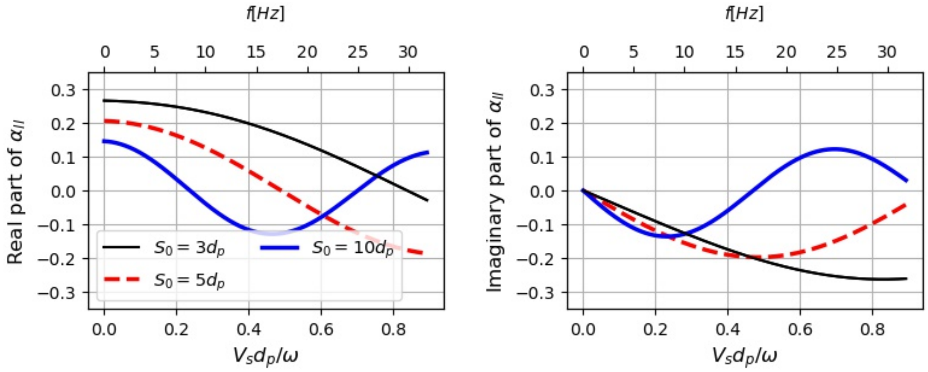

(c) Real part, $\beta_1 = -\beta_2 = 15^0$.

(d) Imaginary part, $\beta_1 = -\beta_2 = 15^0$..

Figure 3.10: Dynamic lateral-lateral interaction factor for batter piles. E_p/E_s = 200, damping ratio β = 0.05 and ρ_s=0.75ρ_p

Note that when $\beta_1 = \beta_2 = 0$, Equation 3.102 reduces to the interaction factor presented by Makris and Gazetas [138] for vertical piles.

Figure 3.10 shows the interaction factor α_{ll} plotted against frequency f and dimensionless frequency a_0 (Equation 3.2). It is observed that the additional lateral displacement of receiver pile i due to the lateral displacement of source pile j decreases as the batter angle increases. The use of a constant attenuation function for lateral-lateral interaction is arguably reasonable due to (1) the decreasing displacements along the pile length and (2) the fact that lateral-lateral interaction decreases with increasing batter angle.

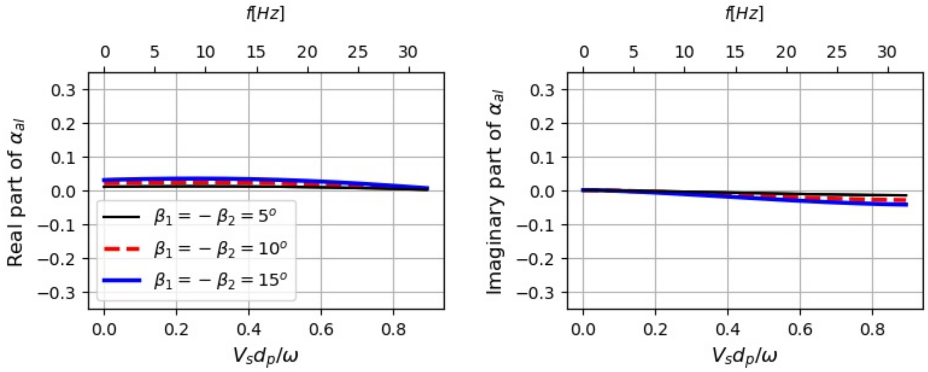

(a) Real part, S/d= 3. **(b)** Imaginary part, S/d= 3.

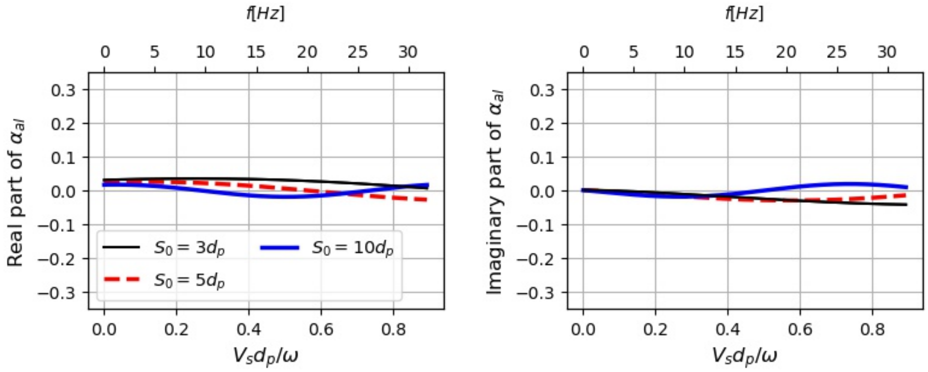

(c) Real part, $\beta_1 = -\beta_2 = 15^0$. **(d)** Imaginary part, $\beta_1 = -\beta_2 = 15^0$..

Figure 3.11: Dynamic axial-lateral interaction factor for batter piles. E_p/E_s = 200, damping ratio β = 0.05 and ρ_s=0.75ρ_p

3.3.7 Axial-lateral interaction

Finally, the mathematical formulation for the axial displacement of receiver pile i due to the lateral displacement of source pile j is the non-homogeneous differential equation for the dynamic bar, i.e.,

$$\begin{aligned} E_pA_p\frac{\partial^2 u(z)}{\partial z^2} - \left((k_z - m_p\omega^2) + i\omega c_z\right) u(z) = \\ -(k_z + i\omega c_z)\psi_w W_0 \sin(\beta_2 - \beta_1)(\sin\lambda z + \cos\lambda z)e^{-\lambda z} \end{aligned} \tag{3.103}$$

Assuming a constant attenuation function, the general solution is obtained as

$$u(z) = Ae^{\Lambda z} + Be^{-\Lambda z} + \frac{\Gamma_{al}\left((\Lambda^2 - 2\lambda^2)\cos\lambda z + (\Lambda^2 + 2\lambda^2)\sin\lambda z\right)}{\Lambda^4 + 4\lambda^4} e^{-\lambda z} \tag{3.104}$$

where

$$\Gamma_{al} = \frac{(k_z + i\omega c_z)\psi_w W_0 \sin(\beta_2 - \beta_1)}{E_p A_p} \tag{3.105}$$

The boundary conditions imply that A must vanish if $u(z)$ is to remain finite as z approaches infinity. Also, the axial force at the top of the receiver pile must be zero. Enforcing the boundary conditions, the total solution may be expressed as

$$u(z) = \frac{4\lambda^3\Gamma_{al}}{\Lambda(\Lambda^4 + 4\lambda^4)} e^{-\Lambda z} + \frac{\Gamma_{al}\left((\Lambda^2 - 2\lambda^2)\cos\lambda z + (\Lambda^2 + 2\lambda^2)\sin\lambda z\right)}{(\Lambda^4 + 4\lambda^4)} e^{-\lambda z} \tag{3.106}$$

Figure 3.8(b) compares the total, particular and homogeneous solution presented in Equation 3.106. It is clear that the particular solution is negligible except for a small contribution at the top. Therefore, the particular solution may for all practical purposes be neglected. Note that the differential equation is a function of the spatial coordinate z (not time), and that the homogeneous part is therefore present throughout the harmonic, steady-state motion. The axial receiver pile deflection may thus be reduced to

$$u(z) = \frac{4\Gamma_{al}\lambda^3}{\Lambda(\Lambda^4 + 4\lambda^4)} e^{-\Lambda z} \tag{3.107}$$

The interaction factor is expressed by dividing Equation 3.107 by Equation 3.93. At the pile head ($z = 0$), the interaction factor is

$$\alpha_{al} = \frac{4\lambda^3 \left(k_z + i\omega c_z\right) \psi_w \sin(\beta_2 - \beta_1)}{\Lambda(\Lambda^4 + 4\lambda^4) E_p A_p} \tag{3.108}$$

Figure 3.11 shows the interaction factor α_{al} plotted against frequency f and dimensionless frequency a_0 (Equation 3.2). It is observed that the additional axial displacement of receiver pile i due to the lateral displacement of source pile j increases as the batter angle increases, which argues against the use of a constant attenuation function. However, the axial-lateral interaction factor is generally small compared to the other interaction factors.

3.4 Pile groups

3.4.1 Assembly

This section provides a procedure for establishing a diagonal impedance matrix for vertical and batter pile groups based the single pile impedances presented in Chapter 3.2 and the pile-soil-pile interaction factors presented in Chapter 3.3.

The single pile impedance matrix may be expressed as

$$\boldsymbol{K^{*g}_{S,i}} = \boldsymbol{\bar{K}^{g}_{S,i}} + i\boldsymbol{C^{g}_{S,i}} = \boldsymbol{t_i}\boldsymbol{K^{*l}_{S,i}}\boldsymbol{t_i}^T = \begin{bmatrix} k^g_{S,uu,i} & k^g_{G,uw,i} & k^g_{G,u\theta,i} \\ k^g_{S,wu,i} & k^g_{S,ww,i} & k^g_{G,w\theta,i} \\ k^g_{S,\theta u,i} & k^g_{S,\theta w,i} & k^g_{G,\theta\theta,i} \end{bmatrix} \tag{3.109}$$

where $\boldsymbol{\bar{K}^{g}_{S,i}}$ is the dynamic stiffness of pile i in global coordinates, $\boldsymbol{C^{g}_{S,i}}$ is the damping coefficient of pile i in global coordinates, $\boldsymbol{t_i}$ is the coordinate transformation matrix and

$$\boldsymbol{K^{*l}_{S,i}} = \begin{bmatrix} k^l_{S,uu,i} & 0 & 0 \\ 0 & k^l_{S,ww,i} & k^l_{S,w\theta,i} \\ 0 & k^l_{S,\theta w,i} & k^l_{S,\theta\theta,i} \end{bmatrix} \tag{3.110}$$

is the complex impedance matrix of pile i in local coordinates. The matrix entries $k^l_{S,uu,i}$ and $k^l_{S,ww,i}$ are given by Equations 3.31, 3.32, 3.69 and 3.70. Otherwise, we have used the expressions presented by Gazetas [90]. We assume that there is no contact between the pile cap and the soil, i.e. all forces and moments from the pile cap are transferred through the piles. In addition to the force distribution from the pile cap, pile-soil-pile interaction effects must be considered. Due to the rigidity of the pile cap, the total displacement of the single pile is approximately equal to the pile group displacement.

With reference to Figure 3.12, the displacement of the single pile i in global coordinates is expressed as

$$\boldsymbol{d^g_i} = \begin{bmatrix} u^g_i \\ w^g_i \\ \theta^g_i \end{bmatrix} = \sum_{j=1}^{N} \boldsymbol{\alpha^g_{ij}} \boldsymbol{d^g_j} \tag{3.111}$$

where N is the total number piles, $\boldsymbol{d^g_j}$ is the displacement of the source pile j due to its own load and

$$\boldsymbol{\alpha^g_{ij}} = \boldsymbol{t_i}\, \boldsymbol{\alpha^l_{ij}}\, \boldsymbol{t_j}^T \tag{3.112}$$

is the interaction factor matrix between receiver pile i and source pile j in global coordinates. Here, $\boldsymbol{\alpha^l_{ij}}$ is the interaction factor matrix between receiver pile i and source pile j in local coordinates.

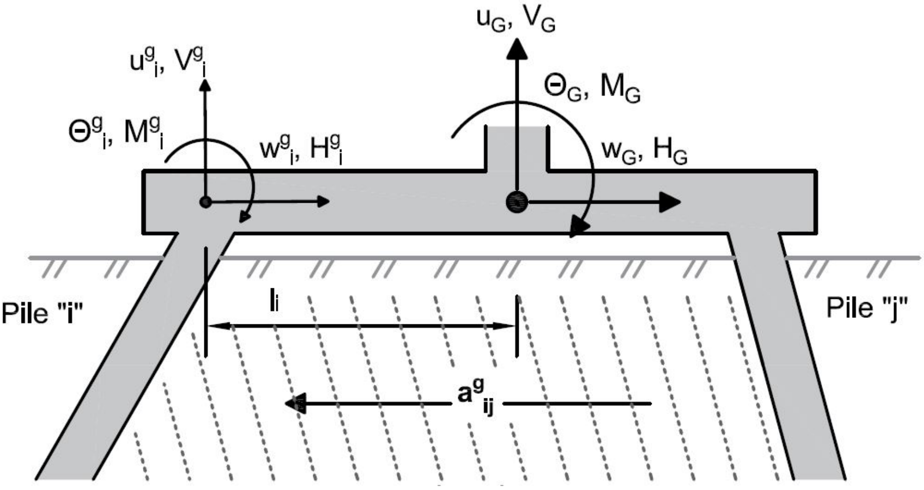

Figure 3.12: Schematic sketch of the pile group stiffness matrix

The horizontal displacement of pile i may be expressed as

$$w_i^g = \sum_{j=1}^{N} w_{i,j}^g = \sum_{j=1}^{N} \frac{H_j^g}{k_{S,ww,j}^g} \alpha_{wi,wj}^g = w_G \tag{3.113}$$

where $w_{i,j}^g$ is the horizontal displacement of pile i due to horizontal loading of pile j, H_j^g is the horizontal force in pile j, $\alpha_{wi,wj}^g$ is the interaction factor representing the additional horizontal displacement in pile i due to a horizontal displacement in pile j and w_G is the horizontal pile group displacement. Note that the interaction factor $\alpha_{wi,wj}^g = 1$ if $i = j$. The N equations are solved for N horizontal forces H_j^g as functions of w_G and the horizontal complex impedance is determined as

$$k_{G,ww}^* = \sum_{j=1}^{N} H_j^g(w_G = 1) \tag{3.114}$$

Similarly, we can express the vertical displacement as function of vertical forces and corresponding stiffness components and interaction factors, i.e.,

$$u_i^g = \sum_{j=1}^{N} u_{i,j}^g = \sum_{j=1}^{N} \frac{V_j^g}{k_{S,uu,j}^g} \alpha_{ui,uj}^g = u_G \tag{3.115}$$

The vertical complex impedance is determined as

$$k^*_{G,uu} = \sum_{j=1}^{N} V^g_j(u_G = 1) \tag{3.116}$$

Finally, the rotational impedance is assembled on the basis of individual vertical pile forces and moments. The vertical displacement in pile i i given as

$$u^g_i = \sum_{j=1}^{N} u^g_{i,j} = \sum_{j=1}^{N} \frac{V^g_j}{k^g_{S,uu,j}} \alpha^g_{ui,uj} = \theta_G l_i \tag{3.117}$$

where l_i is the distance between the global node and pile i. The rotational impedance is determined as

$$k^*_{G,\theta\theta} = \sum_{j=1}^{N} V^g_j(\theta_G = 1) + \sum_{j=1}^{N} k^l_{S,\theta\theta,i}(\theta_G = 1) \tag{3.118}$$

and the diagonal impedance matrix is expressed as

$$\boldsymbol{K^*_G} = \bar{\boldsymbol{K}}_{\boldsymbol{G}} + i\omega \boldsymbol{C_G} = \begin{bmatrix} k^*_{G,uu} & 0 & 0 \\ 0 & k^*_{G,ww} & 0 \\ 0 & 0 & k^*_{G,\theta\theta} \end{bmatrix} \tag{3.119}$$

3.4.2 Validation

Comparison against PILES

First, the closed-form model is compared to the rigorous solution PILES developed by Kaynia [134]. The results are presented in terms of absolute values, real parts and imaginary parts for pile spacing S_0 equal to $3d_p$, $5d_p$ and $10d_p$, $E_p/Es =$ 1000, $L/d = 40$, damping ratio $\beta = 0.05$ and $\rho_s = 0.75\rho_p$ for a 2x1 pile group. Normalization is achieved by dividing the respective impedance values with the summed static stiffness of two vertical, individual piles. The normalized impedance values are plotted against frequency f and the dimensionless angular frequency a_0 given by Equation 3.2.

Figure 3.13 shows the horizontal impedance $k^*_{G,ww}$. Overall, it is observed that the closed-form model (denoted ANA in the plots) produces relatively accurate results for absolute values, admittedly with slight overestimation at certain frequencies. The approximately same accuracy is observed for all three pile spacings. Real

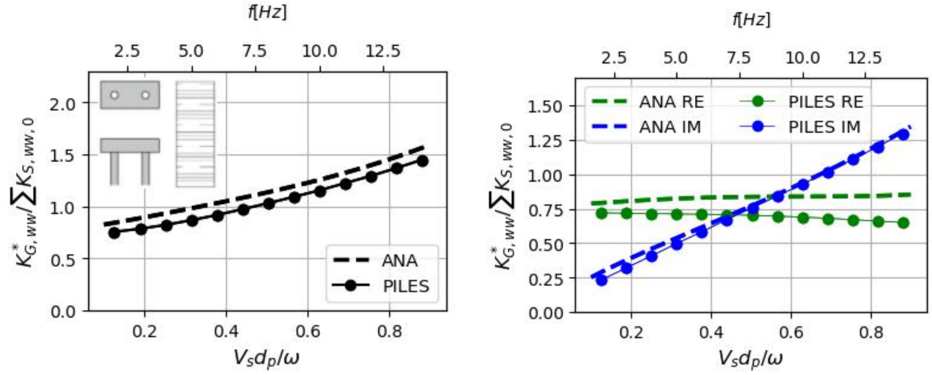

(a) Absolute, $S/d = 3$

(b) Real and imaginary, $S/d = 3$

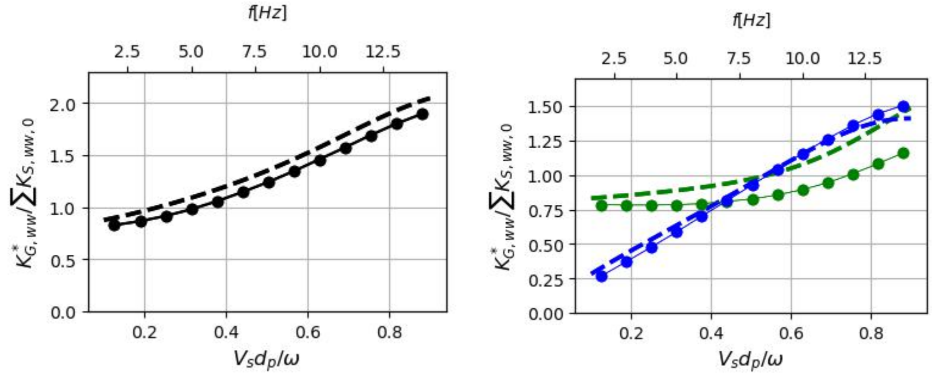

(c) Absolute, $S/d = 5$

(d) Real and imaginary, $S/d = 5$

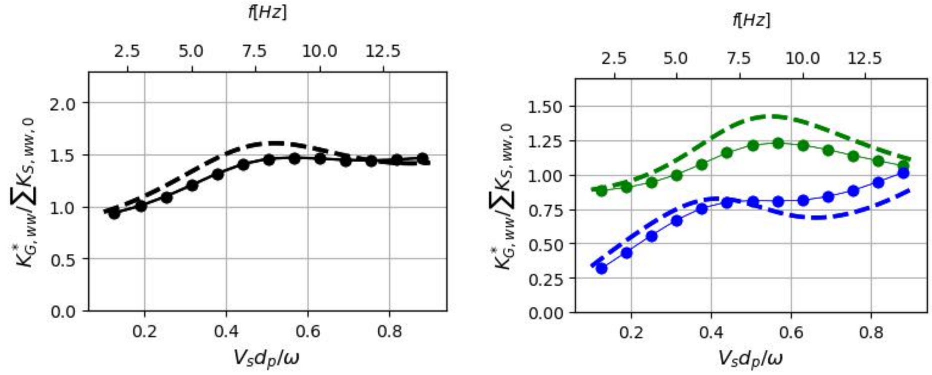

(e) Absolute, $S/d = 10$

(f) Real and imaginary, $S/d = 10$

Figure 3.13: Horizontal impedance $k^*_{G,ww}$. Comparison against PILES [134]. $L/d = 40$, $E_p/E_s = 1000$, damping ratio $\beta = 0.05$, $\beta_1 = \beta_2 = 0°$ and $\rho_s = 0.75\rho_p$

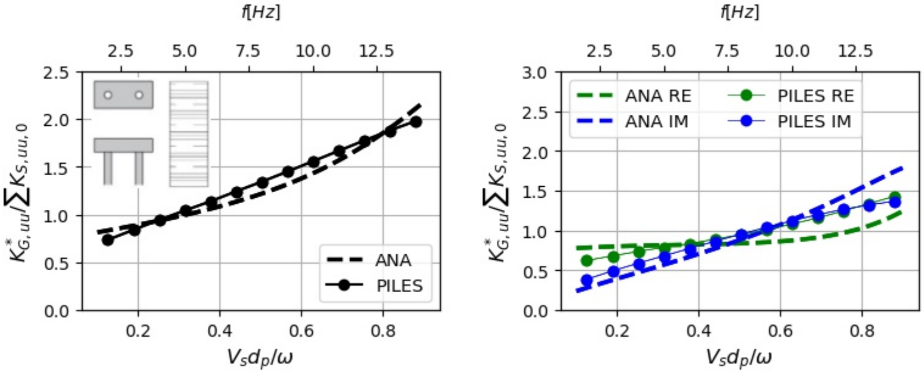

(a) Absolute, $S/d = 3$

(b) Real and imaginary, $S/d = 3$

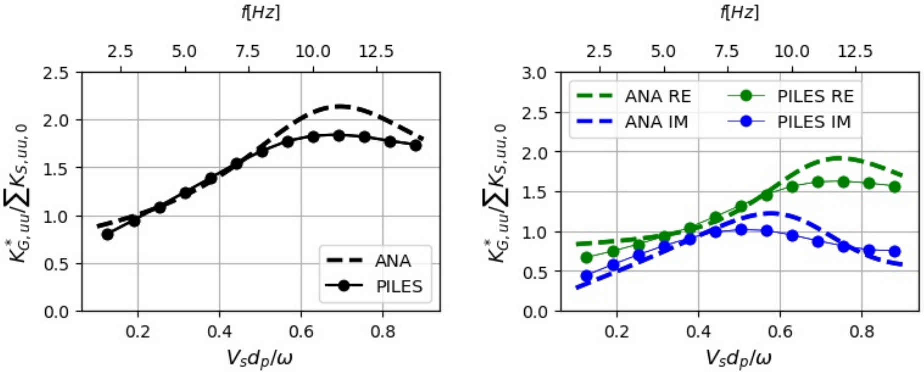

(c) Absolute, $S/d = 5$

(d) Real and imaginary, $S/d = 5$

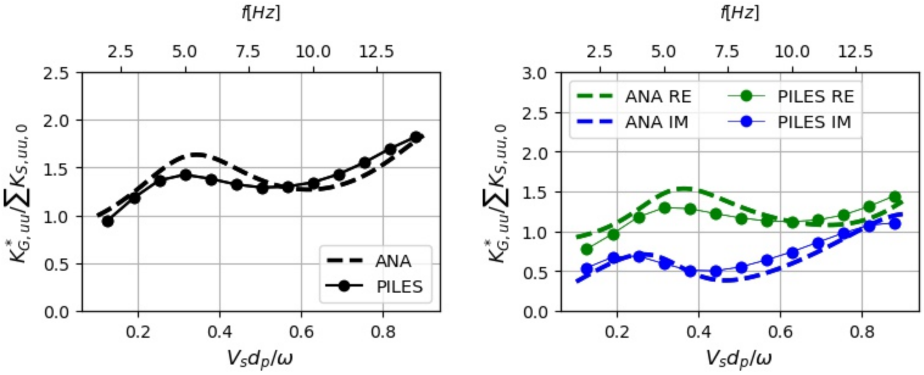

(e) Absolute, $S/d = 10$

(f) Real and imaginary, $S/d = 10$

Figure 3.14: Vertical impedance $k^*_{G,uu}$. Comparison against PILES [134]. $L/d = 40$, $E_p/E_s = 1000$, damping ratio $\beta = 0.05$, $\beta_1 = \beta_2 = 0°$ and $\rho_s = 0.75\rho_p$

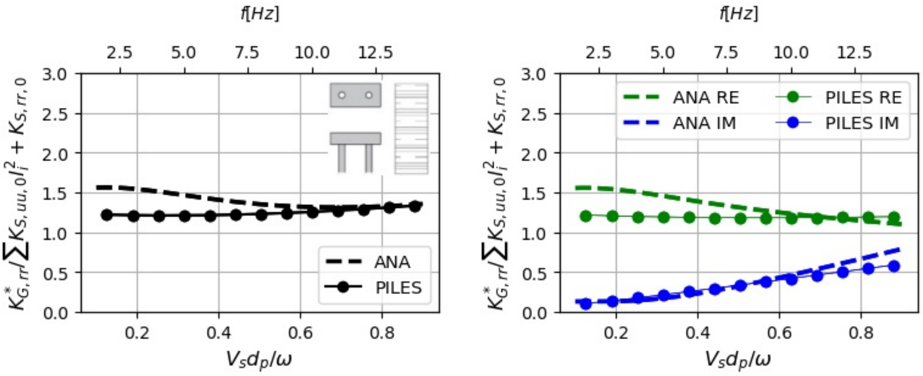

(a) Absolute, $S/d = 3$ **(b)** Real and imaginary, $S/d = 3$

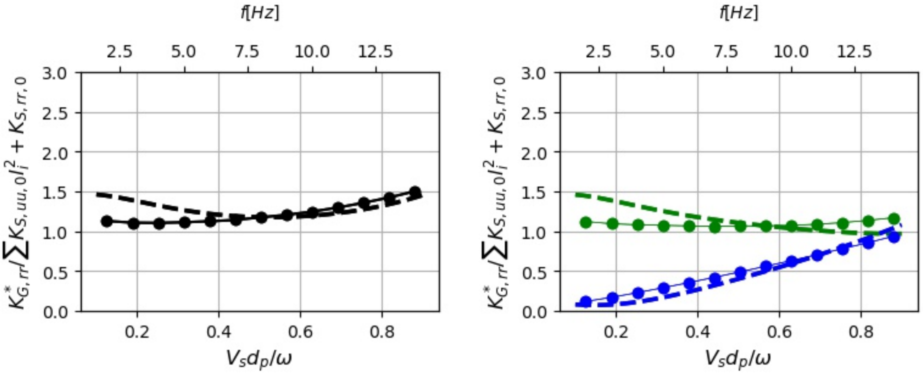

(c) Absolute, $S/d = 5$ **(d)** Real and imaginary, $S/d = 5$

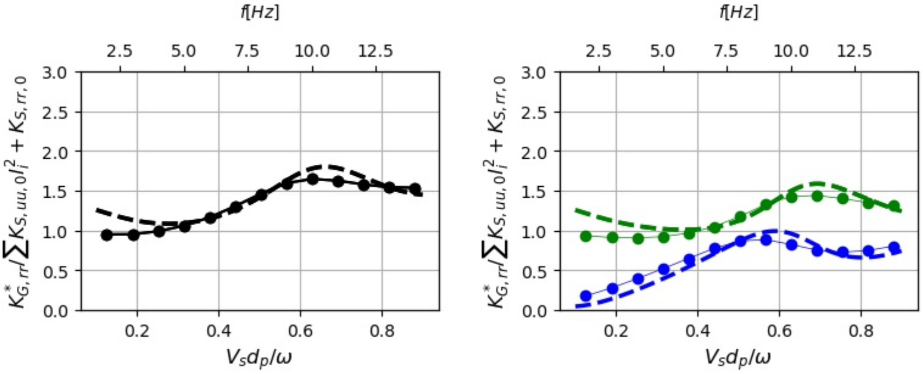

(e) Absolute, $S/d = 10$ **(f)** Real and imaginary, $S/d = 10$

Figure 3.15: Rotational impedance $k^*_{G,\theta\theta}$. Comparison against PILES [134]. $L/d = 40$, $E_p/E_s = 1000$, damping ratio $\beta = 0.05$, $\beta_1 = \beta_2 = 0°$ and $\rho_s = 0.75\rho_p$

and imaginary parts are captured fairly well, although somewhat less accurately than the absolute values. Most importantly, it is evident that the model is able to capture trends with respect to both frequency and pile spacing for absolute, real and imaginary parts.

Figure 3.14 shows the horizontal impedance $k^*_{G,uu}$. As for horizontal impedance, the closed-form model produces relatively accurate results for absolute values, and slightly less accurate results real and imaginary parts. Trends with respect to both frequency and pile spacing for absolute, real and imaginary parts are captured rather well.

Figure 3.15 shows the rotational impedance $k^*_{G,\theta\theta}$. The model produces satisfactory results, but the accuracy is somewhat lower compared to horizontal and vertical impedance. This may be observed for all three pile spacings. The relative inaccuracy stems from the real part and is most prominent in the low-frequency range. In fact, rotational impedance is captured quite well as the frequency increases.

Comparison against OpenSees MP

It should be noted that PILES [134] is restricted to vertical piles only. In order to evaluate the effect of batter angle, the closed-form model is compared to a rigorous finite element model constructed in OpenSees MP in terms of horizontal impedance $k^*_{G,ww}$. The results are presented as absolute values for pile spacing S_0 equal to $3d_p$, $5d_p$ and $10d_p$, $L/d = 40$, damping ratio $\beta = 0.05$ and $\rho_s = 0.75\rho_p$ for a 2x1 pile group. In addition, four different batter angles (0°, 5°, 10° 15°) and two different E_p/E_s-ratios (200 and 1000) are considered. The chosen batter angles are considered within the realistic range in practical design. As previously, normalization is achieved by dividing the respective impedance values with the summed static stiffness of two vertical, individual piles and the normalized impedance values are plotted against frequency f and the dimensionless angular frequency a_0 given by Equation 3.2. The results are shown in Figures 3.16 - 3.21, where each figure shows four plots with different batter angle, fixed pile spacing and fixed E_p/E_s-ratio. Taking into consideration that the complexity of the problem is primarily governed by the pile-soil-pile interaction, it is crucial to investigate the accuracy of the analytical model in context with the dynamic response of single piles. Therefore, each plot includes the corresponding impedance of two single piles (or pile group impedance without pile-soil-pile interaction) with corresponding batter angle computed using the finite element model.

The closed-form model is derived based on the assumption that free-vibration response is negligible. Except for higher load frequencies in some system configura-

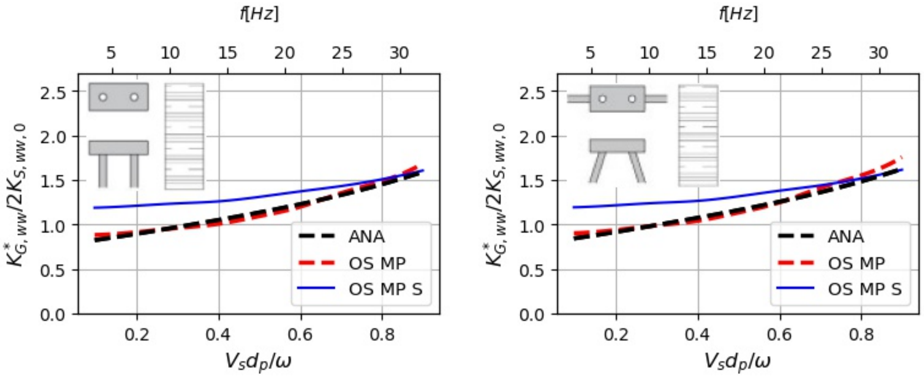

(a) Batter angle β_1 = -β_2 = 0^0 **(b)** Batter angle β_1 = -β_2 = 5^0

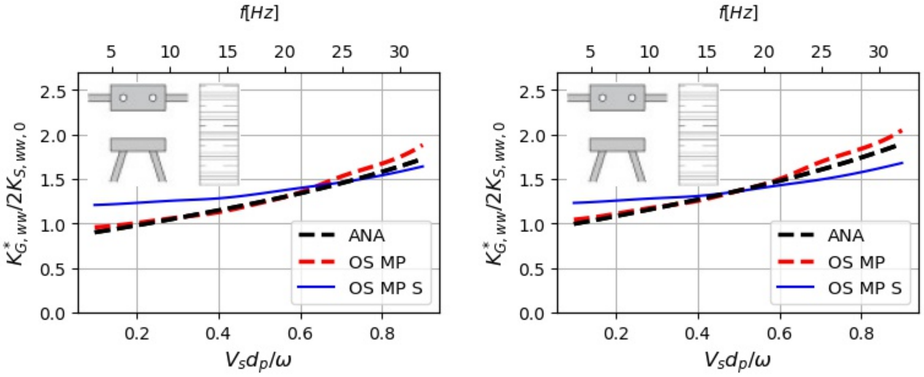

(c) Batter angle β_1 = -β_2 = 10^0 **(d)** Batter angle β_1 = -β_2 = 15^0

Figure 3.16: Horizontal impedance $k^*_{G,ww}$. $L/d = 40$, $E_p/E_s = 200$, damping ratio $\beta = 0.05$, $\rho_s = 0.75\rho_p$ and $S_0 = 3d$

tions, this assumption is indeed confirmed by the finite element model. Even when there is a notable contribution, it can be shown that the free-vibration response dies out rather quickly. Also, the evaluation of dynamic impedance, rather than e.g. maximum response values, pertains intrinsically to the steady-state vibration. For the finite element model, the load is applied for a duration of 1.00 second using 200 time steps, and the impedance values are obtained by averaging the absolute values of maximum and minimum displacements during the steady-state response.

Figure 3.16 shows the results for $E_p/E_s = 200$ and $S_0 = 3d_p$. The closed-form model matches the finite element model quite well for all four batter angles, and it is able to capture trends with respect to batter angle and frequency. It should

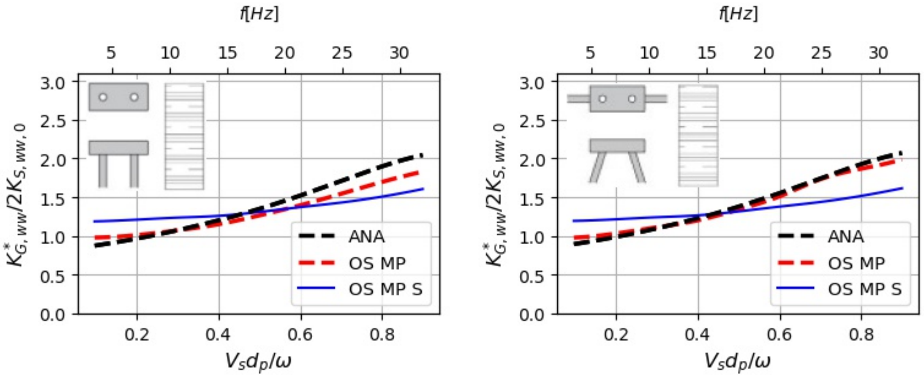

(a) Batter angle β_1 = -β_2 = 0^0 **(b)** Batter angle β_1 = -β_2 = 5^0

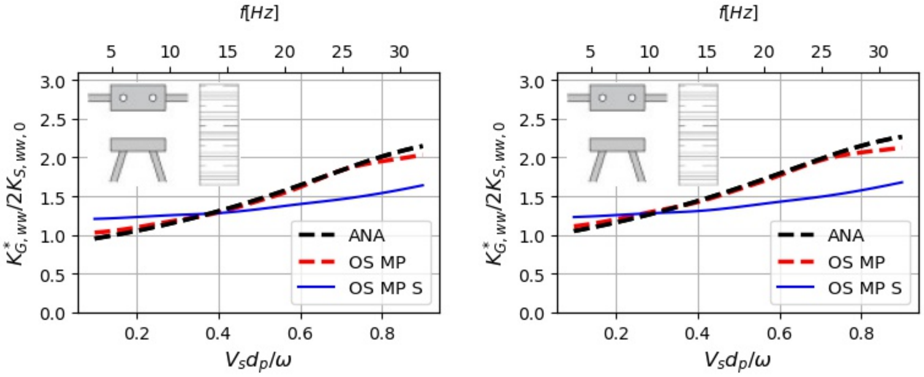

(c) Batter angle β_1 = -β_2 = 10^0 **(d)** Batter angle β_1 = -β_2 = 15^0

Figure 3.17: Horizontal impedance $k^*_{G,ww}$. $L/d = 40$, $E_p/E_s = 200$, damping ratio $\beta = 0.05$, $\rho_s = 0.75\rho_p$ and $S_0 = 5d$

be noted that the difference between the pile group impedances (black and red lines) and the summed single pile impedance (blue line), implicitly represent the pile-soil-pile interaction effects. In this case, it is evident that the pile-soil-pile interaction yields more frequency-dependent behaviour. More specifically, pile-soil-pile interaction reduces impedance in the low-frequency range and increase impedance in the high frequency range for the considered range of frequencies.

Figure 3.17 shows the results for $E_p/E_s = 200$ and $S_0 = 5d_p$. It observed that the closed-form model matches the finite element model with approximately the same accuracy as for the configuration with $S_0 = 3d_p$. As expected, the results show that the pile-soil-pile interaction increase/reduction frequency range shifts as the

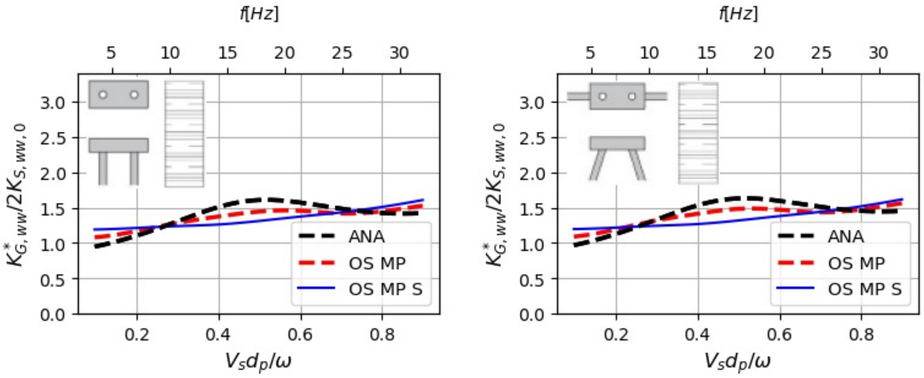

(a) Batter angle β_1 = -β_2 = 0^0

(b) Batter angle β_1 = -β_2 = 5^0

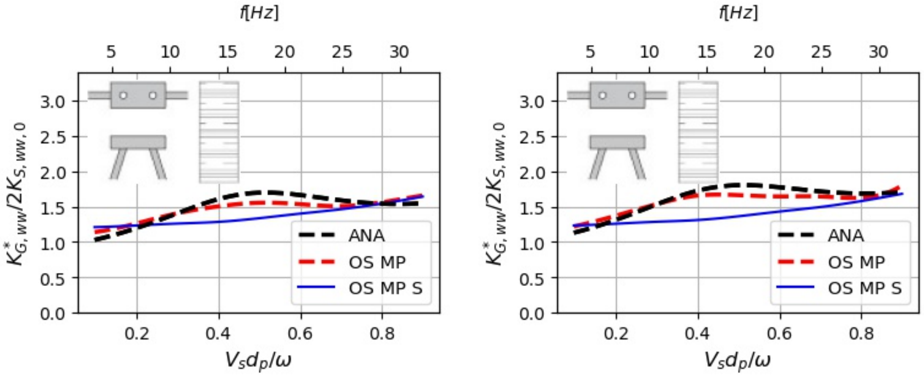

(c) Batter angle β_1 = -β_2 = 10^0

(d) Batter angle β_1 = -β_2 = 15^0

Figure 3.18: Horizontal impedance $k^*_{G,ww}$. $L/d = 40$, $E_p/E_s = 200$, damping ratio $\beta = 0.05$, $\rho_s = 0.75\rho_p$ and $S_0 = 10d$

pile spacing increases.

Figure 3.17 shows the results for $E_p/E_s = 200$ and $S_0 = 10d_p$. The results show similar accuracy and trends as the configurations with $S_0 = 3d_p$ and $S_0 = 5d_p$.

Figures 3.19 - 3.21 show the same results as those presented above, but with $E_p/E_s = 1000$. The results reveal similar accuracy and trends as the configurations with $E_p/E_s = 200$. Hence, for the considered E_p/E_s-ratios, the results indicate that soil stiffness only has a minor influence on the relative behaviour of a pile group when considering linear elastic response.

In order to validate the closed-form model for larger pile groups, the closed-form

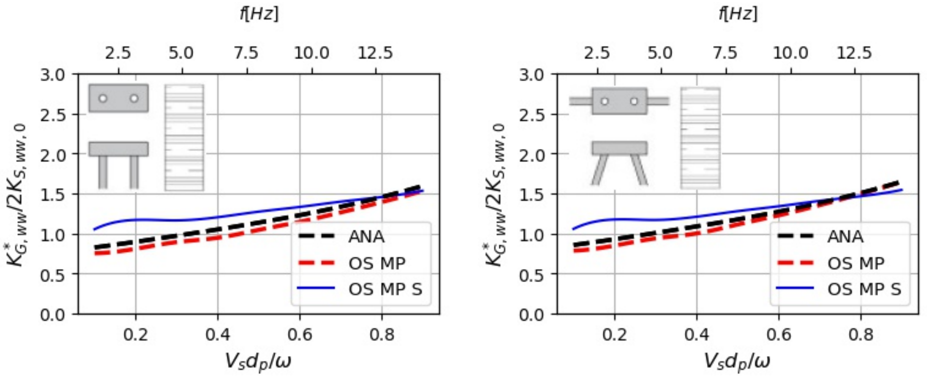

(a) Batter angle β_1 = -β_2 = 0^0 **(b)** Batter angle β_1 = -β_2 = 5^0

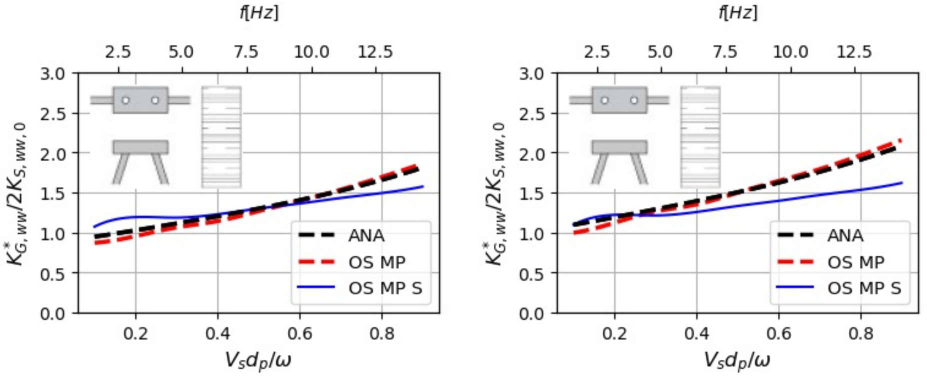

(c) Batter angle β_1 = -β_2 = 10^0 **(d)** Batter angle β_1 = -β_2 = 15^0

Figure 3.19: Horizontal impedance $k^*_{G,ww}$. $L/d = 40$, $E_p/E_s = 1000$, damping ratio $\beta = 0.05$, $\rho_s = 0.75\rho_p$ and $S_0 = 3d$

model is compared to OpenSees MP in terms of horizontal impedance $k^*_{G,ww}$ for a three-by-three pile group with both vertical and batter piles. The piles in the mid-row are vertical, and the piles in the two outer rows are battered outwards. The results are shown in Figure 3.22. As for the two-by-one pile group, the closed-form model matches the finite element model fairly well, and it is able to capture the effect of batter angle and frequency.

3.4.3 Effect of batter angle

The main novelty of the proposed model lies within its ability to capture trends with respect to batter angle. It is therefore interesting to investigate the effect of

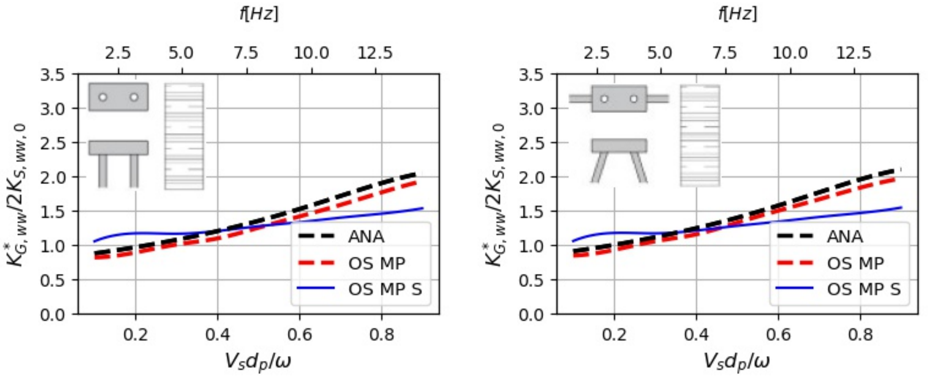

(a) Batter angle β_1 = -β_2 = 0^0 **(b)** Batter angle β_1 = -β_2 = 5^0

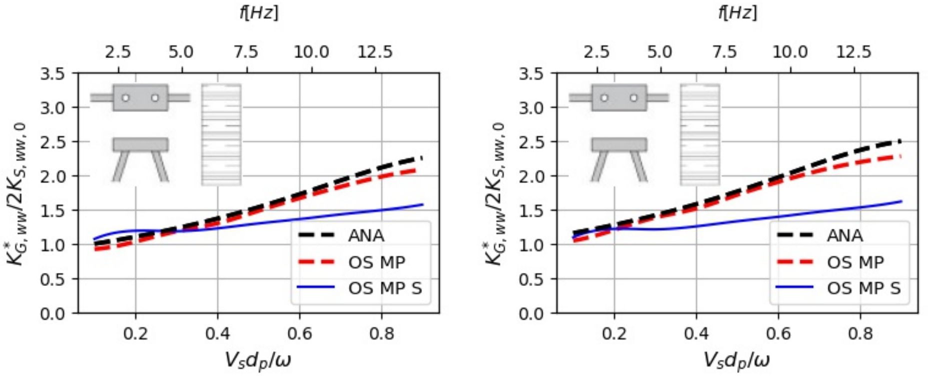

(c) Batter angle β_1 = -β_2 = 10^0 **(d)** Batter angle β_1 = -β_2 = 15^0

Figure 3.20: Horizontal impedance $k^*_{G,ww}$. $L/d = 40$, $E_p/E_s = 1000$, damping ratio $\beta = 0.05$, $\rho_s = 0.75\rho_p$ and $S_0 = 5d$

batter angle with respect to horizontal, vertical and rotational impedance.

Figure 3.23 shows the impedances of the three-by-three pile group, where each plot shows four different batter angles (0°, 5°, 10° 15°). As expected, the horizontal impedance $k^*_{G,uu}$ is most sensitive to batter angle, where the impedance increases as batter angle increases. This is explained by the fact that axial pile impedance is greater than transverse pile impedance. Hence, for a battered pile, the axial components influence the horizontal impedance to a greater degree compared to the opposite case. The vertical impedance $k^*_{G,ww}$ is influenced by batter angle only at or near the peaks, where the impedance decreases as batter angle increases. Otherwise, the vertical impedance is nearly independent of batter angle.

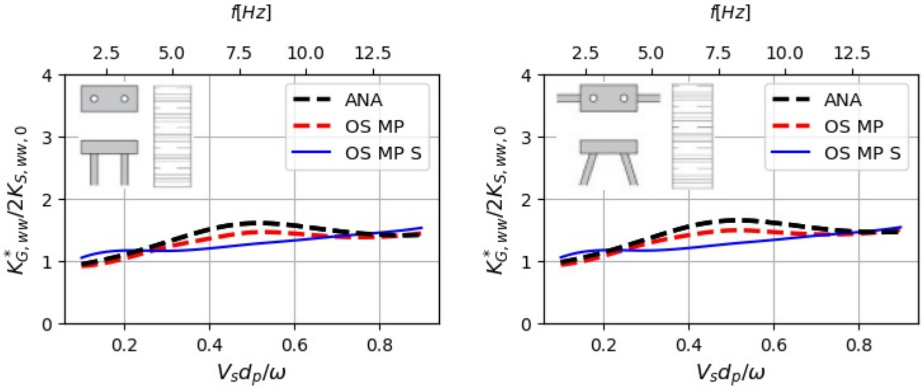

(a) Batter angle β_1 = -β_2 = 0^0

(b) Batter angle β_1 = -β_2 = 5^0

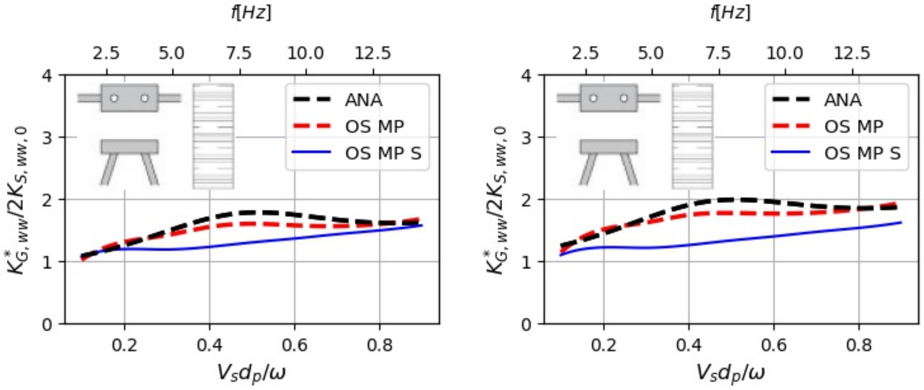

(c) Batter angle β_1 = -β_2 = 10^0

(d) Batter angle β_1 = -β_2 = 15^0

Figure 3.21: Horizontal impedance $k^*_{G,ww}$. $L/d = 40$, $E_p/E_s = 1000$, damping ratio $\beta = 0.05$, $\rho_s = 0.75\rho_p$ and $S_0 = 10d$

The rotational $k^*_{G,\theta\theta}$ is also relatively independent of batter angle, slightly less so than vertical impedance. This is attributed to the following; the rotation a pile group is mainly resisted by vertical forces, especially for large pile spacing. However, the individual pile moments also contribute to rotation resistant. Therefore, it is expected that rotational impedance is slightly less dependent on batter angle compared to vertical impedance. As for vertical impedance, the rotational impedance decreases as batter angle increases.

It is also observed that the real and imaginary parts are approximately equally influenced by batter angle.

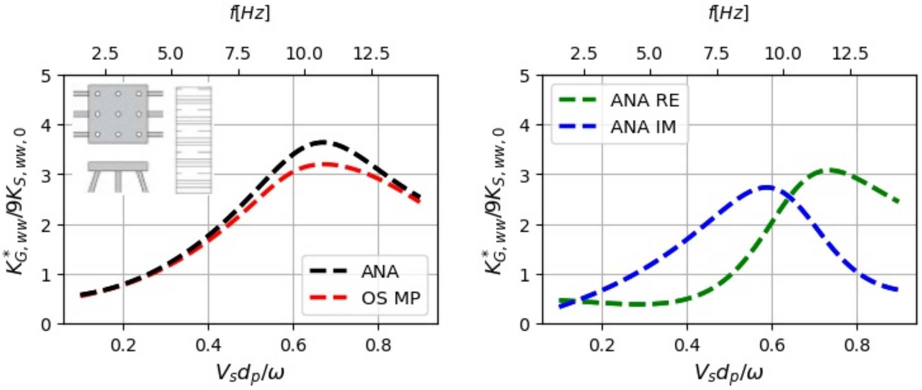

(a) Absolute **(b)** Real and imaginary

Figure 3.22: Horizontal stiffness $k^*_{G,ww}$ of a 3x3 pile group with both vertical and batter piles. $\beta_1 = -\beta_2 = 15^0$, $L/d = 40$, $E_p/E_s = 1000$, damping ratio $\beta = 0.05$, $\rho_s = 0.75\rho_p$ and $S_0 = 3d$

3.4.4 Limitations and applicability

Indeed, the closed-form model is able produce the trends associated with pile distance and frequency rather well, but the general inaccuracy of such methods must be recognized. In addition to the inaccuracy introduced by the various simplifications, linear methods are strongly limited in the sense that they cannot capture material (soil) and geometrical (formation of gap) non-linearity, both of which are to be expected during strong earthquake shaking and corresponding inertial loading. The closed-form model is also limited to uniform soil profiles, long (floating) piles, cylindrical pile shapes and fixed-head conditions. Even so, the applicability of the closed-form model includes (but is not restricted to) the following:

1. Low-exaction seismic problems and vibration problems.
2. Early-stage design or whenever approximate solution are sought.
3. Rough validation of rigorous models.
4. In practical design situations, it is often interesting to observe trends rather than response values with respect to certain parameters. The closed-form model may be applied as an efficient tool to asses the effect of batter angle, pile spacing and excitation frequency.

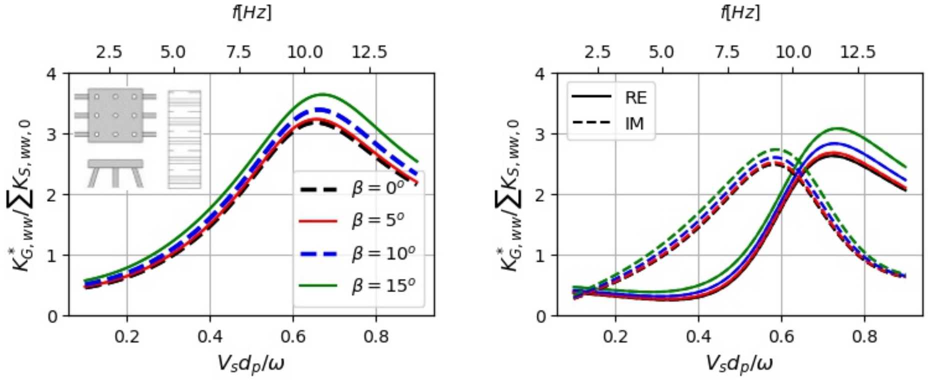

(a) Absolute $K^*_{G,ww}$ **(b)** Real and imaginary $K^*_{G,ww}$

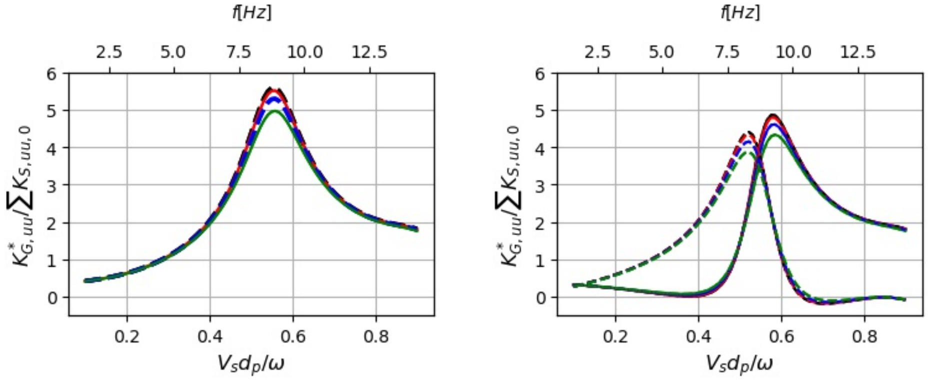

(c) Absolute $K^*_{G,uu}$ **(d)** Real and imaginary $K^*_{G,uu}$

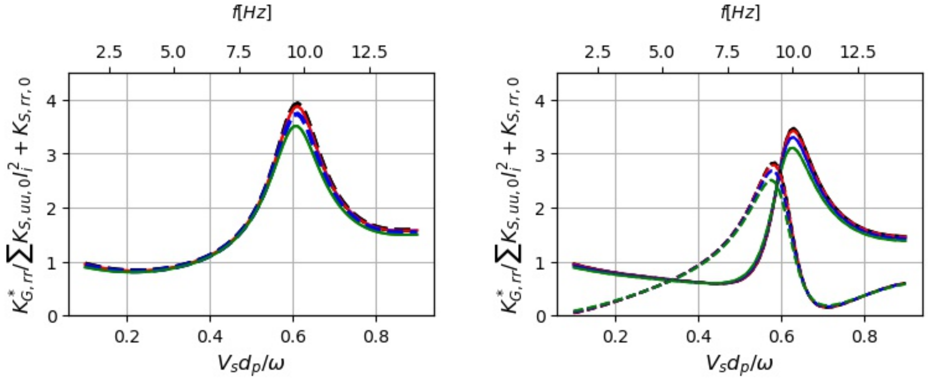

(e) Absolute $K^*_{G,\theta\theta}$ **(f)** Real and imaginary $K^*_{G,\theta\theta}$

Figure 3.23: Horizontal, vertical and rotational impedance for a 3x3 pile group. $L/d = 40$, $E_p/E_s = 1000$, damping ratio $\beta = 0.05$, $\beta_1 = \beta_2 = 0°$ and $\rho_s = 0.75\rho_p$

5. Simplified methods are generally well-suited for educational purposes. Rigorous finite element models are able to produce accurate results for a variety of structural and geotechincal problems. For better or worse, numerical models tend to embody and thus conceal some of the phenomena related to geodynamics and soil-structure-interaction, which are often important in the pursuit of mastering structural and geotechnical engineering. The derivation of the closed-form model elucidates many aspects related to structural dynamics, geodynamics, soil-pile interaction and their interplay with each other.

3.5 Hybrid model

3.5.1 Assembly

The hybrid model may be considered as an extension of the presented model, where the limitations of the closed-form solution are, at least partly, bested by solving the differential equation numerically.

The hybrid model is constructed in Matlab [223]. The piles are represented using Euler-Bernoulli beams, the soil resistance is modelled using Winkler springs and dashpots in accordance with Equations 3.1 and 3.3, and the pile-soil-pile interaction is simulated using uni-axial elements based on the attenuation functions given in Equations 3.71 - 3.74. The pile-soil-pile interaction element connects the horizontally aligned nodes in each beam. See illustration in Figure 3.24. By considering transverse, rotational and axial degrees of freedom in each node, the complex stiffness matrix of the pile-soil-pile interaction element is obtained as

$$K^*_{pspi} = -L_e \begin{bmatrix} 0 & 0 & 0 & k_{pspi,1} & 0 & k_{pspi,2} \\ 0 & 0 & 0 & 0 & 0 & 0 \\ 0 & 0 & 0 & k_{pspi,3} & 0 & k_{pspi,4} \\ k_{pspi,1} & 0 & k_{pspi,3} & 0 & 0 & 0 \\ 0 & 0 & 0 & 0 & 0 & 0 \\ k_{pspi,2} & 0 & k_{pspi,4} & 0 & 0 & 0 \end{bmatrix} \tag{3.120}$$

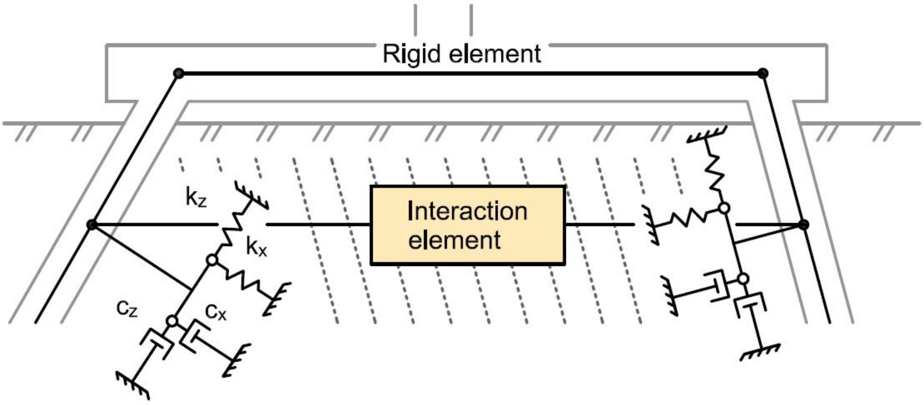

Figure 3.24: Schematic sketch of the hybrid model.

where

$$k_{pspi,1} = \cos(\beta_1 - \beta_2)\psi_w(k_x + i\omega c_x) \tag{3.121a}$$

$$k_{pspi,2} = -\sin(\beta_1 - \beta_2)\psi_w(k_z + i\omega c_z) \tag{3.121b}$$

$$k_{pspi,3} = \sin(\beta_1 - \beta_2)\psi_u(k_x + i\omega c_x) \tag{3.121c}$$

$$k_{pspi,4} = \cos(\beta_1 - \beta_2)\psi_u(k_z + i\omega c_z) \tag{3.121d}$$

and L_e is the element length. The pile-soil-pile interaction element stiffness matrix is complex since damping is directly incorporated into the matrix entries. The global stiffness matrix is thus also complex. Alternatively, the pile-soil-pile interaction element stiffness matrix may be split into separate stiffness and damping matrices, both of which are real. E.g, $k_{pspi,1}$ may be split into stiffness and damping contributions, i.e.,

$$k_{pspi,1} = \cos(\beta_1 - \beta_2)\ |real(\psi_w)|\ k_x, \quad c_{pspi,1} = \cos(\beta_1 - \beta_2)\ |imag(\psi_w)|\ c_x \tag{3.122}$$

The pile-soil-pile interaction element matrices are then assembled into the global stiffness and damping matrices,

$$K_{pspi} \to \boldsymbol{K},\ C_{pspi} \to \boldsymbol{C} \tag{3.123}$$

where both $\boldsymbol{K}$ and $\boldsymbol{C}$ only contain real entries.

The pile cap is represented by adding a high-stiffness member between the two top nodes in each beam. Additional damping is added as Rayleigh damping.

3.5.2 Validation

The results are presented in terms of absolute values of the horizontal impedance $k^*_{G,ww}$ for pile spacing S_0 equal to $3d_p$, $5d_p$ and $10d_p$, batter angles equal to $10°$ and $15°$, $E_p/Es = 200$, $L/d = 40$, damping ratio $\beta = 0.05$ and $\rho_s = 0.75\rho_p$ for a 2x1 pile group.

First, it is observed that the hybrid model (HYB) and closed-form model (ANA) match well, admittedly with less accuracy for close pile spacing. In addition, Figures 3.25(a) and 3.25(b) show that the difference increases with increasing batter angle. Interestingly, the closed-form model shows better agreement with the finite element model compared to the hybrid model for all configurations and most frequencies. Nonetheless, there are two obvious advantages to the hybrid model compared to the closed-form model. First, the hybrid model allows for arbitrary pile length and boundary conditions (fixed-head, hinged-head, frictional and end-bearing) whereas the closed-form model demands an unique solution for every different combination of boundary conditions. Second, the hybrid model may easily be extended to include any of type of superstructure, and thus allows for direct solutions of seismic excitation problems. The main (and obvious) disadvantage of the hybrid model compared to the closed-form model is that the former requires discretization of the problem.

3.6 Summary

The diagonal impedance matrix presented in this chapter was obtained by simplifying the closed-form solutions for a BWF-problem including pile-soil-pile interaction. This has been achieved by eliminating parts of the solution that are considered to have a negligible contribution. The proposed model consists of easy-to-use, spreadsheet-friendly expressions with well-known input variables. It has been demonstrated that the closed-form model, although limited, is able to represent the trends associated with batter angle, pile distance and frequency rather well.

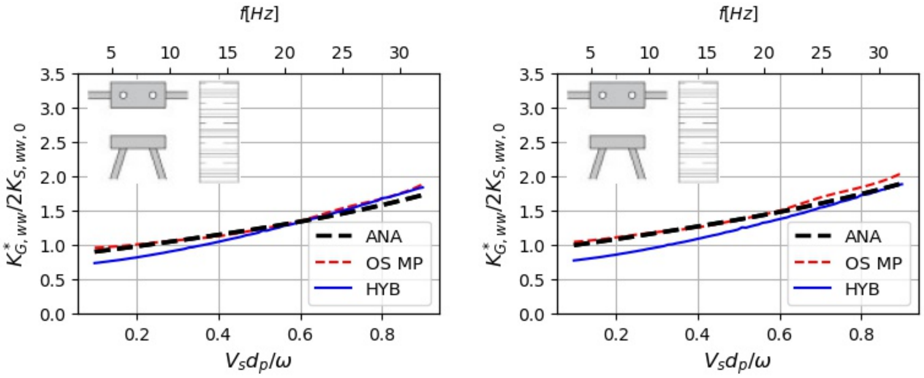

(a) Batter angle β_1 = -β_2 = 10^0 and S_0 = $3d$ **(b)** Batter angle β_1 = -β_2 = 15^0 and S_0 = $3d$

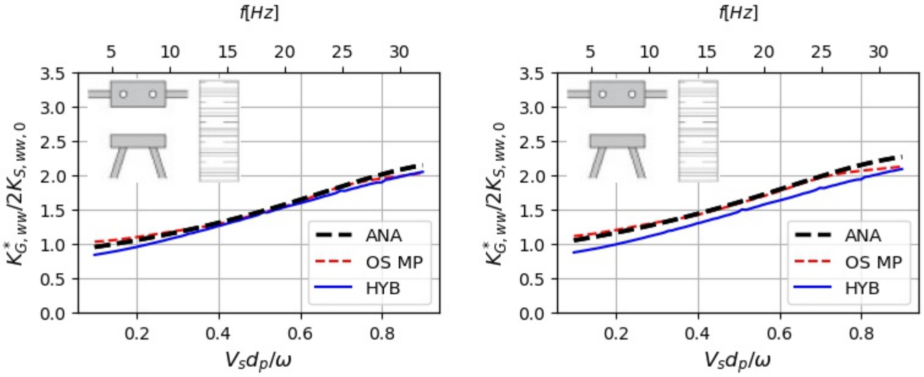

(c) Batter angle β_1 = -β_2 = 10^0 and S_0 = $5d$ **(d)** Batter angle β_1 = -β_2 = 15^0 and and S_0 = $5d$

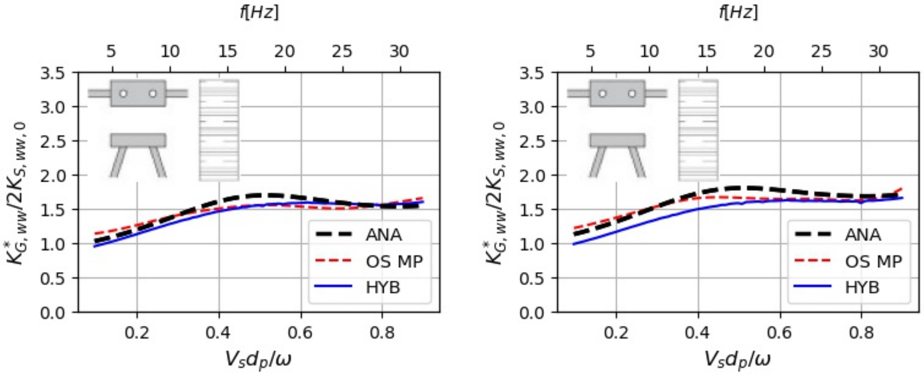

(e) Batter angle β_1 = -β_2 = 10^0 and S_0 = $10d$ **(f)** Batter angle β_1 = -β_2 = 15^0 and S_0 = $10d$

Figure 3.25: Horizontal impedance $k^*_{G,ww}$. $L/d = 40$, $E_p/E_s = 200$, damping ratio $\beta = 0.05$ and $\rho_s = 0.75\rho_p$

Chapter 4

Macro-element (nonlinear stiffness matrix)

4.1 Introduction

Pile groups pose difficulties in structural and geotechnical engineering when the objective is to determine the seismic response of both structure and foundation. Researchers have proposed numerous linear solutions for estimating dynamic impedance of pile groups [90, 134, 135, 138, 140, 211, 212, 213, 214, 215, 216, 217, 218, 219, 220], but these methods are restricted to small displacements. During seismic excitation, and particularly in the presence of large inertial forces, piles are subject to large displacements that mobilize highly nonlinear behaviour such as soil-wedge type failure, flow-around failure, gap-formation and sliding. Although these effects may be captured using sophisticated numerical tools, such methods are often time-consuming, complex and generally unsuitable for practical engineering.

To the authors knowledge, there are no macro-elements developed for pile groups with vertical and batter piles that take into account the inelastic behaviour of both pile and soil. The objective of this study is to formulate a practical macro-element with three degrees of freedom for vertical and batter pile groups. Since macro-elements are most suitable for practical engineering and design tools, the use of such elements should be more attractive than finite element modelling of the entire system. Consequently, certain criteria will be emphasized in the formulation. First, the macro-element does not have to capture all the features of a rigorous finite element model, but it needs to capture the trends intrinsic to pile group configuration and soil profile. Second, the formulation must be robust with respect to both pile group configuration and numerical implementation. Third, the calibration must be straight-forward and independent of pile and soil properties, soil profile and pile group configuration. To achieve robustness with respect to pile group configuration and straight-forward calibration procedures, the numerical scheme presented in this study is based on de-coupled, single pile response. Each pile consists of two separate load-displacement formulations (axial and transverse) that take a displacement increment as input and return a tangent stiffness value. The effect of rotation is implicitly incorporated in the transverse load-displacement formulation. The global tangent stiffness matrix (which is passed to the global solution in a finite element code) is assembled on the basis of the single pile tangent stiffness values. The presented macro-element does not require pre-defined failure surfaces or other parameters, and is therefore not restricted to a specific foundation configuration, soil profile or soil type. It should be noted that even though the calibration in this paper is achieved using detailed finite element models, the macro-element may be calibrated using any type of nonlinear pile-soil model. However, there are limitations that must be addressed. First, the macro-element is formulated for seismic design purposes where large displacements are expected. It is assumed that geometric damping (frequency-dependent) is negligible compared to material damping (frequency-independent). The constitutive model is therefore rate-independent. Second, pile-soil-pile interaction is neglected. This assumption admittedly decreases the accuracy of the proposed model when the piles are closely spaced. While it is possible to approximately include pile-soil-pile interaction, it should be noted that recent studies [196, 224] have shown that pile-to-pile interaction is less significant when piles undergo large displacements in soft, inelastic soil. Third, the macro-element is formulated such that pile-cap rotation is resisted by vertical pile-head loads only. This assumption may also decrease the accuracy when the piles are closely spaced. Finally, axial and transverse response is de-coupled. It is assumed that the active length contributes to transverse resistance while the soil below the active length contributes to axial resistance. This assumptions strictly limits the formulation to long piles. The effect of axial load on bending capacity is not considered.

This chapter is divided in five sections. Section 4.2 briefly describes the finite element model used for validation. Section 4.3 presents the theoretical framework and validation of the single pile macro-elements. Section 4.4 outlines the pile group tangent stiffness matrix assembly and demonstrates the pile group macro-element performance for numerous configurations. The conclusion is given in Section 4.5. Note that the numerical implementation of the macro-element is presented in Chapter 5.

4.2 Validation model

The macro-element is validated by finite element models constructed in OpenSees MP [186] together with the pre- and post-processing tool STKO [187]. The soil profile and cross section of the concrete pile are shown in Figure 4.1. The piles are modelled using displacement-based beam elements. The nonlinear behaviour of reinforced concrete is represented using fibre sections. The confined and unconfined concrete is simulated using the uni-axial material models *ConfinedConcrete01* [191] and *Concrete01* [192], respectively. The cylindrical strength f_{pc} is $45MPa$ and the initial elastic stiffness modulus E_c is $36GPa$. The reinforcement is simulated using the uni-axial material model *Steel02* [193]. The yield strength f_y is $487MPa$ and the initial elastic stiffness modulus E_s is $185GPa$. The soil is divided in six layers along the pile length, where each layer has a height $h_{lay} = 3m$. The soil is modelled using eight-noded hexahedral elements with a single integration point to prevent locking behaviour. The adopted soil model *Pressure Independent Multi-Yield* is an elastic-plastic, soil model suited for clay [188]. The reader is referred to Section 2.2 for a detailed description of the soil material model, soil profile and meshing strategies. The pile-soil interface is modelled using frictional contact elements based on the Mohr-Coulomb criterion, penalty constraints and an implicit-explicit solution scheme [187, 197]. Multi-stage analyses are performed to capture the correct stress state prior to the quasi-static pile-head loading. The first stage is a gravity analysis of the soil domain. In the second stage, a new gravity analysis is performed where the soil corresponding to the pile geometry is removed. In the third stage, a new gravity analysis is performed which includes the piles and contact elements. In the fourth and final stage, the quasi-static pile-head load analysis is performed. Prior to each analysis, the displacement field is set equal to zero. The system is solved using the Krylov-Newton implicit scheme [208].

4.3 Single piles

4.3.1 One-dimensional bounding plasticity

Several researchers have successfully implemented bounding surface plasticity models for shallow and deep foundations [163, 164, 165, 168, 175, 171, 172]. The macro-element presented in this paper is based on the bounding surface plasticity theory with radial mapping [125, 126]. There are three major aspects that distinguish bounding surface plasticity from conventional rate-independent plasticity. First, the current load is limited by a bounding surface. Second, the current load surface is also the yield surface, which implies that a purely elastic domain does

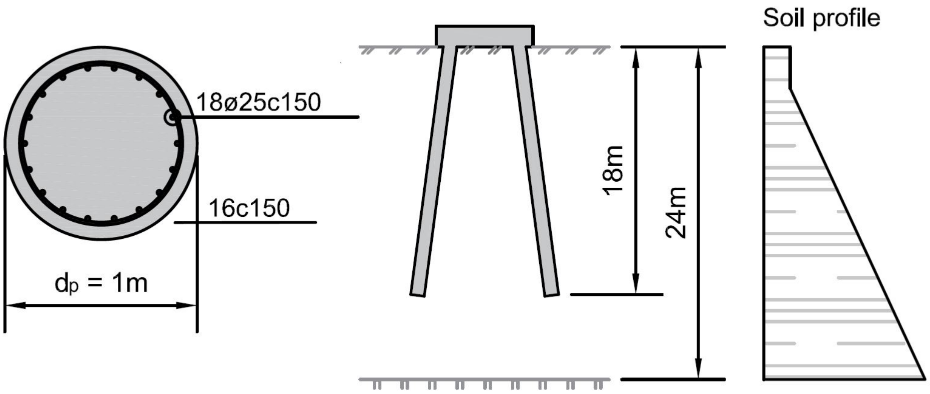

Figure 4.1: System configuration

not exist (except for an infinitesimal range at initial loads or load reversals). Third, the evolution of internal variables is governed only by the distance from the current load to an image point on the bounding surface, which implies that there is no need for an explicit description of a hardening variable. Since the macro-element in this study considers un-coupled single pile response, we will henceforth refer to points (or loads) rather than surfaces. The general formulation presented in this section applies for both transverse and axial loading.

Displacement and rotation rates are decomposed into elastic and plastic components, i.e.,

$$\dot{d} = \dot{d}^{el} + \dot{d}^{pl} \tag{4.1}$$

The rate of generalized forces is expressed as

$$\dot{F} = K^{el}\,\dot{d}^{e} = K^{el}(\dot{d} - \dot{d}^{pl}) \tag{4.2}$$

where F is the force and K^{el} is the elastic stiffness. The bounding load is constrained through

$$G(\bar{F}, \zeta) = 0 \tag{4.3}$$

where ζ represents a set of internal variables and $\bar{F}$ is the image point. In the one-dimensional case, $\bar{F}$ is simply the bounding load magnitude. If we assume that both the current load and the bounding load are centred at the origin, the image point may be expressed through a simple mapping rule

$$\bar{F}(F, \lambda) = \lambda F = \frac{1}{\delta} F \tag{4.4}$$

where λ is the load parameter varying from infinity (when the current load is zero) to unity (when the current load is equal to the image point) and δ is the ratio between current load and the image point, varying from zero (when the current load is zero) to unity (when the current load is equal to the image point). The relationship between F and $\bar{F}$ expressed in Equation 4.4 is referred to as radial mapping. Since the evolution of internal variables is controlled by a function that only depends on the distance between the current load and the image point, Equation 4.3 may be written as

$$G(\bar{F}, \lambda) = 0 \tag{4.5}$$

The evolution of plastic displacements is given by the plastic flow rule

$$\dot{d}^{pl} = \dot{\gamma}\ sign(F) \tag{4.6}$$

where the plastic multiplier γ is zero during elastic response and greater than zero during plastic response. The hardening rule may be expressed as

$$\dot{\lambda} = \dot{\gamma}\mu \tag{4.7}$$

where μ is the hardening parameter. The consistency condition

$$\dot{\gamma}\dot{G} = 0 \tag{4.8}$$

ensures that the image point always coincides with the bounding load. It then follows that

$$\dot{G}(\bar{F}, \lambda) = \frac{\partial G}{\partial \bar{F}} \left(\frac{\partial \bar{F}}{\partial F} \frac{\partial F}{\partial t} + \frac{\partial \bar{F}}{\partial \lambda} \frac{\partial \lambda}{\partial t} \right) = 0 \implies \lambda \dot{F} + F \dot{\gamma} \mu = 0 \tag{4.9}$$

Solving for $\dot{\gamma}$ gives

$$\dot{\gamma} = -\frac{\lambda \dot{F}}{F \mu} = -\frac{\lambda}{\mu F\, sign(F)} \dot{F}\, sign(F) = -\frac{1}{K^{pl}} \dot{F}\, sign(F) \tag{4.10}$$

and the plastic modulus is expressed as

$$K^{pl} = -\frac{\mu}{\lambda} F\ sign(F) \tag{4.11}$$

In conventional rate-independent plasticity, the hardening parameter μ must be defined explicitly in order to obtain the plastic modulus. Here, it is only required that the plastic modulus is (1) a function of λ (or δ) , (2) is infinite during the initial elastic response, (3) vanishes on the bounding point and (4) varies monotonically between the extremes.

Several researches [163, 164, 172] have used the expression

$$K^{pl}(\delta) = K_0^{pl} \ln \left(\frac{1}{\delta} \right) \tag{4.12}$$

to describe monotonic loading for both shallow and deep foundations, where K_0^{pl} is a calibration parameter. In order to completely describe the cyclic behaviour of foundations, it is necessary to distinguish between virgin loading (backbone curve), reloading and unloading. Chatzigogos et al. [163, 164] used the expression

$$K^{pl}(\lambda, \lambda_{min}) = K_0^{pl} \ln \left[\left(\frac{\lambda}{\lambda_{min}} \right)^{n_r} \lambda \right] \tag{4.13}$$

to represent a slightly less plastic behaviour during reloading for shallow foundations. Here, λ_{min} is the minimum load parameter obtained during the previous loading steps and n_r is a calibration parameter. However, unloading was described as purely elastic (which is not a realistic assumption for cyclic pile response). Correia [171] and Correia and Pecker [172] simulated the cyclic behaviour of a laterally loaded pile using

$$K^{pl}(\delta_1, \delta_2) = K_0^{pl} \left[\ln \left(\frac{1}{\delta_1} \right) + \ln \left(\frac{1}{\delta_2} \right)^{n_{ur}} \right] \tag{4.14}$$

for both unloading and reloading. Here, δ_1 is the ratio between the first loading surface and the bounding surface, δ_2 is the ratio between second loading surface and the virgin loading surface and n_{ur} is a calibration parameter. Equation 4.14 implies that when the current load reaches the virgin loading surface ($\delta_2 = 1$), the expression reduces to Equation 4.12 and the plastic modulus obtained at the last virgin load state is retrieved. The advantage of this formulation is that (1) unloading is inelastic, (2) there is a smooth transition between unloading and reloading and (3) overshooting is avoided at the virgin loading surface. However, this approach produces unrealistically soft behaviour upon partial reloading, especially as the second loading surface expands near the virgin loading surface. In this study, unloading and reloading are formulated using a different approach, and the formulations depend on the force-displacement relationship. A complete description of the plastic modulus evolution is given in the following sections.

The solution scheme is expressed in terms of normalized forces, displacements and stiffness values, i.e.,

$$H_n = \frac{H}{H_{fail}}, \quad K_{H,n}^{el} = \frac{K_H^{el} d_p}{H_{fail}}, \quad w_n = \frac{w}{d_p} \tag{4.15a}$$

$$V_n = \frac{V}{V_{fail}}, \quad K_{V,n}^{el} = \frac{K_V^{el} d_p}{V_{fail}}, \quad u_n = \frac{u}{d_p} \tag{4.15b}$$

where H is the transverse load, V is the axial load, w is the transverse displacement, u is the axial displacement, H_{fail} and V_{fail} are the ultimate (bounding) loads, K^{el} is the initial, elastic stiffness, n indicates a normalized value and d_p is the pile diameter.

4.3.2 Plastic modulus evolution for transverse response

For one-dimensional plasticity problems where displacements are decomposed as expressed in Equation 4.1, the normalized tangent stiffness is given as

$$K_{H,tan,n} = \frac{K^{el}_{H,n} K^{pl}_{H,n}}{K^{el}_{H,n} + K^{pl}_{H,n}} \tag{4.16}$$

If $K^{pl}_{H,n}$ is infinite, $K_{H,tan,n}$ reduces to the normalized, elastic stiffness $K^{el}_{H,n}$. If $K^{pl}_{H,n}$ is zero, $K_{H,tan,n}$ is also zero. In essence, the formulation of a bounding plasticity model condenses into determining the evolution of the plastic modulus between the initial, elastic load (where the tangent stiffness is equal to the elastic stiffness) and the ultimate load (where the tangent stiffness is zero). In order to correctly represent the evolution of the plastic modulus within the framework of the presented macro-element, it is necessary to distinguish between virgin loading, unloading and reloading.

Virgin loading is described by the mapping rule

$$\lambda H_n = 1 \tag{4.17}$$

such that

$$\delta_1 = \frac{1}{\lambda} \tag{4.18}$$

The plastic modulus is expressed as

$$K^{pl}_{H,v,n}(\delta_1) = K^{pl}_{0,H,n} \ln\left(\frac{1}{\delta_1}\right) \tag{4.19}$$

where $K^{pl}_{0,H,n}$ is a calibration parameter.

Reloading is described by a different mapping rule. In addition to the current loading point and the image point, it is also necessary to keep track of the virgin loading point and the loading point associated with the last initial unloading and reloading state. Figure 4.2 shows a schematic representation of loading points for

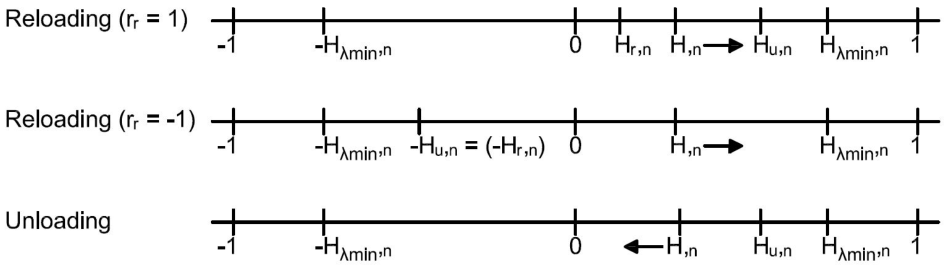

Figure 4.2: Schematic sketch of transverse loading points for reloading and unloading

reloading and unloading. Note that we need to separate between reloading in the direction of the last initial unloading point and reloading in the opposite direction of the last initial unloading point. This may be achieved through the parameter

$$r_r = sign(H_{u,n} H_n) \tag{4.20}$$

where $H_{u,n}$ is the last initial unloading point. To the authors knowledge, this parameter was first introduced by Correia [171]. The image point and the virgin loading point are given by

$$\lambda H_n = 1, \quad \lambda_{min} H_{\lambda_{min},n} = 1 \tag{4.21}$$

where λ_{min} is the load parameter associated with the virgin loading point. The reloading point is expressed as

$$r_r \lambda_r H_{r,n} = 1 \tag{4.22}$$

where $H_{r,n}$ and λ_r are the load and load parameter associated with the last initial reloading point. If r_r is positive, reloading is in the same direction as the last initial unloading point. Otherwise, it is in the opposite direction. Note that if r_r is negative, the last initial reloading point and the last initial unloading point represent the same loading point.

If δ_2 is the ratio between the second loading point and the virgin loading point (as defined by Correia [171] and Correia and Pecker [172]), δ_2 is expressed as

$$\delta_2 = \frac{|H_n - H_{r,n}|}{|H_{\lambda_{min},n} - H_{r,n}|} = \frac{\left|\dfrac{1}{\lambda} - \dfrac{r_r}{\lambda_r}\right|}{\left|\dfrac{1}{\lambda_{min}} - \dfrac{r_r}{\lambda_r}\right|} = \frac{\dfrac{\lambda_r - \lambda r_r}{\lambda \lambda_r}}{\dfrac{\lambda_r - \lambda_{min} r_r}{\lambda_{min} \lambda_r}} = \frac{\lambda_{min}(\lambda_r - \lambda r_r)}{\lambda(\lambda_r - \lambda_{min} r_r)} \tag{4.23}$$

As mentioned, this formulation may yield somewhat soft response for partial reloading. In this study, we propose to redefine δ_2 as the similarity ratio between the second loading point and the *virgin loading point span*, i.e,

$$\delta_2 = \frac{|H_n - H_{r,n}|}{|2H_{\lambda_{min},n}|} = \frac{\left|\dfrac{1}{\lambda} - \dfrac{r_r}{\lambda_r}\right|}{\left|\dfrac{2}{\lambda_{min}}\right|} = \frac{\lambda_{min}(\lambda_r - \lambda r_r)}{2\lambda\lambda_r} \tag{4.24}$$

The plastic modulus is then obtained as

$$K^{pl}_{H,ur,n}(\delta_2) = K^{pl}_{0,H,n}\left[\ln\left(\frac{1}{\delta_{max}}\right) + \ln\left(\frac{1}{\delta_2}\right)^{n_{ur,H}}\right] \tag{4.25}$$

where $n_{ur,H}$ is a calibration parameter, δ_2 is given by Equation 4.24 and δ_{max} is the similarity ratio corresponding to the virgin loading point.

Unloading is also described by an unique mapping rule. The image point and the virgin loading point are now located on opposite sides such that

$$-\lambda H_n = 1, \quad \lambda_{min}H_{\lambda_{min},n} = 1 \tag{4.26}$$

The unloading point is mapped as

$$-\lambda_u H_{u,n} = 1 \tag{4.27}$$

where λ_u is the load parameter associated with the last initial unloading point. If δ_2 is the ratio between the second loading point and the virgin loading point, then

$$\delta_2 = \frac{|H_n - H_{u,n}|}{|H_{\lambda_{min},n} - H_{u,n}|} = \frac{\left|\dfrac{-1}{\lambda} + \dfrac{1}{\lambda_u}\right|}{\left|\dfrac{1}{\lambda_{min}} + \dfrac{1}{\lambda_u}\right|} = \frac{\dfrac{\lambda - \lambda_u}{\lambda\lambda_u}}{\dfrac{\lambda_{min} + \lambda_u}{\lambda_{min}\lambda_u}} = \frac{\lambda_{min}(\lambda - \lambda_u)}{\lambda(\lambda_{min} + \lambda_u)} \tag{4.28}$$

This expression applies only if δ_2 for reloading is defined by Equation 4.23. Otherwise, the plastic modulus becomes discontinuous at the point of zero loading. Instead, we redefine δ_2 similar to reloading, i.e.,

$$\delta_2 = \frac{|H_n - H_{u,n}|}{|2H_{\lambda_{min},n}|} = \frac{\left|\dfrac{-1}{\lambda} + \dfrac{1}{\lambda_u}\right|}{\left|\dfrac{2}{\lambda_{min}}\right|} = \frac{\lambda_{min}(\lambda - \lambda_u)}{2\lambda\lambda_u} \tag{4.29}$$

and use Equation 4.25 to compute the plastic modulus.

The formulation presented above completely describes the evolution of the plastic modulus for arbitrary transverse loading. There are, however, some features of the formulation that should be noted:

1. Equations 4.24 and 4.25 imply that the transition from reloading to virgin loading is smooth only when unloading from virgin loading (closed-loop cycles). For partial unloading/reloading cycles, the plastic modulus is discontinuous in transition from reloading to virgin loading.

2. Since the explicit description of loading points (δ_1 and δ_2) is limited to two, overshooting is only avoided at the virgin loading point.

3. At the point of zero loading, λ is infinite. It then observed that both Equation 4.24 and Equation 4.29 reduce to

$$\delta_2 = \frac{\lambda_{min}}{2\lambda_u} \tag{4.30}$$

   since λ_r is equal to λ_u when r_r is negative, implying that the plastic modulus is continuous at the transition between unloading and reloading.

Transverse-rotational coupling is implicitly introduced using modification factors for H_n and $K^{el}_{H,n}$. It should be noted that macro-elements may be considered as multi-directional, nonlinear springs, where the yield surface is defined as a combination of forces and moments. For the presented macro-element formulation, that implies a two-dimensional, pre-defined failure surface (moment and transverse force). The formulation is then limited by the fact that every combination of pile and soil profile requires an unique determination of the failure surface, which can be a cumbersome task. However, if the transverse-rotational coupling is formulated implicitly, there is no need for a complete description of a failure surface, only a limited set of failure loads. Hence, the reason for describing coupling implicitly is to allow for unrestricted calibration procedures without the need for pre-defined failure surfaces.

The following expressions for the modification factors are proposed:

$$\frac{\gamma_\theta}{\gamma_w} \geq 0: \quad \zeta_H = 1 - \left[(1 - n_{w\theta,1})\frac{\gamma_\theta}{\gamma_w}\right] \geq n_{w\theta,2} \tag{4.31a}$$

$$\zeta_K = 1 - \left[(1 - n_{w\theta,1})\frac{\gamma_\theta}{\gamma_w}\right] \tag{4.31b}$$

$$-1 \leq \frac{\gamma_\theta}{\gamma_w} < 0: \quad \zeta_H = 1 \tag{4.31c}$$

$$\zeta_K = 1 \tag{4.31d}$$

$$\frac{\gamma_\theta}{\gamma_w} < -1: \quad \zeta_H = \left|\frac{\gamma_w}{\gamma_\theta}\right| + \left(1 - \left|\frac{\gamma_w}{\gamma_\theta}\right|\right) |n_{w\theta,2}| \tag{4.31e}$$

$$\zeta_K = \left|\frac{\gamma_\theta}{\gamma_w}\right| \tag{4.31f}$$

where

$$\gamma_w = \frac{\Delta w}{w_{fail}}, \quad \gamma_\theta = \frac{\Delta \theta}{\theta_{free}}, \quad n_{w\theta,1} = \frac{H_{free}}{H_{fail}} > 0, \quad n_{w\theta,2} = \frac{H_{fail,rot}}{H_{fail}} < 0 \tag{4.32}$$

Here, Δw is the current displacement increment, $\Delta\theta$ is the current rotation increment, w_{fail} is the displacement at failure for a fixed-head pile, θ_{free} is the rotation of a free-head pile at w_{fail}, H_{free} is the transverse load of a free-head pile at w_{fail} and $H_{fail,rot}$ is the failure load for pure rotation. Figure 4.3 shows a plot of the modification factors plotted against the ratio γ_θ/γ_w for typical load ratios. The following should be noted:

1. For $\gamma_\theta/\gamma_w \geq 0$:
   (a) When γ_θ/γ_w is small, then $\zeta_H = \zeta_K = 1$. The plastic modulus equals fixed-head conditions.
   (b) When $\gamma_\theta/\gamma_w = 1$, then $\zeta_H = \zeta_K = n_{w\theta,1}$. The plastic modulus equals free-head conditions.
   (c) When γ_θ/γ_w is large, then ζ_H is a negative number restricted by $n_{w\theta,2}$ and ζ_K is an arbitrarily large, negative number. The plastic modulus equals pure rotation conditions.

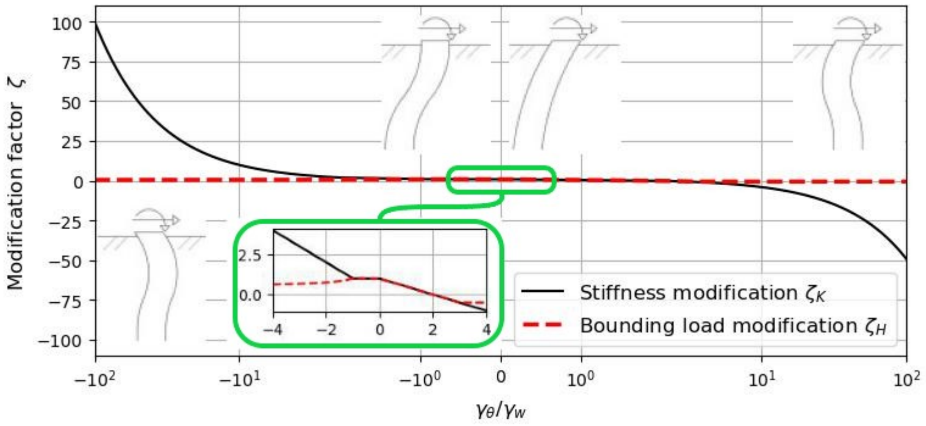

Figure 4.3: Implicit transverse-rotational modification factors. $n_{w\theta,1} = 0.5$ and $n_{w\theta,2} = -0.5$

2. For $-1 \leq \gamma_\theta/\gamma_w < 0$, then $\zeta_H = \zeta_K = 1$. The plastic modulus equals fixed-head conditions. It is assumed that when $\gamma_\theta/\gamma_w = -1$, transverse loads are mainly caused by transverse displacements.

3. For $\gamma_\theta/\gamma_w < -1$:

   (a) When $|\gamma_\theta/\gamma_w| \approx 1$, then $\zeta_H = \zeta_K = 1$. The plastic modulus equals fixed-head conditions.

   (b) When $|\gamma_\theta/\gamma_w|$ is large, then $\zeta_H = n_{w\theta,2}$ and ζ_K is a large number. The plastic modulus equals pure rotation conditions.

4.3.3 Plastic modulus evolution for axial response

Similar to transverse loading, it is necessary to distinguish between virgin loading, unloading and reloading. In addition, axially loaded concrete piles behave differently in tension and compression.

Virgin loading in tension is described similar to transverse response. In compression, the response is mainly elastic until a cut-off load $V_{el,n}$ is reached. For this range, it is proposed that the plastic modulus varies as

$$K^{pl}_{V,vc,n}(\delta_1) = K^{pl}_{0,V,n}\left[\left(1-\frac{\delta_1}{\delta_{el}}\right)\ln\left(\frac{1}{\delta_{int}}\right)+\left(\frac{\delta_1}{\delta_{el}}\right)\ln\left(\frac{1}{\delta_1}\right)\right] \tag{4.33}$$

where δ_{el} is the similarity ratio between the cut-off load and the bounding load, δ_{int} is the similarity ratio between an initial, infinitesimal load and the bounding load and $K^{pl}_{0,V,n}$ is a calibration parameter. Once the cut-off load is exceeded, the plastic modulus varies as

$$K^{pl}_{V,vc,n}(\delta_1) = K^{pl}_{0,V,n} \ln\left(\frac{1}{\delta_1}\right) \tag{4.34}$$

Reloading is also defined separately for compression and tension. The similarity ratio δ_2 is defined as for transverse response, but the variation of the plastic modulus differs in tension and compression. In tension, the plastic modulus varies with Equation 4.25 (with axial parameters). In compression, it is suggested that the plastic modulus is infinite when reloading is in the direction of the last initial unloading point ($r_r = 1$) and

$$\begin{aligned} K^{pl}_{V,rc,n}(\delta_2) =& K^{pl}_{0,V,n}\left[\left(\ln\left(\frac{1}{\delta_{max}}\right) + \ln\left(\frac{1}{\delta_2}\right)^{n_{ur}}\right)\delta_u^{n_{r,V}}\right. \\ & \left. + \ln\left(\frac{1}{\delta_{int}}\right)\left(1-\delta_u^{n_{r,V}}\right)\right] \end{aligned} \tag{4.35}$$

when reloading in the opposite direction of the last initial unloading point ($r_r = -1$). Here, δ_u is similarity ratio for the last unloading point and $n_{r,V}$ is a calibration parameter.

Unloading is also defined separately for compression and tension. The similarity ratio δ_2 is defined as for transverse response. In tension, the plastic modulus varies with Equation 4.25 (with axial parameters). In compression, unloading is mainly elastic and the plastic modulus is infinitely high. The following features of the formulation should be noted:

1. When virgin loading starts, δ_1 is low and the plastic modulus expressed in Equation 4.33 reduces to

$$K^{pl}_{V,vc,n} = K^{pl}_{0,V,n} \ln\left(\frac{1}{\delta_{int}}\right) \tag{4.36}$$

The initial parameters λ_{int} and δ_{int} are infinite and zero only in a theoretical sense. Numerically, λ_{int} is an arbitrary large number and δ_{int} is an arbitrary small number that need to be predefined in the numerical scheme. Simulations using programming language Python 3 [225] show that

$$\lambda_{int} = 10^{(O+12)}, \quad \delta_{int} = \frac{1}{\lambda_{int}} \tag{4.37}$$

where

$$O = \log^{10}(K^{el}_{V,v,n}) \tag{4.38}$$

is a good approximation with respect to desired behaviour and numerical stability. Hence, Equation 4.36 represents a relatively high plastic modulus, which through Equation 4.16 (with axial parameters) gives a tangent stiffness value approximately equal to the initial, elastic stiffness. As the load reaches the cut-off load, i.e. when δ_1 is equal to δ_{el}, Equation 4.33 reduces to Equation 4.34, implying that the plastic modulus is continuous throughout virgin loading.

2. When unloading in compression, the plastic modulus is given by Equation 4.36 and the tangent stiffness approximately equals the elastic stiffness.

3. When reloading in compression after unloading from tension ($r_r = -1$), and the last unloading point in tension is equal to the bounding load ($\delta_u = 1$), Equation 4.35 reduces to Equation 4.25 (with axial parameters). In that case, the plastic modulus is continuous at the transition between unloading and reloading since unloading from tension is also described by Equation 4.25. However, when the last unloading point in tension is near zero (δ_u is a small number), Equation 4.35 reduces to Equation 4.36 and the reloading path equals the unloading path. The calibration parameter $n_{r,V}$ may be considered as a parameter that controls the transition between unloading in tension and reloading in compression between the above-mentioned extremes. When reloading in compression after unloading from compression ($r_r = 1$), the plastic modulus is always defined by Equation 4.36.

4.3.4 Calibration

As mentioned earlier, the developed macro-element does not require pre-defined failure surfaces or other parameters and may be calibrated using any type of non-linear pile-soil model. Vertical pile models may be used for batter piles assuming realistic batter angles up to approximately 15 degrees. There are in total 14 parameters that must be determined. Nine parameters, namely H_{fail}, K^{el}_H, w_{fail}, θ_{free}, H_{free}, H_{rot}, V_{fail}, V_{el} and K^{el}_V, are directly retrieved from the calibration analysis. They may also be taken from closed-form solutions for simple soil profiles. The remaining five parameters ($K^{pl}_{0,H}$, $n_{ur,H}$, $K^{pl}_{0,V}$, $n_{ur,V}$, $n_{r,V}$) are obtained by matching the area enclosed by the load path using the macro-element with the corresponding results from the calibration analysis. The parameters are summarized in Table 4.1. The given values represent the pile-soil system evaluated in the following sections. The parameters may be determined through the following steps:

Table 4.1: Calibration parameters

Transverse		
H_{fail}	955.3 kN	Transverse, fixed-head failure load.
H_{free}	510.4 kN	Transverse, free-head load at w_{fail}.
H_{rot}	-602.6 kN	Transverse failure load for pure rotation.
K_H^{el}	55.7 MN/m	Initial, fixed-head elastic transverse stiffness.
$K_{0,H}^{pl}$	33.4 MN/m	Transverse, fixed-head plastic modulus constant.
w_{fail}	100 mm	Transverse displacement at H_{fail}
θ_{free}	0.022 rad	Rotation at w_{fail} for free-head conditions.
$n_{ur,H}$	0.8	Controls transverse unloading/reloading.
Axial		
V_{fail}	4332.0 kN	Axial failure load.
V_{el}	-2000.0 kN	Axial elastic/plastic cut-off load.
K_V^{el}	320.3 MN/m	Initial, elastic axial stiffness.
$K_{0,V}^{pl}$	128.1 MN/m	Axial plastic modulus constant.
$n_{ur,V}$	0.8	Controls axial unloading/reloading curve shape.
$n_{r,V}$	0.021	Controls unloading/reloading transition.

1. Perform a pushover analysis up to failure for pure transverse pile-head loading with all other degrees of freedom fixed. Determine H_{fail}, w_{fail} and K_H^{el} and $K_{0,H}^{pl}$.

2. Perform an one-cycle analysis up to w_{fail} for pure transverse pile-head loading with all other degrees of freedom fixed. Determine $n_{ur,H}$.

3. Perform a pushover analysis up to w_{fail} for pure transverse loading for a free-head pile. Determine θ_{free} and H_{free}.

4. Perform a pushover analysis up to failure for pure rotational loading with all other degrees of freedom fixed. Determine $H_{fail,rot}$.

5. Perform a pushover analysis up to failure for pure axial pile-head loading in tension with all other degrees of freedom fixed. Determine V_{fail}, K_V^{el} and $K_{0,V}^{pl}$.

6. Perform a pushover analysis up to failure for pure axial pile-head loading in compression with all other degrees of freedom fixed. Determine V_{el}.

7. Perform a two-cycle analysis up to u_{max} for pure axial pile-head loading with all other degrees fixed. Determine $n_{ur,V}$ and $n_{r,V}$.

4.3.5 Validation

The single pile macro-elements are validated in this section against the finite element model presented in Sections 2.2 and 4.2 for various loading conditions. The numerical implementation of the macro-element is presented in Section 5.2.2.

Transverse response

Transverse response is shown in Figures 4.4 and 4.5. Figure 4.4(a) shows the cyclic response when rotation is fixed. Virgin loading, unloading and reloading are well defined in a global sense, but there are minor pinching effects caused by the concrete material model that are not fully captured by the macro-element. Figure 4.4(b) shows the cyclic response for a combination of in-phase transverse displacements and rotations corresponding to a free-head pile, i.e. when $\gamma_\theta/\gamma_w = 1$. The stiffness and bounding load reduction are well captured. Figure 4.4(c) shows the cyclic response for transverse out-of-phase displacements and rotations. Compared to the case with fixed rotation shown in Figure 4.4(a), the transverse response is only slightly altered. Hence, the assumption that transverse loads are mainly caused by transverse displacements when $\gamma_\theta/\gamma_w = -1$ seems reasonable. Figure 4.4(d) shows that small displacements with fixed rotation are well captured. Figure 4.4(e) shows in-phase small displacements and relatively large rotations. It is observed that transverse forces are negative when transverse displacements are positive. In this case, γ_θ/γ_w is relatively large and rotations also contribute to the generation of transverse forces. When displacements and rotations are in phase, rotations cause negative transverse forces. Figure 4.4(f) shows out-of-phase small displacements and rotations. In this case, rotations cause positive transverse forces. The results in Figure 4.4 show that the implicit transverse-rotational coupling factors expressed in Equations 4.31 and 4.32 are able to modify stiffness and bounding load quite accurately for most combinations of displacements and rotations. Figure 4.4 also shows that the transition from reloading to virgin loading is smooth for closed-loop cycles and that the transition from unloading to reloading (point of zero loading) is smooth. Figures 4.4(d) and 4.4(e) demonstrate that the macro-element is capable of capturing cyclic behaviour for small transverse displacements. However, it is emphasized that the macro-element is not able to simulate frequency-dependent radiation damping, which becomes more important with decreasing displacement amplitudes.

Figure 4.5(a) shows one partial loading cycle. In addition to comparison with

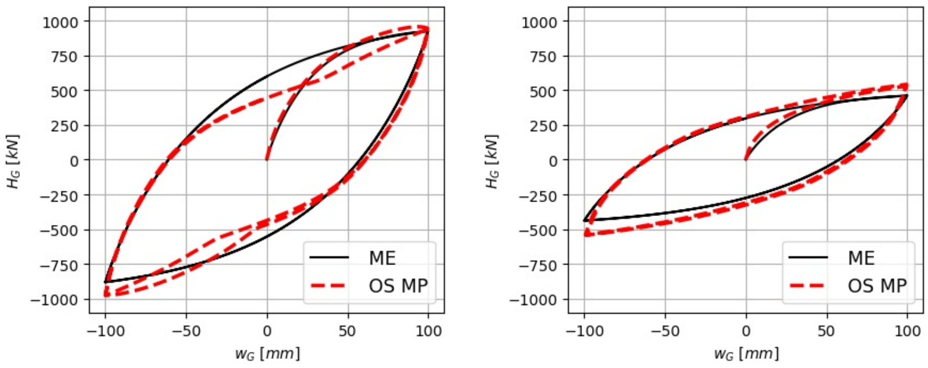

(a) Large cycles, fixed rotation

(b) Large cycles, rotation in phase

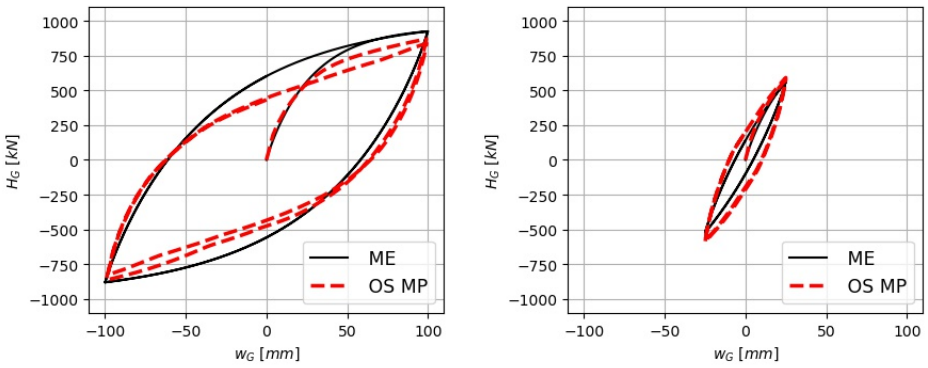

(c) Large cycles, rotation out of phase

(d) Small cycles, rotation fixed

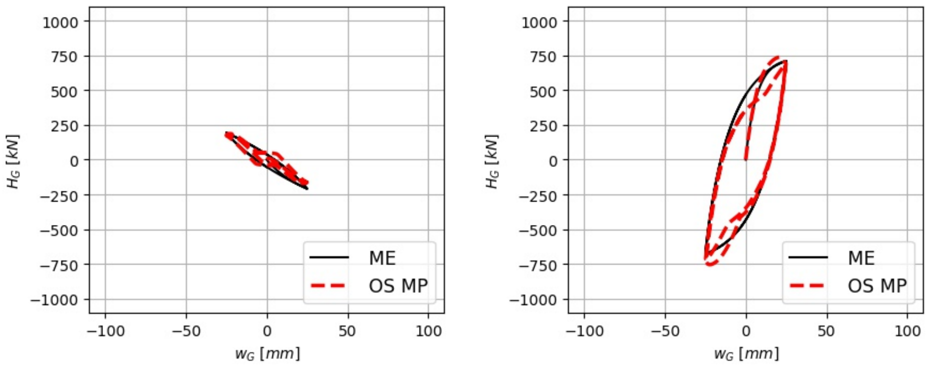

(e) Small cycles, rotation in phase

(f) Small cycles, rotation out of phase

Figure 4.4: Comparison of macro-element and OpenSees MP. Transverse load-displacement relationship. Symmetric response

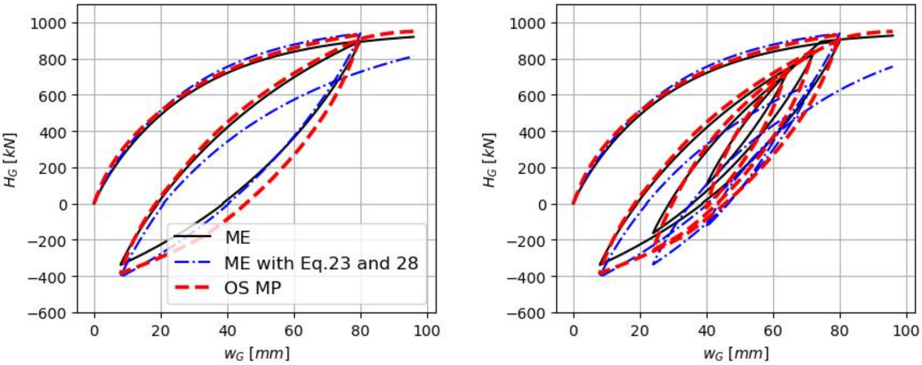

(a) One partial cycle **(b)** Three partial cycles

Figure 4.5: Comparison of macro-element and OpenSees MP. Transverse load-displacement relationship. Asymmetric response

the finite element model, the macro-element is demonstrated using δ_2 defined by Equations 4.23 and 4.28. In this case, it is clear that δ_2 defined by Equations 4.24 and 4.29 produce more accurate behaviour, especially as the load approaches the virgin loading point. Figure 4.5(a) also shows that even though the plastic modulus is discontinuous in transition from reloading to virgin loading, the behaviour is still very close to the finite element model. This behaviour is supported by the findings in *The Pile Soil Analysis* (PISA) Project [176, 226], where design procedures for OWT monopiles were addressed through numerous medium scale field tests. Figure 4.5(b) shows multiple partial loading cycles. The macro-element is generally able to capture this behaviour fairly well, but is should be emphasized that overshooting is only avoided at the virgin loading point. However, this error mainly occurs in the vicinity of the virgin loading point with small magnitude. As for the case with one partial loading cycle, using δ_2 defined by Equations 4.24 and 4.29 produces better results compared to Equations 4.23 and 4.28.

Axial response

Axial response is shown in Figure 4.6. Figures 4.6(a) and 4.6(d) show that cyclic loading with large amplitudes is well simulated. Note that the macro-element is able to capture complex features such as (1) the highly elastic response for virgin loading and unloading and in compression (2) the abrupt stiffness change passing the cut-off load in compression. Figures 4.6(b) and 4.6(e) show that the behaviour under small displacements is also well captured. As for transverse response, it should be noted that the macro-element is not able to simulate frequency-

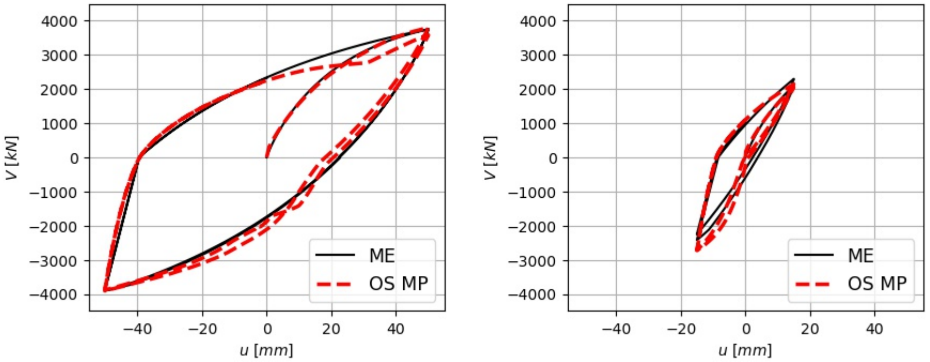

(a) Large cycle, virgin in tension

(b) Small cycle, virgin in tension

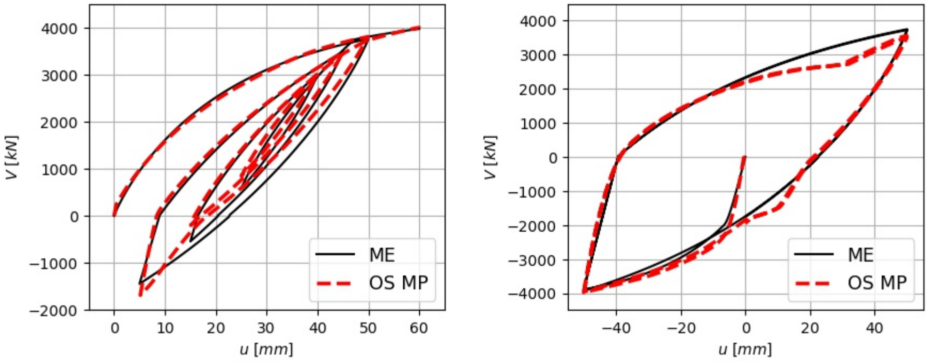

(c) Partial cycles, virgin in tension

(d) Large cycle, virgin in compression

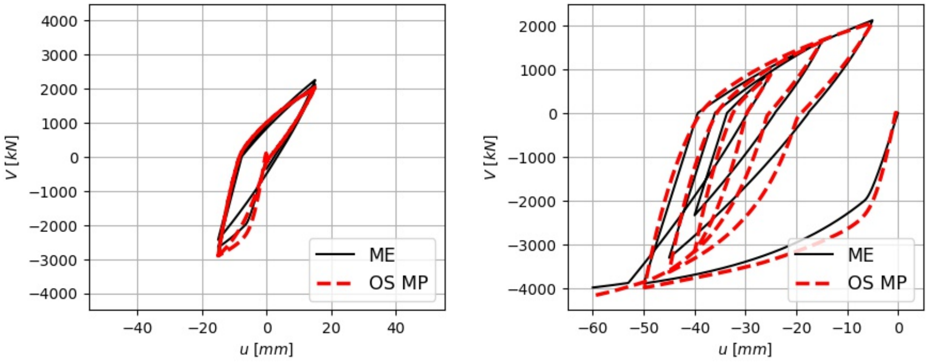

(e) Small cycle, virgin in compression

(f) Partial cycles, virgin in compression

Figure 4.6: Comparison of macro-element versus OpenSees MP. Axial load - displacement relationship.

dependent radiation damping. Figures 4.6(c) and 4.6(f) show that partial loading is fairly well represented, admittedly with some inaccuracy. Most importantly, Figure 4.6(f) shows that Equation 4.35 is able to globally capture the transition between unloading in tension and reloading in compression for a variety of unloading points.

The observed axial behaviour in compression is supported by experimental tests reported in the literature. Chen et al. [227] performed a number of cyclic, axial loading tests on pre-stressed concrete pipe piles in soft clay. The load-displacement curves for quasi-static compression tests showed similar trends for virgin loading and unloading as observed in this study. Drbe and El Naggar [228] performed full-scale load tests on micro-piles in cohesive soil. Quasi-static tests for loading, unloading and partial loading in compression showed the same tendency as the results obtained in this study.

4.4 Pile groups

4.4.1 Assembly

The single pile formulations for the individual load-displacement relationships has been presented in the previous sections. This section provides a procedure for establishing a three degree-of-freedom stiffness matrix based on the single pile formulations. The macro-element is validated for a variety of pile configurations, batter angles and soil profiles. It is also demonstrated how the macro-element may be employed to obtain linear-equivalent properties.

With reference to Figure 4.7, the displacement increment of the single pile i is expressed as

$$\Delta \boldsymbol{d_i^l} = \begin{bmatrix} \Delta u_i^l \\ \Delta w_i^l \end{bmatrix} = \boldsymbol{t_i}^T \Delta \boldsymbol{d_i^g} \tag{4.39}$$

where $\boldsymbol{d_i^l}$ is the displacement vector of pile i in local coordinates, $\boldsymbol{t_i}$ is the coordinate transformation matrix and $\boldsymbol{d_i^g}$ is the displacement vector of pile i in global coordinates. The tangent stiffness matrix of a single pile i in global coordinates is expressed as

$$\boldsymbol{K_{S,i}^g} = \boldsymbol{t_i} \boldsymbol{K_{S,i}^l} \boldsymbol{t_i}^T \tag{4.40}$$

where $\boldsymbol{K_{S,i}^g}$ is the tangent stiffness matrix of a single pile i in local coordinates and $k_{S,uu,i}^l$ and $k_{S,ww,i}^l$ are the tangent stiffness values returned by the respective

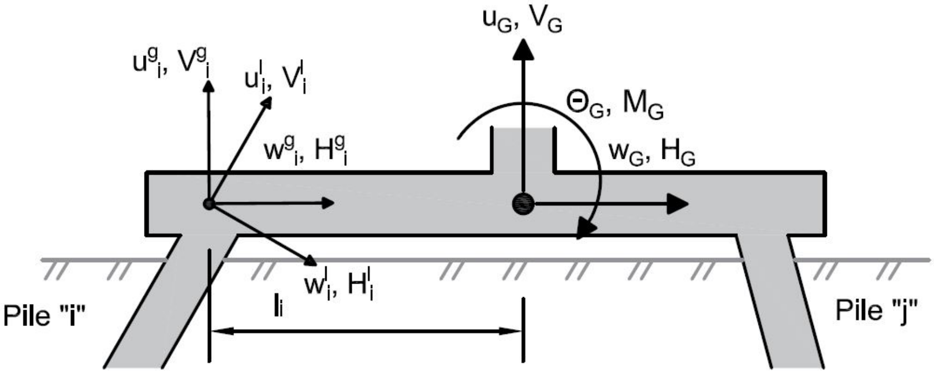

Figure 4.7: Schematic sketch of the pile group stiffness matrix.

single pile formulations. The pile group stiffness matrix is expressed as

$$\boldsymbol{K_G} = \begin{bmatrix} k_{G,uu} & k_{G,uw} & k_{G,u\theta} \\ k_{G,wu} & k_{G,ww} & k_{G,w\theta} \\ k_{G,\theta u} & k_{G,\theta w} & k_{G,\theta\theta} \end{bmatrix} \tag{4.41}$$

The matrix entries in $\boldsymbol{K_G}$ are obtained by enforcing unit displacements and rotations (in turn) and solving the equilibrium equations, i.e.,

$$k_{G,uu} = \sum_{i=1}^{N} k^g_{S,uu,i}, \quad k_{G,wu} = \sum_{i=1}^{N} k^g_{S,wu,i}, \quad k_{G,\theta u} = \sum_{i=1}^{N} k^g_{S,uu,i} l_i \tag{4.42a}$$

$$k_{G,uw} = \sum_{i=1}^{N} k^g_{S,uw,i}, \quad k_{G,ww} = \sum_{i=1}^{N} k^g_{S,ww,i}, \quad k_{G,\theta w} = \sum_{i=1}^{N} k^g_{S,uw,i} l_i \tag{4.42b}$$

$$k_{G,u\theta} = \sum_{i=1}^{N} k^g_{S,uu,i} l_i, \quad k_{G,w\theta} = \sum_{i=1}^{N} k^g_{S,wu,i} l_i, \quad k_{G,\theta\theta} = \sum_{i=1}^{N} k^g_{S,uu,i} l_i^2 \tag{4.42c}$$

where l_i is the distance from the global node to the pile-node i and N is the number of piles. We assume that there is no contact between the pile cap and the soil, i.e. all the forces and moments from the pile cap are transferred through the piles. Note that (1) l_i is set negative when the corresponding pile is located on the right hand side of the global node, (2) the pile-cap rotation is resisted by vertical pile-head loads only and (3) the local nodes are internal element nodes that are not a part of the global solution.

4.4.2 Validation

A 2x1 pile group with vertical piles and $S_0/d_p = 5$ is subjected to harmonic, in-phase horizontal displacements and rotations. The results are shown in Figure 4.8. Figure 4.8(a) shows the results for large displacements and small rotations. Figures 4.8(b) and 4.8(c) show the same results, but with increasing rotation. It is clear that the implicit transverse-rotational coupling modifies horizontal stiffness and bounding load quite accurately in all three cases. The moment-rotation relationships match the finite element model fairly well, but it is evident that the accuracy decreases for small rotations. The same analyses are carried out for a 2x1 pile group with batter piles ($S_0/d_p = 5$ and $\beta = 15°$). The results are shown in Figure 4.9. As for the vertical pile group, the macro-element shows good agreement with the finite element model. The moment-rotation relationships are particularly well captured, but the horizontal load-displacement relationship is somewhat overestimated. Interestingly, the horizontal stiffness of a batter pile group is practically unaffected by rotation. Since the opposite applies for vertical pile groups, the results indicate that batter piles substantially increase horizontal stiffness, especially at large rotations.

Next, a 3x3 pile group with both vertical and batter piles ($S_0/d_p = 5$ and $\beta = 15°$) is subjected to various combinations of horizontal displacements and rotations. The results are shown in Figures 4.10 and 4.11. Figure 4.10(a) shows the results for in-phase large displacements and small rotations. As for the 2x1 pile group with batter piles, the horizontal load-displacement relationship is somewhat overestimated. The same accuracy is observed in Figure 4.10(b) for in-phase large displacements and large rotations. Figures 4.10(c), 4.11(a) and 4.11(b) show that the macro-element is able to capture in-phase small displacements and large rotations, out-of-phase large displacements and small rotations and out-of-phase large displacements and large rotations. Figure 4.11(c) shows that partial loading is captured with approximately the same accuracy as full cycle loading.

One of the limiting assumptions governing the macro-element formulation is that pile-soil-pile interaction is neglected. Figure 4.12(a) shows the results for a 3x3 pile group with $S_0/d_p = 3$ in the direction of loading. The finite element model shows only slightly softer horizontal response compared to the pile groups with $S_0/d_p = 5$ shown in Figure 4.10(b). These results indicate that neglecting pile-soil-pile interaction may be reasonable for pile groups with realistic S_0/d_p-values and soft soil. It is, however, expected that the accuracy will decrease as the soil stiffness and strength increases. In addition, it was suspected that neglecting pile-head moment would decrease the moment-rotation accuracy for close pile spa-

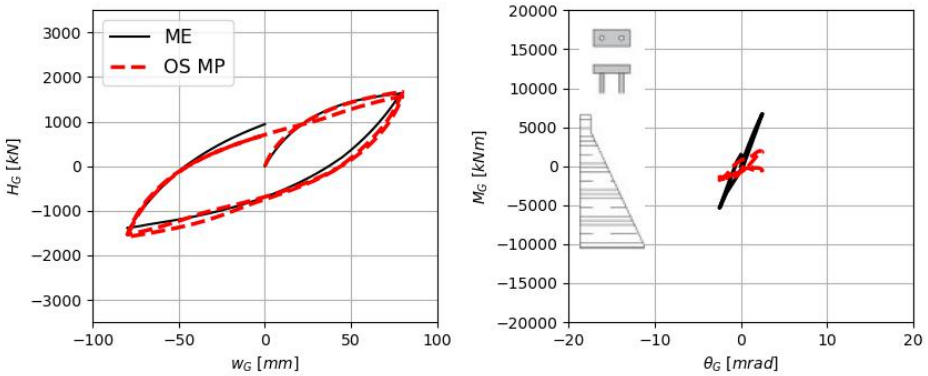

(a) In-phase small rotations

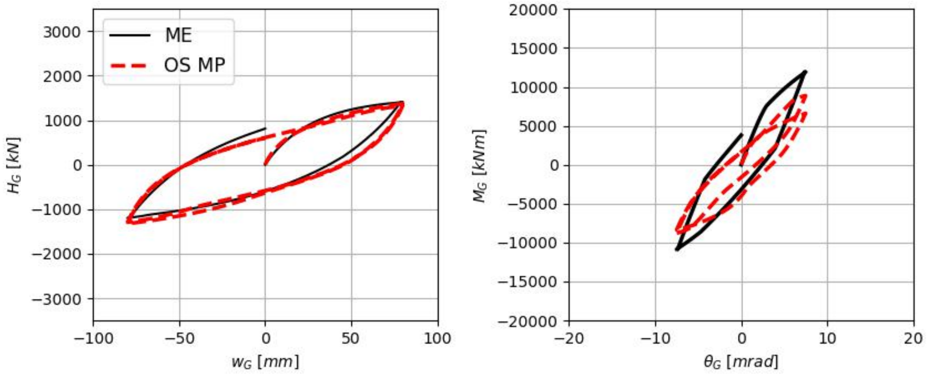

(b) In-phase medium rotations

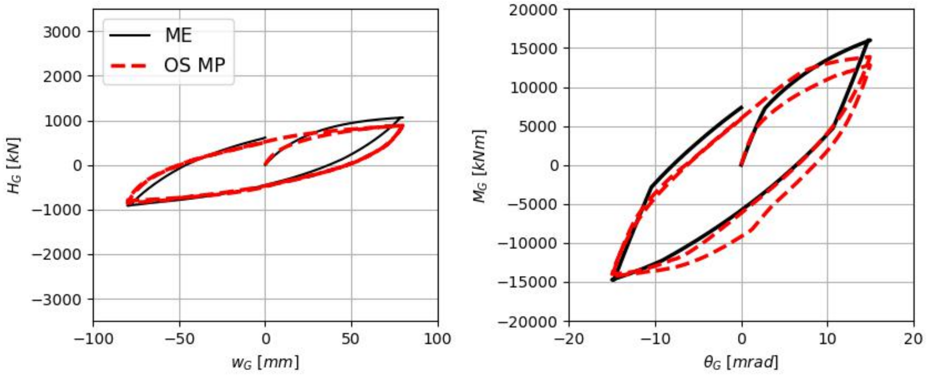

(c) In-phase large rotations

Figure 4.8: Macro-element versus OpenSees MP. 2x1 pile group with vertical piles. $S_0/d_p = 5$

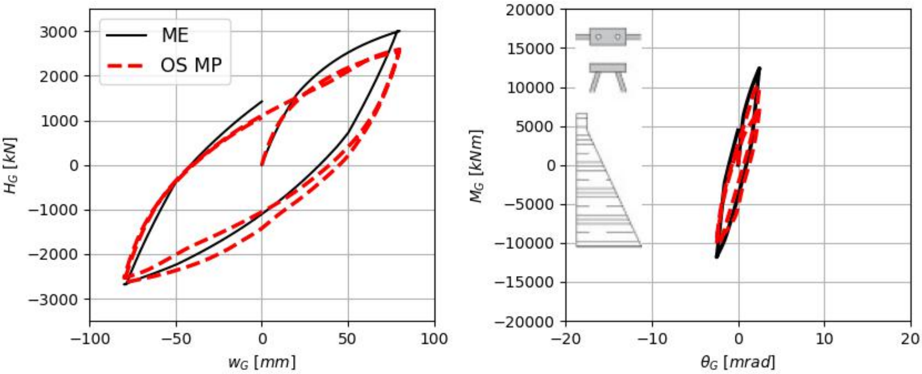

(a) In-phase small rotations

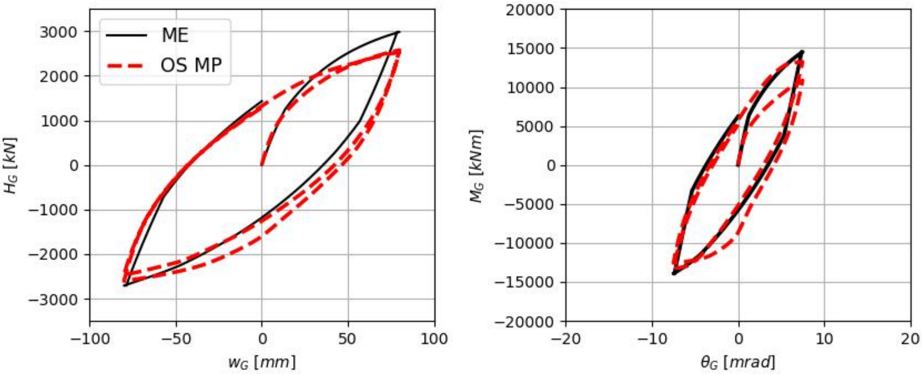

(b) In-phase medium rotations

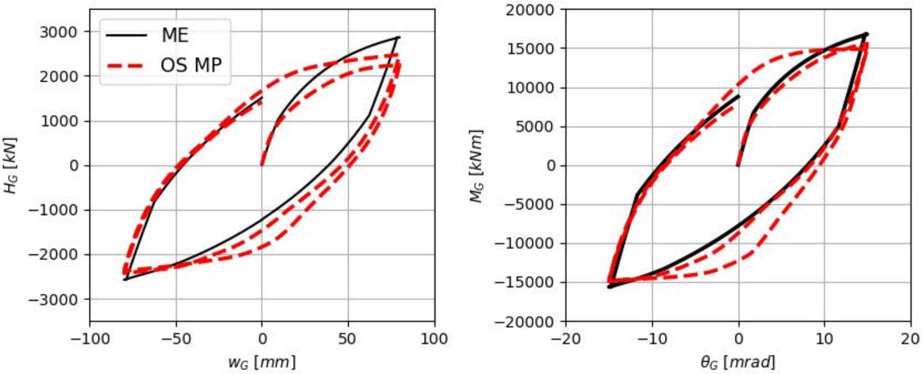

(c) In-phase large rotations

Figure 4.9: Macro-element versus OpenSees MP. 2x1 pile group with batter piles. $S_0/d_p = 5$ and $\beta = 15°$

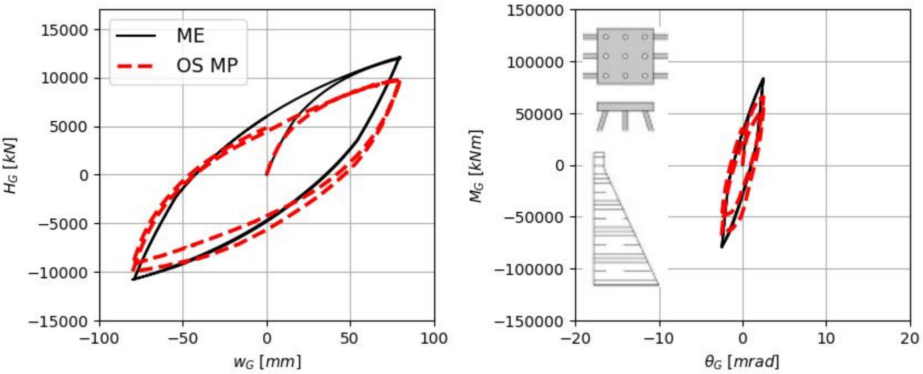

(a) In-phase large displacement and small rotations

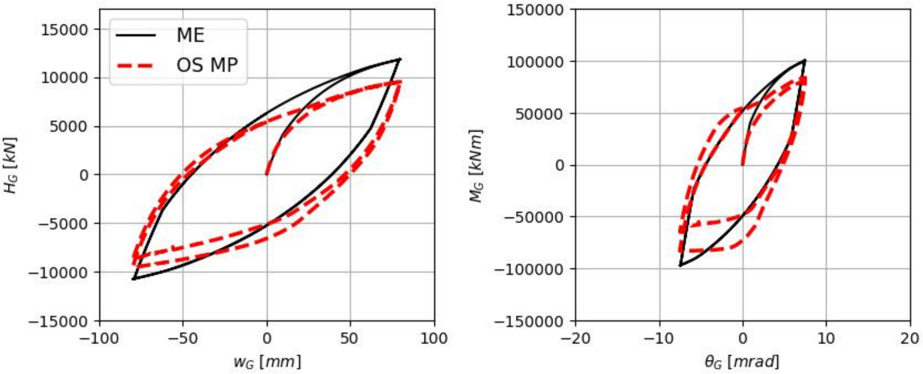

(b) In-phase large displacement and large rotations

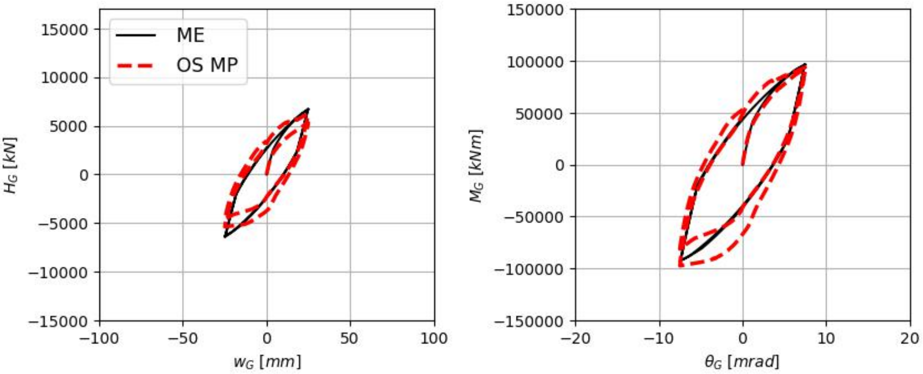

(c) In-phase small displacement and large rotations

Figure 4.10: Macro-element versus OpenSees MP. 3x3 pile group with vertical and batter piles. In-phase displacement and rotations and symmetric loading. $S_0/d_p = 5$ and $\beta = 15°$

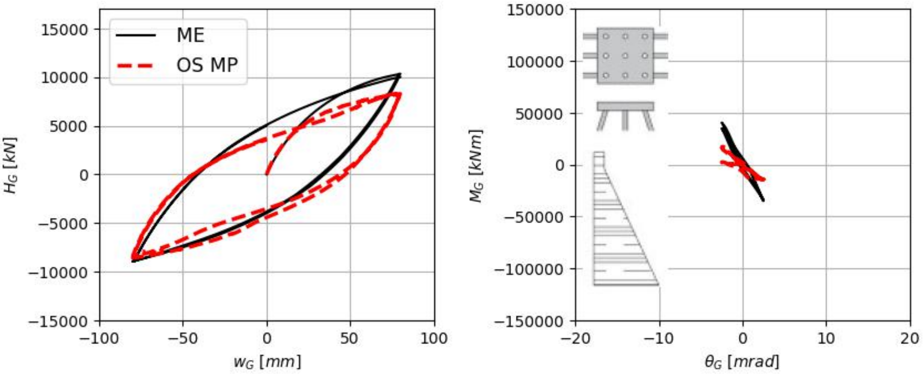

(a) Out-of-phase large displacement and small rotations

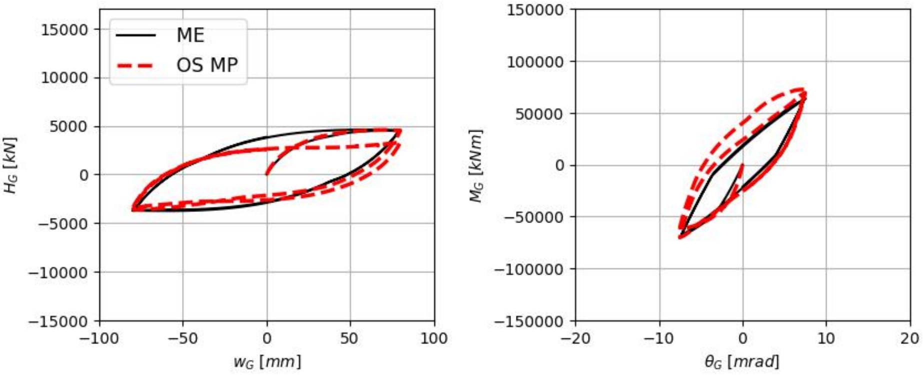

(b) Out-of-phase large displacement and large rotations

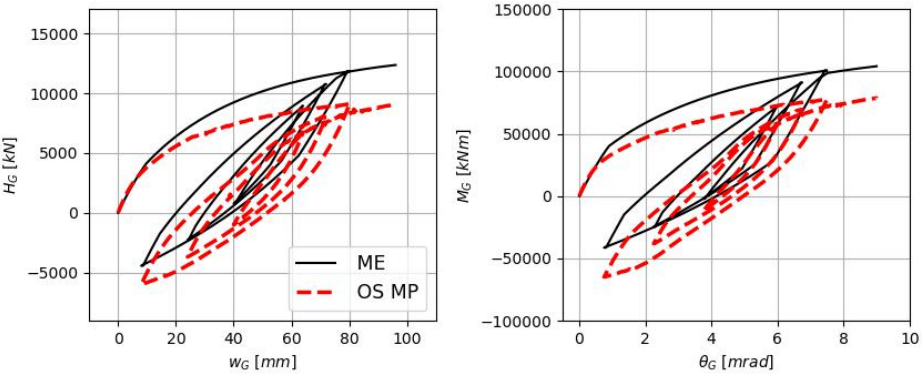

(c) Partial cycles, in-phase displacements and rotations.

Figure 4.11: Macro-element versus OpenSees MP. 3x3 pile group with vertical and batter piles. Out-of-phase displacement and rotations and asymmetric loading. $S_0/d_p = 5$ and $\beta = 15°$

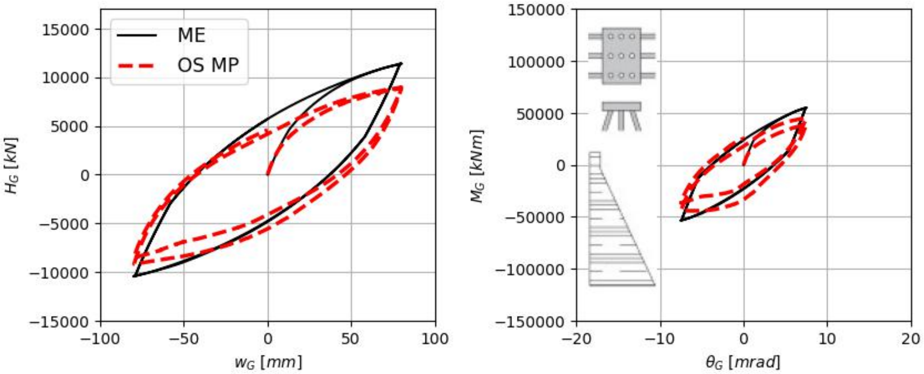

(a) Close pile spacing

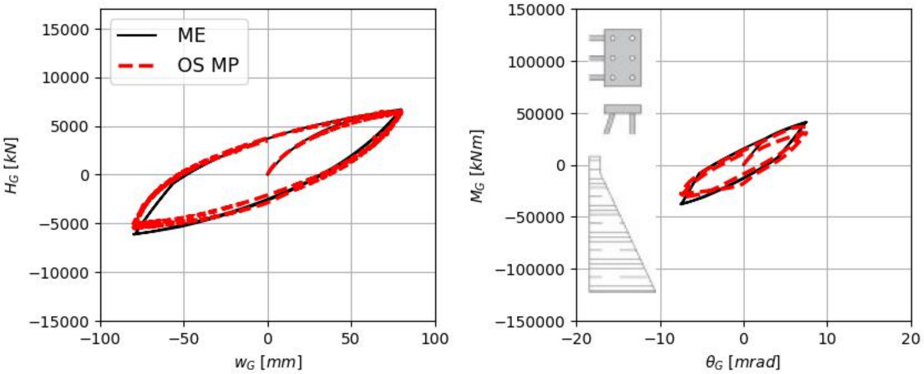

(b) Asymmetric configuration

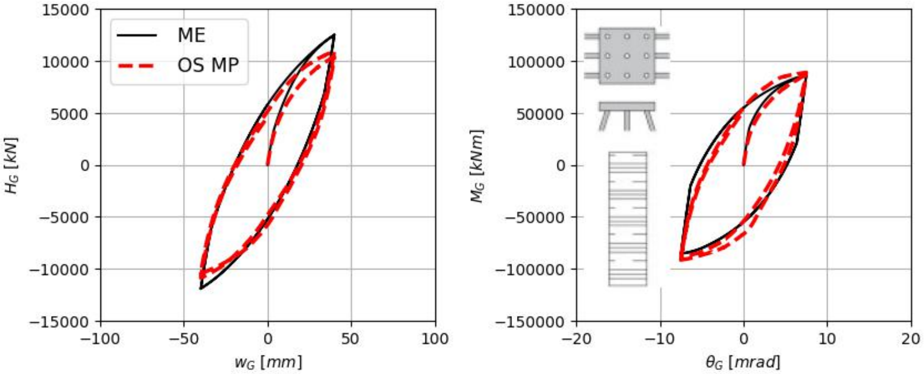

(c) Homogeneous soil profile

Figure 4.12: Macro-element versus OpenSees MP. Different soil profiles and pile group configurations

cing. However, rotation is well captured in this case, and the difference between $S_0/d_p = 3$ and $S_0/d_p = 5$ is evident in Figures 4.12(a) and 4.10(b).

Since the numerical scheme is based on de-coupled, single pile response, the macro-element should not be restricted to symmetric configurations. Figure 4.12(b) shows the results for a 3x2 pile group with asymmetric configuration of batter angles in the direction of loading. The macro-element is in good agreement with the finite element model.

All analyses thus far are performed using the (approximately) linearly varying soil profile shown in Figure 4.1. In order to validate the macro-element for different soil profiles, the 3x3 pile group is analysed in homogeneous soil corresponding to the middle layer of the linearly varying profile. The results in Figure 4.12(c) show that the macro-element matches the finite element model quite well.

The results presented herein indicate that even though the macro-element may be somewhat inaccurate compared to a rigorous finite element model, it is highly capable of capturing trends associated with pile group configuration, batter angle, pile spacing and soil profile. In practical engineering, where actual response values are approached in a broader sense, it is often more important to evaluate trends rather than exact values. The macro-element is therefore particularly suitable in practical design situations or as an efficient tool in parametric analysis for both practical and academic purposes.

4.4.3 Equivalent linear properties

In addition to nonlinear time history analysis, the macro-element may be used to efficiently estimate equivalent linear properties of a pile group. The equivalent linear pile group impedance in complex form is expressed as

$$\bar{K_G} = K_G^{sec}(1 + i2\xi_G) \tag{4.43}$$

where K_G^{sec} is the displacement-dependent secant stiffness and ξ_G is the equivalent viscous damping ratio. The equivalent viscous damping may be estimated using the area based approach first suggested by Jacobsen [229], i.e.,

$$\xi = \frac{W_d}{4\pi W_s} \tag{4.44}$$

where W_d is the energy dissipated in one cycle during the steady state response and W_s is the peak energy during one cycle. The equivalent linear approach is schematically shown in Figures 4.13(a) and 4.13(b) for the 3x3 pile group subjected to harmonic displacements with fixed rotation in linearly varying soil. As displacement increases, the secant stiffness decreases and the damping ratio increases.

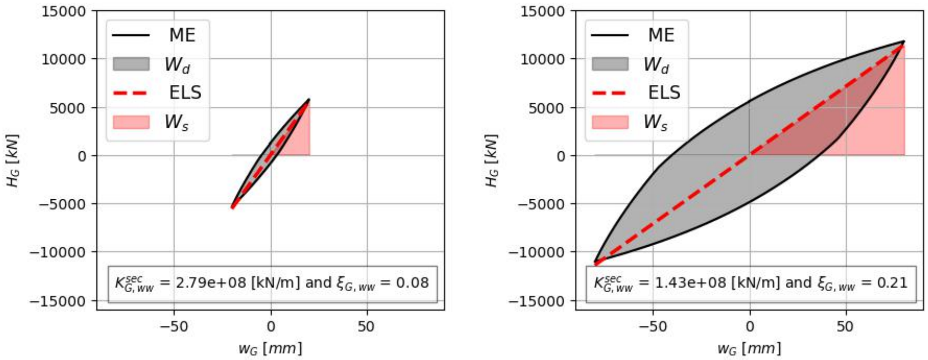

(a) Area-based approach, small cycle **(b)** Area-based approach, large cycle

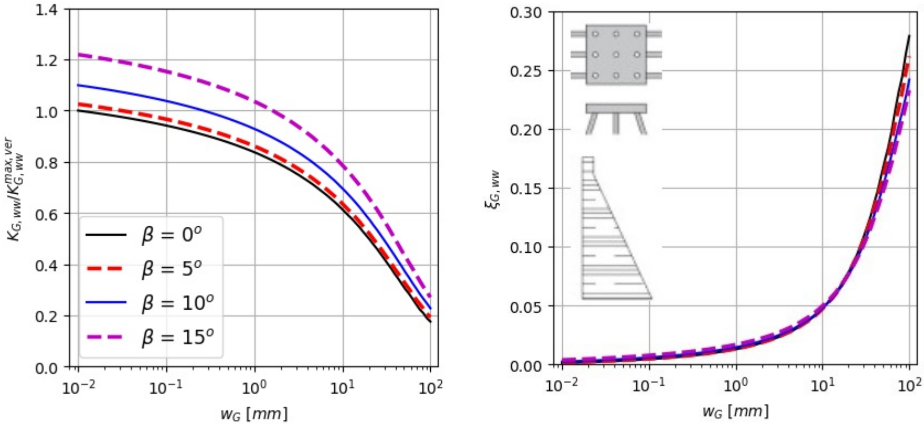

(c) Normalized secant stiffness **(d)** Equivalent viscous damping

Figure 4.13: Equivalent linear properties using the macro-element. 3x3 pile group with vertical and batter piles. $S_0/d_p = 5$ and $\beta = 15°$

The macro-element allows for fast parametric analysis of secant stiffness and damping ratios for a variety of parameters such as pile group configuration, batter angle and pile spacing. As an example, Figure 4.13(c) and 4.13(d) show the secant stiffness and damping ratios for different batter angles as a function of displacement amplitude. In this case, it is clear that secant stiffness is highly dependent on batter angle. The damping ratio, however, is rather unaffected by batter angle. The ability to efficiently assess such values is particularly useful in preliminary design or as means of evaluating the effect of change in later design stages. In addition, governing codes and general design rules are often expressed in terms of simplified, linear values, which in most cases are not easily retrieved using rigorous finite element tools.

4.5 Summary

A novel macro-element for vertical and batter pile groups has been presented. The numerical scheme is based on de-coupled, single pile response without any requirements for pre-defined failure surfaces or other parameters. Although practical, such simplified formulations are bound to limited validity. First, the accuracy is expected to decrease for small displacement since the formulation neglects radiation damping, which becomes more important for small-strain soil deformations. Second, even though the macro-element performs well within the realistic range of pile spacings in soft soil, further studies on the performance in stiffer soils are needed. Third, axial and transverse response is de-coupled, which inherently introduces an error related to the bounding loads and restricts the macro-element to long piles. Nevertheless, it has been demonstrated that the macro-element is capable of capturing trends associated with pile group configuration, batter angle, pile spacing and soil profile.

Chapter 5

Integrated FE software for seismic soil-structure interaction using macro-elements

5.1 Introduction

This chapter presents a new finite element framework for seismic analysis of structures accounting for SSI using the solutions presented in the previous chapters. Although the software is implemented and demonstrated for relatively simple bridges frequently encountered in everyday engineering, the solution is valid for any type of structure that may be represented by planar frames. The finite element code is written using programming language Python 3 [225].

There are several reasons for developing a new (in-house) software rather than implementing the developed solutions in existing codes. First, the formulations (especially the macro-element) consist of somewhat complex algorithms that require in-depth knowledge of the existing architecture in order to be implemented as intended. The development of a global code allows for adjustments of both local and global formulations in order to archive the desired performance. Second, in-house codes allow for relatively easy implementation of added features in future applications. Third, it is rather straight-forward to implement pre-processing schemes, such as parametric analysis and templates. Finally, in-house solutions are easy to customize according to the task at hand, which is a highly desirable feature in practical engineering.

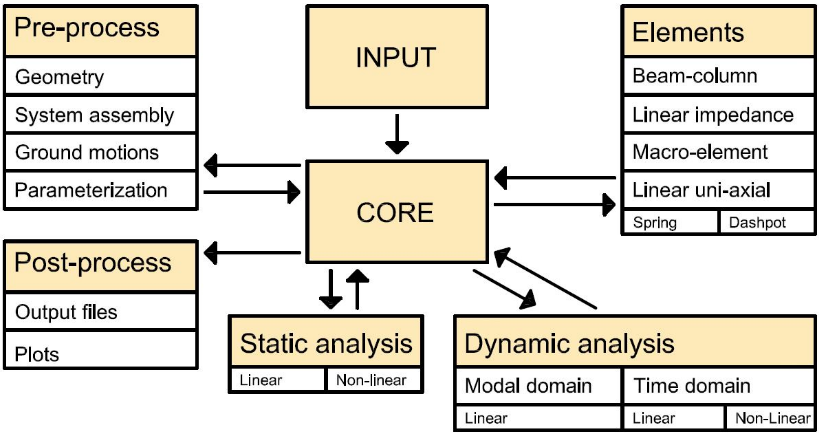

Figure 5.1: Schematic overview over the general code structure

Complying with the underlying philosophy governing the developed solutions thus far, the software is required to entail certain features inherent to practical engineering. Consequently, it is emphasized that the pre- and post-processing procedures are relatively unrestricted, easy to use and involve minimal manual inputting. Also, the solution should utilize relatively well-known computational methods.

The code is architectured module-wise, where the core module controls the dataflow between the other modules. Figure 5.1 shows a schematic overview over the general code structure. It is also worth mentioning specific features such as:

- Prescribed displacement enforced using penalty constraints, such that there is no need to explicitly define the equivalent seismic force vector.
- Automatic processing of NGA-files (.AT2) from the PEER-data base [230]. The user needs only to specify the local file location.
- Classical damping may be added separately to subdomains. E.g., different damping ratios may be defined for foundation and superstructure, respectively. See Figure 5.2.
- Parametric analysis on multiple variables is available.

The main objectives of this chapter is to (1) architecture a finite element software

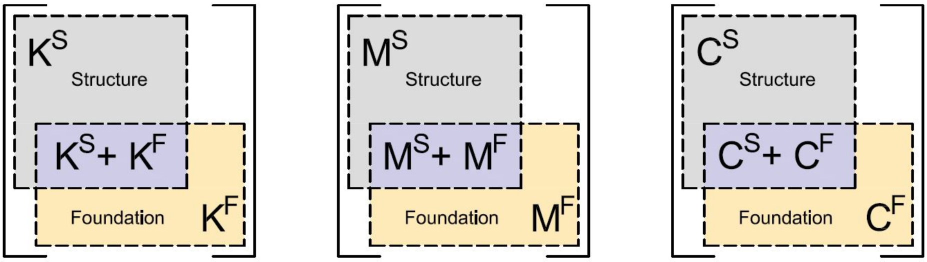

Figure 5.2: Subdivision of stiffness, mass and damping matrix

for seismic analysis of bridges and other relevant structures that utilizes the macro-element and the linear impedance matrix, (2) demonstrate how the macro-element and the linear impedance matrix may be implemented in a general finite element solution and (3) perform a set of *incremental dynamic analyses* (IDA) of an *integral abutment bridge* (IAB) founded on vertical and batter piles in order to evaluate the effect of SSI, batter angle and pile spacing.

This chapter is divided in five sections. Section 5.2 briefly describes the theory and implementation of the time domain solution, with emphasis on the macro-element. Similarly, Section 5.3 describes the theory and implementation of the modal domain solution, with emphasis on the linear impedance matrix. The numerical schemes are presented in terms of general pseudo-codes. Section 5.4 presents a set of IDA-analyses of an IAB, where the effect of SSI, batter angle and pile spacing is evaluated.

5.2 Time domain solution

5.2.1 Integrator and solver

The time domain solution is based on Newmark's method [206], where the governing differential equation is solved at the unknown time step t_i,

$$\boldsymbol{M}\ddot{\boldsymbol{d}}_i + \boldsymbol{C}\dot{\boldsymbol{d}}_i + \boldsymbol{K}\boldsymbol{d}_i = \boldsymbol{F}_i^{ext} \tag{5.1}$$

Such methods are referred to as *implicit methods*. Note that we are using subscript i to indicate the time instance where the state variables are unknown (and consequently subscript $i-1$ to indicate the time instance where the state variables are known). In order to numerically integrate the state variables, the variation of acceleration over a time step

$$\Delta t = t_i - t_{i-1} \tag{5.2}$$

must be assumed. Newmark's method proposes the generalized equations

$$\dot{\boldsymbol{d}}_i = \dot{\boldsymbol{d}}_{i-1} + \Delta t \left[\gamma \ddot{\boldsymbol{d}}_i + (\gamma - 1)\ddot{\boldsymbol{d}}_{i-1}\right] \tag{5.3a}$$

$$\boldsymbol{d}_i = \boldsymbol{d}_{i-1} + \Delta t \dot{\boldsymbol{d}}_{i-1} + \frac{\Delta t^2}{2}\left[2\beta \ddot{\boldsymbol{d}}_i + (1 - 2\beta)\ddot{\boldsymbol{d}}_{i-1}\right] \tag{5.3b}$$

where γ and β are parameters that control the time step variation of acceleration. It is easily shown that $\gamma = 1/2$ and $\gamma = 1/4$ corresponds to the assumption that acceleration over a time step is constant, and that $\gamma = 1/2$ and $\gamma = 1/6$ corresponds to the assumption that acceleration over a time step varies linearly.

Combining Equations 5.1 and 5.3, the state variables at time instance t_i may be determined from known properties and state variables defined at the known time instance t_{i-1}. Note that this approach assumes that the external load vector, together with the mass, stiffness and damping matrices, are not functions of the state variables. That assumptions is only valid for linear systems. In most structural engineering problems, significant nonlinear effects stem from nonlinear material behaviour (nonlinear constitutive models). The resisting force vector is then expressed as

$$\boldsymbol{F}_i^{int} = \boldsymbol{K}(\boldsymbol{d}_i)\boldsymbol{d}_i \tag{5.4}$$

where the stiffness matrix is a function of the state variables. Therefore, the nonlinear system must solved through an iterative procedure. The developed software uses the well-known Newton-Rhapson method [147, 231, 232] to restore the resisting force vector.

The numerical scheme for the nonlinear time domain solution is shown in Algorithm 1. Here, subscript i represents the time step counter, $\hat{\mathbf{F}}$ is the effective force vector, j is the iteration counter, $\mathbf{R}$ is force residual, $\hat{\mathbf{K}}$ is the effective stiffness and $\mathbf{F}^{int}$ is the internal force vector. The convergence criteria may be chosen as residual force, relative residual force, displacement increment, relative displacement increment, incremental work or relative incremental work. Since the frame model typically contains both translational and rotational degrees of freedom in addition to penalty constrains (imposed earthquake motion), it is recommended that the relative incremental displacement is used to check convergence, i.e.,

$$\frac{||\Delta \mathbf{d}_j^T||}{||\Delta \mathbf{d}_{j=0}^T||} \leq \epsilon_d \tag{5.5}$$

Here, $||\cdot||$ denotes the l_{inf}-norm of the vector and ϵ_w is the predefined tolerance.

Algorithm 1 Newmark's method for nonlinear systems

```
procedure NEWMARK
    Initial conditions $\mathbf{d}_0$ and $\dot{\mathbf{d}}_0 \rightarrow \ddot{\mathbf{d}}_0 = \mathbf{M}^{-1}\left(\mathbf{F}_0^{ext} - \mathbf{C}\dot{\mathbf{d}}_0 - \mathbf{K}_0\mathbf{d}_0\right)$
    $a_1 = \frac{1}{\beta\Delta t^2}\mathbf{M} + \frac{\gamma}{\beta\Delta t}\mathbf{C},\ a_2 = \frac{1}{\beta\Delta t}\mathbf{M} + \left(\frac{\gamma}{\beta} - 1\right)\mathbf{C},$
    $a_3 = \left(\frac{1}{2\beta} - 1\right)\mathbf{M} + \Delta t\left(\frac{\gamma}{2\beta} - 1\right)\mathbf{C}$

    while $t_i < t_{max}$ do
        $i = i + 1, \ \ t_i = t_{i-1} + \Delta t$
        $\hat{\mathbf{F}}_i = \mathbf{F}_i^{ext} + a_1\mathbf{d}_{i-1} + a_2\dot{\mathbf{d}}_{i-1} + a_3\ddot{\mathbf{d}}_{i-1}$

        while convergence criteria not met do
            $j = j + 1, \ \ \mathbf{R}_i = \hat{\mathbf{F}}_i - \mathbf{F}_i^{int} - a_1\mathbf{d}_i, \ \ \hat{\mathbf{K}}_{i,j} = \mathbf{K}_i + a_1$
            $\Delta\mathbf{d} = \hat{\mathbf{K}}_i^{-1}\mathbf{R}_i \rightarrow \mathbf{d}_i = \mathbf{d}_i + \Delta\mathbf{d}$
            get $\mathbf{K}_i$ and $\mathbf{F}_i^{int}$

        $\dot{\mathbf{d}}_i = \frac{\gamma}{\beta\Delta t}\left(\mathbf{d}_i - \mathbf{d}_{i-1}\right) + \left(1 - \frac{\gamma}{\beta}\right)\dot{\mathbf{d}}_{i-1} + \Delta t\left(1 - \frac{\gamma}{2\beta}\right)\ddot{\mathbf{d}}_{i-1}$
        $\ddot{\mathbf{d}}_i = \frac{1}{\beta\Delta t^2}\left(\mathbf{d}_i - \mathbf{u}_{i-1}\right) - \frac{1}{\beta\Delta t}\dot{\mathbf{d}}_{i-1} - \left(\frac{1}{2\beta} - 1\right)\ddot{\mathbf{d}}_{i-1}$
```

It can be shown [231, 233] that the Newmark's method is stable when

$$2\beta \geq \gamma \geq \frac{1}{2} \tag{5.6}$$

This implies that the method is *unconditionally stable* for the average acceleration assumption, but *conditionally stable* for the linear acceleration assumption.

It is often desirable to damp out high-frequency response, which may arise from spurious oscillations associated with the discretization of the problem. In order to maintain numerically stability and simultaneously add numerical damping to high-frequency response, it is recommended that

$$\beta = \frac{1}{4}\left(\gamma + \frac{1}{2}\right)^2, \gamma \geq \frac{1}{2} \tag{5.7}$$

where $\gamma = 1/2$ equals no numerial damping [233]. The analysis in the subsequent sections are performed with γ and β according to Equation 5.7.

5.2.2 Macro-element implementation

This section presents the numerical treatment and implementation of the macro-element presented in Chapter 4. In essence, the macro-element serves as a function that provides the global finite element code the foundation stiffness at a certain time instance. The input of that function is a displacement increment, and the output is a coupled tangent stiffness matrix with three degrees of freedom. The algorithm assumes that the initial step in the creation of any loading (virgin loading, unloading or reloading) is purely elastic and that the subsequent steps within the respective loading always contain plastic deformations. The corresponding load and the elastic and plastic displacements are determined using a return mapping algorithm.

The cutting plane algorithm [234, 235, 236], which is a variation of the return mapping algorithm, has been adopted by researchers [163, 164, 171, 172] in the formulation of macro-elements for both shallow and deep foundations. The same approach will be used here. The main concept of the cutting-plane algorithm is to explicitly integrate the state variables and iterate the solution until a constraining condition is satisfied. Here, this implies using Equations 4.1, 4.2, 4.6, 4.7 and 4.10

Algorithm 2 General single-pile tangent stiffness

```
Input $\Delta d$
procedure TANGENT
    if i = 0 then
        $k_S^l = K^{el}$
    else
        $\Delta F = K^{el}\,\Delta d \rightarrow F_{trial} = F_{i-1} + \Delta F,\ \text{and}\ \lambda_{trial} = \frac{1}{F_{trial}}$
        if $\left(F_{trial} < F_{i-1} > F_{i-2}$ or $F_{trial} > F_{i-1} < F_{i-2}\right)$ and $i > 1$ then
            Reversal $\rightarrow F_i = F_{trial}, \lambda_i = \lambda_{trial}$ and $k_S^l = K^{el}$
            if $\lambda_i \leq \lambda_{min}$ then
                Virgin state $\rightarrow \lambda_{min} = \lambda_i$
            else
                if $\lambda_i > \lambda_{i-1}$ and $F_i\, F_{i-1} > 0$ then
                    Unloading state $\rightarrow F_u = F_{i-1}$ and $\lambda_u = \lambda_{i-1}$
                else
                    Reloading state $\rightarrow F_r = F_{i-1}$ and $\lambda_r = \lambda_{i-1}$
        else
            Not reversal $\rightarrow$ get TANGENT_RETURN
```

to obtain the elastic displacement, plastic displacement, load and load multiplier using values from the previous iteration or the last converged step. The consistency condition in Equation 4.9 is linearized and solved for the plastic multiplier and the state variables are updated. Convergence is achieved when both the displacement residual and the bounding point equation are within a prescribed tolerance value.

Algorithm 2 shows the general part of the single-pile tangent stiffness scheme, i.e. the part of the algorithm that is valid for both transverse and axial response. Here, k^l_S is the single pile tangent stiffness in local coordinates, F_{trial} is the trial load, λ_{trial} is trial load parameter, λ_{min} is the minimum load parameter obtained during the previous loading steps, F_u is the load associated with the last initial unloading state, λ_u is the load parameter associated with the last initial unloading state, F_r is the load associated with the last initial reloading state, λ_r is the load parameter associated with the last initial reloading state and *TANGENT_RETURN* is the return mapping numerical scheme, which differs for transverse and axial response. For convenience, the subscript n that implies normalized values has been

Algorithm 3 Return mapping for horizontal tangent stiffness $k^l_{S,ww}$

```
procedure TANGENT_RETURN_H
    while $|R_i| < R_{tol}$ and $f_i < f_{tol}$ do
        if j = 0 then
            $w^{el}_i = w^{el}_{i-1}$, $w^{pl}_i = w^{pl}_{i-1}$, $\lambda_i = \lambda_{i-1}$, $\Delta\gamma = 0$, $H_i = H_{trial}$
        else
            if $\lambda_{trial} \leq \lambda_{min}$ then
                Virgin state $\rightarrow K^{pl}_H = K^{pl}_{H,v}$
            else if $(\lambda_{trial} > \lambda_{min})$ and $(\lambda_{trial} > \lambda_{i-1})$ and $(H_i \, H_{i-1} > 0)$ then
                Unloading state $\rightarrow K^{pl}_H = K^{pl}_{H,u}$
            else
                Reloading state $\rightarrow K^{pl}_H = K^{pl}_{H,r}$
            $w^{el}_i = \dfrac{\Delta H}{K^{el}_H}, \; w^{pl}_i = \Delta\gamma \operatorname{sgn}(H_i), \; \lambda_i = \lambda_i - \dfrac{\Delta\gamma \, \lambda_i \, K^{pl}_H}{\operatorname{sgn} H_i},$
            $R_i = w_i - w^{el}_i - w^{pl}_i, \; f_i = |H_i \lambda_i| - 1$
            $\Delta\gamma = \dfrac{f_i + \big(\lambda_i \operatorname{sgn}(H_i) K^{el}_H\big)}{\lambda_i \big(K^{el}_H + K^{pl}_H\big)}, \; \Delta H = K^{el}_H \big(R_i - \Delta\gamma \operatorname{sgn}(H_i)\big)$
            $H_i = H_i + \Delta H$
    return $k^l_{S,ww} = \dfrac{K^{el}_H K^{pl}_H}{K^{el}_H + K^{pl}_H}$
```

Algorithm 4 Return mapping for axial tangent stiffness $k^l_{S,uu}$

```
procedure TANGENT_RETURN_V
    while $|R_i| < R_{tol}$ and $f_i < f_{tol}$ do
        if j = 0 then
            $u^{el}_i = u^{el}_{i-1}$, $u^{pl}_i = u^{pl}_{i-1}$, $\lambda_i = \lambda_{i-1}$, $\Delta\gamma = 0$, $V_i = V_{trial}$
        else
            if $\lambda_{trial} \leq \lambda_{min}$ then
                if $V_i > 0$ then
                    Virgin state, tension → $K^{pl}_V = K^{pl}_{V,vt}$
                else
                    if $\lambda_i > \lambda_{el}$ then
                        Virgin state, compression → $K^{pl}_V = K^{pl}_{V,vc}$ (Eq. 4.33)
                    else
                        Virgin state, compression → $K^{pl}_V = K^{pl}_{V,vc}$ (Eq. 4.34)
            else if $(\lambda_{trial} > \lambda_{min})$ and $(\lambda_{trial} > \lambda_{i-1})$ and $(V_i\ V_{i-1} > 0)$ then
                if $V_i > 0$ then
                    Unloading state, tension → $K^{pl}_V = K^{pl}_{V,ut}$
                else
                    Unloading state, compression → $K^{pl}_V = K^{pl}_{V,uc}$
            else
                if $V_i > 0$ then
                    Reloading state, tension → $K^{pl}_V = K^{pl}_{V,rt}$
                else
                    if $r_r = 1$ then
                        Reloading state, compression → $K^{pl}_V = \infty$
                    else if $r_r = -1$ then
                        Reloading state, compression → $K^{pl}_V = K^{pl}_{V,rc}$ (Eq. 4.35)
            $u^{el}_i = \dfrac{\Delta V}{K^{el}_V},\ \ u^{pl}_i = \Delta\gamma\,\mathrm{sgn}(V_i),\ \ \lambda_i = \lambda_i - \dfrac{\Delta\gamma\,\lambda_i\,K^{pl}_V}{\mathrm{sgn}\,V_i},$
            $R_i = u_i - u^{el}_i - u^{pl}_i,\ \ f_i = |V_i \lambda_i| - 1$
            $\Delta\gamma = \dfrac{f_i + \big(\lambda_i\,\mathrm{sgn}(V_i) K^{el}_V\big)}{\lambda_i\big(K^{el}_V + K^{pl}_V\big)},\ \ \Delta V = K^{el}_V\big(R_i - \Delta\gamma\,\mathrm{sgn}(V_i)\big)$
            $V_i = V_i + \Delta V$
    return $k^l_{S,uu} = \dfrac{K^{el}_V K^{pl}_V}{K^{el}_V + K^{pl}_V}$
```

omitted from the presented algorithms in this section. Nevertheless, normalized values are assumed in all cases.

Algorithm 3 shows the return mapping scheme for transverse response. Here, w^{el} is the elastic displacement, w^{pl} is the plastic displacement, γ is the plastic multiplier, R is the displacement residual and f is the bounding point equation. Similarly, Algorithm 4 shows the return mapping for axial response.

For practical purposes, the presented algorithms only show selected parts of the total numerical scheme. Assessment of the implicit transverse-rotational coupling, pile group assembly, and the interaction with the global code are also important aspects of the macro-element algorithm in terms of stability and efficiency.

5.3 Modal domain solution

5.3.1 Domain transformation

The equation of motion of an undamped system with N degrees of freedom may be expressed as

$$\boldsymbol{M}\ddot{\boldsymbol{d}} + \boldsymbol{K}\boldsymbol{d} = \boldsymbol{0} \tag{5.8}$$

Considering that free vibration is harmonic, the response in the i^{th} mode may be expressed as

$$\boldsymbol{d} = \boldsymbol{\phi}_i q_i \tag{5.9}$$

where $\boldsymbol{\phi_i}$ is the $Nx1$ normalized mode shape vector and $q_i = q_i(t)$ is the corresponding modal response scalar. Combining Equations 5.8 and 5.9 gives

$$\left(\boldsymbol{K} - \omega_i^2 \boldsymbol{M}\right)\boldsymbol{\phi} = 0 \rightarrow \boldsymbol{M}^{-1}\boldsymbol{K}\boldsymbol{\Phi} = \omega_i^2 \boldsymbol{\Phi} \tag{5.10}$$

which is identified as the eigenvalue problem. The solution of Equation 5.10 yields N eigenvectors $\boldsymbol{\phi}$ and N eigenvalues ω^2, implying that the eigenvectors represent the natural mode shapes and the eigenvalues implicitly represent the natural frequencies.

Eigenvectors are inherently orthogonal to each other, which is a very powerful property that allows for the uncoupling of the N equations of motion by performing a domain transformation from nodal to modal coordinates. First, the natural modes are assembled to form the *modal matrix*, i.e.,

$$\boldsymbol{\Phi} = \begin{bmatrix}\boldsymbol{\phi}_1 & \boldsymbol{\phi}_2 & \dots & \boldsymbol{\phi}_N\end{bmatrix} \tag{5.11}$$

The total displacement may then be expressed as the sum of modal contributions, i.e.,

$$\boldsymbol{d} = \sum_{i=1}^{N} \boldsymbol{\phi_i} q_i = \boldsymbol{\Phi q} \tag{5.12}$$

Considering a damped system subjected to external forces, the equation of motion is expressed as

$$\boldsymbol{M\ddot{d}} + \boldsymbol{C\dot{d}} + \boldsymbol{Kd} = \boldsymbol{F}^{ext} \tag{5.13}$$

Inserting Equation 5.12 into Equation 5.13 and pre-multiplying with $\boldsymbol{\Phi}^T$, the equation of motion in modal coordinates is expressed as

$$\boldsymbol{\Phi}^T \boldsymbol{M\Phi\ddot{q}} + \boldsymbol{\Phi}^T \boldsymbol{C\Phi\dot{q}} + \boldsymbol{\Phi}^T \boldsymbol{K\Phi q} = \boldsymbol{\Phi}^T \boldsymbol{F}^{ext} \tag{5.14}$$

where

$$\boldsymbol{M}_m = \boldsymbol{\Phi}^T \boldsymbol{M\Phi} \tag{5.15a}$$

$$\boldsymbol{K}_m = \boldsymbol{\Phi}^T \boldsymbol{K\Phi} \tag{5.15b}$$

$$\boldsymbol{F}_m^{ext} = \boldsymbol{\Phi}^T \boldsymbol{F}^{ext} \tag{5.15c}$$

are the modal mass matrix, modal stiffness matrix and modal load vector. The modal mass and stiffness matrices are both diagonal matrices due to the orthogonality of the mode shape vectors. The modal damping matrix

$$\boldsymbol{C}_m = \boldsymbol{\Phi}^T \boldsymbol{C\Phi} \tag{5.16}$$

is generally not diagonal. However, when classical damping is used, that is when the damping matrix is mass proportional, stiffness proportional or a combination of the two (Rayleigh damping), the damping matrix is also diagonal. In that case, Equation 5.13 represents a set of N uncoupled differential equations that can solved independently for q_i. The total displacement is then retrieved using Equation 5.12.

5.3.2 Linear impedance matrix implementation

The modal approach is not strictly suitable for assessing linear SSI-problems since the stiffness expressions associated with foundation and soil are generally frequency-dependent. In that case, frequency-domain analysis provide the mathematically sound and accurate solution. Although there are especially developed software packages for SSI-problems in the frequency domain [237], such solutions are not particularly convenient in practical engineering. In fact, solving structural engineering problems in the modal domain rather than the frequency domain provides several advantages. First the modal approach provides useful information in terms of modal shapes and the corresponding natural frequencies (dynamic properties of the structure), which are concealed in time- or frequency domain solutions. Second, modal analysis are the standard option in most commercial software packages, and the modal superposition concept is familiar for most practicing engineers. Third, modal analysis are an inherent part of the commonly used *response spectrum analysis*.

The solution of SSI-problems in the modal domain has been discussed by several authors [238, 239, 240, 241]. Perhaps most practically, and especially in cases where estimates are sought, the frequency-dependent foundation stiffness may be approximated as the constant value corresponding to the fundamental frequency of the soil-structure system. The constant value may be computed by iterating on the eigenvalue-problem until the assumed frequency matches the computed eigenvalue. With reference to Equation 3.119, the constant foundation stiffness is then determined as

$$\boldsymbol{K}^F = Re(\boldsymbol{K}_G^*(\omega_{i=1})) \tag{5.17}$$

and the foundation damping ratio in each mode is

$$\boldsymbol{\xi}_i^F = \frac{Im(\boldsymbol{K}_G^*(\omega_i))}{2Re(\boldsymbol{K}_G^*(\omega = 0))} \tag{5.18}$$

The following should be noted:

1. Iterating on all modes (and not only the fundamental mode) provides the accurate mode shapes and natural frequencies for each individual mode. However, the eigenvectors are then not orthogonal and the modal responses cannot be superimposed.
2. Although the stiffness term is assessed for the fundamental mode only, the damping ratios are determined separately for each mode.
3. The damping ratio $\boldsymbol{\xi}_i^F$ is bound to maximum 30% of the computed value, as suggested by Kolias et al. [241].
4. The presented impedance matrix is a closed-form solution limited to homogeneous deposits, while the considered profile varies linearly from a certain depth. However, as is the case in many situations, the upper part of the soil is homogeneous. Since the upper part is considered the most important in terms of pile behaviour (at least for transverse response), the linear impedance matrix may be used as an approximation.

5.4 Seismic analysis of an integral abutment bridge

5.4.1 Investigated system

Bridges are often designed as statically determinate systems which usually requires the use of bearings and expansion joints. During the life-span of a bridge, these mechanical elements require expensive maintenance routines. Integral abutment bridges (IABs) are monolithic structures without such elements. They are unique in the sense that substantially less maintenance is required compared to structures with bearings and expansion joints. In addition, the construction costs are generally lower, the durability is higher and the seismic hazards are lower due to the absence of weak components. Therefore, IABs are popular among consultants, contractors and governmental road maintenance departments. However, monolithic structures are sensitive to restraint forces such as thermal effects, creep and shrinkage. Furthermore, the monolithic connections increase the overall soil-structure interaction during seismic excitation. For those reasons, IABs make an excellent case study in the context of this thesis. The reader is referred to the literature [242, 243] for further details on IABs.

The investigated system is a monolithic, one-spanned IAB with relatively stub frame abutments. See Figure 5.3. The abutments are founded on a 3-by-3 pile-group with both vertical and batter piles in soft clay. The superstructure is presented using linear beam-column elements, which limits the nonlinear response to the foundation only. The abutment-backfill interaction is not considered, which in

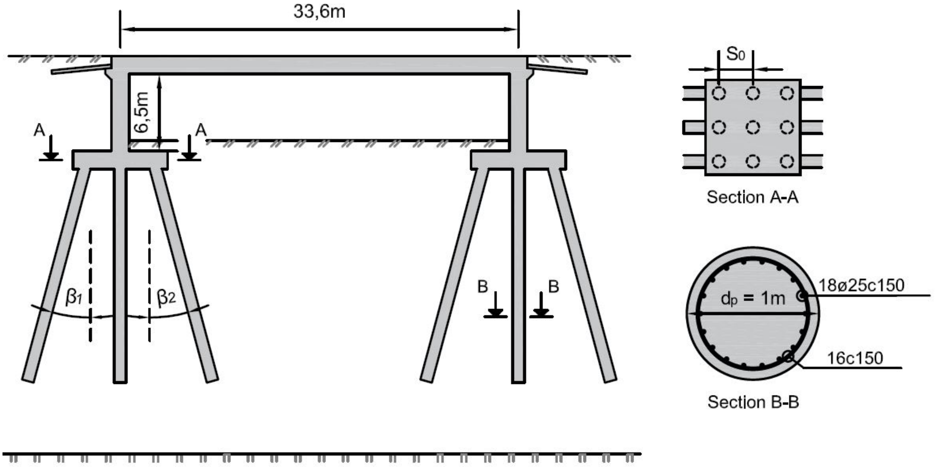

Figure 5.3: Elevation view of the analysed bridge.

practice is highly significant for the overall seismic response of an IAB. The soil profile is described in Chapter 2.

Due to symmetry, only half of the model is considered. The nodes corresponding to the plane cutting the mid-span are fixed in the vertical direction, but are free to rotate and translate in the horizontal direction. For seismic analyses, the loads are applied as imposed displacements using the penalty approach.

5.4.2 Validation

Time domain solution

The nonlinear time domain solution is validated using a fully coupled, three-dimensional finite element model described in Sections 2.2 and 4.2. It should be noted that the contact elements available in OpenSees MP produce in some cases rather noisy results for transient analyses, which may occur even for integration schemes with numerical damping such as the Hilber-Hughes-Taylor method [204, 205]. Therefore, the interface between the pile and soil (beams and solids) is modelled using rigid-link-constraints (full bonding), connecting each beam node to the corresponding soil nodes such that the pile section in the given beam node acts like a rigid disk. The macro-element is thus calibrated using a model without contact elements (for the validation case only).

Figure 5.4 compares the macro-element solution against OpenSees MP in terms of deck displacements and accelerations when the deck is subjected to a horizontal, harmonic load

$$F(t) = 1.2\cos(2\pi f t)\,[MN] \tag{5.19}$$

for f equal to $1Hz$ and $3Hz$. The results show that the macro-element solution performs quite well for both frequencies. Figure 5.5 compares the macro-element solution against OpenSees MP in terms of deck displacement and acceleration for seismic loading. The input motion is the Kocaeli Gebze time history record with $V_{s,30} = 792m/s$ representing soft rock. The input motion is scaled to $PGA = 1$. For the fully coupled OpenSees MP model, the displacement history is applied at the base (rock). For the macro-element model, a nonlinear free-field analysis is first performed using the same modelling strategies as the validation model. The free-field displacement history is then applied at the base node of the macro-element, which inherently neglects kinematic interaction. The results indicate that the macro-element is able simulate the seismic response with reasonable accuracy, admittedly with some overestimation of deck acceleration. It is worth mentioning that the OpenSees model uses the Hilber-Hughes-Taylor method, while the macro-element solution uses the Newmark's method, where the former is more effective

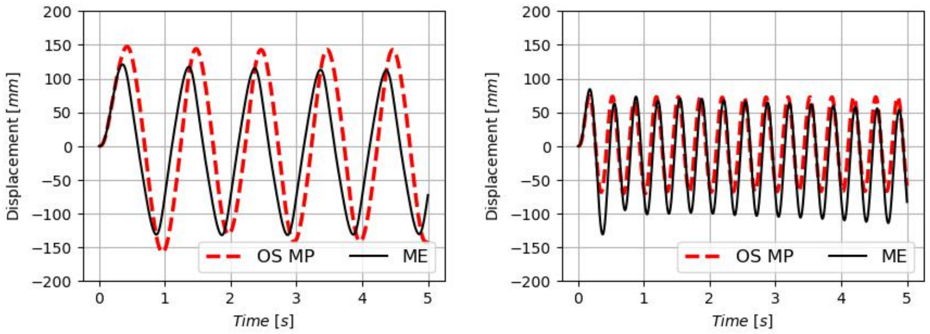

(a) Lateral deck displacement, $1Hz$ **(b)** Lateral deck displacement, $3Hz$

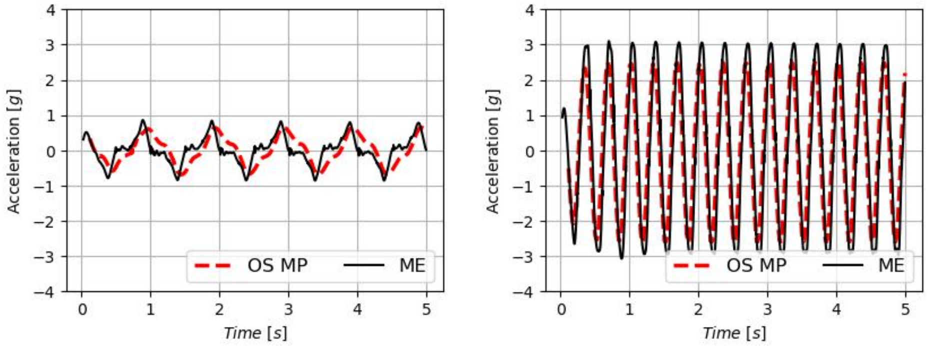

(c) Lateral deck acceleration, $1Hz$ **(d)** Lateral deck acceleration, $3Hz$

Figure 5.4: Comparison of the macro-element solution against OpenSees MP. Harmonic loading

in damping out high-frequency response.

As mentioned in Chapter 1, analysing soil-structure problems using macro-elements inherently introduces an approximation since the analysis is fundamentally nonlinear, while kinematic and inertial effects are not assessed simultaneously. Consequently, the results presented in Figure 5.4 demonstrate the *presented macro-element* performance, while Figure 5.5 illustrates, at least suggestively, the accuracy of the *macro-element approach* in general.

Modal domain solution

The linear modal domain solution is compared against the linear time domain solution for fixed conditions and seismic loading. Figure 5.6 shows the deck displacement and acceleration when the structure is subjected to the Imperial Valley-06

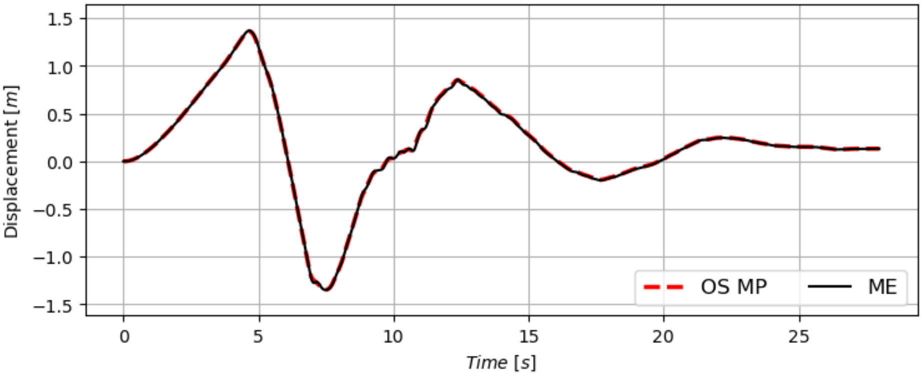

(a) Deck displacement

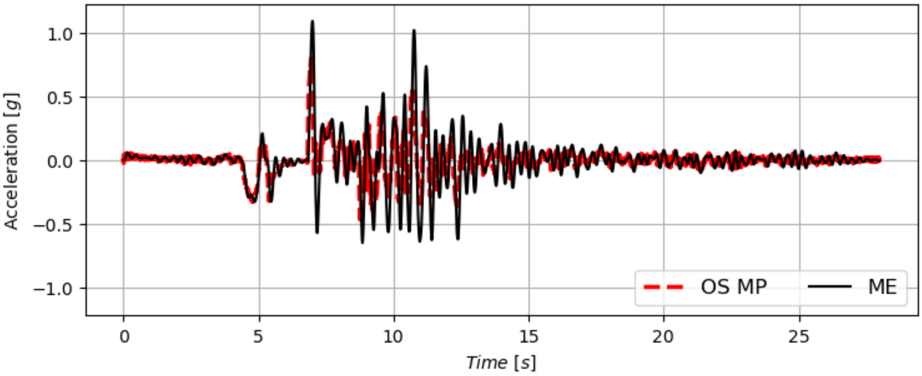

(b) Deck acceleration

Figure 5.5: Comparison of the macro-element solution against OpenSees MP. Seismic loading

ground motion scaled to $PGA = 1g$. As expected, the results show a nearly perfect match.

Note that the dynamic, frequency-dependent response using the linear impedance matrix has been validated in Chapter 3.

5.4.3 Incremental dynamic analysis

In this section, a series of *incremental dynamic analysis* (IDA) are performed in order to evaluate the effect of linear and nonlinear SSI, batter angle and pile-spacing. IDA is a parametric analysis method that evaluates the structural performance under seismic loads, where the computational model is subjected to one or more

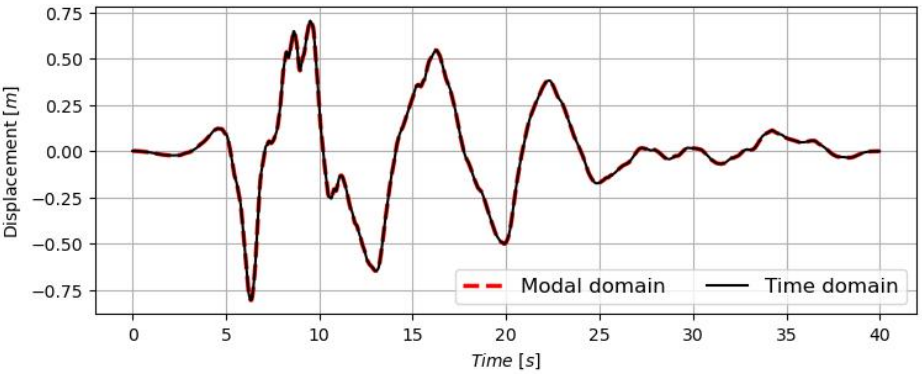

(a) Deck displacement

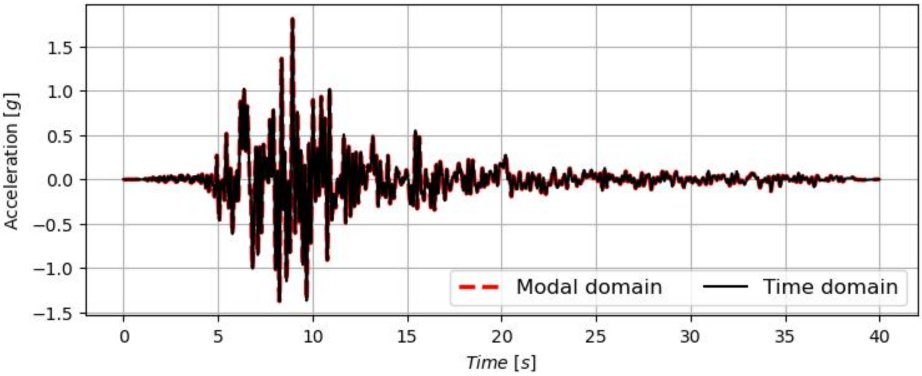

(b) Deck acceleration

Figure 5.6: Comparison of modal domain and time domain solution. Seismic loading

ground motion records scaled to different levels of intensity [244]. The results (IDA-curves) provide a relationship between a response parameter and intensity level, which may further be analyzed in a statistical sense. In the present context, IDA-curves provide an excellent demonstration of the developed solutions and how they might influence seismic design.

As mentioned in Chapter 2, an important part of the SSI-analysis is the assessment of foundation input motion (FIM). As mentioned earlier, an attempt was made to explore the feasibility of using nonlinear kinematic interactions factors to estimate FIM, but this approach was based on the results of comprehensive finite element analyses. If this step were to be included in a simplified method that emphasizes practicality, it would make the overall solution strategy more complicated,

Table 5.1: Selected earthquake records from PEER Ground Motion Database [230]

Earthquake	RSN	**PGA [g]**	$\mathbf{M_w}$	$\mathbf{V_{s,30}}$ **[m/s]**
Imperial Valley-06, USA, 1979	170	0.212	6.53	192
Coalinga-01, USA, 1983	326	0.110	6.36	173
Morgan Hill, USA, 1984	462	0.071	6.19	199
Superstition Hills-01, USA, 1987	718	0.131	6.22	179
Loma Prieta, USA, 1989	738	0.268	6.93	190
Northridge-01, USA, 1994	1049	0.461	6.69	191
Kobe, Japan, 1995	1114	0.348	6.90	198
Parkfield-02, USA, 2004	4107	0.605	6.00	178
Christchurch, New Zealand, 2011	8064	0.384	6.20	198

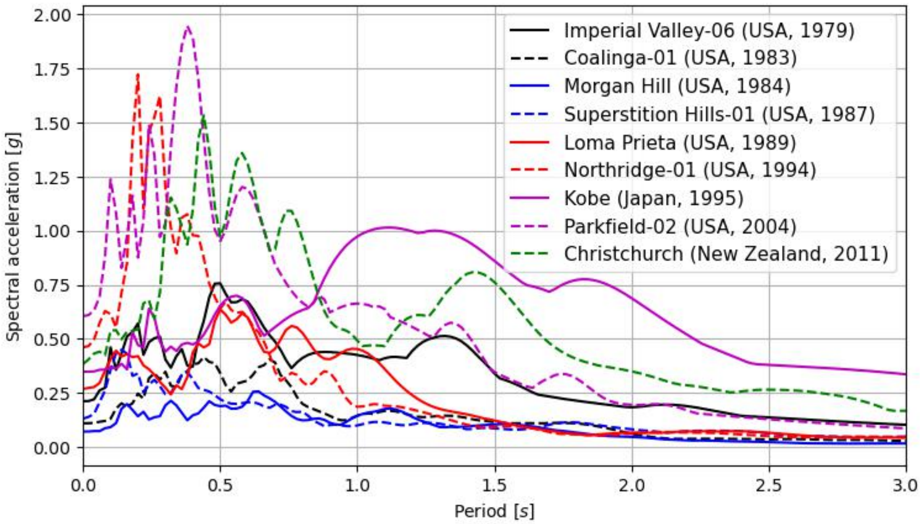

Figure 5.7: Unscaled response spectra

potentially causing it to lose its intended purpose. The analyses presented herein are therefore performed by enforcing the ground motion displacement histories at the base, which inherently neglects the kinematic response. Furthermore, since the analyses only involve models where the input motions are directly enforced at foundation level, the ground motion records are selected such that they represent soft soil. This is achieved by limiting $V_{s,30}$ to maximum $200m/s$. Table 5.1 shows the selected ground motions records and their key characteristics. Here, RSN is the database number, PGA is the non-scaled peak ground acceleration, M_w is the earthquake magnitude and $V_{s,30}$ is average shear wave velocity for the top 30 meters of the soil. Figure 5.7 shows the unscaled response spectra.

Each ground motion record is analyzed for eight PGA-values ranging from $0.1g$ to $2.2g$. While it is acknowledged that such high PGA values are not realistic for soft soil, the analysis is carried out up to 2.2 PGA to effectively illustrate the effect of non-linearity. The results are presented for 9 different response parameters, namely horizontal displacement residual, rotation, and acceleration for both foundation and deck, in addition to base level vertical force, shear force and moment. The displacement residual refers to the residual between deck/foundation and input motion. The IDA-curves are presented as the median for all considered models. The individual results and $16-18\%$ fractile is shown for the nonlinear (macro-element) model only.

Effect of SSI

The IDA-curves are obtained for three different analyses; (1) nonlinear analysis using the macro-element (nonlinear SSI), linear analysis using the impedance matrix (linear SSI) and linear analysis with fixed base condition (neglected SSI). It is recognized that the IDA-analysis is by definition nonlinear. However, in the context of this thesis, linear analyses were performed to clearly demonstrate the effect of linear and nonlinear SSI in comparison to fixed-base conditions.

Figure 5.8 shows the IDA-curves for horizontal displacement residual, rotation, and acceleration of the foundation. Clearly, there is no residual displacement nor rotation at the foundation level for fixed conditions. The results show that nonlinear SSI substantially increases the foundation displacement residual and rotation. SSI also increases foundation accelerations for most PGA-values.

Figure 5.9 shows the IDA-curves for horizontal displacement residual, rotation, and acceleration at the deck level. Linear and nonlinear SSI yield approximately the same deck displacement residual up to a certain value. As PGA increases, nonlinear SSI yields substantially larger values. nonlinear SSI reduces deck rotations and accelerations compared to linear SSI and fixed conditions as PGA increases.

Figure 5.10 shows the IDA-curves for vertical force, shear force and moment at the base level (top foundation). In all cases, nonlinear SSI reduces the forces and moments as PGA increases.

Appendix A shows the hysteretic force-displacement and moment-rotation curves

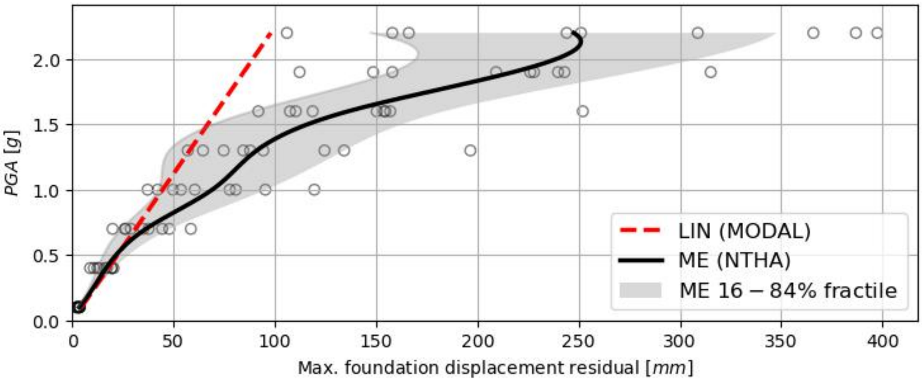

(a) Displacement residual

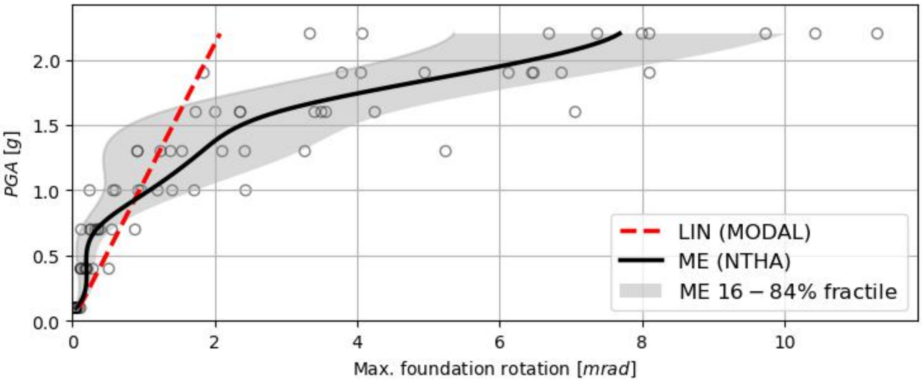

(b) Rotation

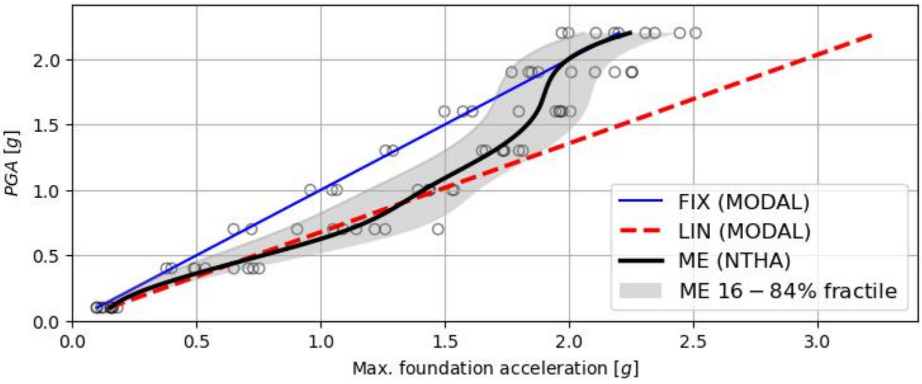

(c) Acceleration

Figure 5.8: IDA-curves showing the effect of SSI. Foundation response

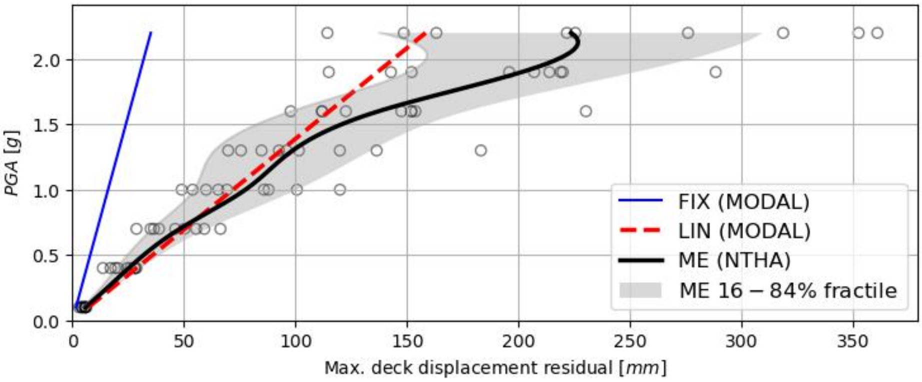

(a) Displacement residual

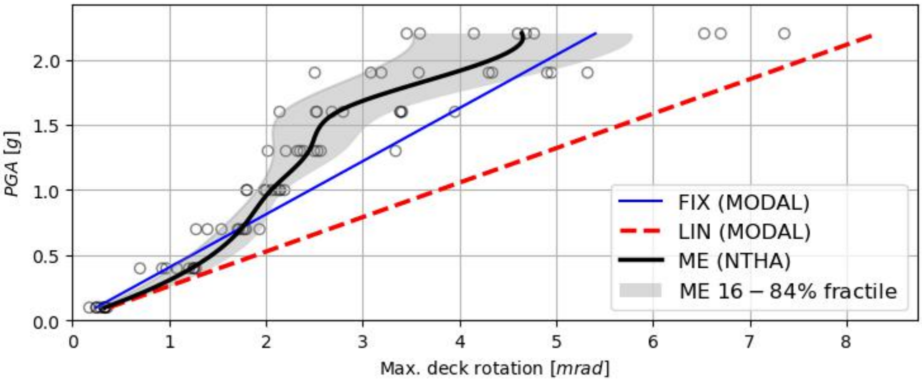

(b) Rotation

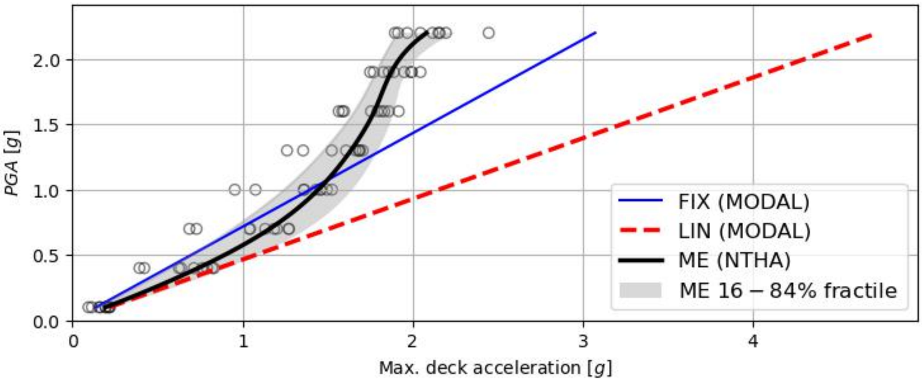

(c) Acceleration

Figure 5.9: IDA-curves showing the effect of SSI. Deck response

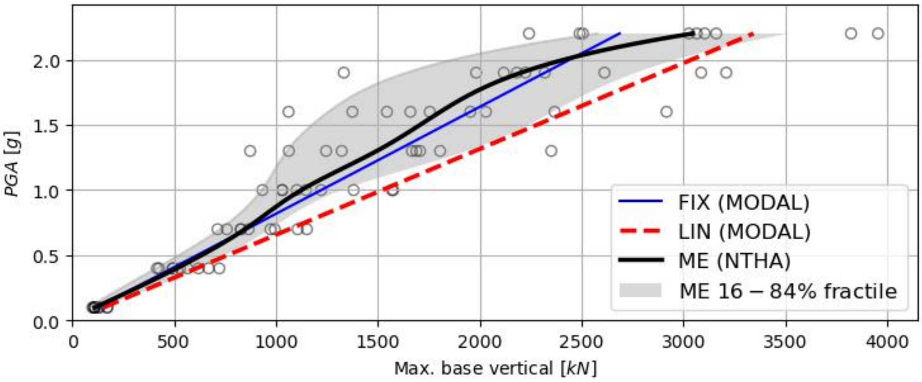

(a) Vertical force

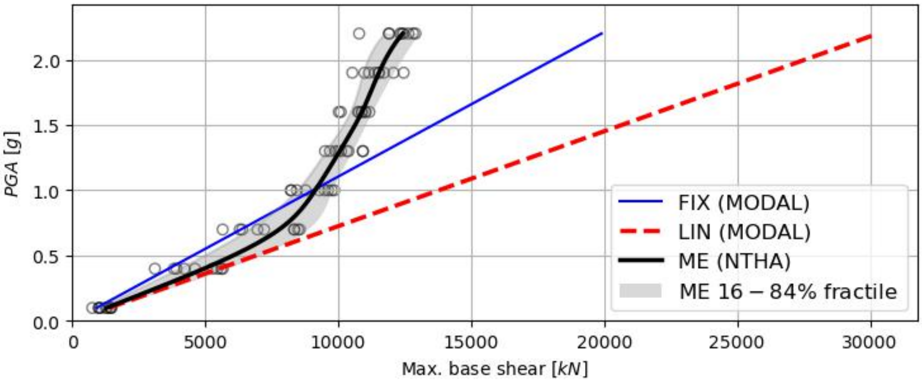

(b) Shear force

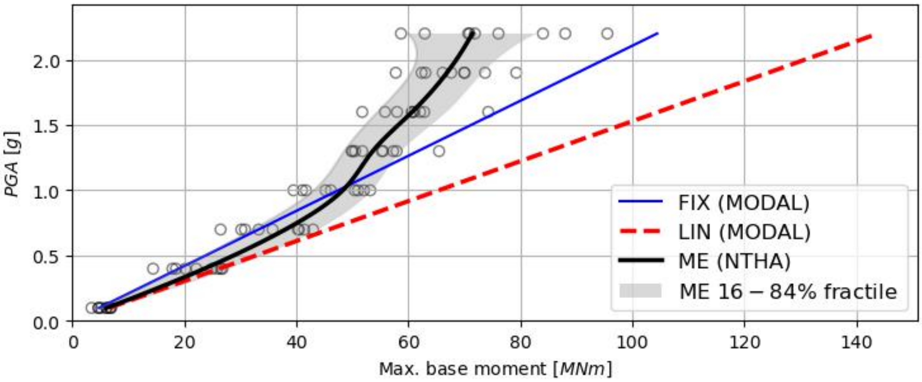

(c) Moment

Figure 5.10: IDA-curves showing the effect of SSI. Base forces and moment

for each nonlinear time history analysis (NTHA). The plots provide further insight on how the base response evolves from linear to nonlinear domain as PGA increases.

It is particularly interesting to note that linear and nonlinear SSI converge for low PGA-values. This observations strengthens the validity and usefulness of the linear impedance matrix in combination with the modal approach as an efficient and easy-to-use tool for estimation of low-strain seismic response. However, it should be noted that when assessing low-strain vibration problems where accuracy is of greater importance, frequency domain solutions should be used.

It is also interesting to note that both linear and nonlinear SSI increase several of the response parameters compared to fixed conditions. The considered system is a relatively stiff structure founded on soft soil. The fixed-base fundamental period of the structure is $T_n = 0.21s$, while the flexible-base fundamental period (using the linear SSI-approach) is $\tilde{T}_n = 0.36s$. This yields

$$\frac{\tilde{T}_n}{T_n} = 1.73 \tag{5.20}$$

which is considered to be a large period lengthening. The detrimental effect of SSI is perhaps expected when considering the response spectra shown in Figure 5.7. It is clear that several of the ground motions attain larger spectral accelerations for periods longer than the fundamental fixed-base period. Introducing SSI, it is thus very likely that the fundamental mode (and consequently any higher mode), contributes to an increase in spectral acceleration. Even for the nonlinear case, which may cause even larger period lengthening, but simultaneously increases the overall damping, SSI increases several of the response parameters for lower PGA-values, i.e. when the foundation responds relatively linear.

To further clarify the discussion above, the IDA-curves for base shear and base moment are normalized by the fixed-base response and plotted against PGA. The results are shown in Figure 5.11. The lines showing fixed-base and linear SSI are of course constant with respect to the normalized response, where the former is equal to unity. It observed that linear SSI increases the shear forces and moments by approximately 50% and 35%, respectively. nonlinear SSI converges with linear SSI as PGA tends towards zero, i.e. when the macro-element relatively linear. As PGA increases, nonlinear SSI yields larger period lengthening (lower stiffness), but also additional system damping. The normalized response decays, but it is still greater than unity up till approximately 1 PGA. Figure 5.11 gives a rather clear overview of how linear and nonlinear SSI affect the respective response parameters in terms of ground motion intensity. In essence, these plots are merely an altern-

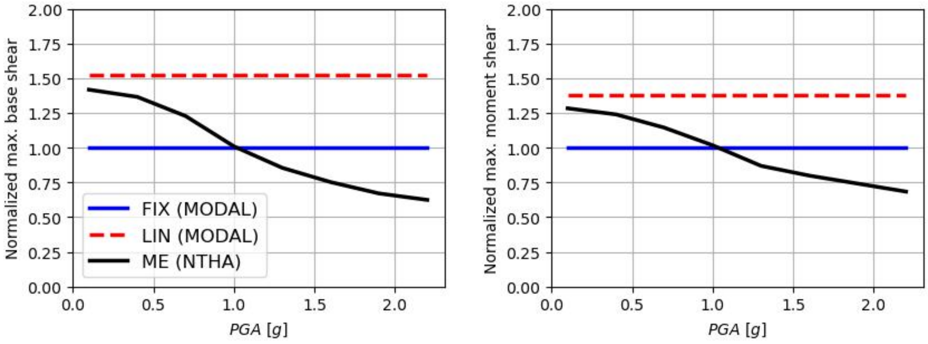

(a) Shear **(b)** Moment

Figure 5.11: IDA-curves normalized by fixed-base response

ative representation of the typical IDA-curves. A broader understanding of the linear/nonlinear domain transition (stiffness reduction and damping increase) may be obtained by studying the hysteretic curves in Appendix A.

Effect of batter angle

The effect of batter angle is evaluated by comparing the results (macro-element approach) using four different combination of batter angles β_1 and β_2 with constant pile spacing $S_0 = 5d_p$.

Figure 5.12 shows the IDA-curves for horizontal displacement residual, rotation, and acceleration of the foundation. Increasing batter angle decreases the displacement residual and increases rotation for high PGA. Perhaps somewhat interesting, increasing batter angle decreases rotation for low PGA and increases foundation acceleration for moderate and high PGA. The latter may be attributed to the fact that batter piles increase the elastic domain in the horizontal direction, and hence also the accelerations as PGA increases.

Figure 5.13 shows the IDA-curves for horizontal displacement residual, rotation, and acceleration at the deck level. Similar trends are observed as for foundation response, but with somewhat less difference between vertical and batter pile groups.

Figure 5.14 shows the IDA-curves for vertical force, shear force and moment at the base level (top foundation). In all cases, increasing batter angle increases forces and moments as PGA increases.

It is also observed that the asymmetric configuration ($\beta_1 = 15^0$ and $\beta_2 = 0^0$) is very close to the symmetric configuration ($\beta_1 = \beta_1 = 7.5^0$) for several response parameters.

Effect of pile spacing

The effect of pile spacing is evaluated by comparing the results (macro-element approach) using three different pile spacing's ($3d_p$, $5d_p$ and $10d_p$) with vertical piles only.

Figure 5.15 shows the IDA-curves for horizontal displacement residual, rotation, and acceleration of the foundation. Increasing pile spacing decreases the foundation rotation and has a negligible effect on foundation acceleration. There are no clear trends with respect to displacement residual.

Figure 5.16 shows the IDA-curves for horizontal displacement residual, rotation, and acceleration at the deck level. Similar trends are observed as for foundation response.

Figure 5.17 shows the IDA-curves for vertical force, shear force and moment at the base level (top foundation). Increasing pile spacing decreases vertical forces, slightly increases shear forces, at least for high PGA-values, and increases moments.

Other remarks

The ability to perform IDA analyses for a number of key variables is a powerful tool in the early design stage of any structures prone to seismic loading. In the context of macro-elements, or any simplified approach for that matter, such analyses allow the engineers to efficiently form a clear overview of how a given change in the design will affect the seismic performance of the structure. This is particularly useful when considering that the complete design of structures reaches far beyond seismic design, and involves several other demands that must be fulfilled.

5.5 Summary

A new finite element framework for seismic analysis of structures accounting for linear and nonlienar SSI was presented. Although the software was implemented and demonstrated for relatively simple bridges frequently encountered in everyday engineering, the solution is valid for any type of structure that may be represented by planar frames. The previously developed macro-element and linear impedance matrix were implemented in a time and modal domain solution, respectively. The software was demonstrated by performing an extensive set of IDA analyses, where the effect of linear and nonlinear SSI, batter angle, pile spacing and asymmetric configuration were addressed and discussed.

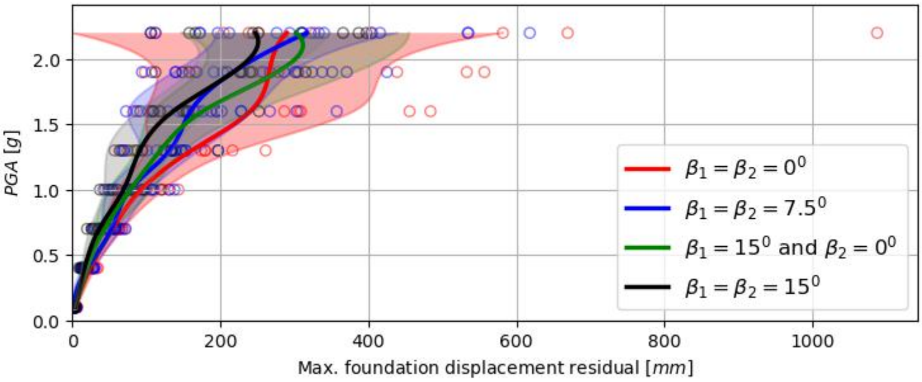

(a) Displacement residual

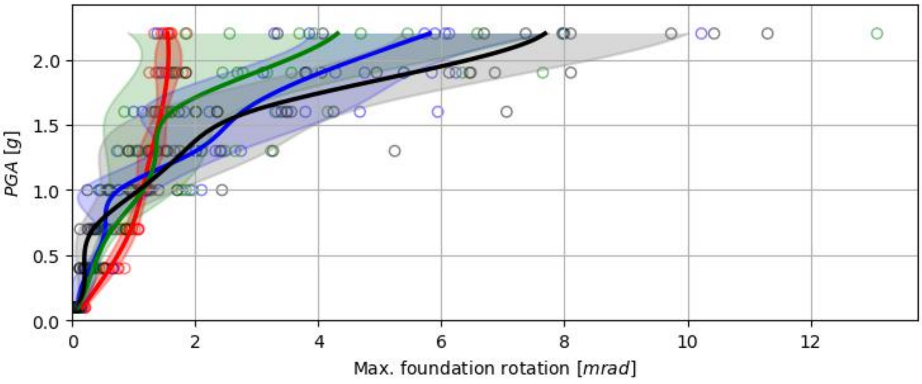

(b) Rotation

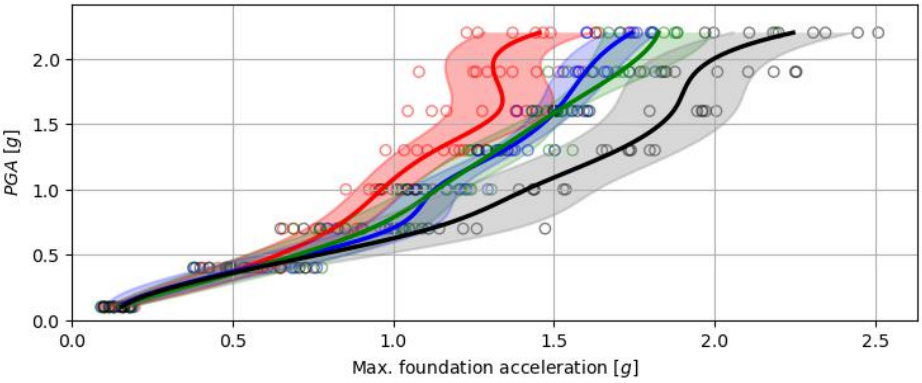

(c) Acceleration

Figure 5.12: IDA-curves showing the effect of batter angle. Foundation response

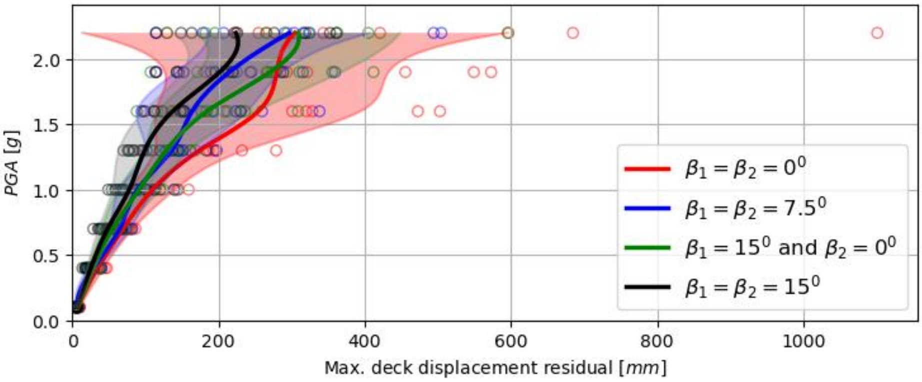

(a) Displacement residual

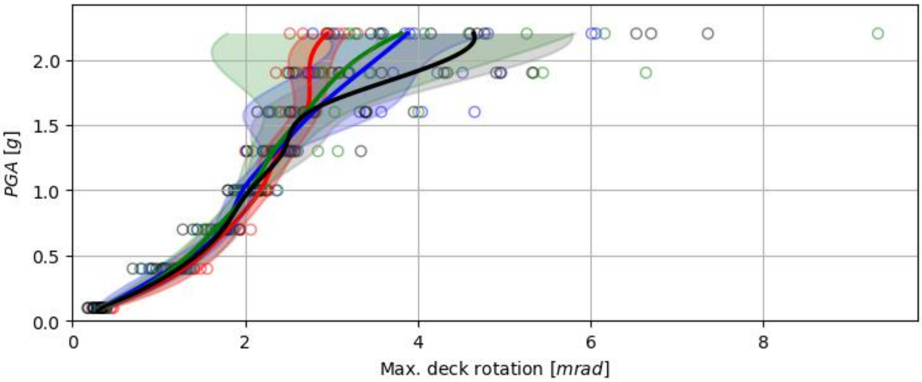

(b) Rotation

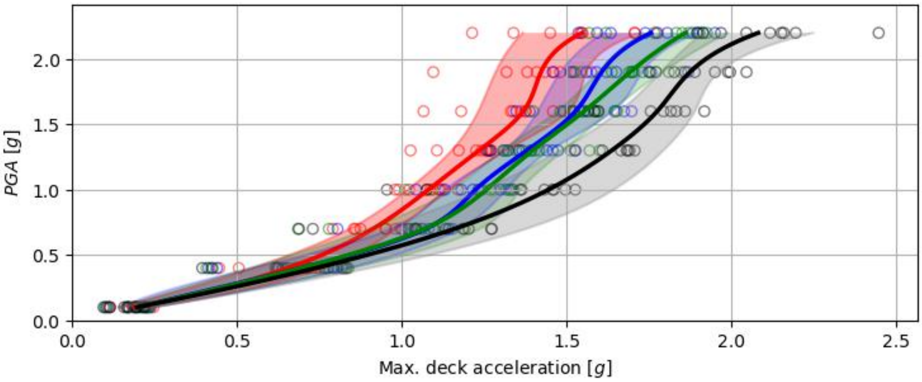

(c) Acceleration

Figure 5.13: IDA-curves showing the effect of batter angle. Deck response

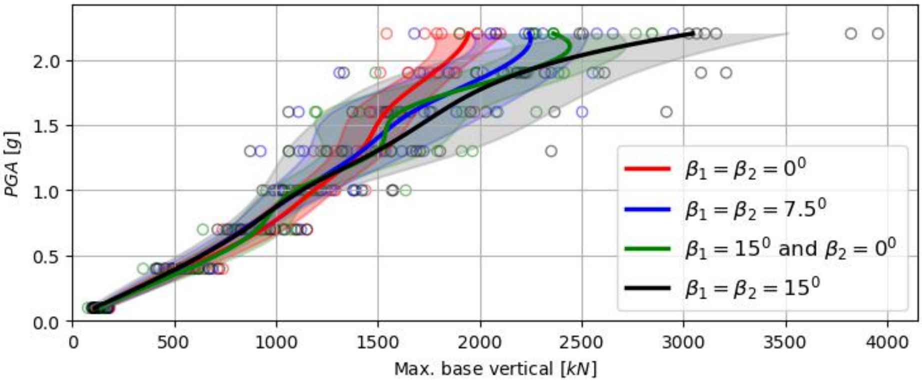

(a) Vertical force

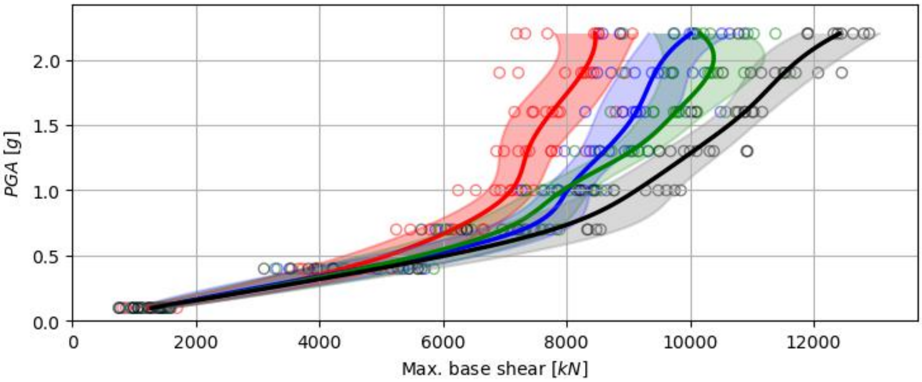

(b) Shear force

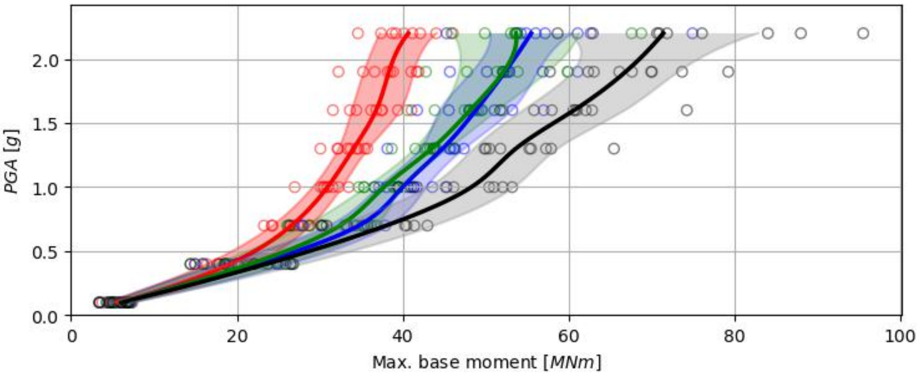

(c) Moment

Figure 5.14: IDA-curves showing the effect of batter angle. Base forces and moment

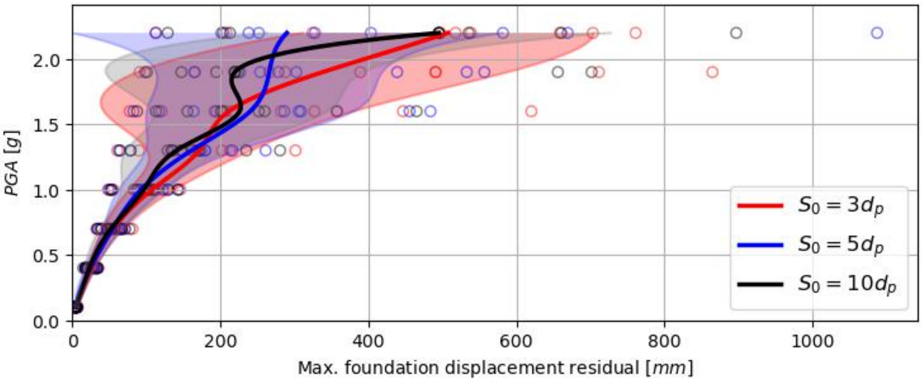

(a) Displacement residual

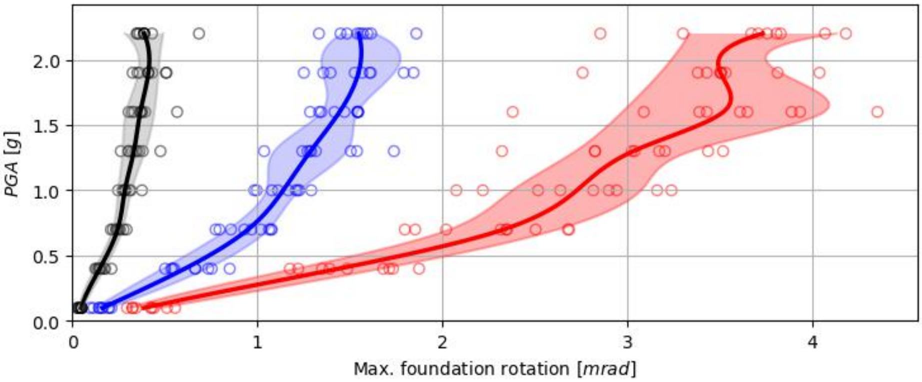

(b) Rotation

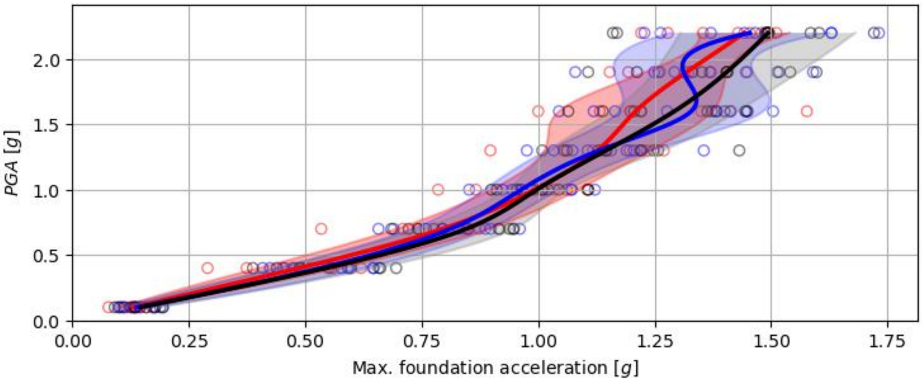

(c) Acceleration

Figure 5.15: IDA-curves showing the effect of pile spacing. Foundation response

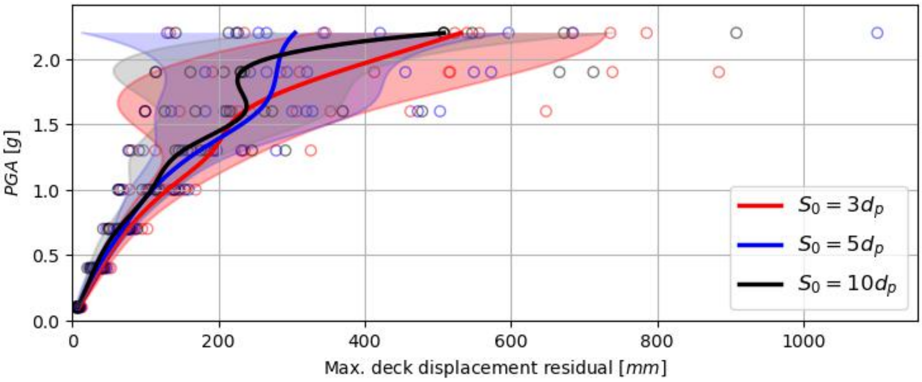

(a) Displacement residual

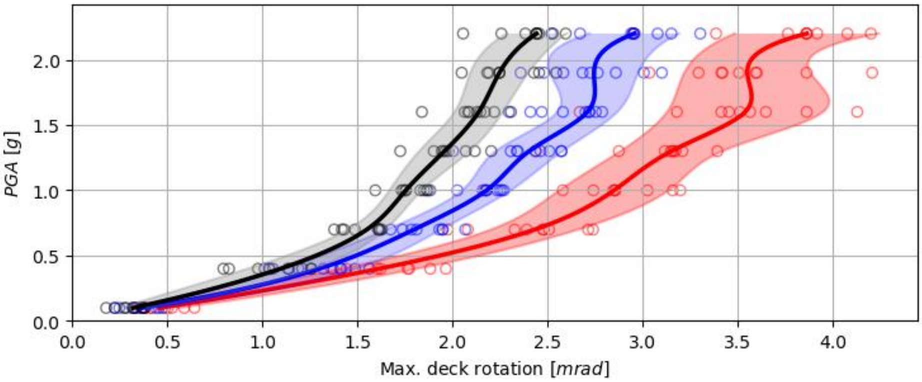

(b) Rotation

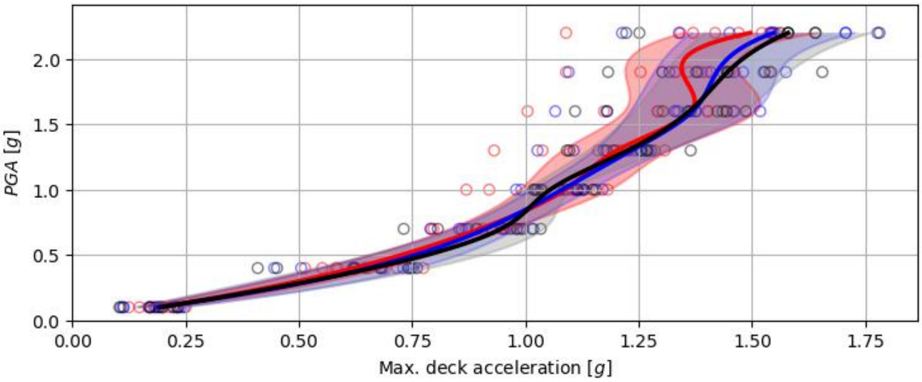

(c) Acceleration

Figure 5.16: IDA-curves showing the effect of pile spacing. Deck response

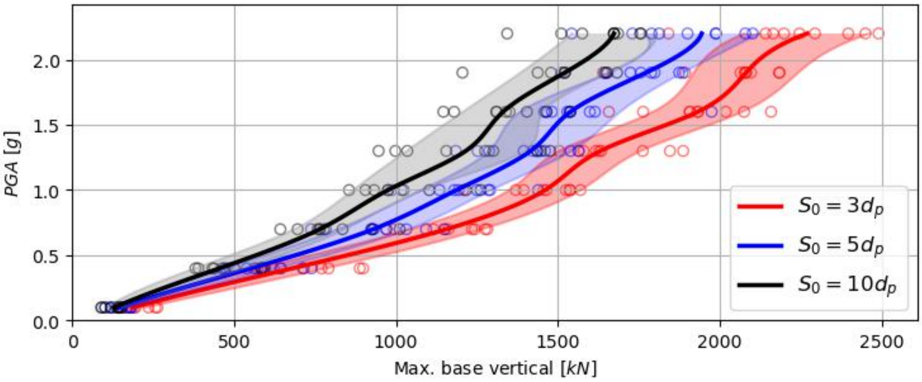

(a) Vertical force

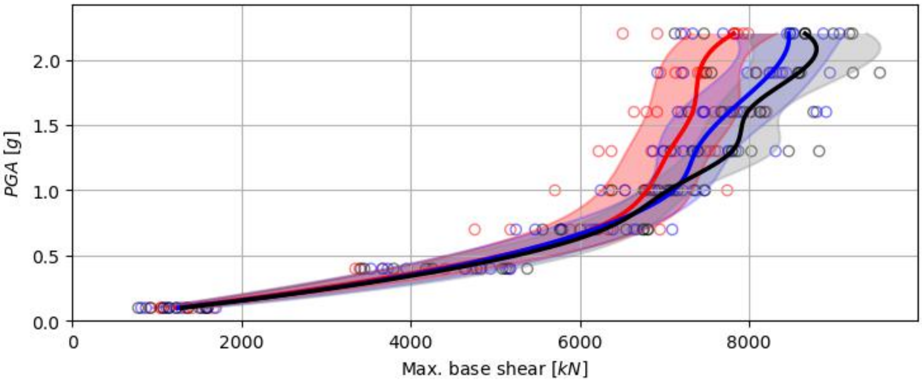

(b) Shear force

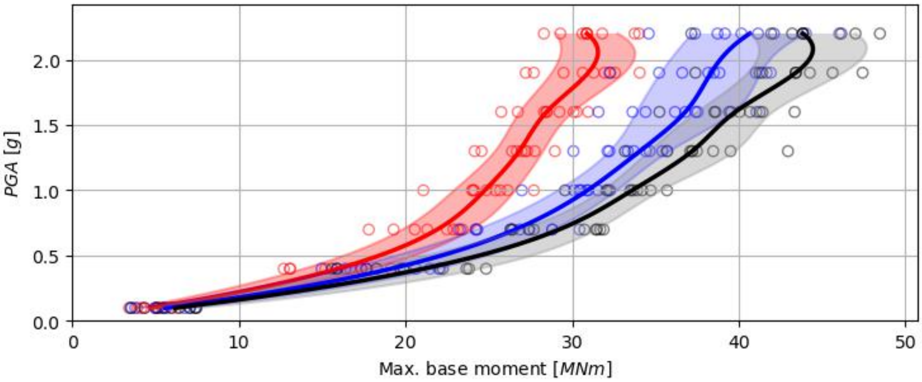

(c) Moment

Figure 5.17: IDA-curves showing the effect of pile spacing. Base forces and moment

Chapter 6

Conclusions and perspectives

6.1 Conclusions

This thesis assessed the seismic response of bridges supported by deep foundations with vertical and batter piles accounting for soil-structure interaction in four parts. The main objective of the thesis was to aid the industry with practical computational methods for analyzing structures, particularly bridges, that are supported by deep foundations using both vertical and batter piles.

The first part (Chapter 2) investigated the kinematic response of vertical and batter pile groups by evaluating how non-linearity, batter angle, pile spacing and excitation frequency affected pile-cap displacements, rotations, maximum pile moments, shear forces and axial forces.

First, a series of harmonic base motion analyses were performed for different pile group configurations. It was found that non-linearity had a profound impact on the horizontal kinematic interaction, where nonlinear models in some cases amplified the ground motion for a wide range of configurations and frequencies. Soil non-linearity significantly increased rotational kinematic interaction for all considered configurations, but substantially reduced displacements and rotations amplitudes. Soil non-linearity also produced less frequency-dependent results. Further, it was found that increasing batter angle decreased horizontal displacements, increased pile-cap rotations, and increased moments, shear forces and normal forces. It was also found that increasing pile spacing decreased pile-cap rotation, while batter angle simultaneously became a more governing factor. Moments and shear forces generally increased with increasing pile spacing, while axial forces simultaneously decreased. Increasing base motion amplitude did not significantly affect the kinematic interaction, but generally increased displacements, rotations, moments, shear forces and axial forces. Pile-cap displacements, rotations, pile moments, shear forces and axial forces generally decreased with increasing frequency, primarily driven by the short-wavelength excitation causing reversing soil displacements over the pile length. Batter angle became less important as frequency increased. Different deformation patterns occurred for vertical and batter pile groups. Pile-cap displacements and rotations were in phase for vertical pile groups and out of phase for batter pile groups, which indicated that the increased pile-cap rotation of batter pile groups is not solely caused by increased axial force magnitude, but also by the direction in which they act.

Next, it was explored how the frequency-dependent findings related to the system response when subjected to real earthquake time histories. For input motions with high PGA, the spectral accelerations of the pile-cap were in some cases lower compared to the spectral acceleration of the input motion. Batter pile groups generally yielded lower spectral accelerations, and the difference between vertical and batter pile groups was almost independent of period. Estimation using nonlinear kinematic interaction factors conservatively estimated the pile-cap displacements and rotations, while roughly captured the effects with respect to batter angle and frequency content.

The second part (Chapter 3) introduced a diagonal impedance matrix for vertical and batter pile groups in linear, homogeneous soil that takes into account pile-soil-pile interaction. The solution is suited for low-exaction seismic problems, vibration problems or estimates in the early-stage design process. The impedance matrix was obtained by simplifying the closed-form solutions of a BWF-problem including pile-soil-pile interaction. This was achieved by eliminating parts of the solution that were considered to have a negligible contribution. The proposed model consists of easy-to-use, spreadsheet-friendly expressions with well-known input variables. However, the limitation of such methods must be recognized. In addition to the inaccuracy introduced by the various simplifications, linear methods are strongly limited in the sense that they cannot capture material (soil) and geometrical (formation of gap) non-linearity, both of which are to be expected during strong earthquake shaking and corresponding inertial loading. The closed-form model is also limited to uniform soil profiles, long (floating) piles, cylindrical pile shapes and fixed-head conditions. Even so, it has been demonstrated that the closed-form model is able to represent the trends associated with batter angle, pile distance and frequency rather well.

The third part (Chapter 4) presented a novel macro-element for vertical and batter pile groups. The solution is intended for realistic nonlinear time-history analyses and efficient estimation of equivalent linear properties. The numerical scheme is based on de-coupled, single pile response, where each pile consists of two separate load-displacement formulations (axial and transverse) that take a displacement increment as input and return a tangent stiffness value. The effect of rotation is implicitly incorporated in the transverse load-displacement formulation. The global tangent stiffness matrix (which is passed to the global solution in a finite element code) is assembled on the basis of the single pile tangent stiffness values. The presented macro-element does not require pre-defined failure surfaces or other parameters, and is therefore not restricted to a specific foundation configuration, soil profile or soil type. The macro-element may be calibrated using any type of nonlinear pile-soil model. Although practical, such simplified formulations are bound to limited validity. First, the accuracy is expected to decrease for small displacement since the formulation neglects radiation damping, which becomes more important for small-strain soil deformations. Second, even though the macro-element performs well within the realistic range of pile spacings in soft soil, further studies on the performance in stiffer soils are needed. Third, axial and transverse response are de-coupled, which inherently introduces an error related to the bounding loads and restricts the macro-element to long piles. Nevertheless, it has been demonstrated that the macro-element is capable of capturing trends associated with pile group configuration, batter angle, pile spacing and soil profile.

The fourth part (Chapter 5) presented a new finite element framework for seismic analysis of structures accounting for linear and nonlienar SSI. Although the software was implemented and demonstrated for relatively simple bridges frequently encountered in everyday engineering, the solution is valid for any type of structure that may be represented by planar frames. The previously developed macro-element and linear impedance matrix were implemented in a time and modal domain solution, respectively. The software was demonstrated by performing an extensive set of IDA analyses, where the effect of linear and nonlinear SSI, batter angle, pile spacing and asymmetric configuration were addressed and discussed.

6.2 Perspectives

Closed-form kinematic interactions factors accounting for nonlinear soil

Although an attempt was made to examine how nonlinear kinematic interaction factors could provide an estimate of FIM, they were based on the results of rigorous finite element analyses. A future study on nonlinear kinematic interactions that could provide closed-form estimates taking into account nonlinear soil behaviour could potentially improve the macro-element approach.

Macro-element: Radiation damping

The macro-element formulation neglects the frequency-dependent radiation damping. For larger displacements, hysteretic damping is expected to dominate the overall damping, and the macro-element may yield reasonable result without further modification. It is possible to approximate radiation damping using the expressions available in the literature [90]. However, these expressions are strictly unsuitable for nonlinear time domain solutions because they are dependent on both frequency and soil stiffness. As an approximation, radiation damping may be added by appropriately selecting frequency and soil stiffness for the task at hand. Since radiation damping increases with frequency, the fundamental frequency may be used in order to minimize potentially excessive damping. The constant soil stiffness may chosen to match the expected shear strain level, which may be approximated according to EC8-Part 5, Table 4.1 [245]. It should be noted that radiation damping vanishes for frequencies lower than the fundamental frequency of the soil deposit, or negligible in the case of a rigid bedrock at relatively shallow depth. Therefore, whether or not to include radiation damping should depend on the task hand. A dedicated study on the implementation, as well as the importance, of radiation damping in the context of the macro-element solution would be valuable.

Macro-element: Pile-soil-pile interaction

The macro-element formulation also neglects pile-soil-pile interaction. As previously discussed, this assumption may decrease the accuracy of the macro-element when the piles are closely spaced. The limited set of analyses presented herein showed that the macro-element performed well for pile spacing's down to $3d_p$, but the analyses were limited to soft soil were it is expected that pile-soil-pile interaction is relatively low [196, 224]. In the context of nonlinear macro-elements, including pile-soil-pile interaction should consider the effect of yielding, preferably through the use of simplified, closed-form solutions.

Macro-element: Bar-beam coupling

The macro-element formulations assumes that the axial and transverse response are de-coupled, which inherently introduces an error related to the bounding load. Considering that the implicit transverse-rotational coupling was implemented successfully, similar strategies may be explored for transverse-axial coupling.

Expansion to 3D

Both the linear impedance matrix and the macro-element are restricted to planar analysis. It would add great value if the formulations, and particularly the macro-element, were extended to three dimensions.

Nonlinear structural behaviour

The analysis in Chapter 5 were restricted to nonlinear foundation response. In reality, nonlinear behaviour extends to all parts of the structure. The in-house software may easily be extended to include inelastic behaviour of the superstructure using either lumped plasticity models or fiber sections.

Backfill-interaction

The interaction between the bridge abutment and the backfill soil is an important part of the overall seismic response. First, the backfill soil causes additional input motion along the abutment wall. Second, the backfill-interaction introduces additional inertia loads on the bridge, which in some cases may be of considerable magnitude, depending on the size of the backfill soil [246]. Third, the backfill-soil may yield additional hysteretic and radiation damping. A practical and simplified approach accounting for the above-mentioned effects would be particularly useful in the assessment of embedded (or partly embedded) structures such IABs and culverts.

REFRENCES

[1] M. Cemalovic, J. B. Husebø, and A. M. Kaynia, "Simplified computational methods for estimating dynamic impedance of batter pile groups in homogeneous soil," *Earthquake Engineering & Structural Dynamics*, vol. 50, no. 14, pp. 3894–3915, 2021.

[2] M. Cemalovic, J. B. Husebø, and A. M. Kaynia, "Kinematic response of vertical and batter pile groups in non-linear soft soil," *Earthquake Engineering & Structural Dynamics*, vol. 51, no. 10, pp. 2248–2266, 2022.

[3] M. Cemalovic, J. M. Castro, and A. M. Kaynia, "Practical macro-element for vertical and batter pile groups," *Earthquake Engineering & Structural Dynamics*, vol. 52, no. 4, pp. 1091–1111, 2023.

[4] E. Kausel, "Early history of soil–structure interaction," *Soil Dynamics and Earthquake Engineering*, vol. 30, no. 9, pp. 822–832, 2010.

[5] M. Lou, H. Wang, X. Chen, and Y. Zhai, "Structure–soil–structure interaction: Literature review," *Soil dynamics and earthquake engineering*, vol. 31, no. 12, pp. 1724–1731, 2011.

[6] U. O. f. D. R. R. Centre for Research on the Epidemiology of Disasters (CRED), "The human cost of disasters: An overview of the last 20 years (2000–2019)," 2020.

[7] G. Gazetas and G. Mylonakis, "Seismic soil-structure interaction: new evidence and emerging issues," *Geotechnical special publication*, no. 75 II, pp. 1119–1174, 1998.

[8] U.S. Geological Survey, “Harthquake hazards.” https://www.usgs.gov/media/slideshows/1989-loma-prieta.

[9] R. B. Seed, “Preliminary report on the principal geotechnical aspects of the october 17, 1989, loma prieta earthquake,” *Report No. UCB/EERC-90/05*, 1990.

[10] S. Ravazi, A. Fahker, and S. R. Mirghaderi, “An insight into the bad reputation of batter piles in seismic performance of wharves,” in *4th international conference on earthquake geotechnical engineering, Thessaloniki, June*, vol. 2528, 2007.

[11] C. E. de Normalisation, “Eurocode 8: Design of structures for earthquake resistance: Part 1: General rules, seismic actions and rules for buildings,” 2004.

[12] M. Sadek and S. Isam, “Three-dimensional finite element analysis of the seismic behavior of inclined micropiles,” *Soil Dynamics and Earthquake Engineering*, vol. 24, no. 6, pp. 473–485, 2004.

[13] N. Gerolymos, A. Giannakou, I. Anastasopoulos, and G. Gazetas, “Evidence of beneficial role of inclined piles: observations and summary of numerical analyses,” *Bulletin of Earthquake Engineering*, vol. 6, no. 4, pp. 705–722, 2008.

[14] A. Giannakou, N. Gerolymos, G. Gazetas, T. Tazoh, and I. Anastasopoulos, “Seismic behavior of batter piles: elastic response,” *Journal of Geotechnical and Geoenvironmental Engineering*, vol. 136, no. 9, pp. 1187–1199, 2010.

[15] C. Medina, L. A. Padrón, J. J. Aznárez, and O. Maeso, “Influence of pile inclination angle on the dynamic properties and seismic response of piled structures,” *Soil Dynamics and Earthquake Engineering*, vol. 69, pp. 196–206, 2015.

[16] S. Carbonari, M. Morici, F. Dezi, F. Gara, and G. Leoni, “Soil-structure interaction effects in single bridge piers founded on inclined pile groups,” *Soil Dynamics and Earthquake Engineering*, vol. 92, pp. 52–67, 2017.

[17] S. Escoffier, “Experimental study of the effect of inclined pile on the seismic behavior of pile group,” *Soil Dynamics and Earthquake Engineering*, vol. 42, pp. 275–291, 2012.

[18] R. Subramanian and A. Boominathan, "Dynamic experimental studies on lateral behaviour of batter piles in soft clay," *International Journal of Geotechnical Engineering*, vol. 10, no. 4, pp. 317–327, 2016.

[19] M. Bharathi, R. Dubey, and S. K. Shukla, "Experimental investigation of vertical and batter pile groups subjected to dynamic loads," *Soil Dynamics and Earthquake Engineering*, vol. 116, pp. 107–119, 2019.

[20] R. E. Harn, "Have batter piles gotten a bad rap in seismic zones?(or everything you wanted to know about batter piles but were afraid to ask)," *Ports 2004: Port Development in the Changing World*, pp. 1–10, 2004.

[21] E. Winckler, "Die lehre von elastizitat und festigkeit (on elasticity and fixity)," *Prague, 182p*, 1867.

[22] M. Hetényi and M. I. Hetbenyi, *Beams on elastic foundation: theory with applications in the fields of civil and mechanical engineering*, vol. 16. University of Michigan press Ann Arbor, MI, 1946.

[23] B. McClelland and J. A. Focht Jr, "Soil modulus for laterally loaded piles," *Transactions of the american society of civil engineers*, vol. 123, no. 1, pp. 1049–1063, 1958.

[24] B. B. Broms, "Lateral resistance of piles in cohesive soils," *Journal of the Soil Mechanics and Foundations Division*, vol. 90, no. 2, pp. 27–64, 1964.

[25] B. B. Broms, "Lateral resistance of piles in cohesionless soils," *Journal of the Soil Mechanics and Foundations Division*, vol. 90, no. 3, pp. 123–158, 1964.

[26] H. Matlock and L. C. Reese, "Generalized solutions for laterally loaded piles," *Journal of the Soil Mechanics and foundations Division*, vol. 86, no. 5, pp. 63–92, 1960.

[27] H. Matlock and L. C. Reese, "Generalized solutions for laterally loaded piles," *Transactions of the American Society of Civil Engineers*, vol. 127, no. 1, pp. 1220–1247, 1962.

[28] H. Matlock, "Correlation for design of laterally loaded piles in soft clay," in *Offshore technology conference*, OnePetro, 1970.

[29] L. C. Reese, W. R. Cox, and F. D. Koop, "Field testing and analysis of laterally loaded piles om stiff clay," in *Offshore technology conference*, OnePetro, 1975.

[30] R. Welch and L. Reese, “Lateral load behavior of drilled shafts. report 89-10,” *Center for Highway Research, University of Texas at Austin*, 1972.

[31] L. C. Reese, W. R. Cox, and F. D. Koop, “Analysis of laterally loaded piles in sand,” in *Offshore Technology Conference*, OnePetro, 1974.

[32] L. Reese and K. Nyman, “Field load test of instrumented drilled shafts at islamorada,” *Florida. a report to Girder Foundation and Exploration Coporation, Clearwater, Florida*, 1978.

[33] W. R. Cox, L. C. Reese, and B. R. Grubbs, “Field testing of laterally loaded piles in sand,” in *Offshore Technology Conference*, OnePetro, 1974.

[34] S.-T. Wang, “Design of pile foundations in liquefied soils,” *Proc. Geotech. Earthq. Engrg. and Soil Dynamics III, 1998*, vol. 2, pp. 1331–1343, 1998.

[35] M. Simpson, D. Brown, *et al.*, “Development of py curves for piedmont residual soils.,” 2003.

[36] K. M. Rollins, T. M. Gerber, J. D. Lane, and S. A. Ashford, “Lateral resistance of a full-scale pile group in liquefied sand,” *Journal of Geotechnical and Geoenvironmental Engineering*, vol. 131, no. 1, pp. 115–125, 2005.

[37] R. Johnson, R. L. Parsons, S. Dapp, and D. Brown, “Soil characterization and py curve development for loess,” tech. rep., 2007.

[38] R. Liang, K. Yang, and J. Nusairat, “p-y criterion for rock mass,” *Journal of geotechnical and geoenvironmental engineering*, vol. 135, no. 1, pp. 26–36, 2009.

[39] K. W. Franke and K. M. Rollins, “Simplified hybrid p-y spring model for liquefied soils,” *Journal of geotechnical and geoenvironmental engineering*, vol. 139, no. 4, pp. 564–576, 2013.

[40] J. M. Duncan, L. T. Evans Jr, and P. S. Ooi, “Lateral load analysis of single piles and drilled shafts,” *Journal of geotechnical engineering*, vol. 120, no. 6, pp. 1018–1033, 1994.

[41] D. A. Brown, S. A. Hidden, and S. Zhang, “Determination of py curves using inclinometer data,” *Geotechnical Testing Journal*, vol. 17, no. 2, pp. 150–158, 1994.

[42] S.-S. Lin and J.-C. Liao, “Lateral response evaluation of single piles using inclinometer data,” *Journal of Geotechnical and Geoenvironmental Engineering*, vol. 132, no. 12, pp. 1566–1573, 2006.

[43] P. L. Pinto, B. Anderson, and F. C. Townsend, “Comparison of horizontal load transfer curves for laterally loaded piles from strain gages and slope inclinometer: A case study,” in *Field instrumentation for soil and rock*, ASTM International, 1999.

[44] M. Ashour, G. Norris, and P. Pilling, “Lateral loading of a pile in layered soil using the strain wedge model,” *Journal of geotechnical and geoenvironmental engineering*, vol. 124, no. 4, pp. 303–315, 1998.

[45] M. Ashour and G. Norris, “Modeling lateral soil-pile response based on soil-pile interaction,” *Journal of Geotechnical and Geoenvironmental Engineering*, vol. 126, no. 5, pp. 420–428, 2000.

[46] M. Ashour, G. Norris, and P. Pilling, “Strain wedge model capability of analyzing behavior of laterally loaded isolated piles, drilled shafts, and pile groups,” *Journal of Bridge Engineering*, vol. 7, no. 4, pp. 245–254, 2002.

[47] M. Ashour and G. Norris, “Lateral loaded pile response in liquefiable soil,” *Journal of Geotechnical and Geoenvironmental Engineering*, vol. 129, no. 5, pp. 404–414, 2003.

[48] L.-Y. Xu, F. Cai, G.-X. Wang, and K. Ugai, “Nonlinear analysis of laterally loaded single piles in sand using modified strain wedge model,” *Computers and Geotechnics*, vol. 51, pp. 60–71, 2013.

[49] M. Hajialilue-Bonab, Y. Sojoudi, A. J. Puppala, *et al.*, “Study of strain wedge parameters for laterally loaded piles,” *Int. J. Geomech*, vol. 10, no. 1061, pp. 143–152, 2013.

[50] M. Heidari, H. El Naggar, M. Jahanandish, and A. Ghahramani, “Generalized cyclic p–y curve modeling for analysis of laterally loaded piles,” *Soil Dynamics and Earthquake Engineering*, vol. 63, pp. 138–149, 2014.

[51] K. Kim, B. H. Nam, and H. Youn, “Effect of cyclic loading on the lateral behavior of offshore monopiles using the strain wedge model,” *Mathematical Problems in Engineering*, vol. 2015, 2015.

[52] L.-Y. Xu, F. Cai, G.-X. Wang, and G.-X. Chen, “Nonlinear analysis of single laterally loaded piles in clays using modified strain wedge model,” *International Journal of Civil Engineering*, vol. 15, no. 6, pp. 895–906, 2017.

[53] W. Peng, M. Zhao, Y. Xiao, C. Yang, and H. Zhao, “Analysis of laterally loaded piles in sloping ground using a modified strain wedge model,” *Computers and Geotechnics*, vol. 107, pp. 163–175, 2019.

[54] L.-Y. Xu, F. Cai, and Y.-Y. Xue, “Implementation of state-dependent plasticity model in strain wedge model for laterally loaded piles in sand,” *Marine Georesources & Geotechnology*, vol. 37, no. 5, pp. 622–632, 2019.

[55] H. Matlock, S. H. Foo, *et al.*, “Simulation of lateral pile behavior under earthquake motion,” in *From Volume I of Earthquake Engineering and Soil Dynamics–Proceedings of the ASCE Geotechnical Engineering Division Specialty Conference, June 19-21, 1978, Pasadena, California. Sponsored by Geotechnical Engineering Division of ASCE in cooperation with:*, no. Proceeding, 1978.

[56] T. Kagawa and L. M. Kraft, “Lateral load-deflection relationships of piles subjected to dynamic loadings,” *Soils and Foundations*, vol. 20, no. 4, pp. 19–36, 1980.

[57] T. Kagawa and L. M. Kraft Jr, “Seismic p y responses of flexible piles,” *Journal of the Geotechnical Engineering Division*, vol. 106, no. 8, pp. 899–918, 1980.

[58] H. Matlock, G. R. Martin, I. P. Lam, and C.-F. Tsai, “Soil-pile interaction in liquefiable cohesionless soils during earthquake loading,” in *Proceedings of an International Conference on Recent Advances in Geotechnical Earthquake Engineering and Soil Dynamics, St. Louis, Missouri*, vol. 2, 1981.

[59] T. Kagawa and L. M. Kraft Jr, “Lateral pile response during earthquakes,” *Journal of the Geotechnical Engineering Division*, vol. 107, no. 12, pp. 1713–1731, 1981.

[60] D. P. Carter, *A non-linear soil model for predicting lateral pile response*. PhD thesis, ResearchSpace@ Auckland, 1984.

[61] T. Nogami and K. Konagai, “Time domain flexural response of dynamically loaded single piles,” *Journal of Engineering Mechanics*, vol. 114, no. 9, pp. 1512–1525, 1988.

[62] T. Nogami and K. Konagai, “Time domain axial response of dynamically loaded single piles,” *Journal of Engineering Mechanics*, vol. 112, no. 11, pp. 1241–1252, 1986.

[63] T. Nogami, J. Otani, K. Konagai, and H.-L. Chen, "Nonlinear soil-pile interaction model for dynamic lateral motion," *Journal of Geotechnical Engineering*, vol. 118, no. 1, pp. 89–106, 1992.

[64] M. H. El Naggar and M. Novak, "Non-linear model for dynamic axial pile response," *Journal of geotechnical engineering*, vol. 120, no. 2, pp. 308–329, 1994.

[65] M. El Naggar and M. Novak, "Nonlinear lateral interaction in pile dynamics," *Soil Dynamics and Earthquake Engineering*, vol. 14, no. 2, pp. 141–157, 1995.

[66] M. El Naggar and M. Novak, "Nonlinear analysis for dynamic lateral pile response," *Soil Dynamics and Earthquake Engineering*, vol. 15, no. 4, pp. 233–244, 1996.

[67] D. Badoni and N. Makris, "Nonlinear response of single piles under lateral inertial and seismic loads," *Soil Dynamics and Earthquake Engineering*, vol. 15, no. 1, pp. 29–43, 1996.

[68] M. J. Pender and S. Pranjoto, "Gapping effects during cyclic lateral loading of piles in clay," in *Proceedings 11th World Conference on Earthquake Engineering, Mexico, Paper*, no. 1007, 1996.

[69] R. W. Boulanger, C. J. Curras, B. L. Kutter, D. W. Wilson, and A. Abghari, "Seismic soil-pile-structure interaction experiments and analyses," *Journal of geotechnical and geoenvironmental engineering*, vol. 125, no. 9, pp. 750–759, 1999.

[70] N. Gerolymos and G. Gazetas, "Phenomenological model applied to inelastic response of soil-pile interaction systems," *Soils and Foundations*, vol. 45, no. 4, pp. 119–132, 2005.

[71] E. Taciroglu, C. Rha, and J. W. Wallace, "A robust macroelement model for soil-pile interaction under cyclic loads," *Journal of geotechnical and geoenvironmental engineering*, vol. 132, no. 10, pp. 1304–1314, 2006.

[72] C. Rha and E. Taciroglu, "Coupled macroelement model of soil-structure interaction in deep foundations," *Journal of Engineering Mechanics*, vol. 133, no. 12, pp. 1326–1340, 2007.

[73] N. Allotey and M. H. El Naggar, "Generalized dynamic winkler model for nonlinear soil–structure interaction analysis," *Canadian Geotechnical Journal*, vol. 45, no. 4, pp. 560–573, 2008.

[74] L. M. Kraft Jr, R. P. Ray, and T. Kagawa, “Theoretical t-z curves,” *Journal of the Geotechnical Engineering Division*, vol. 107, no. 11, pp. 1543–1561, 1981.

[75] J. Chin and H. Poulus, “A “tz” approach for cyclic axial loading analysis of single piles,” *Computers and Geotechnics*, vol. 12, no. 4, pp. 289–320, 1991.

[76] H. Zhu and M.-F. Chang, “Load transfer curves along bored piles considering modulus degradation,” *Journal of Geotechnical and Geoenvironmental Engineering*, vol. 128, no. 9, pp. 764–774, 2002.

[77] S. Nanda and N. Patra, “Theoretical load-transfer curves along piles considering soil nonlinearity,” *Journal of Geotechnical and Geoenvironmental Engineering*, vol. 140, no. 1, pp. 91–101, 2014.

[78] A. H. Bateman, J. J. Crispin, P. J. Vardanega, and G. E. Mylonakis, “Theoretical t-z curves for axially loaded piles,” *Journal of Geotechnical and Geoenvironmental Engineering*, vol. 148, no. 7, p. 04022052, 2022.

[79] R. D. Mindlin, “Force at a point in the interior of a semi-infinite solid,” *physics*, vol. 7, no. 5, pp. 195–202, 1936.

[80] H. G. Poulos, “Behavior of laterally loaded piles: I-single piles,” *Journal of the Soil Mechanics and Foundations Division*, vol. 97, no. 5, pp. 711–731, 1971.

[81] H. G. Poulos, “Behavior of laterally loaded piles: Ii-pile groups,” *Journal of the Soil Mechanics and Foundations Division*, vol. 97, no. 5, pp. 733–751, 1971.

[82] M. Novak, “Dynamic stiffness and damping of piles,” *Canadian Geotechnical Journal*, vol. 11, no. 4, pp. 574–598, 1974.

[83] M. Novak, “Vertical vibration of floating piles,” *Journal of the Engineering Mechanics Division*, vol. 103, no. 1, pp. 153–168, 1977.

[84] T. Nogami and M. Novak, “Resistance of soil to a horizontally vibrating pile,” *Earthquake Engineering & Structural Dynamics*, vol. 5, no. 3, pp. 249–261, 1977.

[85] T. Nogami and M. Novák, “Soil-pile interaction in vertical vibration,” *Earthquake Engineering & Structural Dynamics*, vol. 4, no. 3, pp. 277–293, 1976.

[86] M. Novak and T. Nogami, “Soil-pile interaction in horizontal vibration,” *Earthquake Engineering & Structural Dynamics*, vol. 5, no. 3, pp. 263–281, 1977.

[87] M. Novak, F. Aboul-Ella, and T. Nogami, “Dynamic soil reactions for plane strain case,” *Journal of the Engineering Mechanics Division*, vol. 104, no. 4, pp. 953–959, 1978.

[88] M. F. Randolph, “The response of flexible piles to lateral loading,” *Geotechnique*, vol. 31, no. 2, pp. 247–259, 1981.

[89] G. Gazetas and R. Dobry, “Horizontal response of piles in layered soils,” *Journal of Geotechnical engineering*, vol. 110, no. 1, pp. 20–40, 1984.

[90] G. Gazetas, “Foundation vibrations,” in *Foundation engineering handbook*, pp. 553–593, Springer, 1991.

[91] K. Krabbenhøft, “Basic computational plasticity,” *University of Denmark*, 2002.

[92] F. Irgens, *Continuum mechanics.* Springer Science & Business Media, 2008.

[93] H. Tresca, “Mémoire sur l’écoulement des corps solides soumis à des fortes pressions, compte-rendu, 59,” 1864.

[94] R. v. Mises, “Mechanik der festen körper im plastisch-deformablen zustand,” *Nachrichten von der Gesellschaft der Wissenschaften zu Göttingen, Mathematisch-Physikalische Klasse*, vol. 1913, pp. 582–592, 1913.

[95] A. Hershey, “The plasticity of an isotropic aggregate of anisotropic face-centered cubic crystals,” 1954.

[96] D. C. Drucker and W. Prager, “Soil mechanics and plastic analysis or limit design,” *Quarterly of applied mathematics*, vol. 10, no. 2, pp. 157–165, 1952.

[97] P. V. Lade and J. M. Duncan, “Elastoplastic stress-strain theory for cohesionless soil,” *Journal of the Geotechnical Engineering Division*, vol. 101, no. 10, pp. 1037–1053, 1975.

[98] H. Matsuoka and T. Nakai, “Relationship among tresca, mises, mohr-coulomb and matsuoka-nakai failure criteria,” *Soils and Foundations*, vol. 25, no. 4, pp. 123–128, 1985.

[99] R. Hill, “A theory of the yielding and plastic flow of anisotropic metals,” *Proceedings of the Royal Society of London. Series A. Mathematical and Physical Sciences*, vol. 193, no. 1033, pp. 281–297, 1948.

[100] F. Barlat, J. W. Yoon, and O. Cazacu, “On linear transformations of stress tensors for the description of plastic anisotropy,” *International Journal of Plasticity*, vol. 23, no. 5, pp. 876–896, 2007.

[101] D. C. Drucker, R. E. Gibson, and D. J. Henkel, “Soil mechanics and work-hardening theories of plasticity,” *Transactions of the American Society of Civil Engineers*, vol. 122, no. 1, pp. 338–346, 1957.

[102] J. T. Christian, *Plane-strain deformation analysis of soil.* PhD thesis, Massachusetts Institute of Technology, 1966.

[103] F. L. DiMaggio and I. S. Sandler, “Material model for granular soils,” *Journal of the Engineering mechanics Division*, vol. 97, no. 3, pp. 935–950, 1971.

[104] F. L. DiMaggio and I. Sandler, “The effect of strain rate on the constitutive equations of rocks,” tech. rep., WEIDLINGER (PAUL) NEW YORK, 1971.

[105] J. Isenberg, D. Vaughan, and I. Sandler, “Nonlinear soil-structure interaction,” *Final Report Weidlinger Associates*, 1978.

[106] I. Sandler and M. Baron, “Recent developments in the constitutive modeling of geological materials,” in *Proceedings of the 3rd Conference on Numerical Methods in Geomechanics, Aachen, Wittke (ed), Balkema/Rotterdam*, vol. 1, pp. 363–376, 1979.

[107] H. Levine, *A two-surface plastic and microcracking model for plain concrete.* ASME, 1982.

[108] I. Sandler, F. DiMaggio, and M. Baron, “An extension of the cap model for the inclusion of pore pressure effects and kinematic hardening in a cap model representation of an anisotropic wet clay,” *Mechanics of Engineering Materials, John Wiley*, 1983.

[109] J. Mould, H. Levine, and D. Tennant, “Evaluation of a rate-dependent three invariant softening model for concrete,” *Fracture and Damage in Quasibrittle Structures, edited by ZP Bazant, Z. Bittnar, M. Jirasek and J. Mazars, E & FN Spon, Chapman and Hall, London, UK*, p. 231, 1994.

[110] T. Benz, M. Wehnert, and P. Vermeer, “A lode angle dependent formulation of the hardening soil model,” in *The 12th International Conference of International Association for Computer Methods and Advances in Geomechanics (IACMAG)*, pp. 1–6, 2008.

[111] M. Jefferies and K. Been, *Soil liquefaction: a critical state approach.* CRC press, 2015.

[112] W. D. Iwan, “On a class of models for the yielding behavior of continuous and composite systems,” 1967.

[113] Z. Mroz, “On the description of anisotropic workhardening,” *Journal of the Mechanics and Physics of Solids*, vol. 15, no. 3, pp. 163–175, 1967.

[114] Z. Mroz, “Elastoplastic and viscoplastic constitutive models for soils with application to cyclic loading,” *Soil mechanics-transient and cyclic loads*, pp. 173–217, 1982.

[115] J. H. Prévost, “Plasticity theory for soil stress-strain behavior,” *Journal of the Engineering Mechanics Division*, vol. 104, no. 5, pp. 1177–1194, 1978.

[116] J. H. Prevost, “A simple plasticity theory for frictional cohesionless soils,” *International Journal of Soil Dynamics and Earthquake Engineering*, vol. 4, no. 1, pp. 9–17, 1985.

[117] E. J. Parra-Colmenares, *Numerical modeling of liquefaction and lateral ground deformation including cyclic mobility and dilation response in soil systems.* Rensselaer Polytechnic Institute, 1996.

[118] A. Elgamal, Z. Yang, and E. Parra, “Computational modeling of cyclic mobility and post-liquefaction site response,” *Soil Dynamics and Earthquake Engineering*, vol. 22, no. 4, pp. 259–271, 2002.

[119] A. Elgamal, Z. Yang, E. Parra, and A. Ragheb, “Modeling of cyclic mobility in saturated cohesionless soils,” *International Journal of Plasticity*, vol. 19, no. 6, pp. 883–905, 2003.

[120] Z. Yang and A. Elgamal, “Influence of permeability on liquefaction-induced shear deformation,” *Journal of Engineering Mechanics*, vol. 128, no. 7, pp. 720–729, 2002.

[121] Z. Yang, A. Elgamal, and E. Parra, “Computational model for cyclic mobility and associated shear deformation,” *Journal of Geotechnical and Geoenvironmental Engineering*, vol. 129, no. 12, pp. 1119–1127, 2003.

[122] A. Khosravifar, A. Elgamal, J. Lu, and J. Li, “A 3d model for earthquake-induced liquefaction triggering and post-liquefaction response,” *Soil Dynamics and Earthquake Engineering*, vol. 110, pp. 43–52, 2018.

[123] Y. Dafalias and E. Popov, “A model of nonlinearly hardening materials for complex loading,” *Acta mechanica*, vol. 21, no. 3, pp. 173–192, 1975.

[124] Y. Dafalias, “Bounding surface formulation of soil plasticity,” *Soil mechanics-transient and cyclic loads*, pp. 253–282, 1982.

[125] Y. F. Dafalias, “Bounding surface plasticity. i: Mathematical foundation and hypoplasticity,” *Journal of engineering mechanics*, vol. 112, no. 9, pp. 966–987, 1986.

[126] Y. F. Dafalias and L. R. Herrmann, “Bounding surface plasticity. ii: Application to isotropic cohesive soils,” *Journal of Engineering Mechanics*, vol. 112, no. 12, pp. 1263–1291, 1986.

[127] M. Fragiadakis and M. Papadrakakis, “Modeling, analysis and reliability of seismically excited structures: computational issues,” *International journal of computational methods*, vol. 5, no. 04, pp. 483–511, 2008.

[128] A. Calabrese, J. P. Almeida, and R. Pinho, “Numerical issues in distributed inelasticity modeling of rc frame elements for seismic analysis,” *Journal of Earthquake Engineering*, vol. 14, no. S1, pp. 38–68, 2010.

[129] J. E. Luco and L. Contesse, “Dynamic structure-soil-structure interaction,” *Bulletin of the Seismological Society of America*, vol. 63, no. 4, pp. 1289–1303, 1973.

[130] G. Mylonakis and G. Gazetas, “Seismic soil-structure interaction: beneficial or detrimental?,” *Journal of earthquake engineering*, vol. 4, no. 3, pp. 277–301, 2000.

[131] J. Avilés and L. E. Pérez-Rocha, “Soil–structure interaction in yielding systems,” *Earthquake engineering & structural dynamics*, vol. 32, no. 11, pp. 1749–1771, 2003.

[132] M. El Naggar, “Bridging the gap between structural and geotechnical engineers in ssi for performance-based design,” in *Special Topics in Earthquake Geotechnical Engineering*, pp. 315–351, Springer, 2012.

[133] E. Kausel, R. V. Whitman, J. P. Morray, and F. Elsabee, “The spring method for embedded foundations,” *Nuclear Engineering and design*, vol. 48, no. 2-3, pp. 377–392, 1978.

[134] A. M. Kaynia, “Dynamic stiffnesses and seismic response of pile groups.,” Research Report R82-03, Dept. Civil Eng. MIT, Cambridge, USA, 1982.

[135] A. M. Kaynia and E. Kausel, “Dynamics of piles and pile groups in layered soil media,” *Soil Dynamics and Earthquake Engineering*, vol. 10, no. 8, pp. 386–401, 1991.

[136] K. Fan, G. Gazetas, A. Kaynia, E. Kausel, and S. Ahmad, “Kinematic seismic response of single piles and pile groups,” *Journal of Geotechnical Engineering*, vol. 117, no. 12, pp. 1860–1879, 1991.

[137] G. Gazetas, “Seismic response of end-bearing single piles,” *International Journal of Soil Dynamics and Earthquake Engineering*, vol. 3, no. 2, pp. 82–93, 1984.

[138] N. Makris and G. Gazetas, “Dynamic pile-soil-pile interaction. part ii: Lateral and seismic response,” *Earthquake engineering & structural dynamics*, vol. 21, no. 2, pp. 145–162, 1992.

[139] N. Makris, “Soil–pile interaction during the passage of rayleigh waves: an analytical solution,” *Earthquake engineering & structural dynamics*, vol. 23, no. 2, pp. 153–167, 1994.

[140] G. Gazetas, K. Fan, and A. Kaynia, “Dynamic response of pile groups with different configurations,” *Soil Dynamics and Earthquake Engineering*, vol. 12, no. 4, pp. 239–257, 1993.

[141] M. Kavvads and G. Gazetas, “Kinematic seismic response and bending of free-head piles in layered soil,” *Geotechnique*, vol. 43, no. 2, pp. 207–222, 1993.

[142] G. Mylonakis and G. Gazetas, “Kinematic pile response to vertical p-wave seismic excitation,” *Journal of Geotechnical and geoenvironmental Engineering*, vol. 128, no. 10, pp. 860–867, 2002.

[143] F. Dezi, S. Carbonari, and G. Leoni, “A model for the 3d kinematic interaction analysis of pile groups in layered soils,” *Earthquake Engineering & Structural Dynamics*, vol. 38, no. 11, pp. 1281–1305, 2009.

[144] A. M. Kaynia, “Dynamic response of pile foundations with flexible slabs,” *Earthquakes and Structures*, vol. 3, no. 3-4, pp. 495–506, 2012.

[145] G. Anoyatis, R. Di Laora, A. Mandolini, and G. Mylonakis, “Kinematic response of single piles for different boundary conditions: analytical solutions and normalization schemes,” *Soil Dynamics and Earthquake Engineering*, vol. 44, pp. 183–195, 2013.

[146] G. M. Alamo, J. J. Aznárez, L. A. Padrón, A. E. Martinez-Castro, and O. Maeso, “Importance of using accurate soil profiles for the estimation of pile kinematic input factors,” *Journal of Geotechnical and Geoenvironmental Engineering*, vol. 145, no. 8, p. 04019035, 2019.

[147] T. Belytschko, W. K. Liu, B. Moran, and K. Elkhodary, *Nonlinear finite elements for continua and structures*. John Wiley & Sons, 2014.

[148] B. Kolbein, *Engineering approach to finite element analysis of linear structural mechanics problems*. Akademika Publishing, 2015.

[149] R. Nova and L. Montrasio, “Settlements of shallow foundations on sand,” *Géotechnique*, vol. 41, no. 2, pp. 243–256, 1991.

[150] R. Paolucci, “Simplified evaluation of earthquake-induced permanent displacements of shallow foundations,” *Journal of Earthquake Engineering*, vol. 1, no. 03, pp. 563–579, 1997.

[151] S. Pedretti, “Nonlinear seismic soil-foundation interaction: analysis and modelling method,” *PhD. Department of Structural Engineering, Politecnico di Milano, Italy*, 1998.

[152] G. Gottardi, G. Houlsby, and R. Butterfield, “Plastic response of circular footings on sand under general planar loading,” *Géotechnique*, vol. 49, no. 4, pp. 453–469, 1999.

[153] Y. Le Pape and J.-G. Sieffert, “Application of thermodynamics to the global modelling of shallow foundations on frictional material,” *International Journal for Numerical and Analytical Methods in Geomechanics*, vol. 25, no. 14, pp. 1377–1408, 2001.

[154] C. Cremer, A. Pecker, and L. Davenne, “Cyclic macro-element for soil–structure interaction: material and geometrical non-linearities,” *International Journal for Numerical and Analytical Methods in Geomechanics*, vol. 25, no. 13, pp. 1257–1284, 2001.

[155] C. Cremer, A. Pecker, and L. Davenne, “Modelling of nonlinear dynamic behaviour of a shallow strip foundation with macro-element,” *Journal of Earthquake Engineering*, vol. 6, no. 02, pp. 175–211, 2002.

[156] C. Martin and G. Houlsby, “Combined loading of spudcan foundations on clay: laboratory tests,” *Géotechnique*, vol. 50, no. 4, pp. 325–338, 2000.

[157] C. Martin and G. Houlsby, “Combined loading of spudcan foundations on clay: numerical modelling,” *Géotechnique*, vol. 51, no. 8, pp. 687–699, 2001.

[158] G. T. Houlsby and M. J. Cassidy, “A plasticity model for the behaviour of footings on sand under combined loading,” *Géotechnique*, vol. 52, no. 2, pp. 117–129, 2002.

[159] M. Cassidy, C. Martin, and G. Houlsby, “Development and application of force resultant models describing jack-up foundation behaviour,” *Marine structures*, vol. 17, no. 3-4, pp. 165–193, 2004.

[160] G. Houlsby, M. Cassidy, and I. Einav, “A generalised winkler model for the behaviour of shallow foundations,” *Géotechnique*, vol. 55, no. 6, pp. 449–460, 2005.

[161] I. Einav and M. J. Cassidy, “A framework for modelling rigid footing behaviour based on energy principles,” *Computers and Geotechnics*, vol. 32, no. 7, pp. 491–504, 2005.

[162] D. Salciarini and C. Tamagnini, “A hypoplastic macroelement model for shallow foundations under monotonic and cyclic loads,” *Acta Geotechnica*, vol. 4, no. 3, pp. 163–176, 2009.

[163] C. Chatzigogos, A. Pecker, and J. Salencon, “Macroelement modeling of shallow foundations,” *Soil Dynamics and Earthquake Engineering*, vol. 29, no. 5, pp. 765–781, 2009.

[164] C. Chatzigogos, R. Figini, A. Pecker, and J. Salençon, “A macroelement formulation for shallow foundations on cohesive and frictional soils,” *International Journal for Numerical and Analytical Methods in Geomechanics*, vol. 35, no. 8, pp. 902–931, 2011.

[165] R. Figini, R. Paolucci, and C. Chatzigogos, “A macro-element model for non-linear soil–shallow foundation–structure interaction under seismic loads: theoretical development and experimental validation on large scale

tests," *Earthquake Engineering & Structural Dynamics*, vol. 41, no. 3, pp. 475–493, 2012.

[166] L. B. Ibsen, A. Barari, and K. A. Larsen, "Adaptive plasticity model for bucket foundations," *Journal of Engineering Mechanics*, vol. 140, no. 2, pp. 361–373, 2014.

[167] A. Foglia, G. Gottardi, L. Govoni, and L. B. Ibsen, "Modelling the drained response of bucket foundations for offshore wind turbines under general monotonic and cyclic loading," *Applied Ocean Research*, vol. 52, pp. 80–91, 2015.

[168] K. S. Skau, G. Grimstad, A. M. Page, G. R. Eiksund, and H. P. Jostad, "A macro-element for integrated time domain analyses representing bucket foundations for offshore wind turbines," *Marine Structures*, vol. 59, pp. 158–178, 2018.

[169] J. Tistel and G. Grimstad, "A macro model description of the non-linear anchor block foundation behavior," in *Insights and Innovations in Structural Engineering, Mechanics and Computation*, pp. 2078–2084, CRC Press, 2016.

[170] M. Millen, M. Cubrinovski, S. Pampanin, and A. Carr, "A macro-element for the modelling of shallow foundation deformations under seismic load," *Soil Dynamics and Earthquake Engineering*, vol. 106, pp. 101–112, 2018.

[171] A. Correia, "A pile-head macro-element approach to seismic design of monoshaft-supported bridges," *Unpublished PhD thesis). European School for Advanced Studies in Reduction of Seismic Risk (ROSE School), Pavia, Italy*, 2011.

[172] A. A. Correia and A. Pecker, "Nonlinear pile-head macro-element for the seismic analysis of structures on flexible piles," *Bulletin of Earthquake Engineering*, vol. 19, no. 4, pp. 1815–1849, 2021.

[173] Z. Li, P. Kotronis, S. Escoffier, and C. Tamagnini, "A hypoplastic macroelement for single vertical piles in sand subject to three-dimensional loading conditions," *Acta Geotechnica*, vol. 11, no. 2, pp. 373–390, 2016.

[174] Z. Li, P. Kotronis, S. Escoffier, and C. Tamagnini, "A hypoplastic macroelement formulation for single batter piles in sand," *International Journal for Numerical and Analytical Methods in Geomechanics*, vol. 42, no. 12, pp. 1346–1365, 2018.

[175] A. M. Page, G. Grimstad, G. R. Eiksund, and H. P. Jostad, “A macro-element pile foundation model for integrated analyses of monopile-based offshore wind turbines,” *Ocean Engineering*, vol. 167, pp. 23–35, 2018.

[176] B. W. Byrne, R. A. McAdam, H. J. Burd, G. T. Houlsby, C. M. Martin, W. J. P. Beuckelaers, L. Zdravkovic, D. Taborda, D. Potts, R. Jardine, *et al.*, “Pisa: new design methods for offshore wind turbine monopiles,” *Offshore Site Investigation Geotechnics 8th International Conference Proceeding*, pp. 142–161, 2017.

[177] J. Pérez-Herreros, *Dynamic soil-structure interaction of pile foundations: experimental and numerical study*. PhD thesis, École centrale de Nantes, 2020.

[178] Z. Li, *Etude expérimentale et numérique de fondations profondes sous sollicitations sismiques: pieux verticaux et pieux inclinés*. PhD thesis, Ecole Centrale de Nantes, 2014.

[179] C. Medina, L. A. Padrón, J. J. Aznárez, A. Santana, and O. Maeso, “Kinematic interaction factors of deep foundations with inclined piles,” *Earthquake engineering & structural dynamics*, vol. 43, no. 13, pp. 2035–2050, 2014.

[180] F. Dezi, S. Carbonari, and M. Morici, “A numerical model for the dynamic analysis of inclined pile groups,” *Earthquake Engineering & Structural Dynamics*, vol. 45, no. 1, pp. 45–68, 2016.

[181] S. Carbonari, M. Morici, F. Dezi, and G. Leoni, “Analytical evaluation of impedances and kinematic response of inclined piles,” *Engineering Structures*, vol. 117, pp. 384–396, 2016.

[182] M. N. Hussien, M. Karray, T. Tobita, and S. Iai, “Kinematic and inertial forces in pile foundations under seismic loading,” *Computers and Geotechnics*, vol. 69, pp. 166–181, 2015.

[183] S. Brandenberg, B. Turner, and J. Stewart, “Influence of kinematic ssi on foundation input motions for pile-supported bridges,” 2017.

[184] Y. Wang and R. P. Orense, “Numerical analysis of seismic performance of inclined piles in liquefiable sands,” *Soil Dynamics and Earthquake Engineering*, vol. 139, p. 106274, 2020.

[185] J. Rajeswari and R. Sarkar, “A three-dimensional investigation on performance of batter pile groups in laterally spreading ground,” *Soil Dynamics and Earthquake Engineering*, vol. 141, p. 106508, 2021.

[186] F. McKenna, M. H. Scott, and G. L. Fenves, “Nonlinear finite-element analysis software architecture using object composition,” *Journal of Computing in Civil Engineering*, vol. 24, no. 1, pp. 95–107, 2010.

[187] ASDEA Software, “Stko 2021 v.2.0.5,” 2020. Pre- and postprocessing tool kit for OpenSees.

[188] Q. Gu, J. P. Conte, A. Elgamal, and Z. Yang, “Finite element response sensitivity analysis of multi-yield-surface j2 plasticity model by direct differentiation method,” *Computer methods in applied mechanics and engineering*, vol. 198, no. 30-32, pp. 2272–2285, 2009.

[189] G. Mesri, “New design procedure for stability of soft clays,” *Journal of Geotechnical and Geoenvironmental Engineering*, vol. 101, no. Discussion, 1975.

[190] K. H. Andersen, “Cyclic soil parameters for offshore foundation design,” *Frontiers in offshore geotechnics III*, vol. 5, 2015.

[191] M. D’Amato, F. Braga, R. Gigliotti, S. Kunnath, and M. Laterza, “A numerical general-purpose confinement model for non-linear analysis of r/c members,” *Computers & structures*, vol. 102, pp. 64–75, 2012.

[192] I. D. Karsan and J. O. Jirsa, “Behavior of concrete under compressive loadings,” *Journal of the Structural Division*, vol. 95, no. 12, pp. 2543–2564, 1969.

[193] F. C. Filippou, E. P. Popov, and V. V. Bertero, “Effects of bond deterioration on hysteretic behavior of reinforced concrete joints,” 1983.

[194] R. Sarkar and B. Maheshwari, “Effects of separation on the behavior of soil-pile interaction in liquefiable soils,” *International Journal of Geomechanics*, vol. 12, no. 1, pp. 1–13, 2012.

[195] A. Rahmani and A. Pak, “Dynamic behavior of pile foundations under cyclic loading in liquefiable soils,” *Computers and Geotechnics*, vol. 40, pp. 114–126, 2012.

[196] K. Kanellopoulos and G. Gazetas, “Vertical static and dynamic pile-to-pile interaction in non-linear soil,” *Géotechnique*, vol. 70, no. 5, pp. 432–447, 2020.

[197] J. Oliver, A. E. Huespe, and J. Cante, “An implicit/explicit integration scheme to increase computability of non-linear material and contact/friction problems,” *Computer Methods in Applied Mechanics and Engineering*, vol. 197, no. 21-24, pp. 1865–1889, 2008.

[198] J. F. Hall, “Problems encountered from the use (or misuse) of rayleigh damping,” *Earthquake engineering & structural dynamics*, vol. 35, no. 5, pp. 525–545, 2006.

[199] F. A. Charney, “Unintended consequences of modeling damping in structures,” *Journal of structural engineering*, vol. 134, no. 4, pp. 581–592, 2008.

[200] L. Petrini, C. Maggi, M. N. Priestley, and G. M. Calvi, “Experimental verification of viscous damping modeling for inelastic time history analyzes,” *Journal of Earthquake Engineering*, vol. 12, no. S1, pp. 125–145, 2008.

[201] F. Serón, F. Sanz, M. Kindelan, and J. Badal, “Finite-element method for elastic wave propagation,” *Communications in applied numerical methods*, vol. 6, no. 5, pp. 359–368, 1990.

[202] J. Lysmer and R. L. Kuhlemeyer, “Finite dynamic model for infinite media,” *Journal of the Engineering Mechanics Division*, vol. 95, no. 4, pp. 859–878, 1969.

[203] O. Zienkiewicz, N. Bicanic, and F. Shen, “Earthquake input definition and the trasmitting boundary conditions,” in *Advances in computational nonlinear mechanics*, pp. 109–138, Springer, 1989.

[204] H. M. Hilber, T. J. Hughes, and R. L. Taylor, “Improved numerical dissipation for time integration algorithms in structural dynamics,” *Earthquake Engineering & Structural Dynamics*, vol. 5, no. 3, pp. 283–292, 1977.

[205] H. M. Hilber and T. J. Hughes, “Collocation, dissipation and [overshoot] for time integration schemes in structural dynamics,” *Earthquake Engineering & Structural Dynamics*, vol. 6, no. 1, pp. 99–117, 1978.

[206] N. M. Newmark, “A method of computation for structural dynamics,” *Journal of the engineering mechanics division*, vol. 85, no. 3, pp. 67–94, 1959.

[207] K.-J. Bathe, “Conserving energy and momentum in nonlinear dynamics: a simple implicit time integration scheme,” *Computers & structures*, vol. 85, no. 7-8, pp. 437–445, 2007.

[208] M. H. Scott and G. L. Fenves, “Krylov subspace accelerated newton algorithm: application to dynamic progressive collapse simulation of frames,” *Journal of Structural Engineering*, vol. 136, no. 5, pp. 473–480, 2010.

[209] H. G. Poulos, “Raked piles - virtues and drawbacks,” *Journal of geotechnical and geoenvironmental engineering*, vol. 132, no. 6, pp. 795–803, 2006.

[210] C. Medina, J. J. Aznárez, L. A. Padrón, and O. Maeso, “Seismic response of deep foundations and piled structures considering inclined piles,” in *11th World Congress on Computational Mechanics, WCCM 2014, 5th European Conference on Computational Mechanics, ECCM 2014 and 6th European Conference on Computational Fluid Dynamics, ECFD 2014*, 2014.

[211] R. Dobry and G. Gazetas, “Simple method for dynamic stiffness and damping of floating pile groups,” *Geotechnique*, vol. 38, no. 4, pp. 557–574, 1988.

[212] G. Gazetas and N. Makris, “Dynamic pile-soil-pile interaction. part i: Analysis of axial vibration,” *Earthquake Engineering & Structural Dynamics*, vol. 20, no. 2, pp. 115–132, 1991.

[213] N. Makris and G. Gazetas, “Displacement phase differences in a harmonically oscillating pile,” *Geotechnique*, vol. 43, no. 1, pp. 135–150, 1993.

[214] G. Mylonakis and G. Gazetas, “Lateral vibration and internal forces of grouped piles in layered soil,” *Journal of Geotechnical and Geoenvironmental Engineering*, vol. 125, no. 1, pp. 16–25, 1999.

[215] I. Takewaki and A. Kishida, “Efficient analysis of pile-group effect on seismic stiffness and strength design of buildings,” *Soil Dynamics and Earthquake Engineering*, vol. 25, no. 5, pp. 355–367, 2005.

[216] J. Wang, S. Lo, and D. Zhou, “Effect of a forced harmonic vibration pile to its adjacent pile in layered elastic soil with double-shear model,” *Soil Dynamics and Earthquake Engineering*, vol. 67, pp. 54–65, 2014.

[217] H. Ghasemzadeh and M. Alibeikloo, “Pile–soil–pile interaction in pile groups with batter piles under dynamic loads,” *Soil Dynamics and Earthquake Engineering*, vol. 31, no. 8, pp. 1159–1170, 2011.

[218] M. Ghazavi, P. Ravanshenas, and M. H. El Naggar, “Interaction between inclined pile groups subjected to harmonic vibrations,” *Soils and foundations*, vol. 53, no. 6, pp. 789–803, 2013.

[219] J. Wang, D. Zhou, T. Ji, and S. Wang, “Horizontal dynamic stiffness and interaction factors of inclined piles,” *International Journal of Geomechanics*, vol. 17, no. 9, p. 04017075, 2017.

[220] C. Goit and M. Saitoh, “Experimental approach on the pile-to-pile interaction factors and impedance functions of inclined piles,” *Géotechnique*, vol. 66, no. 11, pp. 888–901, 2016.

[221] G. Gazetas and R. Dobry, “Simple radiation damping model for piles and footings,” *Journal of Engineering Mechanics*, vol. 110, no. 6, pp. 937–956, 1984.

[222] H. G. Poulos, E. H. Davis, *et al.*, *Pile foundation analysis and design*, vol. 397. Wiley New York, 1980.

[223] Mathworks, “Matlab r2019a 9.6.0.1072779,” 2019. Programming platform designed for engineers and scientists.

[224] J. Radhima, K. Kanellopoulos, and G. Gazetas, “Static and dynamic lateral non-linear pile–soil–pile interaction,” *Geotechnique*, pp. 1–16, 2021.

[225] G. Van Rossum and F. L. Drake, *Python 3 Reference Manual*. Scotts Valley, CA: CreateSpace, 2009.

[226] L. Zdravković, R. J. Jardine, D. M. Taborda, D. Abadias, H. J. Burd, B. W. Byrne, K. G. Gavin, G. T. Houlsby, D. J. Igoe, T. Liu, *et al.*, “Ground characterisation for pisa pile testing and analysis,” *Géotechnique*, vol. 70, no. 11, pp. 945–960, 2020.

[227] R.-P. Chen, C.-Y. Peng, J.-F. Wang, and H.-L. Wang, “Field experiments on cyclic behaviors of axially loaded piles jacked in soft clay,” *Journal of Geotechnical and Geoenvironmental Engineering*, vol. 147, no. 3, p. 04020176, 2021.

[228] O. F. E. H. Drbe and M. H. El Naggar, “Axial monotonic and cyclic compression behaviour of hollow-bar micropiles,” *Canadian geotechnical journal*, vol. 52, no. 4, pp. 426–441, 2015.

[229] L. S. Jacobsen, “Damping in composite structures,” *II WCEE, Tokyo, 1960*, 1960.

[230] B. Chiou, R. Darragh, N. Gregor, and W. Silva, “Nga project strong-motion database,” *Earthquake Spectra*, vol. 24, no. 1, pp. 23–44, 2008.

[231] R. D. Cook *et al.*, *Concepts and applications of finite element analysis*. John wiley & sons, 2007.

[232] A. K. Chopra *et al.*, *Dynamics of structures*. Pearson Education Upper Saddle River, NJ, 2012.

[233] T. J. Hughes, *The finite element method: linear static and dynamic finite element analysis*. Courier Corporation, 2012.

[234] J. Simo and M. Ortiz, “A unified approach to finite deformation elastoplastic analysis based on the use of hyperelastic constitutive equations,” *Computer methods in applied mechanics and engineering*, vol. 49, no. 2, pp. 221–245, 1985.

[235] M. Ortiz and J. Simo, “An analysis of a new class of integration algorithms for elastoplastic constitutive relations,” *International journal for numerical methods in engineering*, vol. 23, no. 3, pp. 353–366, 1986.

[236] J. C. Simo and T. J. Hughes, *Computational inelasticity*, vol. 7. Springer Science & Business Media, 2006.

[237] J. Lysmer, F. Ostadan, and C. C. Chin, *A system for analysis of soil-structure interaction*. Geotechnical Engineering Division, Civil Engineering Department, University . . . , 2000.

[238] R. V. Whitman and R. Dobry, “Modal analysis for structures with foundation interaction,” 1972.

[239] J. M. Roesset, R. V. Whitman, and R. Dobry, “Modal analysis for structures with foundation interaction,” *Journal of the Structural Division*, vol. 99, no. 3, pp. 399–416, 1973.

[240] J. Bielak, “Modal analysis for building-soil interaction,” *Journal of the Engineering Mechanics Division*, vol. 102, no. 5, pp. 771–786, 1976.

[241] B. Kolias, M. N. Fardis, A. Pecker, and H. Gulvanessian, “Designers’ guide to eurocode 8: design of bridges for earthquake resistance,” *Designers’ Guide to Eurocodes*, 2012.

[242] S. Dhar and K. Dasgupta, "Seismic soil structure interaction for integral abutment bridges: a review," *Transportation Infrastructure Geotechnology*, vol. 6, no. 4, pp. 249–267, 2019.

[243] S. A. Mitoulis, "Challenges and opportunities for the application of integral abutment bridges in earthquake-prone areas: A review," *Soil Dynamics and Earthquake Engineering*, vol. 135, p. 106183, 2020.

[244] D. Vamvatsikos and C. A. Cornell, "Incremental dynamic analysis," *Earthquake Engineering & Structural Dynamics*, vol. 31, no. 3, pp. 491–514, 2002.

[245] P. Code, "Eurocode 8: Design of structures for earthquake resistance-part 1: general rules, seismic actions and rules for buildings," *Brussels: European Committee for Standardization*, 2005.

[246] J. Zhang and N. Makris, "Kinematic response functions and dynamic stiffnesses of bridge embankments," *Earthquake Engineering & Structural Dynamics*, vol. 31, no. 11, pp. 1933–1966, 2002.

Appendix A

Base force/moment from NTHA ($\beta = 15^0$ and $S_0 = 5m$)

The plots in this appendix show the hysteretic force-displacement and moment-rotation curves for each nonlinear time history analysis (NTHA). Note that the forces and moments are a third of the actual value due to an error (which has since been resolved) in the post-processing module.

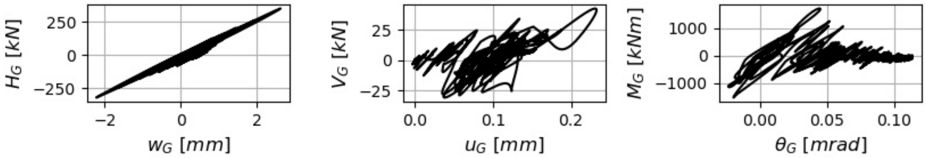

(a) $PGA = 0.1g$

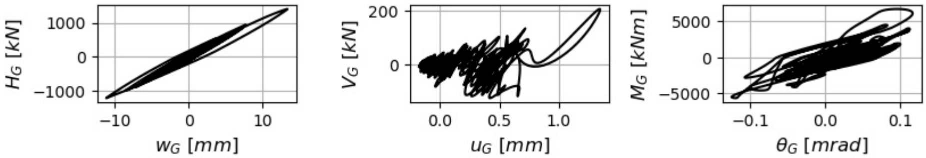

(b) $PGA = 0.4g$

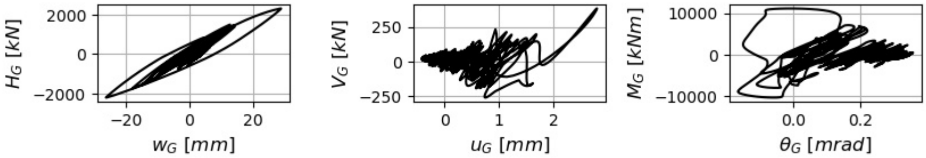

(c) $PGA = 0.7g$

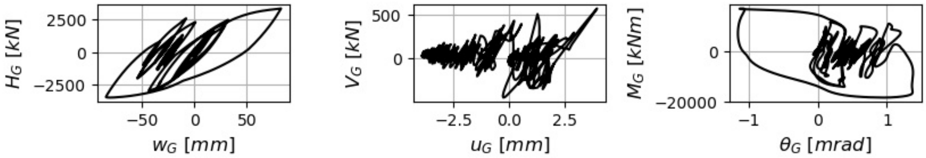

(d) $PGA = 1.3g$

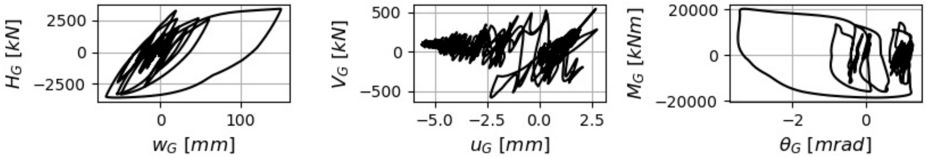

(e) $PGA = 1.6g$

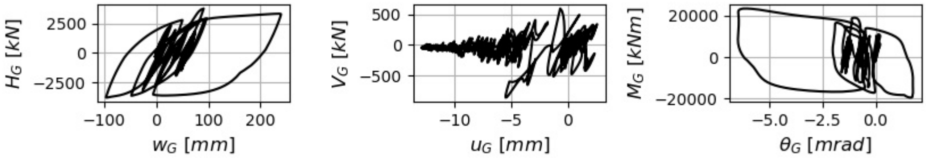

(f) $PGA = 1.9g$

Figure A.1: Foundation response for Imperial Valley-06 (USA, 1979)

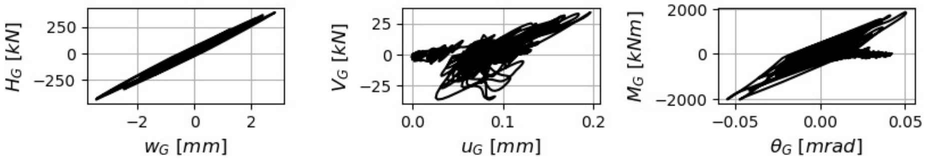

(a) $PGA = 0.1g$

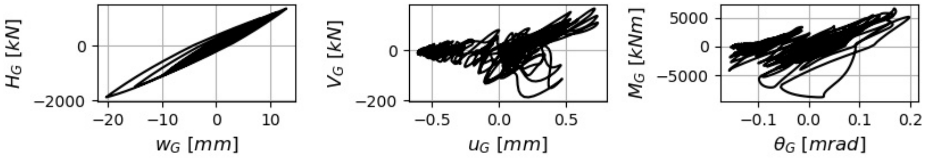

(b) $PGA = 0.4g$

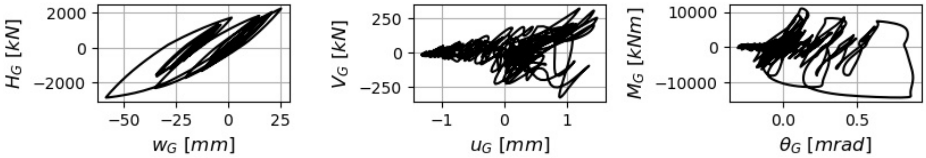

(c) $PGA = 0.7g$

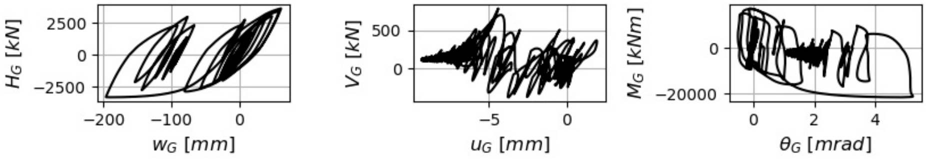

(d) $PGA = 1.3g$

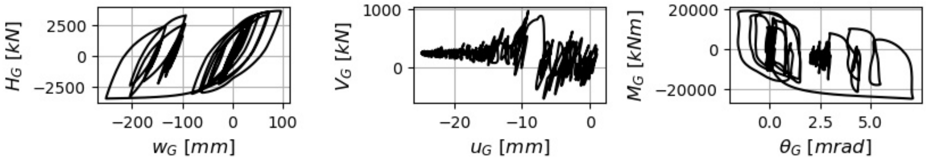

(e) $PGA = 1.6g$

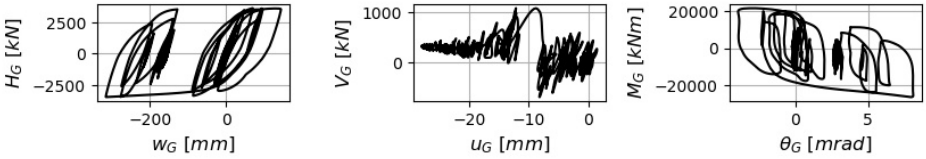

(f) $PGA = 1.9g$

Figure A.2: Foundation response for Coalinga-01 (USA, 1983)

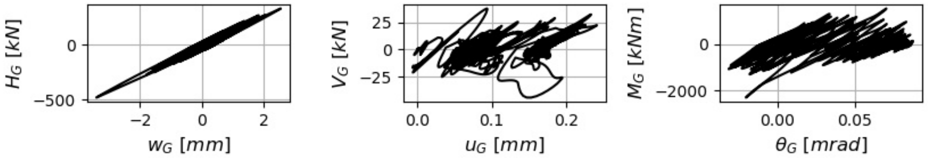

(a) $PGA = 0.1g$

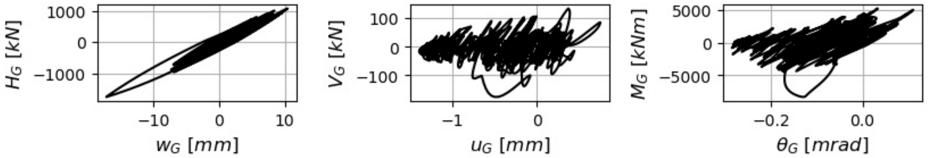

(b) $PGA = 0.4g$

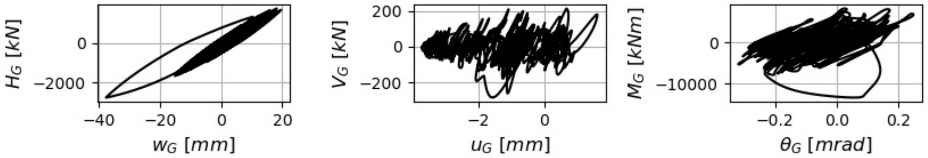

(c) $PGA = 0.7g$

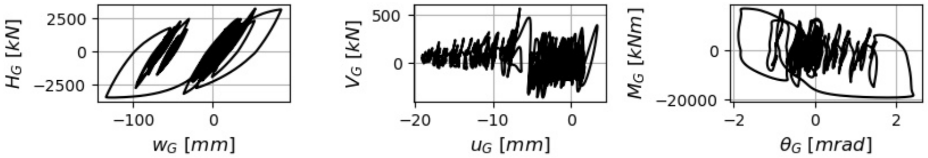

(d) $PGA = 1.3g$

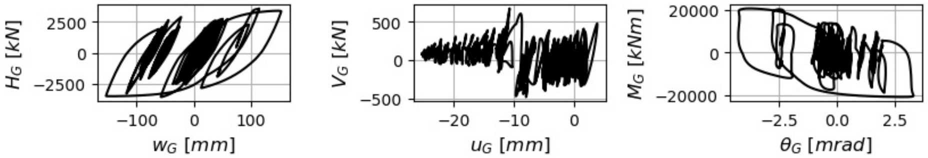

(e) $PGA = 1.6g$

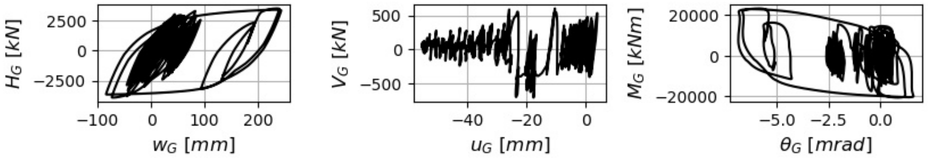

(f) $PGA = 1.9g$

Figure A.3: Foundation response for Morgan Hill (USA, 1984)

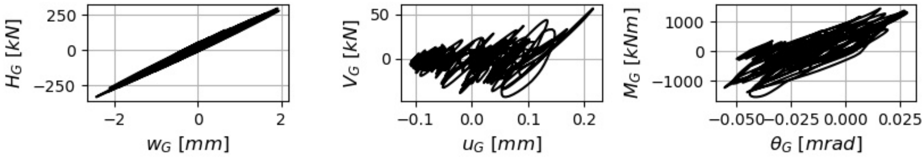

(a) $PGA = 0.1g$

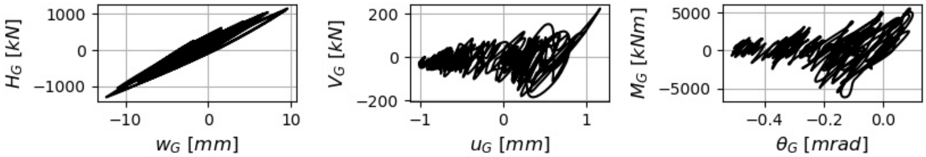

(b) $PGA = 0.4g$

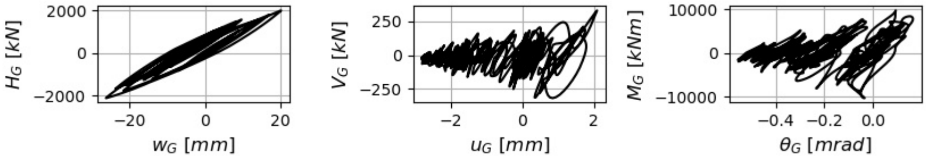

(c) $PGA = 0.7g$

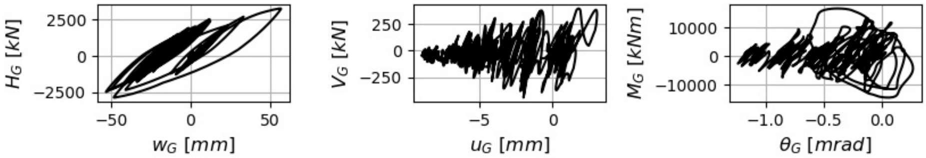

(d) $PGA = 1.3g$

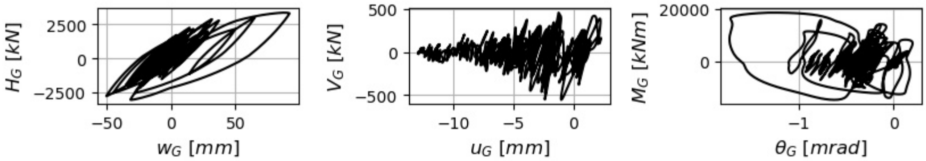

(e) $PGA = 1.6g$

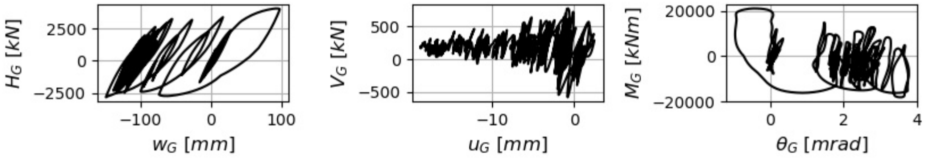

(f) $PGA = 1.9g$

Figure A.4: Foundation response for Superstition Hills-01 (USA, 1987)

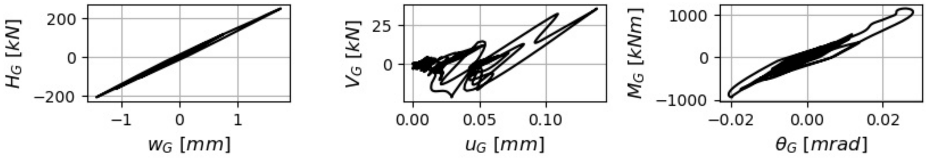

(a) $PGA = 0.1g$

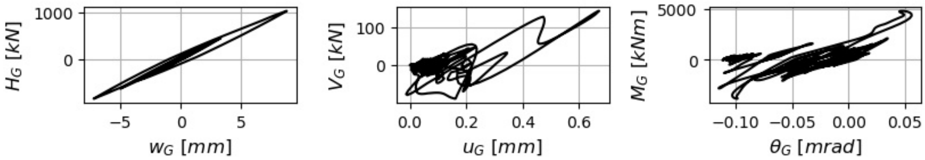

(b) $PGA = 0.4g$

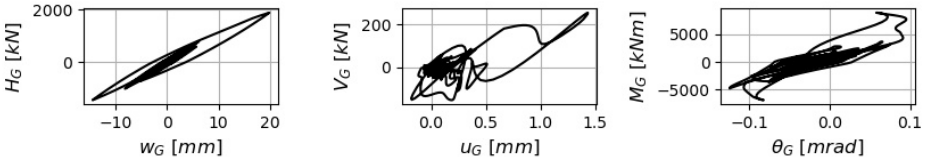

(c) $PGA = 0.7g$

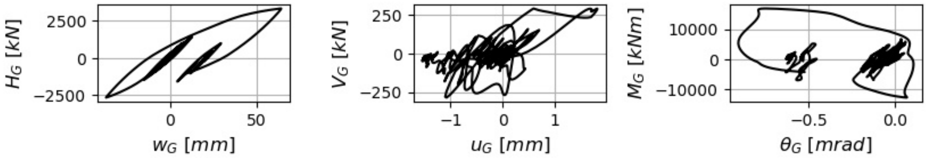

(d) $PGA = 1.3g$

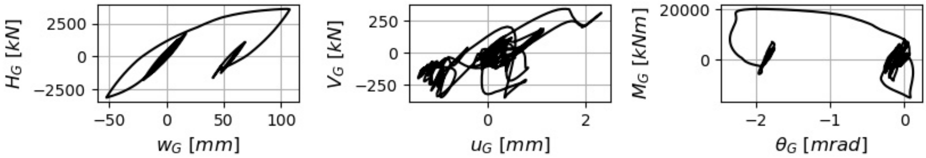

(e) $PGA = 1.6g$

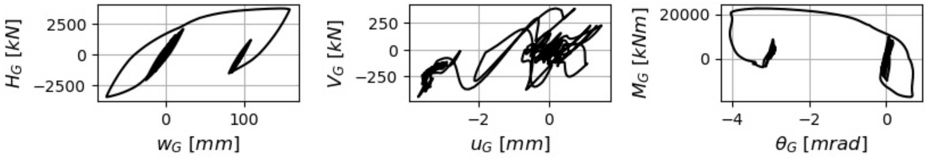

(f) $PGA = 1.9g$

Figure A.5: Foundation response for Loma Prieta (USA, 1989)

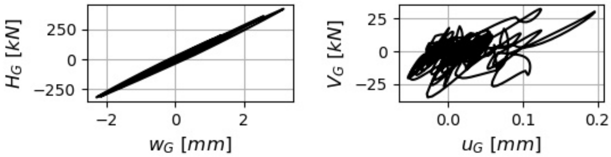

(a) $PGA = 0.1g$

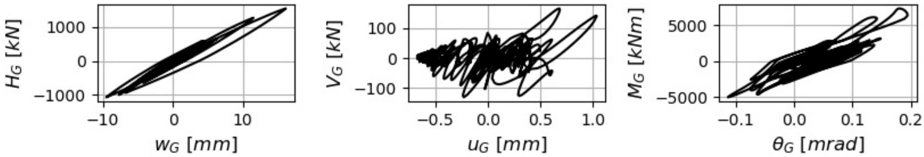

(b) $PGA = 0.4g$

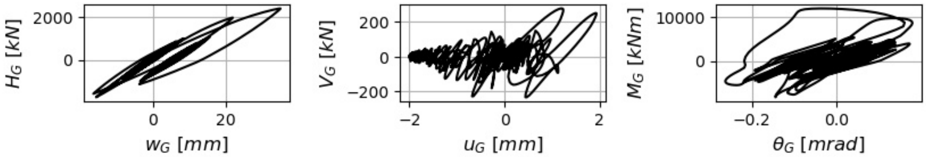

(c) $PGA = 0.7g$

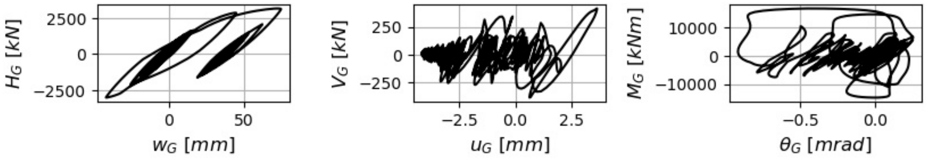

(d) $PGA = 1.3g$

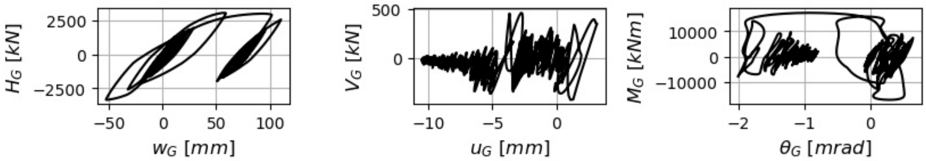

(e) $PGA = 1.6g$

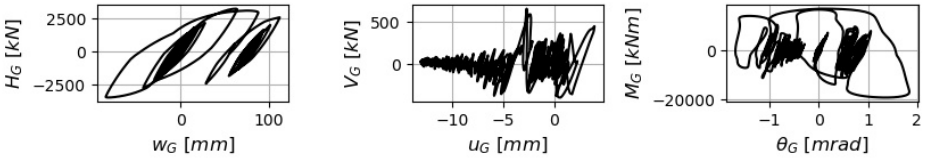

(f) $PGA = 1.9g$

Figure A.6: Foundation response for Northridge-01 (USA, 1994)

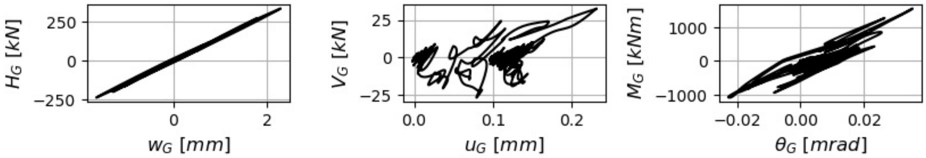

(a) $PGA = 0.1g$

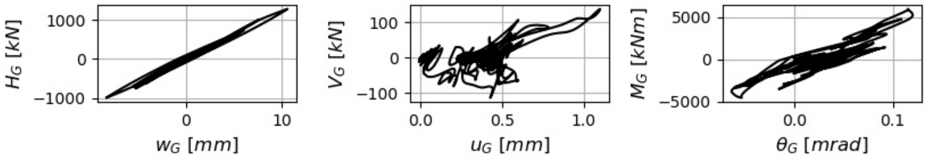

(b) $PGA = 0.4g$

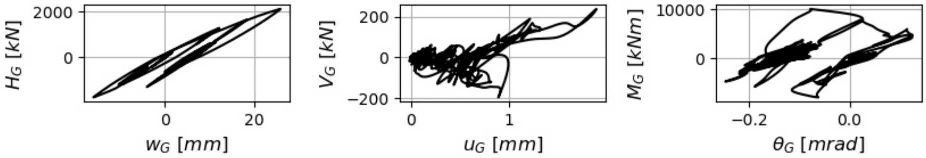

(c) $PGA = 0.7g$

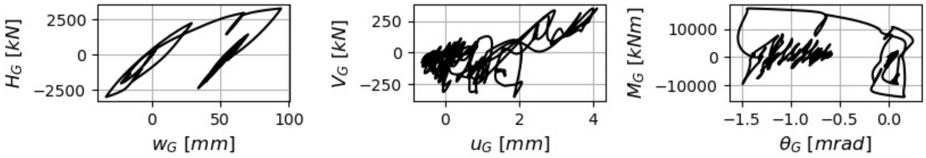

(d) $PGA = 1.3g$

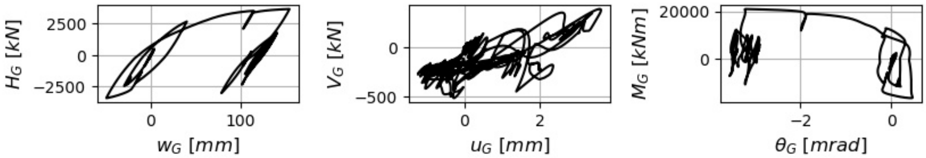

(e) $PGA = 1.6g$

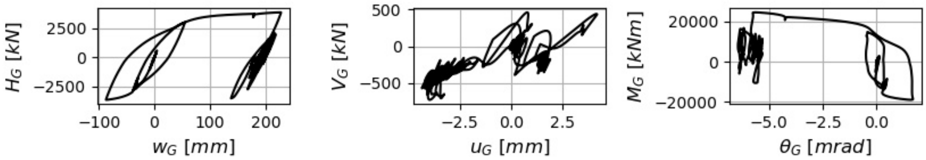

(f) $PGA = 1.9g$

Figure A.7: Foundation response for Kobe (Japan, 1995)

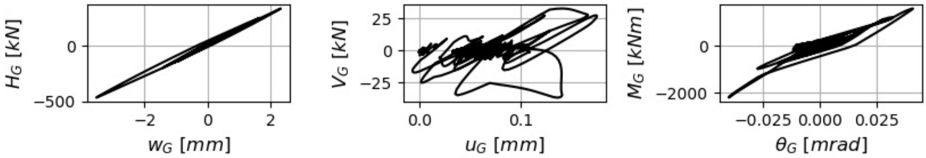

(a) $PGA = 0.1g$

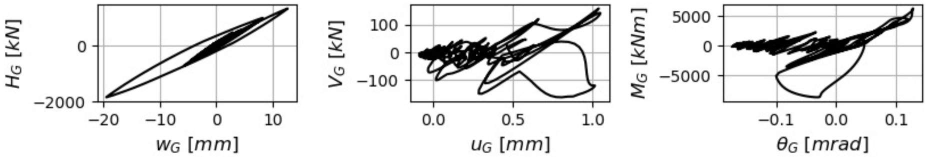

(b) $PGA = 0.4g$

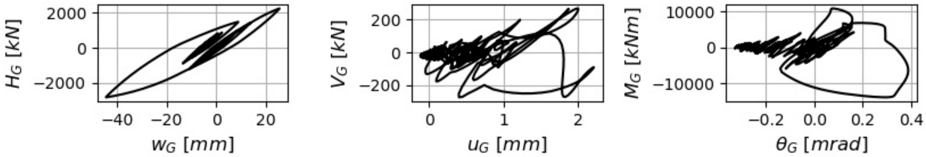

(c) $PGA = 0.7g$

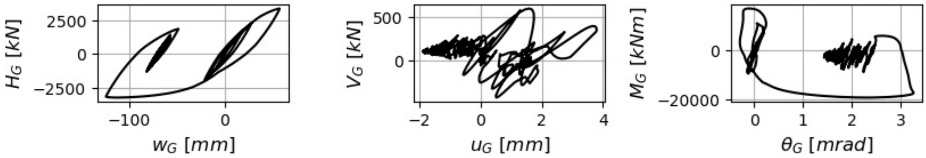

(d) $PGA = 1.3g$

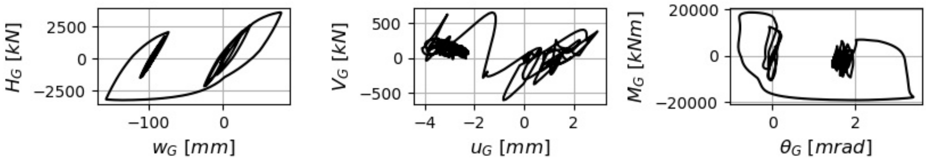

(e) $PGA = 1.6g$

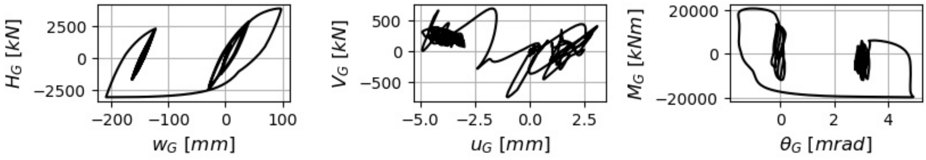

(f) $PGA = 1.9g$

Figure A.8: Foundation response for Parkfield-02 (USA, 2004)

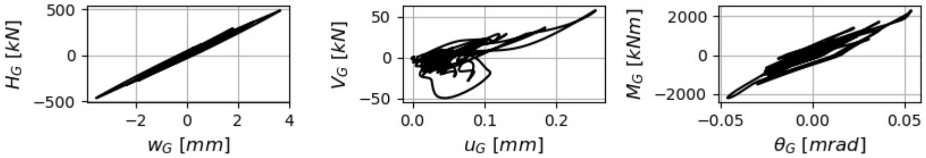

(a) $PGA = 0.1g$

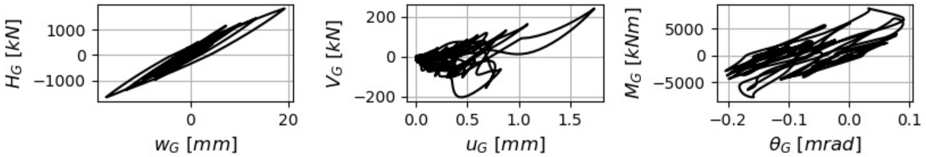

(b) $PGA = 0.4g$

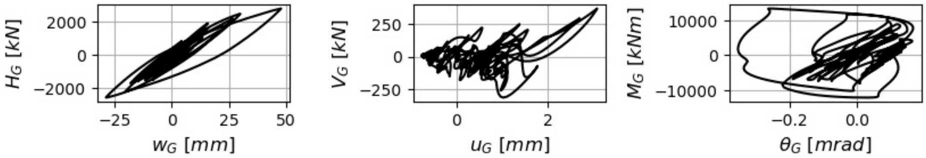

(c) $PGA = 0.7g$

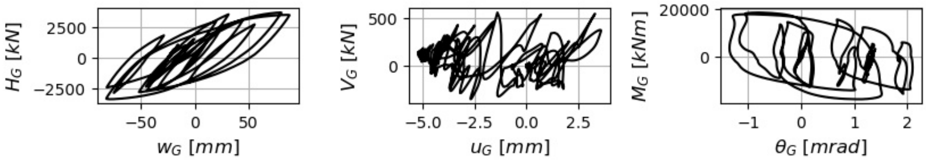

(d) $PGA = 1.3g$

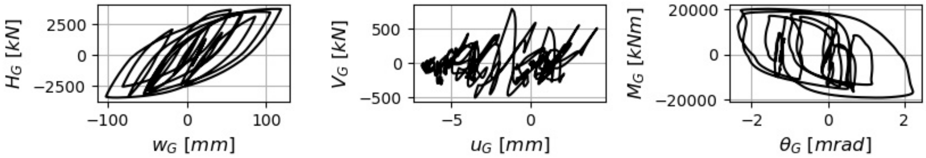

(e) $PGA = 1.6g$

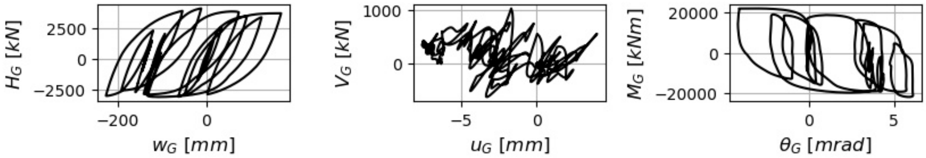

(f) $PGA = 1.9g$

Figure A.9: Foundation response for Christchurch (New Zealand, 2011)

ISBN 978-82-326-7096-3 (printed ver.)
ISBN 978-82-326-7095-6 (electronic ver.)
ISSN 1503-8181 (printed ver.)
ISSN 2703-8084 (online ver.)

NTNU
Norwegian University of
Science and Technology